Lecture Notes in Production Engineering

Ekkard Brinksmeier
Lars Schönemann *Editors*

Ultra-precision High Performance Cutting

Report of DFG Research Unit FOR 1845

Springer

Lecture Notes in Production Engineering

Lecture Notes in Production Engineering (LNPE) is a new book series that reports the latest research and developments in Production Engineering, comprising:

- Biomanufacturing
- Control and Management of Processes
- Cutting and Forming
- Design
- Life Cycle Engineering
- Machines and Systems
- Optimization
- Precision Engineering and Metrology
- Surfaces

LNPE publishes authored conference proceedings, contributed volumes and authored monographs that present cutting-edge research information as well as new perspectives on classical fields, while maintaining Springer's high standards of excellence. Also considered for publication are lecture notes and other related material of exceptionally high quality and interest. The subject matter should be original and timely, reporting the latest research and developments in all areas of production engineering. The target audience of LNPE consists of advanced level students, researchers, as well as industry professionals working at the forefront of their fields. Much like Springer's other Lecture Notes series, LNPE will be distributed through Springer's print and electronic publishing channels. To submit a proposal or request further information please contact Anthony Doyle, Executive Editor, Springer (anthony.doyle@springer.com).

More information about this series at http://www.springer.com/series/10642

Ekkard Brinksmeier · Lars Schönemann
Editors

Ultra-precision High Performance Cutting

Report of DFG Research Unit FOR 1845

Springer

Editors
Ekkard Brinksmeier
Universität Bremen
Bremen, Germany

Lars Schönemann
Leibniz Institute for Materials Engineering
IWT
Bremen, Germany

ISSN 2194-0525 ISSN 2194-0533 (electronic)
Lecture Notes in Production Engineering
ISBN 978-3-030-83764-8 ISBN 978-3-030-83765-5 (eBook)
https://doi.org/10.1007/978-3-030-83765-5

© The Editor(s) (if applicable) and The Author(s), under exclusive license
to Springer Nature Switzerland AG 2022
This work is subject to copyright. All rights are solely and exclusively licensed by the Publisher, whether the whole or part of the material is concerned, specifically the rights of translation, reprinting, reuse of illustrations, recitation, broadcasting, reproduction on microfilms or in any other physical way, and transmission or information storage and retrieval, electronic adaptation, computer software, or by similar or dissimilar methodology now known or hereafter developed.
The use of general descriptive names, registered names, trademarks, service marks, etc. in this publication does not imply, even in the absence of a specific statement, that such names are exempt from the relevant protective laws and regulations and therefore free for general use.
The publisher, the authors and the editors are safe to assume that the advice and information in this book are believed to be true and accurate at the date of publication. Neither the publisher nor the authors or the editors give a warranty, expressed or implied, with respect to the material contained herein or for any errors or omissions that may have been made. The publisher remains neutral with regard to jurisdictional claims in published maps and institutional affiliations.

This Springer imprint is published by the registered company Springer Nature Switzerland AG
The registered company address is: Gewerbestrasse 11, 6330 Cham, Switzerland

Foreword

Although precision manufacturing has a long history, the emergence of precision manufacturing optical surfaces using diamond tools was the result of multiple independent developments from the 1900s through the 1940s. By 1974, precision engineering, and the term nanotechnology, coined by Professor Norio Taniguchi and later quantified by Professor Patrick McKeown as manufacturing accuracy progressed from 1 part in 10^4 to 1 part in 10^8 (typically the ratio of the largest characteristic dimension to the form accuracy). Subsequently, the Royal Society and the Royal Academy of Engineering defined nanomanufacturing as production of structures with form accuracy essential to functional performance better than 100 nm.

Ultra-precision high performance cutting (UP-HPC) adds another critical constraint, which is cost-effective manufacture. Cost is one of the two basic limitations to future advances in ultra-precision manufacturing described by Erwin Loewen. Commercial applications have continued to drive the remarkable growth of ultra-precision machining over the last 80 years. Starting with aspheric Schmidt plate molds, commercial drivers progressed to aspheric camera lens molds, intraocular lenses, contact lens molds, and structured surface enhancing films. Today, molds for cell phone camera lenses, automotive head-up displays, and automotive lighting are just a few of the consumer applications with form accuracy better than 100 nm while exceeding 1 part in 10^5 tolerance ratios.

An indispensable force enabling this continued growth is the relationship between research institutes and industry. While industry must recognize new ultra-precision manufacturing opportunities, research institutes must accept the associated risk of developing new tools and processes with their deeper understanding and detailed analyses. Researchers must demonstrate feasibility of novel processes and allow industry to focus on implementations that satisfy the requirements of the market cost effectively.

Such is the case with this exemplary work funded by the German Research Foundation and directed by Professor Dr.-Ing. Ekkard Brinksmeier and Dr.-Ing. Lars Schönemann in collaboration with researchers from Bremen University and the Leibniz University Hannover. Beginning with an ingenious design using multiple diamond tools and thermal positioning, they have attacked the productivity problem at the source. Next, they have demonstrated the benefits of diamond machining metals and semiconductor materials at high speed. This is followed by an ambitious project to implement an electromagnetic linear stage for high precision machining. They have developed and demonstrated several tools which automatically balance a high-speed spindle to precision grades to eliminate time-consuming manual balancing. Finally, all of these improvements are enhanced by the development of a new control strategy to enable increased axis speeds for ultra-precision high performance cutting.

For more than 30 years, Professor Brinksmeier and his collaborators have addressed critical technology gaps in ultra-precision manufacturing. Their legacy includes unique solutions to some of our most difficult manufacturing challenges as well as producing an entire generation of precision engineers with contributions to international audiences at JSPE, ASPE, and euspen. Although it is difficult to predict what the driving markets for ultra-precision manufacturing will be in the coming years, it is clear that a cooperative relationship between research institutes and industry continues to be necessary.

March 2021

Byron R. Knapp
Senior Engineer

Preface

This book comprises recent results for increasing the performance of ultra-precision machining processes, focusing on diamond milling. It primarily serves as the final report of the German research unit FOR1845 "Ultra-precision High Performance Cutting" funded by the German Research Foundation (DFG) from April 2014 to June 2020, which is gratefully acknowledged by the authors. At the same time, the book also reveals remarkable results and potentials for further developments of ultra-precision machining and thus addresses both, scientists and industry.

The idea of increasing the performance of ultra-precision machining processes by the application of extremely high cutting speeds was forged by Prof. Ekkard Brinksmeier and Dr. Werner Preuß from the Laboratory for Precision Machining (LFM) in Bremen already in 2010. It quickly became clear that the research field for achieving this goal is not solely focused on the machining processes, but entails machine tool technology and software/control design as well. Thus, Prof. Berend Denkena from the Institute for Production Engineering and Machine Tools at the Leibniz University Hannover and Prof. Bernd Kuhfuss from the Machine Tool Department of Bremen University were asked to join the effort for proposing a joint research group. After several rounds of discussion, five relevant topics were identified and shaped into project proposals. After review by the DFG, funding was granted and the research began in the year 2014 under the technical leadership of Dr. Lars Schönemann, LFM Bremen. Detailed descriptions of the research results gained over the past 6 1/2 years can be found in this book. Some of the initial goals of the research unit were very visionary. Even if some limitations had to be accepted in the implementation, the results achieved clearly show promising paths for a more economical ultra-precision manufacturing. This should be an inspiration for all of us to build on what we have achieved and to continue to develop these advanced technologies.

During the course of the research unit, more than 20 researchers and technicians as well as numerous students were involved in the research work and contributed to the overall goal of increasing the performance of ultra-precision machining by writing their theses, presenting the work at numerous conferences, and publishing the results in relevant journals as well as this book. Their support and dedication to this work are highly appreciated.

April 2021

Ekkard Brinksmeier
Lars Schönemann

Contents

List of Contributors

Daniel Berger MAPEX Center for Materials and Processes, University of Bremen, Bremen, Germany;
Leibniz Institute for Materials Engineering IWT, Bremen, Germany

Benjamin Bergmann Institute of Production Engineering and Machine Tools IFW, Leibniz University Hannover, Garbsen, Germany

Ekkard Brinksmeier Leibniz Institute for Materials Engineering IWT, Bremen, Germany;
MAPEX Center for Materials and Processes, University of Bremen, Bremen, Germany

Berend Denkena Institute of Production Engineering and Machine Tools IFW, Leibniz University Hannover, Garbsen, Germany

Timo Dörgeloh Leibniz Institute for Materials Engineering IWT, Bremen, Germany

Johannes Hochbein Bremen Institute for Mechanical Engineering bime and MAPEX Center for Materials and Processes, University of Bremen, Bremen, Germany

Rudolf Krüger Institute of Production Engineering and Machine Tools IFW, Leibniz University Hannover, Garbsen, Germany

Bernd Kuhfuss Bremen Institute for Mechanical Engineering bime and MAPEX Center for Materials and Processes, University of Bremen, Bremen, Germany

Nasrin Parsa Bremen Institute for Mechanical Engineering bime and MAPEX Center for Materials and Processes, University of Bremen, Bremen, Germany

Oltmann Riemer Leibniz Institute for Materials Engineering IWT, Bremen, Germany;
MAPEX Center for Materials and Processes, University of Bremen, Bremen, Germany

Lars Schönemann Leibniz Institute for Materials Engineering IWT, Bremen, Germany;
MAPEX Center for Materials and Processes, University of Bremen, Bremen, Germany

Christian Schenck Bremen Institute for Mechanical Engineering bime and MAPEX Center for Materials and Processes, University of Bremen, Bremen, Germany

Per Schreiber Institute of Production Engineering and Machine Tools IFW, Leibniz University Hannover, Garbsen, Germany

Acronyms

42CrMo4	heat treatable steel type 1.7225/AISI 4140/42CrMo4
AE	acoustic emission
AFM	atomic force microscope
AlMg3	aluminium 3.3535/EN AW-5754/AlMg3
AlMg5	aluminium 3.3555/EN AW-5019/AlMg5
ARM	advanced RISC machines
ASPE	The American Society for Precision Engineering
CCLD	constant current line drive
CEEMD	complementary ensemble empirical mode decomposition
CHR	control parameter calculation method according to Chien, Hrones and Reswick
CIRP	The International Academy for Production Engineering (French: Collège International pour la Recherche en Productique)
CNC	computer numerical control
CPU	central processing unit
CuNi18Zn19Pb1	nickel silver CuNi18Zn19Pb1
CUPE	Cranfield Unit for Precision Engineering
CuZn30	brass 2.0265/EN CW505L/CuZn30
CuZn39Pb3	brass 2.0401/EN CW614N/CuZn39Pb3/MS58
CuZn40Pb2	brass 2.0402/AISI CW617N/CuZn40Pb2
DoF	degrees of freedom
EtherCAT	ethernet for control and automation technology
eu**spen**	The European Society for Precision Engineering and Nanotechnology
FEM	finite element method
FF	feed forward
FFT2	two-dimensional fast Fourier transformation
FOR1845	German research unit ("Forschungsgruppe") No. 1845 Ge germanium

HFIM	high-frequency-impulse-measurement
HPC	high performance cutting
HSC	high speed cutting
HSM	high speed machining
IPC	industrial PC
IR	infrared
IS	input shaping
JL	jerk limitation
JSPE	The Japan Society for Precision Engineering
LED	light emitting diode
LiPo	lithium-ion polymer
LLNL	Lawrence Livermore National Laboratory
MBSM	motion band sub-model
NiP	electroless nickel/nickel phosphorous
OFHC	oxygen-free high conductivity
PEM	predictive error method
PI	proportional-integral controller
PID	proportional-integral-differential controller
PLC	programmable logic controller
PSoC	programmable system on a chip
PWM	pulse width modulation
RBSM	residual band sub-model
RFM	radio frequency module
RISC	reduced instruction set computer
S355J2(+N)	low-alloy steel 1.0577/AISI A738/S355J2(+N)
Si	silicon
SSD	sub surface damage
TCP	tool center point
TP1	sub-project (German: “Teilprojekt”) 1 of the FOR1845 on “Ultra-precision milling with multiple diamond cutting inserts”
TP2	sub-project 2 of the FOR1845 on “Ultra-precision high-speed milling”
TP3	sub-project 3 of the FOR1845 on “Electromagnetic ultra-precision linear guide”
TP4	sub-project 4 of the FOR1845 on “Balancing of spindles for ultra-precision high speed milling”
TP5	sub-project 5 of the FOR1845 on “Model-based toolpath correction for ultra-precision machining”
UDB	universal digital block
UP	ultra-precision
UP-HPC	Ultra-Precision High Performance Cutting
USM	ultrasonic motor
WLI	white light interferometer, a specific type of a coherence scanning interferometer
X40Cr14	stainless steel type 1.2083/AISI 420/X40Cr14

X5CrNi18-10	high-strength steel 1.4301/AISI 304/X5CrNi18-10
ZnS	zinc sulfide
ZnSe	zinc selenide
ZV	zero vibration
ZVD	zero vibration derivative

Symbols

$\overline{\Delta_y}$	μm	mean profile height deviation
α	°	angle of first unbalance mass for rotary redistribution
α	nm mm^{-1} K^{-1}	coefficient of thermal expansion
β	°	angle of second unbalance mass for rotary redistribution
χ_{act}	°	angular spacing of actuators
$\boldsymbol{\delta}$	m	magnetic air gaps
$\Delta\alpha$	°	difference in clearange angle of two tools
Δd	nm	depth difference of machined cutting marks
$\Delta\gamma$	°	difference in rake angle angle of two tools
Δh_{el}	nm	differential elastic springback of a grain
ΔL_{max}	nm	maximum thermal expansion at elevated temperature
ΔL_{min}	nm	minimal required thermal expansion for tool setting
ΔL	nm	thermal expansion of a beam
$\boldsymbol{\Delta q_{pos}}$	μm	vector of position offsets on q
Δr_{fly}	μm	difference in fly-cut radius of two tools
Δs	μm	difference in tool spur/track of two tools
ΔT	K	temperature difference
Δt	s	time interval
$\Delta \mathrm{T}_{max}$	K	maximum allowed temperature difference above ambient
$\Delta \mathrm{T}_{min}$	K	minimal temperature difference for a specific expansion
η	-	thermal absorption
γ	°	rake angle angle of a tool
γ	°	rotation angle of the USM
κ	W m^{-1} K^{-1}	thermal conductivity
λ	nm	wavelength of IR-LED
λ_c	Hz	cut-off frequency used in filters
ω	Hz	rotational frequency
ω	rad s^{-1}	angular velocity of the rotor
φ	°	half-angle of IR-LED
ϕ	°	effective angle of the resultant force
ϕ_{AB}	°	phase shift of travelling waves in the ultrasonic motor
Φ_e	mW	total radiant flux of IR-LED

(continued)

(continued)

ρ	gmm^{-3}	density
ζ	-	damping ratio
A	µm^2	surface area
$\boldsymbol{A}$	-	system matrix of state space model
A	m, *here* µm	(bi-directional) positioning accuracy (ISO 230-2)
a	nm	gain parameter for CHR method ($a = kL/T$)
a_e	µm	width of cut
$\mathrm{AE}_{\mathrm{max}}$	Mv	acoustic emission signal amplitude
A_1, A_2	-	input shaping gains
A_{max}	µm^2	cross section of the tool plunging into the material while cutting
a_{max}	ms^{-2}	acceleration limit
a_{max}	ms^{-2}	acceleration limit
a_p	µm	depth of cut, infeed
$\boldsymbol{B}$	-	input matrix of state space model
C	JK^{-1}	heat capacity
c	ms^{-1}	propagation velocity of radio frequency signals ($\approx 3 \times 108$ ms^{-1})
$\boldsymbol{C}$	-	output matrix of state space model
c_H	-	coherence shock response spectrum
c_p	J kg^{-1} K^{-1}	specific heat capacity
d	mm	diameter of a fly-cutter
$\boldsymbol{D}$	N/(m/s), Nm/(rad/s)	damping matrix of the system model
d_c	nm	critical depth of cut
$\boldsymbol{d_S}$	m	position signals of the air gap sensors
E	Nm^{-2}	Young's modulus
e_{iRj}	µrad	inclination error around j-axis for i-movement
e_{iTj}	µm	straightness error in j-direction for i-movement
e_{p}	gmm	permissible specific unbalance
F	N	resultant force
f_0	Hz	carrier frequency of the RFM module
f	µm	(lateral) feed
f_{-3dB}	Hz	frequency at −3 dB (bandwidth frequency
$\boldsymbol{F_A}$	N	actuator force
f_c	Hz	commutation frequency of the ultrasonic motors
F_c	N	cutting force
$F_{c,\infty}$	N	constant cutting force at infinite speed
$F_{\mathrm{c},var}$	N	variable value of cutting force according to Ben Amor
f_0	Hz	Doppler shift
F_f	N	feed force
F_i	N	force of *i*-axis
F_{imp}	N	impulse force
$\boldsymbol{F_M}$	N	magnet pulling force
F_n	N	normal force
F_p	N	passive force
f_s	Hz	sample rate
F_u	N	centrifugal force
$\boldsymbol{G}$	mm s^{-1}	balancing grade
$h_{cu,max}$	µm	maximum undeformed chip thickness

(continued)

(continued)

$H(f)$	μm N^{-1}	shock response spectrum
HV	N mm^{-2}	Vickers hardness
$\boldsymbol{i}$	A	coil currents of the electromagnets
i_{bal}	-	balancing iteration
I_e	W sr^{-1}	radiant intensity of IR-LED
I_f	A	forward current of IR-LED
j	ms^{-3}	jerk
$\boldsymbol{J_A}$	-	Jacobian matrix for the actuators
$\boldsymbol{J_S}$	-	Jacobian matrix for the air gap sensors
k	Nm^{-1} *here* Nm μm^{-1}	(dynamic) stiffness
$\boldsymbol{K}$	N m^{-1}, Nm rad^{-1}	stiffness matrix of the system model
K_c	MPa$\sqrt{\text{m}}$	fracture toughness
k_c	GPa	specific cutting force
K_D	N sm^{-1}	derivative feedback gain
K_I	N m^{-1} s^{-1}	integral feedback gain
K_P	N m^{-1}	proportional feedback gain
K_p	nm	proportional gain of of thermal actuator controller
K_u	nm	ultimate gain of thermal actuator plant model
L_0	mm	base length of a beam
L_c	km	effective contact length (cumulated)
L	s	delay time for CHR method
l_k	mm	contact length in milling
$\boldsymbol{l_n}$	mm	balance mass vector for rotary redistribution
l_{wp}	mm	workpiece length
$\boldsymbol{M}$	kg mass	matrix of the system model
M	m, *here* μm	(bi-directional) repeatability (ISO 230-2)
m	kg	mass
M_i	Nm	torque of *i*-axis
m_i	kg	balancing masses
m_p	kg	permissible residual unbalance mass
m_r	kg	rotor weight
M_u	Nm	torque generated by the USM
m_u	kg	unbalance mass
n_{act}	-	number of actuators
n	min^{-1}	spindle speed
$\boldsymbol{P}$	kg	parameter vector
P_1	nm	summation of low-frequency parts of the FFT2
P_2	nm μm^{-1}	summation of high-frequency parts of the FFT2
p_{ij}	kg	feed forward parameters axis i to axis j
P_n	-	commutation pulses sent to the ultrasonic motor
$P\_$	W	power of heat source (i.e. Laser or LED)
PV	μm	peak-to-valley
$\boldsymbol{q}$	m, rad	generalized coordinate vector
$\boldsymbol{Q}$	N, Nm	generalize force vector
$\boldsymbol{Q_{ff}}$	N	vector of generalized force offsets

(continued)

(continued)

Q	J	heat input
Q	mm^3 min^{-1}	material removal rate
q_n	µm	generalized coordinate in *n* of levitation guide
$\boldsymbol{Q_{set}}$	N	vector generalized set-point forces
$\boldsymbol{q_{z\_tol}}$	N	allowance for *qz*
r	mm	radial distance for calculation of Doppler shift
r_β	°	cutting edge radius
r_c	mm	correction radius
r_ε	µm	nose radius of a tool
r_{fly}	mm	fly-cut radius
r_i	mm	balancing radii
R_{kin}	nm	kinematic roughness (for optics usually in nanometers)
R	m, *here* µm	(bi-directional) mean positioning error (ISO 230-2)
R_2	-	coefficient of determination
s	µm	raster spacing
S_1, S_2, S_{eq}	mm^2	contact areas in schematic model of contact geometry between tool and workpiece according to Yan et al.
S_A	-	signal for first travelling wave motor
$\mathrm{S_a}$	nm	arithmetic mean height (areal)
S_B	-	signal for second travelling wave motor
S_{p2p}	µm	peak-to-peak value
$\mathrm{S_q}$	nm	mean quadratic height (areal)
S_{std}	µm	standard deviation
Sz	nm	maximum height (areal)
t	s	time
T_0	s	oscillation period
T_a	°C	actuator temperature
t_{acc}	s	acceleration time
T	s	time constant for CHR method
t_{dec}	s	deceleration time
t_{fade}	s	oscillation fading time
t_f	ns	fall time of IR-LED to zero
t_{heat}	s	heating time
$t_{heat,rev}$	s	heating time per revolution
T_i	s	integral time of thermal actuator plant model and/or controller
t_k	µs	contact time in milling
t_{res}	s	residual time
t_r	ns	rise time of IR-LED to full power
T_s	s	shaping delay
t_{total}	s	time per line for exemplary workpiece
$\boldsymbol{U}$	g mm	measured unbalance vector
U_c	g mm	counterbalance
U_f	V	forward voltage of IR-LED
$\boldsymbol{u}$	-	input vector
U	g mm	residual unbalance
v	ms^{-1}	relative spindle speed
v_c	mm min^{-1}	cutting speed
v_c^*	m min^{-1}	critical cutting speed

(continued)

(continued)

v_f	mm min^{-1}	feed velocity
v_{HG}	m min^{-1}	Speed limit, at which the variable part of the cutting force has decreased by 86.5%, according to Ben Amor
V	mm^3	volume
v_{rot}	m ms^{-1}	rotational speed (circumferential speed)
V_s	V	supply voltage of the USM
v_{set}	ms^{-1}	set-point velocity
w	mm	width of the thermal actuator
w_{est}	-	window size
w	-	set-point value
$\boldsymbol{x}$	-	state vector
$\dot{x}$	-	state vector derivative
$\boldsymbol{y}$	-	output vector
z_{ac}	m	acceleration distance
z_{dec}	m	deceleration distance
z_{fade}	m	oscilation fading distance
z_{res}	m	residual distance
$\ddot{z}_{set}$	m s^{-2}	set-point acceleration in z
z_{total}	m	total machining distance

Introduction to Ultra-Precision High Performance Cutting

Lars Schönemann

1 State of the Art in Ultra-Precision Machining

Over the past decades, Ultra-precision (UP) diamond machining has evolved to an established technology for generating complex optical surfaces as well as for producing parts with high mechanical accuracy [7] (see Fig. 1).

In principle, the technology of diamond machining originates from different strands of developments for manufacturing optics (lenses, mirrors and gratings), precision parts (e.g. automotive pistons) or nuclear weapons. For example, the ruling of diffractive gratings by a "diamond point" was accomplished by Rutherford in the 1860s [29], although there are other examples dating back even further. An excellent overview on the historical evolution on diamond machining can be found in the book "*Precision engineering: an evolutionary view*" by Christopher Evans [16]. Initially, precision coordinate measurement machines served as a basis for machine tools in the 1940s [30]. According to Evans, the earliest "well-documented" diamond turning of modern optics (Schmidt Plates for infrared rifle scopes) was carried out by Frank Cooke from Polaroid during World War II [16, p.142].

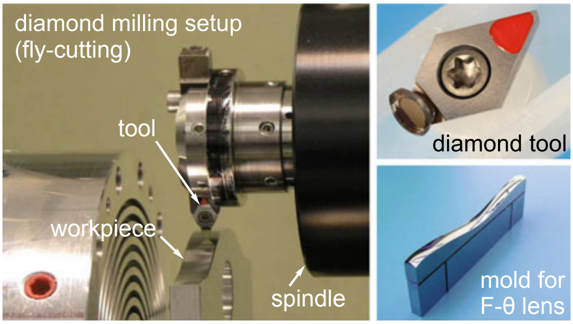

Fig. 1 Exemplary diamond milling (fly-cutting) setup for generating freeform optical surfaces with monocrystalline diamond tools, picture credit [40], License: CC BY 4.0

L. Schönemann (✉)
Leibniz Institute for Materials Engineering IWT, Bremen, Germany

University of Bremen, MAPEX Center for Materials and Processes, Bremen, Germany
e-mail: schoenemann@iwt.uni-bremen.de

E. Brinksmeier and L. Schönemann (eds.), *Ultra-precision High Performance Cutting*,
Lecture Notes in Production Engineering, https://doi.org/10.1007/978-3-030-83765-5_1

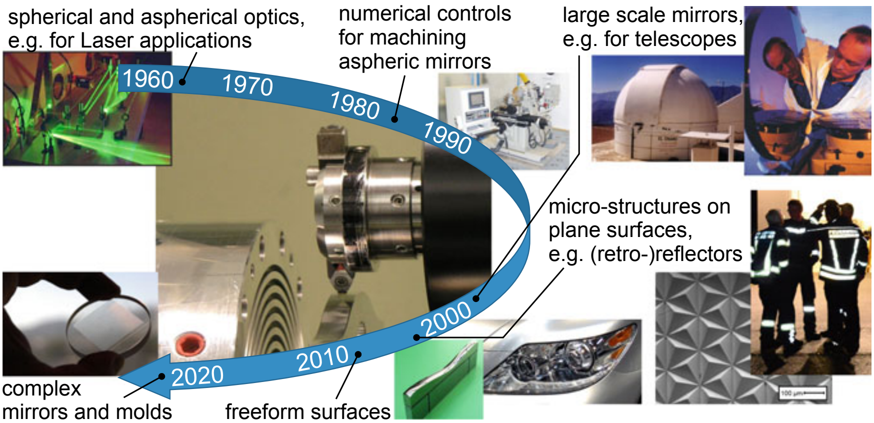

Fig. 2 The evolution of ultra-precision machining, according to [36], picture credits: [19, 33, 34, 37, 47], all other pictures ©Leibniz-IWT

Pioneering work in the 1960s was led by J.B. Bryan at the Lawrence Livermore National Laboratory (LLNL) in the USA (cf. [21]). Notable milestones (cf. Figure 2) were the application of reversal techniques to obtain mechanical parts with the highest degree of precision [31], the development of ultra-precision air bearing spindles [1] with minimal runout, the possibility to shape diamond tools with extremely sharp cutting edges and minimum waviness [17] as well as precision encoders for the exact position location in linear machine axes [9].

By the 1970s, ultra-precision machining had found use in manufacturing computer memory discs or optical components for photocopiers [10], although Saito stated that the greatest success of diamond turning was in generating flats [38]. He described that the applied diamond tools already featured a cutting edge sharpness of 250 Å (≡ 25 nm), which he deduced from the thickness of the generated chips of 750 Å [38]. He also highlighted balancing of the spindles as a crucial setup procedure and pointed out that the belts for connecting the spindles and their motors had to be carefully selected to minimize vibrations. The economic viability of diamond turning was already far superior to conventional techniques, as it enabled the reduction of machining times from several weeks for superpolishing to about one day [38]. Although numerical controls were already available at that time, those were not yet commonly applied.

In the 1980s, diamond machining was further commercialized, when more and more solutions for diamond machining equipment appeared in the market by manufactures in the USA, Germany and Japan [16]. The widespread application of computer numerical control (CNC) established the capability to generate complex surfaces in a fast and flexible way. At this time, Taniguchi published his well-known CIRP Keynote in which he described ultra-precision machining as “those processes/machines by which the highest possible dimensional accuracy is, or has been achieved at a given point in time” and predicted the development of machining accuracy until the 2010s [44].

Several noteworthy ultra-precision machine tools originate from this decade. The DTM-3 is a large diamond turning machine designed by [8] at the LLNL that allows for the machining of optics with a weight of up to 4,500 kg and a diameter of 2.1 m [8]. Therefore, it utilized a horizontally aligned hydrostatic spindle (in contrast to the more commonly applied air bearings) as well as a metrology frame isolated from the machine base and an oil shower for temperature control. It was succeeded by the Large Optics Diamond Turning Machine of the LLNL that utilized a vertical spindle orientation instead [39] and allowed for turning 1,400 kg workpieces with 162 cm diameter and 50 cm height. With its dedicated metrology frame, incorporating seven interferometers as well as capacitive gauges for position feedback, it enabled the generation of metal optics with 25 nm figure accuracy and 5 nm root-mean-square roughness. A large diamond turning machine was also developed at the Cranfield Unit for Precision Engineering (CUPE) by McKeown et al. [28, 48]. One distinct feature of this machine was the application of lightweight steel weldment filled with synthetic granite for the construction of the machine base. A dedicated control system allowed for axis speeds up to 10 mm s^{-1}.

In the 1990s, even more sophisticated control and actuator systems (fast tool servos) were implemented to increase the capabilities of diamond turning in terms of their achievable geometric complexity [15]. The idea behind this actually was much older (see [45, 48] or [14]), but could not be implemented without advanced electronics and microcomputer systems. Despite the advancements in machining performance, some physical principles were not yet completely understood and still relied on empirical knowledge [21]. To fill this gap, Lucca et al. investigated the energy dissipation during cutting [25] and the plastic deformations in the surface layer [27]. Lucca et al. are also the first to use atomic force microscope (AFM) for tool wear characterization [26], which is done in a similar fashion until today.

By the 2000s, developments such as direct drive linear slides, dedicated software and the availability of non-circular cutting edge geometries enabled the manufacture of optics with almost arbitrary freeform shape [36].

Despite the advances in achievable precision and complexity of the parts, the associated processes are still limited in their economic potential [6]. One reason for this is the limited choice of diamond-machinable materials. Typical substrates include copper, aluminum, brass and electroless nickel, whereas particularly steel and other iron-based substrates usually result in catastrophic tool wear [35]. While there are means to counteract this wear, such as vibration assisted machining [32] or chemical treatment of the surface and subsurface layer [4], these approaches are severely limited in their applicability. For example, elliptical vibration is frequently used for cutting molds for optical devices, however, it cannot be applied for high speed cutting applications due to the limited maximum vibration frequency.

Another reason for the limited machining speed is the very time-consuming cutting process with chip thicknesses of only a few microns. Typical circumferential milling tools for fly-cutting feature comparably large swing radii of $r_{fly} = 20\,\mathrm{mm}$ up to 60 mm [11], 95 mm or even larger [43]. Consequently, the inertia upon rotation generates dynamic disturbances [50], which are typically mitigated by limiting the applied spindle speeds between $n = 1,000\,\mathrm{min}^{-1}$, e.g. [49], and 5,000 min^{-1}, e.g.

[24, 50]. In addition, diamond milling is conducted using only a single diamond cutting edge (fly-cutting) to ensure a defined swing radius of the tool [51]. This along with the precision required for mirror surfaces ($Sa < 10$ nm and $PV < 100$ nm being typical thresholds) requires the linear machine axes to be moved at a particularly slow speed to achieve the required feed rate. Overall, the surface generation rate is only at around $2.5\,\mathrm{mm}^2\mathrm{min}^{-1}$ [3] and even the manufacture of small optical surfaces may yield a machining time of multiple hours up to several days [12, 46].

The required precision and temporal stability not only affect the primary machining speed and time, but also all auxiliary processes required for setting up the machine tool, aligning tool and workpiece and balancing the rotor for the milling operation. Many of the concepts known from conventional machining, such as automated tool or part calibration within the machine, automated tool changing or balancing, do not offer the required precision. Therefore, time-consuming manual tool and workpiece setting procedures are required. For example, the spindles are balanced to an ISO balancing grade $< G0.04$ [2] to ensure the safe operation of the air bearings typically applied in UP-machining [20, 23]. Therefore, tiny oscillations of the rotor have to be detected and compensating masses have to be determined [5, 18, 20] and accurately placed at their respective locations on the rotor. So far, automated procedures to achieve this goal are not known. Instead, balancing an ultra-precision spindle is a tedious and time-consuming manual task in which weight is added at specific locations on the rotor until a satisfying balance can be assured. The smaller the masses are, the more difficult this task becomes.

2 The UP-HPC Approach

Ultra-Precision High Performance Cutting (UP-HPC) is a term coined by the German research unit ("Forschungsgruppe") No. 1845 (FOR1845) to subsume all activities around ultra-precision machining at elevated speeds, reducing the primary machining and auxiliary setup times as well as increasing the general process stability.

Both, high speed cutting (HSC) and high performance cutting (HPC) have been applied in conventional machining for several decades and are an essential part of precision machine design since the early 1990s [42] to increase the economic efficiency of milling processes and also to positively influence the material removal mechanisms [13, 41]. More recently, it has been shown that this also applies to micro milling [22]. An application of HSC in UP milling has not yet been approached and thus, the influences on material removal at this scale are not well-researched.

This was the reason for the initiation of the research unit FOR1845 in early 2014 by the Universities of Bremen and Hannover. It consists of five sub-projects (German: "Teilprojekte", TP), each targeting a specific approach to UP-HPC:

TP1 "Ultra-precise milling with multiple diamond cutting edges"
aimed to develop a tool setting mechanism based on thermal expansion to align multiple cutting edges in a fly-cutting setup to a common radius (Chapter 2).

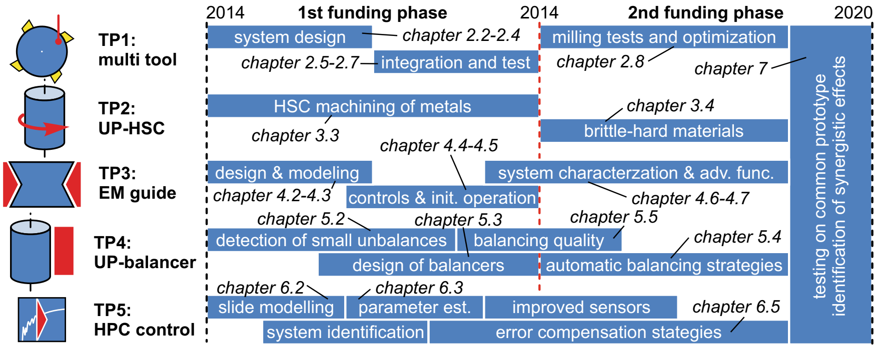

Fig. 3 Approaches of the Research Unit FOR1845 for achieving Ultra-Precision High Performance Cutting

TP2 “Ultra-precision high-speed milling”
focused on the scientific evaluation of high speed cutting with diamond tools, by analyzing its effect on the cutting forces, the resulting wear and, in the case of brittle materials, on the surface integrity (Chapter 3).

TP3 “Electromagnetic ultra-precision linear guide”
developed an electromagnetically guided and driven ultra-precise linear stage that allowed for extremely high feed velocities and enabled an in-process compensation of static and dynamic deviations (Chapter 4).

TP4 “Balancing of spindles for ultra-precision high speed milling”
targeted automated unbalance measurement and compensation techniques that supersede the speed and precision of manual weight-adding procedures by far (Chapter 5).

TP5 “Model-based toolpath correction for ultra-precision machining”
addressed the control-related aspects of UP-HPC by researching in-process analysis and compensation strategies (Chapter 6).

The topics addressed in the sub-projects are depicted in Fig. 3 along with a reference to the chapters of this book which deal with the respective topic.

3 Integration of Developments into a Common Test Stand

Actually, the development of individual measures to improve diamond milling is not sufficient. Rather, it is necessary to test the interaction of the individual developments in a joint test stand, in order to demonstrate the synergistic potential of the individual measures for economical UP machining. Thus, all developments of the FOR1845 were integrated into a common test stand (Fig. 4) which is designed to prove the viability of all approaches (Chapter 7).

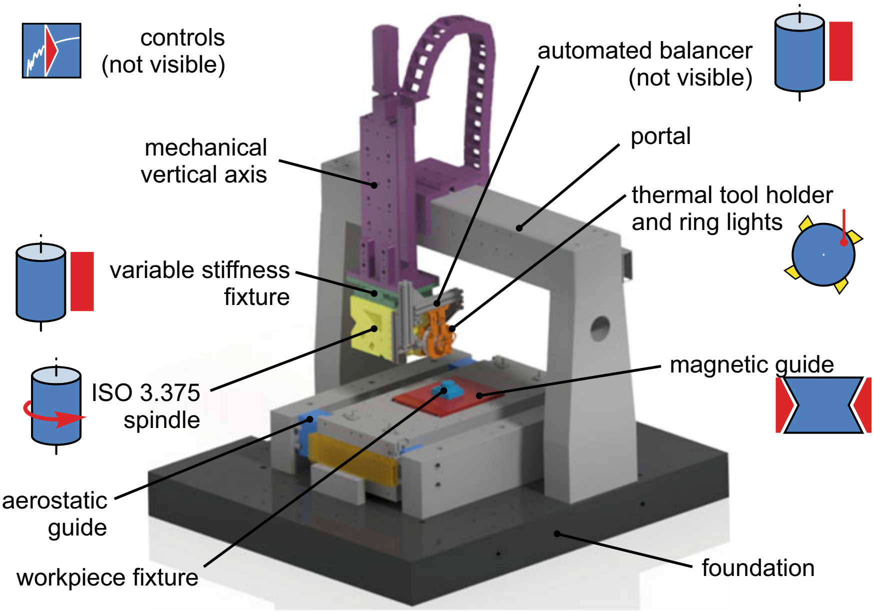

Fig. 4 Concept for the common test stand to integrate all developments of the FOR1845

Specifically, the test stand integrates the following components

a commercial ISO 3.375 air bearing spindle as the main tool spindle allowing for speeds $>5.000\,\mathrm{min}^{-1}$,
the newly developed magnetic linear guide as a high-velocity feed axis,
a commercial aerostatic guide forming a cross-table with the magnetic guide for controls development and test,
the developed variable stiffness fixture to facilitate the unbalance detection,
the developed mechatronic balancers for automated UP-balancing,
the developed thermal tool setting mechanism for aligning multiple cutting edges to a common fly-radius, and
a mechanical vertical axis used for setting the depth of cut. This axis carries the load of many attached components and is only used for static positioning. Thus, a mechanical bearing technology was ranked to be sufficient in this case.

Further details concerning the test stand design and integration of individual components are introduced in Chapters 4 and 6.

The final Chapter 7 gives a retrospective on the highlight work of all projects within the FOR1845 and will also point out particular achievements over the past six years. Moreover, a brief outlook on potential future work will be given.

References

1. Arneson, C., Liebers, M.: History of the blockhead spindle. In: 33rd ASPE Annual Meeting. Las Vegas/NV, 4 November 2018
2. Brandt, C., et al.: Surface generation process with consideration of the balancing state in diamond machining. In: Denkena, B., Hollmann, F. (eds.) Process Machine Interactions. Lecture Notes in Production Engineering, pp. 329–360. Springer, Cham (2013)
3. Brecher, C., Lindemann, D., Merz, M., Wenzel, C., Preuss, W.: Freeform machining of molds for replication of plastic optics. In: Brinksmeier, E., Gläbe, R., Riemer, O. (eds.) Fabrication of Complex Optical Components. Lecture Notes in Production Engineering, pp. 41–52. Springer, Cham (2013)
4. Brinksmeier, E., Gläbe, R., Osmer, J.: Ultra-precision diamond cutting of steel molds. CIRP Ann. **55**(1), 551–554 (2006). https://doi.org/10.1016/S0007-8506(07)60480-6
5. Brinksmeier, E., Gläbe, R., Krause, A.: Precision balancing in ultraprecision diamond machining. In: Thornett, E.E (ed.) 8th International Conference on Laser Metrology, Machine Tool, pp. 262–269. CMM & Robotic Performance (Lamdamap 2007) (2007)
6. Brinksmeier, E., Preuss, W.: Micro-machining. Philos. Trans. R. Soc. A **370**, 3973–3992 (2012). https://doi.org/10.1098/rsta.2011.0056
7. Brinksmeier, E.: Ultraprecision machining. In: CIRP Encyclopedia of Production Engineering, pp. 1–5. Springer, Heidelberg (2018). https://doi.org/10.1007/978-3-642-35950-7_6403-4
8. Bryan, J.B.: Design and construction of an ultraprecision 84 inch diamond turning machine. Precision Eng. **1**(1), 13–17 (1979). https://doi.org/10.1016/0141-6359(79)90071-0
9. Carpenter, A.J.: Locating device for precision tools. U.S. Patent 2 948 817, 9 August 1960
10. Chapman, G.: Ultra-precision Systems; an Enabling Technology for Perfect Surfaces. Technical Report, Moore Nanotechnology Systems (2004)
11. Cheng, M.N., Cheung, C.F., Lee, W.B., To, S., Kong, L.B.: Theoretical and experimental analysis of nano-surface generation in ultra-precision raster milling. Int. J. Mach. Tools Manuf. **48**(10), 1090–1102 (2008). https://doi.org/10.1016/j.ijmachtools.2008.02.006
12. Davies, M.A., Dutterer, B.S., Suleski, T.J., Silny, J.F., Kim, E.D.: Diamond machining of diffraction gratings for imaging spectrometers. Precision Eng. **36**(2), 334–338 (2012). https://doi.org/10.1016/j.precisioneng.2011.09.006
13. Dewes, R.C., Aspinwall, D.K.: A review of ultra high speed milling of hardened steels. J. Mater. Process. Technol. **69**(1–3), 1–17 (1997). https://doi.org/10.1016/S0924-0136(96)00042-8
14. Douglass, S.S.: A Machining System for Turning Nonaxis symmetric surfaces. Ph.D. thesis. University of Tennessee, Knoxville (1983)
15. Dow, T.A., Miller, M.H., Falter, P.J.: Application of a fast tool servo for diamond turning of non rotationally symmetric surfaces. Precision Eng. **13**(4), 243–250 (1991). https://doi.org/10.1016/0141-6359(91)90001-y
16. Evans, C.: Precision engineering : an evolutionary view. Cranfield Press, Bedford, UK (1989)
17. Fernandez-Moran, V.H.: Diamond cutting tool having and edge thickness of 0.001 to 0.01 micron. U.S. Patent 30 60 781 (1954)
18. Grejda, R., Marsh, E., Vallance, R.: Techniques for calibrating spindles with nanometer error motion. Precision Eng. **29**(1), 113–123 (2005). https://doi.org/10.1016/j.precisioneng.2004.05.003
19. GT1976. KLF-A Weißenburg and fire station Weißenburg at Unterabschnitts- Übung at Tiefgrabenrotte, Frankenfels, Austria. CC BY-SA 4.0 (2018). https://de.wikipedia.org/wiki/Datei:2018-09-14_(708)_KLFA_Wei%C3%9Fenburg_and_fire_station_Wei%C3%9Fenburg_at_Unterabschnitts-%C3%9Cbung_at_Tiefgrabenrotte,_Frankenfels,_Austria.jpg. Accessed 25 Feb 2021
20. Huang, P., Lee, W.B., Chan, C.Y.: Investigation of the effects of spindle unbalance induced error motion on machining accuracy in ultra-precision diamond turning. Int. J. Mach. Tools Manuf. **94**, 48–56 (2015). https://doi.org/10.1016/j.ijmachtools.2015.04.007
21. Ikawa, N., et al.: Ultraprecision metal cutting - the past, the present and the future. CIRP Ann. **40**(2), 587–594 (1991). https://doi.org/10.1016/s0007-8506(07)61134-2

22. Jahanmir, S.: Surface integrity in ultrahigh speed micromachining. Procedia Eng. **19**, 156–161 (2011). https://doi.org/10.1016/j.proeng.2011.11.095
23. Knapp, B., Arneson, D., Oss, D., Liebers, M., Vallance, R., Marsh, E.: The importance of spindle balancing for the machining of freeform optics. In: ASPE Spring Topical Meeting, vol. 51, pp. 74–78. ASPE, Raleigh, NC (2011)
24. Kong, L.B., Cheung, C.F., To, S., Lee, W.B.: An investigation into surface generation in ultra-precision raster milling. J. Mater. Process. Technol. **209**(8), 4178–4185 (2009). https://doi.org/10.1016/j.jmatprotec.2008.11.002
25. Lucca, D., Rhorer, R., Komanduri, R.: Energy dissipation in the ultraprecision machining of copper. CIRP Ann. **40**(1), 69–72 (1991). https://doi.org/10.1016/s0007-8506(07)61936-2
26. Lucca, D., Seo, Y., Komanduri, R.: Effect of tool edge geometry on energy dissipation in ultraprecision machining. CIRP Ann. **42**(1), 83–86 (1993). https://doi.org/10.1016/s0007-8506(07)62397-x
27. Lucca, D., Seo, Y., Rhorer, R., Donaldson, R.: Aspects of surface generation in orthogonal ultraprecision machining. CIRP Ann. **43**(1), 43–46 (1994). https://doi.org/10.1016/s0007-8506(07)62160-x
28. McKeown, P.A., Wills-Moren, W., Read, R.F.J., Modjarrad, H.: The design and development of a large ultra-precision CNC diamond turning machine. Adv. Manuf. Processes **1**(1), 133–157 (1986). https://doi.org/10.1080/10426918608953160
29. Michelson, A.A.: The ruling and performance of a ten-inch diffraction grating. In: Proceedings of the National Academy of Sciences of the United States of America, vol. 1, no. 7, pp. 396–400 (1915)
30. Moore Tools. About Moore Tool: Precision Machining Technology, Precision Tools (2021). http://mooretool.com/about.html .Accessed 25 Feb 2021
31. Moore, W.R.: Foundations of Mechanical Accuracy. The Moore Special Tools Company (1970)
32. Moriwaki, T., Shamoto, E.: Ultraprecision diamond turning of stainless steel by applying ultrasonic vibration. CIRP Ann. **40**(1), 559–562 (1991). https://doi.org/10.1016/S0007-8506(07)62053-8
33. NASA. Rayon laser à travers un dispositif optique. public domain (2004). https://commons.wikimedia.org/wiki/File:Laser_optique.jpg. Accessed 25 Feb 2021
34. Negadrive. El Enano robotic telescope, Las Cumbres Observatory. CC BY-SA 3.0 (1999). https://commons.wikimedia.org/wiki/File:El_Enano_robotic_telescope.jpg. Accessed 25 Feb 2021
35. Paul, E., Evans, C.J., Mangamelli, A., McGlauflin, M.L., Polvani, R.S.: Chemical aspects of tool wear in single point diamond turning. Precis. Eng. **18**(1), 4–19 (1996). https://doi.org/10.1016/0141-6359(95)00019-4
36. Preuss, W.: A Guide to Diamond Machining. Shaker-Verlag (2019)
37. Pride, M.: 2010 Lexus LS 460 HID headlamp. CC BY-SA 3.0 (2010). https://commons.wikimedia.org/wiki/File:2010_Lexus_LS_460_Headlight.jpg. Accessed 25 Feb 2021
38. Saito, T.T.: Machining of optics: an introduction. Appl. Optics **14**(8), 1773 (1975). https://doi.org/10.1364/ao.14.001773
39. Saito, T.T., Wasley, R.J., Stowers, I.F., Donaldson, R.R., Thompson, D.C.: Precision and manufacturing at the Lawrence Livermore National Laboratory. In: NASA 2003 Conference, 1 November 1993
40. Schönemann, L., et al.: Synergistic approaches to ultra-precision high performance cutting. CIRP J. Manuf. Sci. Technol. **28**, 38–51 (2020). https://doi.org/10.1016/j.cirpj.2019.12.001
41. Schulz, H., Moriwaki, T.: High-speed machining. CIRP Ann. **41**(2), 637–643 (1992). https://doi.org/10.1016/S0007-8506(07)63250-8
42. Slocum, A.: Precision machine design. Prentice Hall, Englewood Cliffs, N.J (1992)
43. Takasu, S., Masuda, M., Nishiguchi, T., Kobayashi, A.: Influence of study vibration with small amplitude upon surface roughness in diamond machining. CIRP Ann. **34**(1), 463–467 (1985). https://doi.org/10.1016/S0007-8506(07)61812-5
44. Taniguchi, N.: Current status in, and future trends of, ultraprecision machining and ultrafine materials processing. CIRP Ann. **32**(2), 573–582 (1983). https://doi.org/10.1016/s0007-8506(07)60185-1

45. Thompson, D.C.: Theoretical tool movement required to diamond turn an off-axis paraboloid on axis. Technical Report, Lawrence Livermore Laboratory, 19 December 1975
46. Wang, S.J., To, S., Chen, X., Chen, X.D., Ouyang, X.B.: An integrated optimization of cutting parameters and tool path generation in ultraprecision raster milling. Int. J. Adv. Manuf. Technol. **75**(9–12), 1711–1721 (2014). https://doi.org/10.1007/s00170-014-6254-0
47. Werner, M.: Lytro-Light-field camera at Ars Electronica 2013 at Brucknerhaus, Linz, Upper Austria. CC BY-SA 3.0 (2013). https://commons.wikimedia.org/wiki/File:Ars_Electronica_Festival_2013_Lytro_lightfield_photography_03.jpg. Visited 25 Feb 2021
48. Wills-Moren, W., Modjarrad, H., Read, R., McKeown, P.: Some aspects of the design and development of a large high precision CNC diamond turning machine. CIRP Ann. **31**(1), 409–414 (1982). https://doi.org/10.1016/s0007-8506(07)63338-1
49. Wu, Y., Peng, W., Liu, Y.: A novel fabrication method for micro optical waveguide mold based on fly-cutting technology. Optik - Int. J. Light Electr. Optics **124**(9), 867–869 (2013). https://doi.org/10.1016/j.ijleo.2012.02.020
50. Zhang, S.J., To, S.: The effects of spindle vibration on surface generation in ultra-precision raster milling. Int. J. Mach. Tools Manuf. **71**, 52–56 (2013). https://doi.org/10.1016/j.ijmachtools.2013.04.005
51. Zhang, S.J., To, S., Zhu, Z.W., Zhang, G.Q.: A review of fly cutting applied to surface generation in ultra-precision machining. Int. J. Mach. Tools Manuf. **103**, 13–27 (2016). https://doi.org/10.1016/j.ijmachtools.2016.01.001

Diamond Milling with Multiple Cutting Edges

Lars Schönemann, Oltmann Riemer, and Ekkard Brinksmeier

Abstract Ultra-precision milling with multiple diamond cutting edges—which generally is favorable in terms of economic efficiency—requires an in-process tool setting system that allows for the compensation of alignment and fixation errors. Such a system was designed on the basis of thermal expansion as the main means of actuation. The heat input is generated by infrared light diodes which feed the respective energy to the rotating tool contactlessly. It is controlled in a way that ensures that only a specific portion of the tool holder is illuminated and therefore thermally expanded. By measuring the displacement at a reference plane with a capacitive measurement system and feeding it back to the control system, the actual position of the diamond cutting edge can be precisely set in nanometer range. This chapter gives an overview on the main technical developments for the respective prototype system and presents its performance when used in a machining environment.

1 Surface Generation in Diamond Milling

In general, ultra-precision machining with diamond tools (UP-machining) is an indispensable technology of optics manufacturing [6]. UP-milling processes, in particular, allow for the direct generation of complex geometries and freeform shapes with extremely smooth surface roughness and high form accuracy [7, 21]. The economic viability of these technologies is often increased by applying them in replication processes, e.g. by diamond machining the required molds for plastic or glass optics production [4, 18]. With this it is possible to manufacture a large quantity of optical parts from a single master form. Although comparably long processing times are acceptable in this case, the duration of diamond milling an optical mold is still a bottleneck in production, because the machining may require several minutes even for geometrically simple parts and up to multiple hours or even days for complex geometries [3].

L. Schönemann (✉) · O. Riemer · E. Brinksmeier
Leibniz Institute for Materials Engineering IWT, Bremen, Germany
e-mail: schoenemann@iwt.uni-bremen.de

MAPEX Center for Materials and Processes, University of Bremen, Bremen, Germany

E. Brinksmeier and L. Schönemann (eds.), *Ultra-precision High Performance Cutting*,
Lecture Notes in Production Engineering, https://doi.org/10.1007/978-3-030-83765-5_2

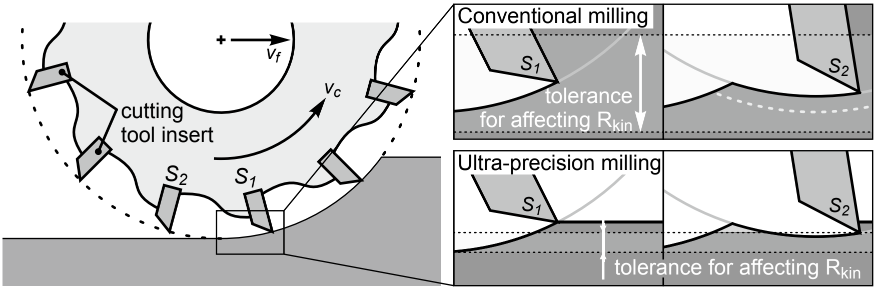

Fig. 1 Engagement conditions for multiple cutting edges in conventional and ultra-precision machining, cf. [11]

One of the reasons for these exceptionally long machining times is the limitation of diamond milling processes to the application of only one single cutting edge. Hence, these processes are also named "fly-cutting". The challenge of utilizing multiple cutting edges in diamond milling is their adjustment to achieve equal and predictable engagement conditions. Upon mounting the tool insert[1] on the tool holder, the manufacturing and assembly tolerances inevitably yield a deviation in fly-cut radius (Δr_{fly}), axial position (Δs, i.e. the subsequent cutting edges not running in the same "track"), and also in engagement angle ($\Delta\alpha$, $\Delta\gamma$). In particular, the axial and radial deviations may yield a magnitude of several micrometers.

Simply speaking, only if the fly-cut radii of all cutting edges feature a maximal difference below the kinematic roughness (in optics machining this typically implies $R_{kin} < 10$ nm), such a setup may be reliably used for machining (Fig. 1).

In reality, however, the associated surface generation is much more complex. When brought into contact with the workpiece, the radial and axial deviation of the cutting tools cause an irregular surface pattern which requires more describing parameters than just the simple formula to approximate the kinematic roughness in fly-cutting ($R_{kin} = f^2/(8r_\varepsilon)$). Instead, the differences in fly-cut radius Δr_{fly}, in axial direction Δs as well as all other geometric deviations such as the differences in shape and waviness of the cutting edge and the relative orientation of the cutting inserts have to be considered. A detailed analysis in 2D, i.e. for the kinematic roughness, can be found in [15]. A 3D-analysis of the generated surface is possible with numerical approaches, as presented in [16] and [17]. Ultimately, even the slightest deviation in any of these parameters results in new surface patterns that are generated and will lead to an undetermined surface roughness compared to fly-cutting with a single cutting edge (Fig. 2).

In summary, all cutting edges have to be aligned with as much precision as possible. The radial deviation Δr_{fly} has to be at least smaller than the maximum undeformed chip thickness $h_{cu,max}$ of the process, for all cutting edges to be involved in the material removal. Preferably, the remaining deviation of all cutting edges has to

---

[1] usually a carbide insert with a diamond soldered on top; the diamond is ground and lapped to form the actual cutting edge.

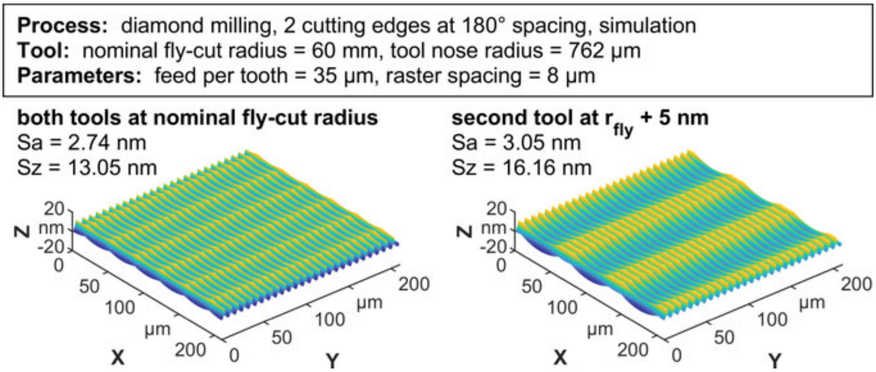

Fig. 2 Simulated surface of a two-tool diamond milling process with and without a deviation in fly-cut radius [17]

be lower than the kinematic roughness R_{kin}, i.e. <10 nm, in order to generate the final surface topography.

2 Tool Adjustment for Diamond Milling

For the compensation of positioning and guidance errors in machine tools, mechatronic components are applied to an increasing degree [8]. Despite the current progress of these technologies, the transferal of conventionally utilized concepts for tool alignment to ultra-precision machining is particularly challenging, as these systems should affect the general machining performance as little as possible. Thus, a combination of flexure hinges and highly precise actuators is commonly chosen [1, 19]. Implementing such alignment systems in milling operations, however, features the additional challenge of the milling tool rotating at high speeds on an air bearing. As a consequence, a lot of effort has to be put into the energy supply and data transfer systems, which ideally need to work contactless (for not disturbing the runout of the spindle) and be as lightweight and compact as possible (for maximizing the dynamics of the process). Systems that have been previously designed were not able to meet all of these requirements. The prototypes presented in [2] and [20] are based on purely mechanical tool setting and thus were not able to achieve the required tool setting precision. The mechatronic device presented in [9] achieves this, but is exceptionally voluminous and heavy due to the inclusion of wireless transmitters and control components on the rotor. This affects the spindle performance negatively and makes it effectively unusable for ultra-precision milling of optical surfaces.

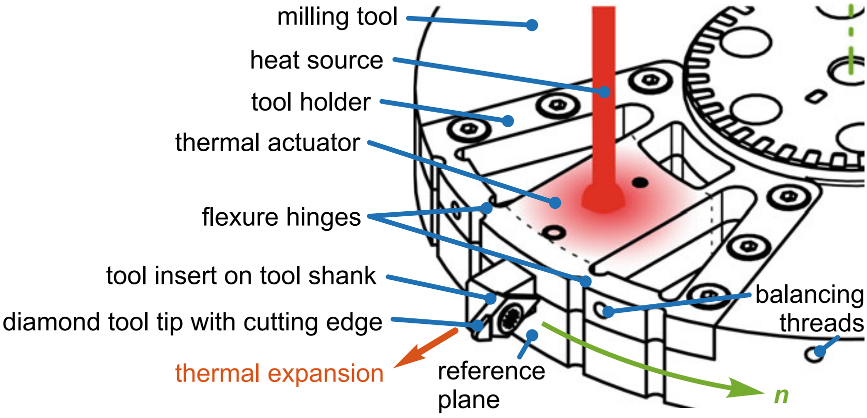

Fig. 3 Principle of an adjustable tool holder for generating a radial tool shift by thermal expansion [17]

2.1 *Concept of Thermal Tool Adjustment*

In the presented research work, the concept of defined thermal expansion was applied. This means that a specific portion of the tool holder is locally heated in order to expand it in radial direction (Fig. 3). Thereby, the tool that is fixed at the end of this "thermal actuator" changes its effective cutting radius. Using a dedicated control of the heat input, the expansion can be controlled in a way that the deviation between the subsequent cutting edges is minimized.

For minimizing the impact on the dynamic performance of the fly-cutter, e.g. the maximum spindle speed or the induced unbalances, the number of mechanical parts and electrical components that have to be integrated on the rotor has to be as low as possible. Heat input can be generated without mechanically contacting the substrate, e.g. by infrared radiation. This offers the unique possibility to place all heat-generating equipment on the static side of the fly-cutting process. In consequence, only very few mechanical parts are required on the rotor.

The required heat input may be calculated on the basis of material parameters and physical correlations. Thus, a mathematical model can be derived and used in the closed loop control of the thermal expansion. Moreover, thermal processes generally are elapsing slowly and thus, a specific thermal state can be maintained easily over a relatively long time by feeding only a minimum amount of heat into the system. This further facilitates the closed loop control. Thereby, it has to be ensured that the system is capsuled in the machine tool so that the delicate thermal state is not affected by coolant and forced convection due to the spindle rotation. This solution also ensures that the thermal state of the actuator does not affect the overall thermal stability of the machine tool. Generally, as only a small expansion of several nanometers is required, the proposed concept should not have a major effect on this issue.

Table 1 Calculations for thermal expansion and heating time

Actuator: steel 42CrMo4, $V = 10 \times 10 \times 30\ mm^3$				
$\alpha = 11.1$ nm mm^{-1} K^{-1}, $\rho = 7.850 \times 10^{-3}$ g mm^{-3}, $c_p = 461$ J kg^{-1} K^{-1}, $\eta = 0.4$				
ΔL	ΔT	Q	P	t_{heat}
10 nm	0.03 K	0.33 J	0.5 W 10 W	1.63 s 0.08 s
3.33 µm	**10 K**	108.57 J	0.5 W 10 W	542.83 s 27.16 s

2.2 Determination of Required Heat Input

Before actually designing holding mechanism for the tool inserts, the concept was validated, both analytically and numerically. A first approximation of the required heat input can be calculated by the standard physical equation of thermal expansion that takes the base length of a beam L_0, the coefficient of thermal expansion of the substrate α and temperature difference ΔT into account (Eq. 1).

$$\Delta L = \alpha \cdot L_0 \cdot \Delta T \tag{1}$$

Given the size of a typical fly-cutter to be approximately 150 mm in diameter, including a $L_0 = 30$ mm sized actuator into this seems reasonable. With the coefficient of thermal expansion being $\alpha \approx 11.1$ nm mm^{-1}K^{-1} for a 42CrMo4 type steel, the required temperature change for a $\Delta L_{min} = 10$ nm calculates to $\Delta T_{min} \approx 0.03$ K. On the other end, the maximum tolerable temperature change is set to $\Delta T_{max} = 10$ K above ambient. This yields a total thermal expansion of $\Delta L_{max} = 3{,}33$ µm.

In order to determine the required heat input Q for such a thermal expansion, the mass $m = v \times \rho$ and the thermal capacity c_p of the actuator have to be considered (Eq. 2).

$$Q = c_p \cdot v \cdot \rho \cdot \Delta T \tag{2}$$

Knowing the required heat input, it is possible to calculate the heating time t_{heat} required by a heat source with a power P and the thermal absorption η of the actuator surface (Eq. 3).

$$t_{heat} = \frac{Q}{\eta \cdot P} \tag{3}$$

In the following Table 1, the heat input and heating time for ΔL_{min} and ΔT_{max} is calculated for two kinds of heat sources, a laser with $P_{\text{Laser}} = 10$ W and an infrared-light emitting diode (IR-LED) with $P_{LED} = 0.5$ W. The calculation shows that the required expansion can be theoretically reached by both sources, though at different heating times.

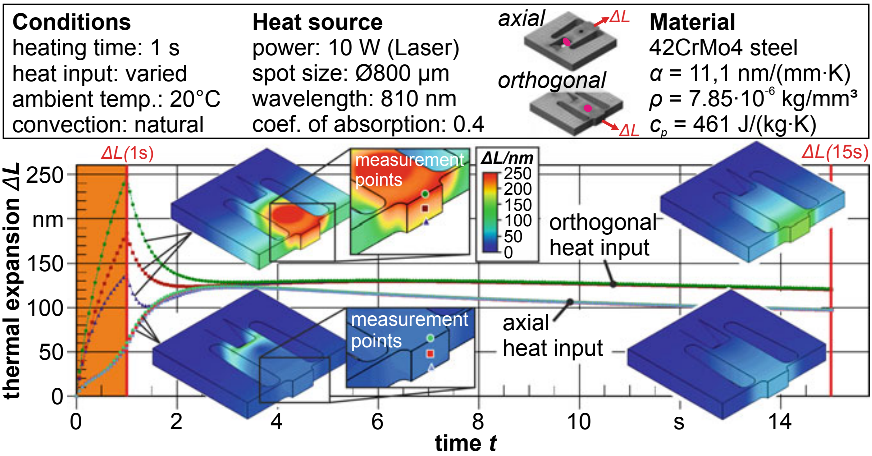

Fig. 4 Thermal expansion for heating an orthogonally and axially coupled thermal actuator with a Laser source ($P_{\text{Laser}} = 10$ W)

For the further analysis of the heat distribution and the 3D elongation of the material, numerical calculations were conducted using "Autodesk Simulation Mechanical 2016". Here, the actuator was modeled as a beam of the aforementioned size which was integrated into a setup for experimental verification. Therefore, the beam was connected to the base by two struts at the rear and two flexure hinges at the front. The setup offers two different setups for the coupling of the heat source: first, an orthogonal coupling in which the heat source is directed to the top (and possibly also the bottom) face of the actuator. Second, an axial coupling in which the heat is introduced to the rear face of the actuator. With the simulations it was investigated whether the orthogonal or axial coupling is preferable for a symmetric expansion and also if a high power (Laser) or low power (IR-LED) heat source is sufficient. For the simulation, the heat input was limited to a 1 s burst for all experiments.

The resulting expansion of heating the actuator by a Laser source is shown in Fig. 4.

Due to the high costs and complexity of integrating a Laser source in such a setup, the orthogonal coupling is limited to be one-sided, i.e. only on the top face of the actuator. This results in a tiling of the front face (at which the tool would be mounted) due to the inhomogeneous heat distribution within the actuator that is visible as a deviation in expansion of the three test points. After switching off the light source, this deviation is quickly reduced to a minimum as the heat distribution and thus the expansion becomes more homogeneous. Overall, an elongation of around $\Delta L = 125$ nm can be achieved without tilting after about 3 s in total using the orthogonal coupling. In contrast, the axial coupling shows a more homogeneous heat distribution from the start, as this setup serves the symmetry of the actuator. Furthermore, it is noticeable that the expansion of the actuator continues even after switching off the Laser due to the spreading of the heat (thermal conduction). After

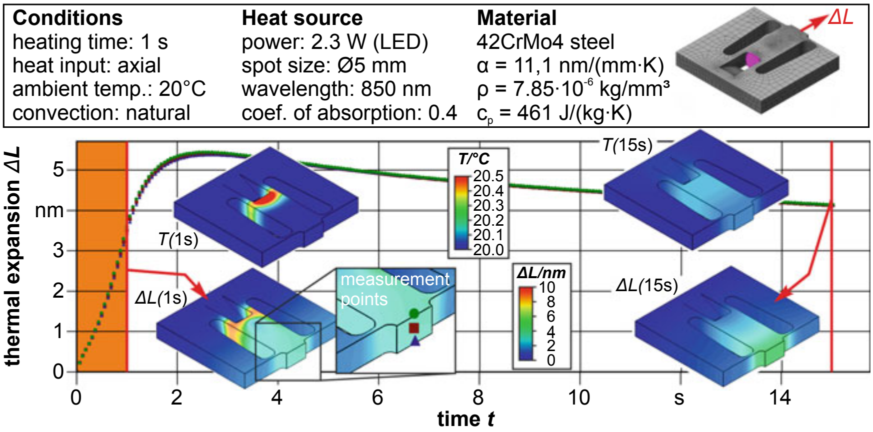

Fig. 5 Thermal expansion for heating an axially coupled thermal actuator with a IR-LED source ($P_{\text{LED}} = 0.5$ W)

3 s of simulated time, the thermal expansion reaches a similar extent than that of the orthogonal coupling. However, the heat is dissipated more quickly in this case and therefore, the thermal expansion also decreases thereafter. Nevertheless, an expansion of 100 nm is still measurable after 15 s in total.

The simulated expansion for using an IR-LED with $P_{\text{LED}} = 0.5$ W as heat source and axial coupling is shown in Fig. 5. The simulation shows that such a LED is capable of achieving an elongation in the nanometer range with a 1 s burst. The maximum expansion is again reached after 3 s of simulated time and measures about $\Delta L = 5.5$ nm. This implies that such an IR-LED might well be sufficient for driving the thermal actuator for the intended purpose of nanometer-precise tool setting. The benefit of this solution would be that a two-sided orthogonal setup could be realized as well, because LED are inexpensive and easy to integrate (both electrically and concerning operator safety).

In addition to the simulations with 42CrMo4 steel, the performance of other steel types has been evaluated as well. In particular, the stainless steel X40Cr14 has proven to deliver an increased thermal expansion (Fig. 6), because of its lower thermal conductivity ($\kappa_{\text{X40Cr14}} = 22.6$ W m^{-1} K^{-1} vs. $\kappa_{\text{42CrMo4}} = 42.6$ W m^{-1} K^{-1}).

2.3 Validation of the Thermal Mechanism in a Static Test Setup

The concept of a thermal actuator was first evaluated in a static test setup. This offered the possibility to minimize the distortion from the rotation of the spindle (noise, centering and roundness error of the reference plane) and also facilitated the

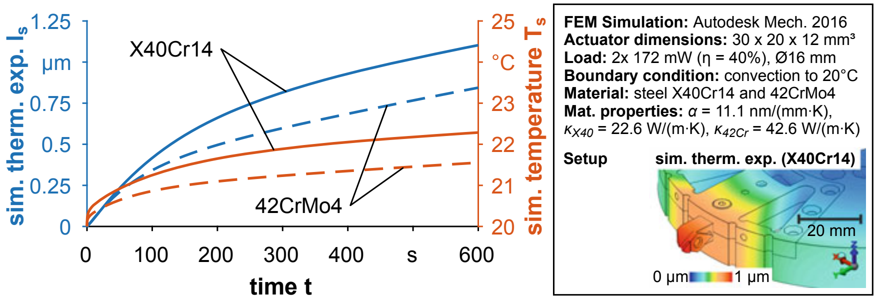

Fig. 6 Comparison of maximum temperature and thermal expansion for 42CrMo4 and X40Cr14 type steel

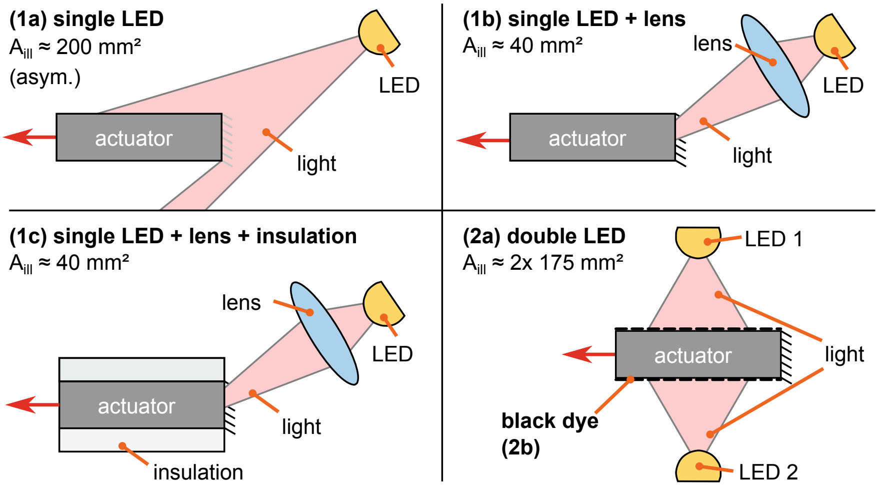

Fig. 7 Configurations of the static test stand for evaluating the thermal actuating principle

test of different heating setups. Four configurations were analyzed in this study: (1a) the illumination of the actuator's rear face with a single LED, (1b) the focusing of the LED radiation on the rear face with an additional lens, (1c) the addition of an insulating layer on the top and bottom face of the actuator to prevent heat loss by convection, and (2a) the illumination of both the top and bottom face of the actuator with two separate LED heat sources. The latter test was repeated with an additional coloring of the actuator faces with black ink (2b) to maximize the heat absorption (Fig. 7).

The results in Fig. 8 indicate that using only a single LED that is directed at the back of the actuator generates a thermal expansion of only ≈250 nm, which is not sufficient. Focusing the light does not generate a positive effect, but reduces the achievable expansion to slightly below 200 nm, which is probably caused by the absorption of the infrared radiation within the added lens. Isolating the actuator

Setup: Static test stand (42CrMo4), actuator: l = 30 mm, w = 10 mm x t = 10 mm
Heat source: Osram SFH-4783, λ_c = 850 nm, ϕ = ±12°, I_e = 2.3 W/sr
Metrology: IBS CPL 490, 2G-C8-0.5, f = 10 kHz

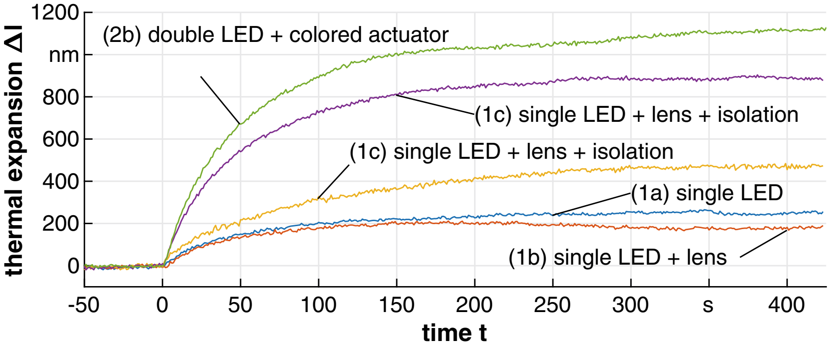

Fig. 8 Step response of the static test stand for the selected configurations

almost doubles the achievable expansion to about 470 nm. The best results can be achieved by using the double-sided LED setup that without any further modifications generates an expansion of 870 nm. When adding a black coloring to the illuminated actuator faces, the heat input is increased further, yielding an expansion of more than 1,100 nm.

Overall, these tests have shown that the general concept of using thermal expansion for tool setting in the nanometer range is basically applicable.

3 Determination of Tool Holder Geometry

The geometry of the actuator has been integrated into the design of a tool holder for diamond milling with two tools. As it is obvious from the calculations and simulations, a thermal tool setting mechanism would achieve the required precision, but with the given constraints on maximum temperature clearly lacks the capacity to achieve a maximal stroke that would suffice the typical tolerances of diamond tool inserts. Therefore, the thermal actuator was extended by a mechanical pre-setting mechanism for a coarse alignment of the cutting edges to the range of the thermal expansion. A detailed description of the initial designs can be found in [10]. These featured a mechanical mechanism that was mounted as an additional component at the front of the thermal actuator. Due to reasons of stability and overall size of the tool holder, this concept was discarded and replaced by an internal mechanism as an integral part of the thermal actuator. This novel design was first presented in [14] and later in more detail in [15].

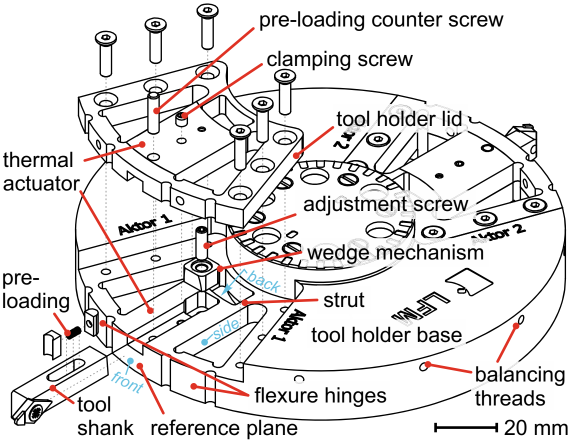

Fig. 9 Final design of a tool holder with two thermal actuators

Table 2 Technical data of tool holder and thermal actuator

Nominal engagement radius r_{fly}	65 mm
Number of actuators n_{act}	2
Spacing of actuators χ_{act}	180°
Dimensions of actuator $l \times w \times h$	$30 \times 20 \times 12$ mm^3
material	Steel X40Cr14
Thermal conductivity κ	22.6 W m^{-1} K^{-1}
Coef. of thermal expansion α	11.1 µm m^{-1} K^{-1}
Coef. of thermal absorption η	≈40%

The final design was made for a tool holder with a nominal diameter of 130 mm and features two beam-like thermal actuators (i.e. two tools) at 180° spacing which can potentially be increased up to four (Fig. 9). Each of the actuators is connected to the base of the tool holder by two struts at the rear and two flexure hinges at the front side while the rest is cut away to minimize thermal conduction to the base. The total dimensions of the actuator are 30 mm in length, 20 mm in width and 12 mm in thickness. The substrate material of the tool holder is X40Cr14 type steel which has shown the most promising results in the simulations. All relevant data are comprised in Table 2.

The mechanical presetting mechanism has been integrated into the thermal actuator and now features the tool shank as a slide. The tool shank is preloaded against a wedge mechanism with a 5° angle. When this wedge is moved by a precision screw, it shifts the tool shank in radial direction with a transmission ratio of $\tan(5°) = 0.0874$. In this way, the tool insert can be positioned across a range of ≈180 µm with a precision of <1 µm (Fig. 10) which is sufficient to compensate for all deviations from fixation.

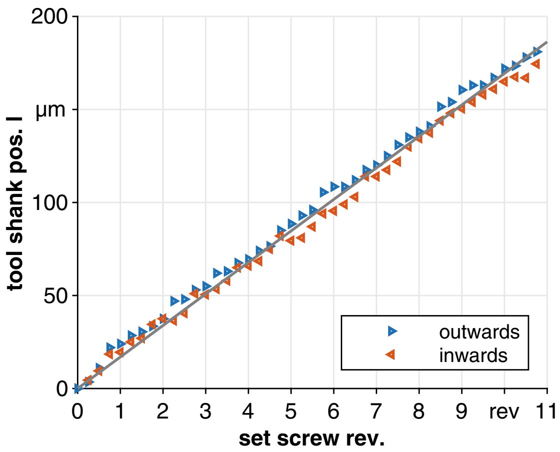

manual tool alignment
wedge angle: 5°
set screw thread: 0.2 mm
set screw increments: 22.5°

metrology
instrument: dial gauge
resolution: 2 μm/div.

fit
gradient: 16.94 μm/rev
Max shift: 181 μm

Fig. 10 Performance of mechanical presetting mechanism

4 Design of a Contactless Heat Input System for a Rotating Actuator

In a static setup, the heat input to the actuator is very simple, as both the heat source and the actuator remain at a fixed position. In contrast, the tool and hence also the actuator are rotating at several hundred revolutions per minute in an actual milling process. The heat transfer via an IR-LED is contactless per se and thus does not raise a problem here. However, the LED has to remain at a fixed position or otherwise the system design would get very complex. Thus, the heat can only be transferred to the actuator within a small timeframe, which is defined by the width of the actuator, circumference on which it is rotating and the spindle speed (Eq. 4).

$$t_{heat,rev} = \frac{w}{2 \cdot \pi \cdot r_{\text{act}} \cdot n/60} \tag{4}$$

At a typical spindle speed for diamond fly-cutting of $n = 1{,}000\ \text{min}^{-1}$, this calculates to $t_{heat,rev} = 4$ ms whereas for high speed cutting at $n = 20{,}000\ \text{min}^{-1}$ it is only $t_{heat,rev} = 200\ \mu$s. In combination with the forced convection due to the rotation, this timespan is not enough to generate a stable elevated temperature of the actuator. As a consequence, a device that allows the heat input to follow the actuator movement has to be devised.

A moving ring light system (patent pending) has been developed to serve this purpose [13]. It consists of multiple LEDs that are evenly distributed along a circle in a way that the peak intensity is directed at the actuator midpoint. All LED are powered by a common energy supply and each LED can be activated by a dedicated transistor, i.e. by a low-power signal line. One or more of these LED are used to

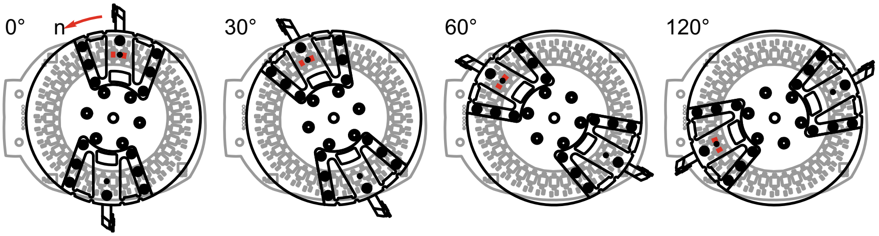

Fig. 11 Principle of the ring light system for a quasi-continuous heating of the thermal actuator. LEDs advance according to the angular position of the target actuator

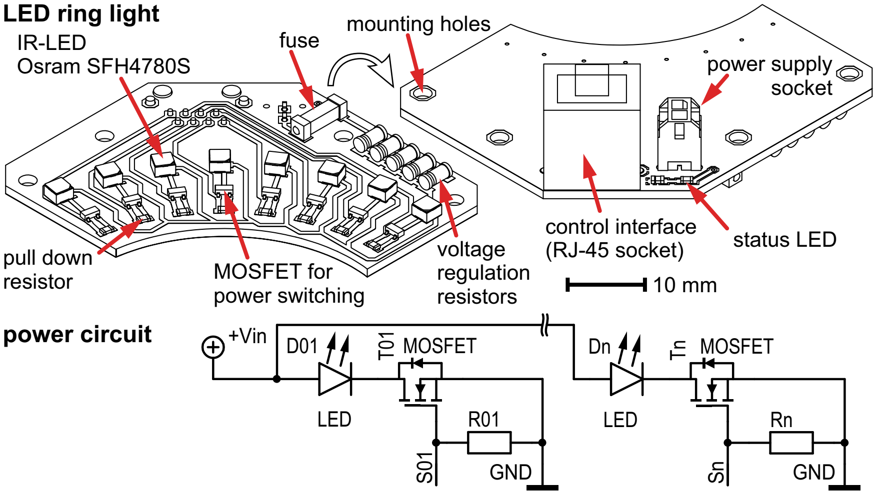

Fig. 12 Ring light (1/4) with 8 IR-LED, switching transistors and common power supply for all LED

illuminate the thermal actuator while the other LED are switched off. Upon rotation of the milling tool, the active LED are advanced along the ring to follow the position of the actuator (Fig. 11), while the body of the ring light stays stationary. In this way, a quasi-constant heating of the actuator is achieved.

For reasons of simplicity, handling and manufacturability, the current ring light system consists of four equal segments that cover a quarter of the ring and incorporate 8 IR-LED each (Fig. 12). In this way, the ring light can be easily dismounted even when enclosing the spindle shaft for illuminating the backside of the actuator. All technical specifications of the ring light systems are comprised in Table 3.

The switching of the LED is performed by a dedicated control electronics which was designed as a shield circuit board for an Arduino Mega 2560 board (Fig. 13). The Arduino evaluates the angular position of the spindle, either directly via the spindle encoder or via photo sensors that detect a scale on the tool holder, and generates the appropriate sequence of activated LED. As the use of LED also enables the

Table 3 Technical specifications of ring light system

Total number of LED	32
Element shape	¼ ring
IR-LED per element	8
IR-LED manufacturer and model	Osram SFH 4780S
Wavelength λ	820 nm
Radiant intensity I_e	2.3 W sr^{-1}
Half-angle φ	±10°
Total radiant flux Φ_e	600 m W
Rise time t_r	8 ns
Fall time t_f	14 ns
Forward voltage U_f	3.3 V
Forward current I_f	0.5 A

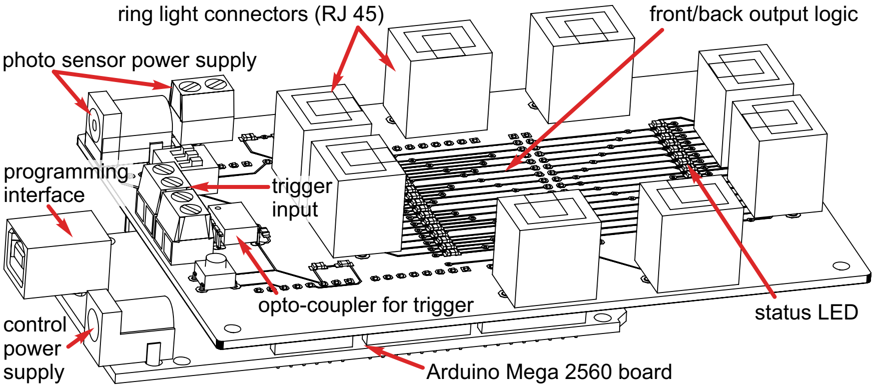

Fig. 13 Circuit board (Arduino Shield) for ring light control

application of double-sided heating, two separate sequences need to be generated for the front and back ring light, as one of them is running clockwise and the other one counter-clockwise to follow the spindle rotation. This is directly done on the circuit board by a hard-wired logic.

5 Experimental Spindle Setup for Tool Holder Evaluation

The evaluation of the finalized thermal tool holder was mainly conduced on two experimental platforms. First, an air-cutting spindle test stand was used on which the tool holder can be analyzed without cutting interaction (Fig. 14).

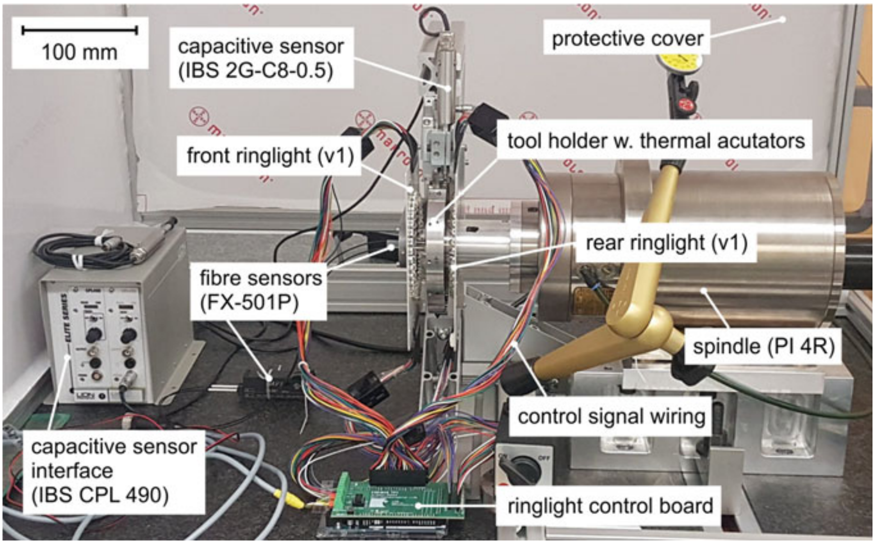

Fig. 14 Offline test stand for evaluating the thermal tool holder on an air-bearing spindle without cutting interaction

It consists of a Professional Instruments 4R air-bearing spindle on which the milling tool incorporating the thermal tool holder is fixed using an adapter which provides the needed clearance for mounting the rear ring light. Furthermore, a fiber sensor (FX-501P by Panasonic) is used to monitor the revolution of the actuator and determine the angular position for advancing the LED. The expansion is evaluated by measuring the position reference plane located below the tool shank on the circumference of the tool holder with a capacitive sensor (IBS 2G-C8-0.5 with a CPL 490 interface).

This setup was later transferred to a Nanotech 500FG machine tool for additional cutting experiments. The 4R air-bearing spindle is mounted on the B-axis table of the machine tool while the workpiece is fixed on the (clamped) main spindle of the 500FG. In addition to the test stand, a dynamometer was placed under the workpiece fixture to be able to measure the development of cutting forces during machining and to correlate this to the thermal expansion. The setup is depicted in Fig. 15 with the initial version of the ring light (v1: 36x LED type SFH4783, single board layout) shown in the left image and the revised ring light system (v2: 32x SFH4780S, quarter segment boards) shown on the right.

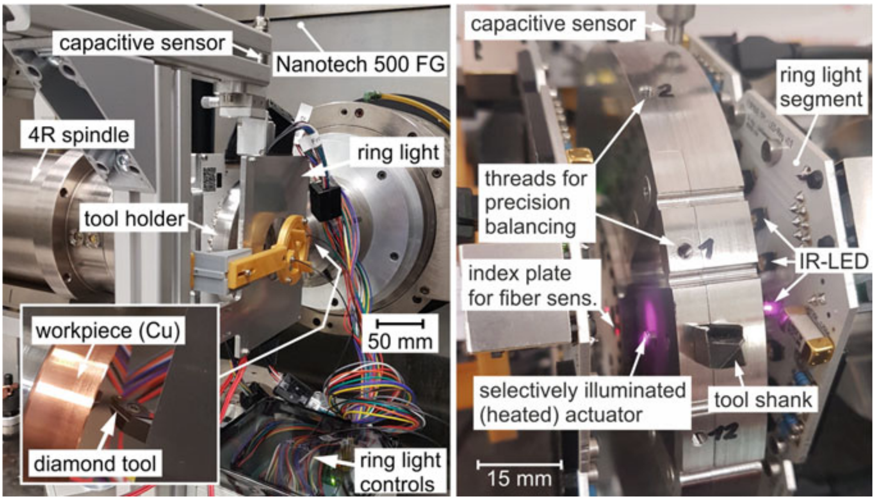

Fig. 15 Machine setup for evaluating the thermal tool holder on a Nanotech 500 FG. Left image shows the complete setup with ring light version 1 and the right image shows a closeup of the setup with the revised ring light (version 2)

6 Assessment of Actuator Performance

6.1 Results from Spindle Tests (No Machining)

When testing the actuator performance under rotation of the spindle, further processing of the measurement data is required. As the position of the reference plane is continuously measured during the process, the signal has to be segmented in order to reflect the position of the respective sections. A complete measurement of several revolutions as well as a zoom to a single revolution is shown in Fig. 16.

Due to the notches of the flexure hinges, the individual sections of the actuator are easily identifiable by the signal dropouts that occur when the capacitive measurements move out of the sensor's range at these points. Thus, they are utilized for the segmentation of the signal. The fully segmented signal consists of eight distinct sections: the two actuators, four flexure hinges (two per actuator) and two large portions in between. The latter should not be affected by the thermal state of the actuator and thus are used as reference. While the flexure hinges expand along with the thermal actuators, their position is of no relevance to the tool setting. However, their position could be evaluated to detect an asymmetry of the thermal expansion due to inhomogeneous heating as a result of misalignment between heat source and actuator.

In order to assess the temporal development of the thermal expansion, the mean position of each segment is determined for each revolution. Therefore, the noise of the signal is first reduced by applying a low-pass Butterworth filter with a cut-off

Setup: PI Model 4R, n = 240 min^{-1}
Heat source: Osram SFH-4783, λ_c = 850 nm, ϕ = ±12°, I_e = 2.3 W/sr
Metrology: IBS CPL 490, 2G-C8-0.5, f = 10 kHz

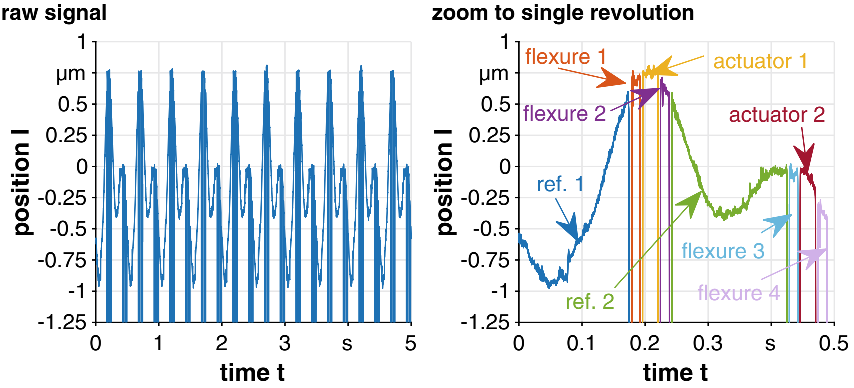

Fig. 16 Measurement of the reference plane with rotating spindle: raw data of 10 consecutive revolutions (left) and segmentation of a single revolution and association to actuator geometry (right)

frequency of $\lambda_c = 100$ Hz. Then, the mean signal of the first couple of revolutions is subtracted from each subsequent revolution in order to remove systematic deviations, like e.g. unbalances or runout errors, from the measurement. Finally, the segments are averaged into a single value which is recorded as the position of the respective segment. The temporal development of an exemplary test run at $n = 240$ min^{-1} is shown in Fig. 17.

Testing for the maximum thermal expansion that can be achieved at selected spindle speeds yields the following graph (Fig. 18).

This shows a clear dependence of the maximum expansion on the applied spindle speed that can be fitted to a logarithmic equation. The faster the speed is set, the more forced convection occurs on the actuator surface, resulting in a cooling of the thermal actuator and thereby a reduction of the maximum expansion. Nevertheless, up to a speed of $n = 1{,}500$ min^{-1} the achievable expansion is deemed sufficient to compensate most residual misalignment of the diamond tools after presetting.

6.2 Open-Loop Performance in Cutting

The tests in an test stand environment (i.e. without actual tool-workpiece interaction) have proven the general applicability of the selected method for tool setting on a rotating spindle. However, in this setup the location of the cutting edge is not determined directly, but measured as a shift of the reference plane situated slightly

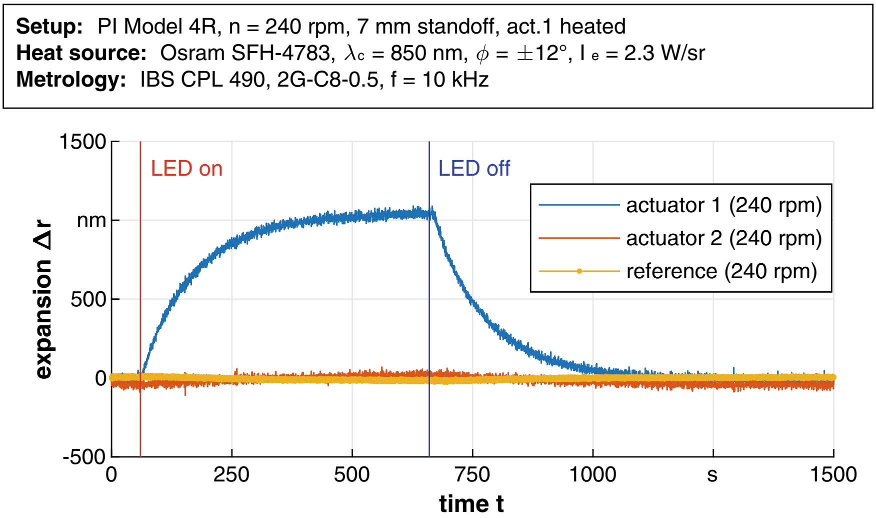

Setup: PI Model 4R, n = 240 rpm, 7 mm standoff, act.1 heated
Heat source: Osram SFH-4783, λ_c = 850 nm, ϕ = ±12°, I_e = 2.3 W/sr
Metrology: IBS CPL 490, 2G-C8-0.5, f = 10 kHz

Fig. 17 Comparison of actuator expansion at 240 min^{-1} for a LED standoff distance of 7 mm; the light rings are switched to full power (1 A per active LED) between $t = 60$ s and 660 s

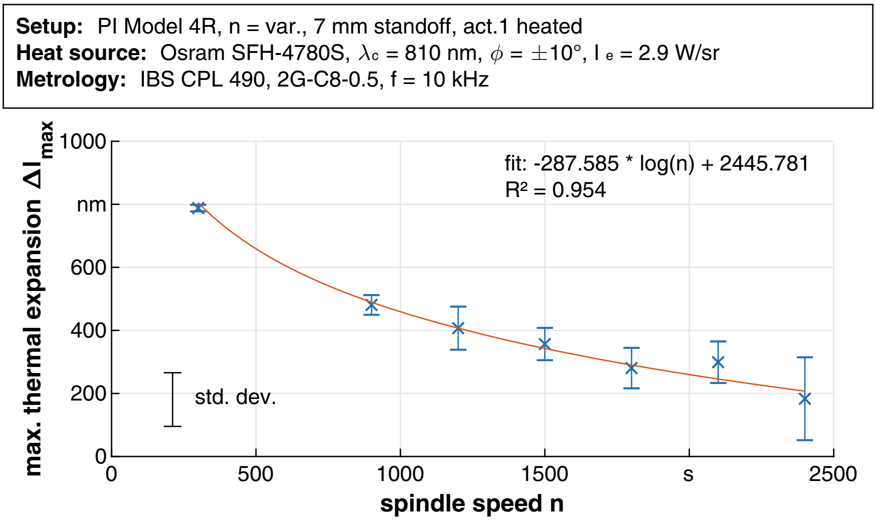

Setup: PI Model 4R, n = var., 7 mm standoff, act.1 heated
Heat source: Osram SFH-4780S, λ_c = 810 nm, ϕ = ±10°, I_e = 2.9 W/sr
Metrology: IBS CPL 490, 2G-C8-0.5, f = 10 kHz

Fig. 18 Maximum thermal expansion for selected spindle speeds

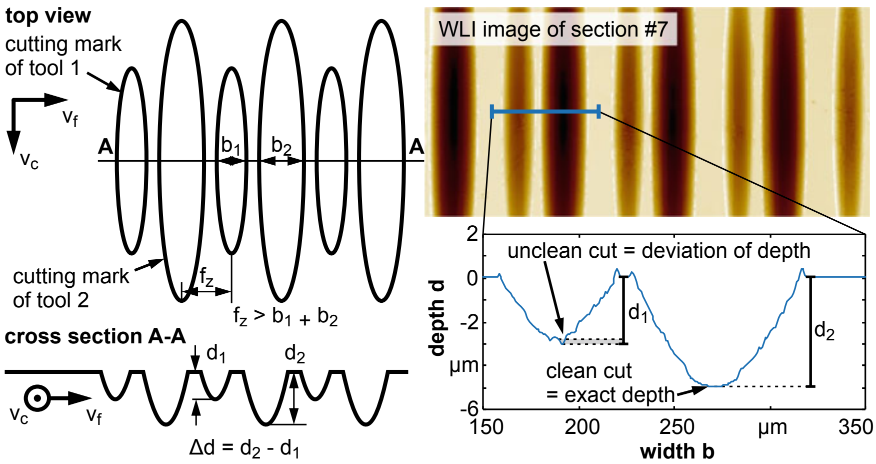

Fig. 19 Generation of isolated cutting marks from two engaged cutting edges by applying elevated cross feed velocity and measurement of generated marks with a WLI for evaluating the depth difference

below the tool shank on the circumference of the tool holder. Thus, it has to be verified whether the thermal expansion also affects the position of the cutting tool as a whole. This can only be analyzed in actual cutting experiments.

Therefore, a strategy was developed in which the tool inserts are mechanically pre-aligned. The infeed of the machine is set such that both cutting edges leave a mark on the surface of the workpiece (Fig. 19).

During cutting the cross feed velocity v_f is then set according to the selected spindle speed so that both tools leave separated marks on the workpiece surface. While heating the actuator with the LED ring light system, a set of these cutting marks is generated at selected time intervals (here: $\Delta t = 1$ s) to inscribe the respective state of the actuator expansion to the workpiece surface. This is later evaluated by measuring the cutting marks with a white light interferometer (WLI, a Talysurf CCI HD was utilized in this study) and determining the depth of the adjacent cutting marks. By comparing the development of the depth difference Δd to the initial state before heating the actuator, the thermal expansion $\Delta L = \Delta d$ of the tool holder is determined. The resulting measurements are shown in Fig. 20.

It can be seen that the mark depth changes according to the shift of the reference plane. However, the depth evaluation is prone to large deviations resulting from the depth measurements and the determination of the correct offsets. Furthermore, registration to the time-based measurements of the reference plane is done manually and thus associated with a deviation as well.

Nevertheless, a shift of the cutting edges along with the reference plane is observed for all measurements up to a spindle speed of $n = 1{,}800\ \text{min}^{-1}$. Higher speeds could not be applied as the maximum feed velocity of the Nanotech 500 FG (max. $v_f = 600\ \text{mm min}^{-1}$) is not sufficient to generate isolated marks in this case. Figure 21

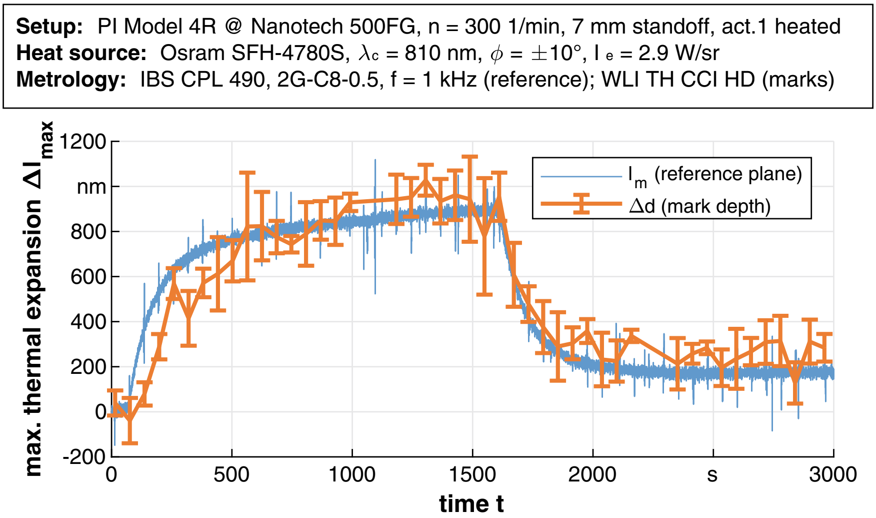

Setup: PI Model 4R @ Nanotech 500FG, n = 300 1/min, 7 mm standoff, act.1 heated
Heat source: Osram SFH-4780S, λ_c = 810 nm, $\phi = \pm 10°$, I_e = 2.9 W/sr
Metrology: IBS CPL 490, 2G-C8-0.5, f = 1 kHz (reference); WLI TH CCI HD (marks)

Fig. 20 Depth difference of cutting marks taken at 1 min intervals compared to the continuously measured expansion of the reference plane for $n = 300\ \text{min}^{-1}$

shows a comparison of the maximum measured difference in mark depth to the maximum expansion of the reference plane. It can be observed that both curves follow the same trend with the expansion measured via the mark depth being slightly below that of the reference plane. Nevertheless, this is considered to be a systematic deviation of the actuator.

7 Control of Actuator Position to Nanometer Precision

The previous measurement have shown that the thermal actuator is generally capable of achieving the required expansion for compensating residual tool misalignment. However, in order to apply the system for the milling of an actual optical surface, the thermal expansion has to be precisely set within its range and this position has to be maintained throughout the whole cutting operation. Thus, a closed loop control of the thermal expansion has been implemented.

7.1 Design of Control Loop

The schematics of the (PI) control loop are shown in Fig. 22. The location of the reference plane l is measured by the capacitive sensor and compared to an initially selected offset L_0 to determine the thermal expansion ΔL_{meas}. This is then compared

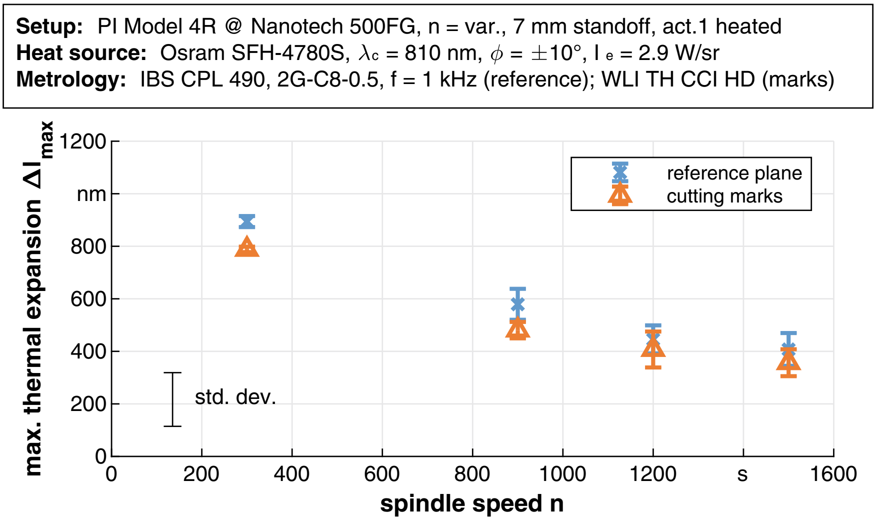

Fig. 21 Maximum thermal expansion of reference plane and depth difference of cutting marks for varied spindle speeds

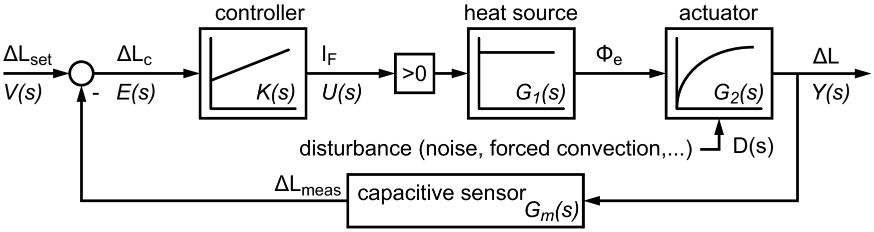

Fig. 22 Control loop for thermal expansion

to the set value of the expansion ΔL_{set} to determine the control offset ΔL_c. A proportional-integral-differential (PID)-controller is used to calculate the necessary forward current for the infrared LED I_f. This generates a radiant flux Φ_e that is directed on the actuator and causes a change of its temperature T_a. Due to the forced convection as a result of the spindle rotation, the actual temperature difference ΔT is reduced. Ultimately, this causes a thermal expansion ΔL of the actuator. Detailed explanations on the development of the control loop can be found in [12].

For the practical application, the sections of heat source, heat transfer, forced convection and actuator expansion are combined into a simplified model, i.e. a transfer function $G(s)$ of the whole system, which is derived from the step response $H(s)$ of the thermal actuator:

$$G(s) = \frac{Y(s)}{U(s)} = H(s) \cdot s \tag{5}$$

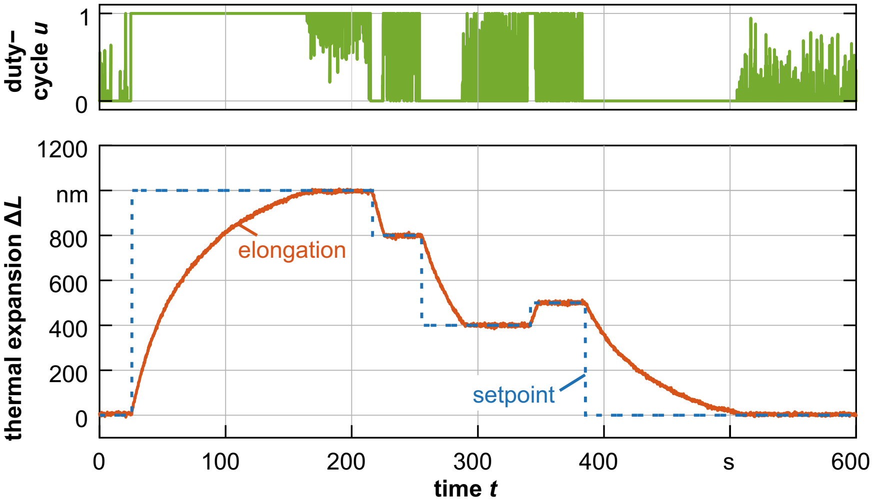

Fig. 23 Results for controlling the thermal expansion in a static setup

$$H(s) = \mathcal{L}\left\{\Delta L_{max} \cdot \left(1 - e^{-t/t_h}\right)\right\} \tag{6}$$

$$G(s) = \frac{\Delta L_{max}}{t_h \cdot s + 1} \tag{7}$$

7.2 Performance of the Control Loop in a Static Setup

Initially, the control loop was developed using a static setup of the actuator, to minimize disturbances from the dynamics of the spindle and to facilitate the acquisition of thermal expansion. With this setup it was verified that the thermal expansion may be controlled in the nanometer range and thereby be applied for tool setting. Figure 23 shows the system response for selected setpoints across the total range of thermal expansion. It can be seen that the targeted expansion is reached without overshoot and that a retraction of the actuator is possible by cooling the actuator (in this case by natural convection). The duty cycle of the LED still shows a lot of noise, which may be attributed to the not optimized control parameters chosen for this experiment.

In order to determine the minimum step size that can be set with the setup, a series of steps was fed to the control system, from ±20 nm down to ±1 nm. It is shown in Fig. 24 that steps down to ±5 nm can be safely set within the system. While the 1 nm steps are also discernible in the graph, these set values cannot reliably be achieved, given the present measurement noise of approx. 6.5 nm.

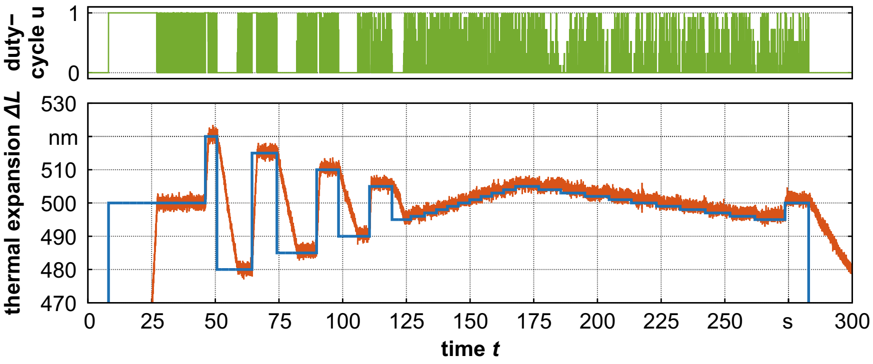

Fig. 24 Step series for determining the minimum control increments for the thermal actuator (static)

7.3 Performance of the Control Loop in a Spindle Setup

For control of the actuator during rotation of the spindle, its position has to be extracted from the roundness measurement of the reference plane. While this may be similarly done to the signal segmentation and analysis, the underlying approach is not suitable for real-time processing during the process. Instead, the position acquisition needs to be triggered per revolution so that only a small portion of the signal is processed (Fig. 25). In this case, the trigger signal is taken from the fiber optics measurement of the angular markings on the tool holder that are primarily used for advancing the LED of the ring lights.

On receiving a trigger signal, a finite number of samples with the selected frequency is acquired (Fig. 25, 1). For further processing and correct detection of all segments, the number of samples should be chosen so that one full revolution of the tool holder is obtained in one pass. For instance, at a typical sample rate of $f_s = 10$ kHz and a spindle speed of $n = 1{,}500\ \text{min}^{-1}$ (25 Hz), at least 400 samples are required. The measurement of a revolution is then aligned to a reference signal (2b), e.g. the mean of several revolutions with a defined heating state. After alignment, the signal dropouts are identified (3) and the data is split at these markers into sub-arrays representing each segment of the tool holder (4). To determine the average expansion of each segment, the difference between the current measurement and the reference is calculated (5) and the median of the resulting array is passed on (6). The median is preferred here over the mean of the segment, as it is more robust.

The extracted position of the actuator segment can then be utilized for building a control loop similar to that of the static setup. This has been done using a digital twin of the actual actuator that mimics its response (i.e. thermal expansion) to the control input (i.e. LED power) on the basis of a plant model (Fig. 26). In this way, the software implementation can be conducted truly independent of the availability of the setup on the machine tool. The internal plant parameters of the digital twin were calculated

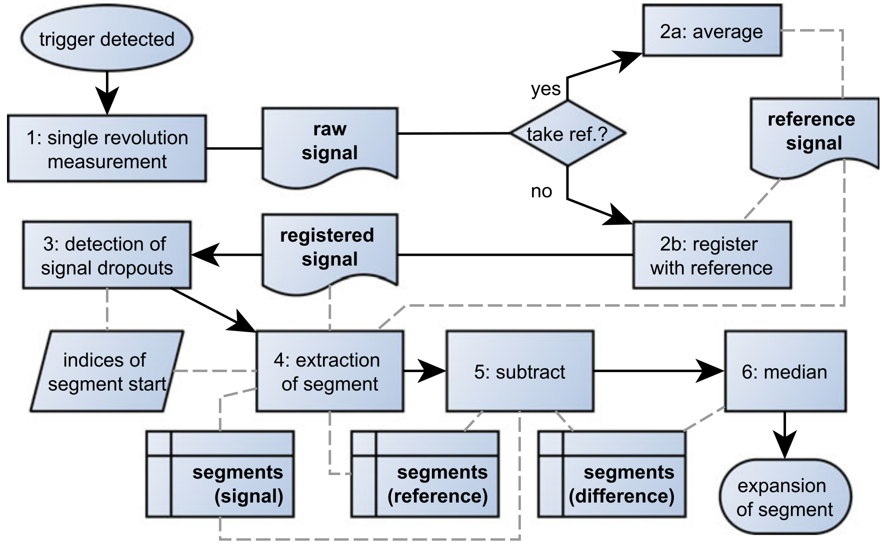

Fig. 25 Triggered data acquisition for determining position of actuator segment

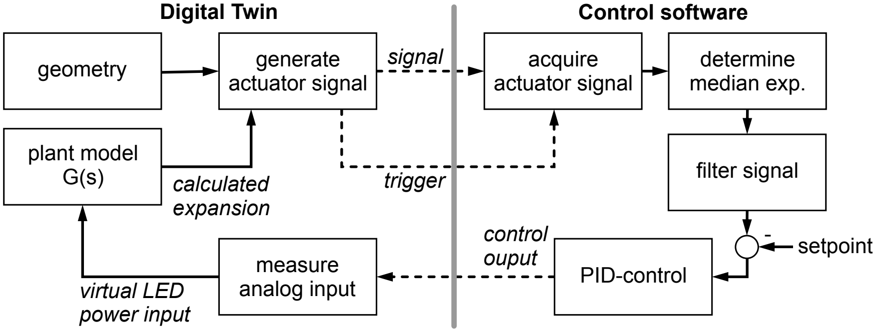

Fig. 26 Schematics of Digital Twin for the offline development of actuator controls

from the measurements obtained for the actual tool holder at $n = 240\ \text{min}^{-1}$, as shown in the previous sections ($K_{u,\text{DT}} = 1{,}102$ nm, $T_{i,\text{DT}} = 49.8$ s, $T_{d,\text{DT}} = 0.02$ s).

It has to be noted that while a spindle speed can be set within the digital twin, this only affects the frequency of the generated signal. The reduced maximum thermal expansion due to the forced convection is not considered in the current implementation, as it is not inherently necessary for the development of the control software. In the present evaluation, the plant model has been derived from a measurement of the actuator taken at low-speed, while the generation rate has been set to elevated spindle speed ($2{,}400\ \text{min}^{-1}$) to minimize the effective processing time of the simulations.

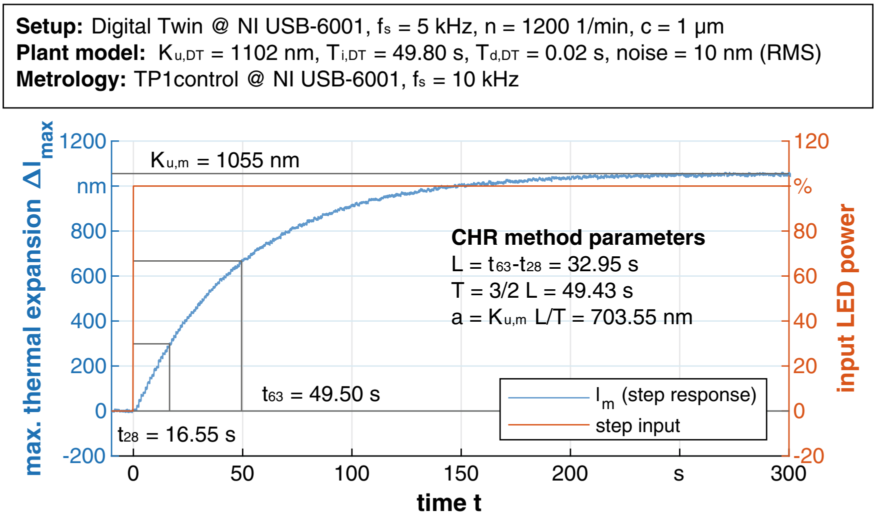

Setup: Digital Twin @ NI USB-6001, f_s = 5 kHz, n = 1200 1/min, c = 1 µm
Plant model: $K_{u,DT}$ = 1102 nm, $T_{i,DT}$ = 49.80 s, $T_{d,DT}$ = 0.02 s, noise = 10 nm (RMS)
Metrology: TP1control @ NI USB-6001, f_s = 10 kHz

CHR method parameters
L = t_{63}-t_{28} = 32.95 s
T = 3/2 L = 49.43 s
a = $K_{u,m}$ L/T = 703.55 nm

Fig. 27 Step response measured using a digital twin of the rotating tool holder and derived plant parameters

To account for possible deviations introduced by the signal splitting and the digital twin setup, the step response of the actuator is measured again with the adapted control software and the plant parameters of the actuator are determined (Fig. 27).

It can be seen that the measured plant parameters and are close to the respective parameters set in the digital twin ($K_{u,m} \approx K_{u,DT}$ and $T \approx T_{i,DT}$) with the dead time being significantly increased compared to the plant model $L \gg T_{d,DT}$. This is caused by expansion not being measured continuously, but once per revolution, i.e. at a significantly reduced frequency. Thus, the reaction of the system is measured later than the actual occurrence of the thermal expansion. Nevertheless, this is automatically considered by the control loop if the plant parameters are determined in this way.

The parameters for the PID controller are then calculated using different approaches. Initially, the method of (CHR) for setpoint accuracy with minimal overshoot was chosen and compared to the CHR calculation for disturbance rejection with minimal overshoot [5]. Additionally, the controller was tested with manually tuned parameters: K_p was chosen higher than the CHR values for potential decrease of rise time and steady-state error, T_i was set to a very long time constant as this is a major factor for decreasing the steady-state error and T_d was set to a small value for improved disturbance rejection. The calculated parameters are listed in Table 4.

The following Fig. 28 shows the response of the system with a closed control loop using the abovementioned PID parameters for a step-input of 500 nm. It can be seen that both parameter sets calculated according to the CHR method resulted in significant overshoot of the actuator position before settling to its final position. The method for setpoint accuracy yields less overshoot, but a significantly longer settling time than the other methods. With the parameters for disturbance rejection,

Table 4 Control parameters for the thermal tool holder (digital twin)

Parameter	CHR (setp. acc.)		CHR (dist. rej.)		Manually tuned	
	Calculation	Value	Calculation	Value	Calculation	Value
K_p	$0.6/a$	0.00085	$0.95/a$	0.00134	“High”	0.0064
T_i	$1 \cdot T$	49.43 s	$2.4 \cdot T$	119.16 s	“Very long”	1,200 s
T_d	$0.5 \cdot L$	16.48 s	$0.42 \cdot L$	13.9 s	“Short”	3 s

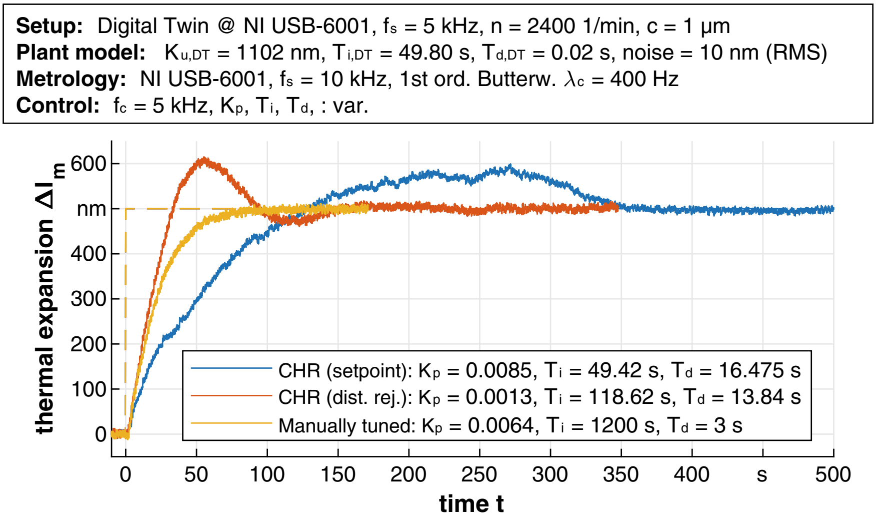

Setup: Digital Twin @ NI USB-6001, f_s = 5 kHz, n = 2400 1/min, c = 1 µm
Plant model: $K_{u,DT}$ = 1102 nm, $T_{i,DT}$ = 49.80 s, $T_{d,DT}$ = 0.02 s, noise = 10 nm (RMS)
Metrology: NI USB-6001, f_s = 10 kHz, 1st ord. Butterw. λ_c = 400 Hz
Control: f_c = 5 kHz, K_p, T_i, T_d, : var.

Fig. 28 Comparison of control parameters for a setpoint of 500 nm using a Digital Twin of the tool holder

the settling time is improved, but the overshoot is further increased. The self-tuned parameters yields the best results in terms of settling time, overshoot and setpoint accuracy and thus are chosen for further analysis.

The controlled response of the system using the self-tuned parameters is applicable across the complete stroke of the actuator as is shown in Fig. 29. As there is no overshoot with these parameters, the system may well be utilized for in-process re-setting of the tool, e.g. to compensate for gradual tool wear or low-dynamic disturbances.

With the given noise of the system (10 nm RMS), the system follows inputted setpoints down to ±5 nm, as depicted in Fig. 30.

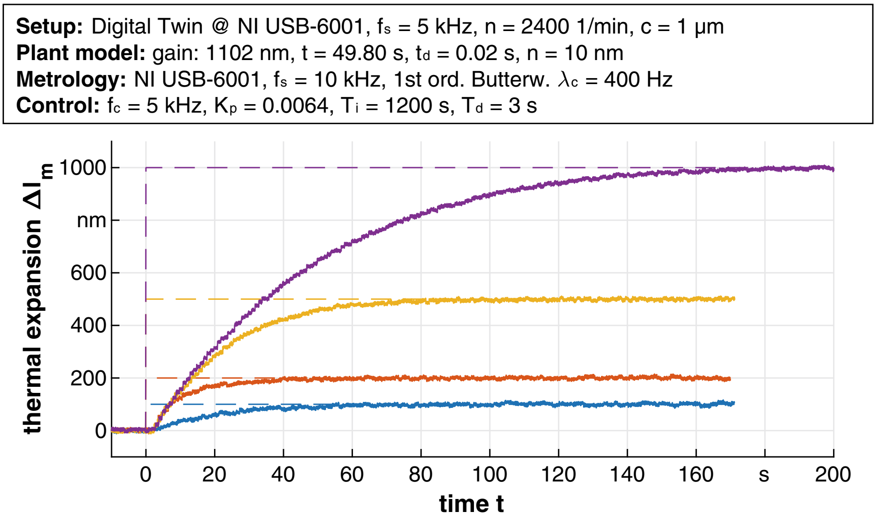

Setup: Digital Twin @ NI USB-6001, f_s = 5 kHz, n = 2400 1/min, c = 1 µm
Plant model: gain: 1102 nm, t = 49.80 s, t_d = 0.02 s, n = 10 nm
Metrology: NI USB-6001, f_s = 10 kHz, 1st ord. Butterw. λ_c = 400 Hz
Control: f_c = 5 kHz, K_p = 0.0064, T_i = 1200 s, T_d = 3 s

Fig. 29 Closed loop control of actuator position (Digital Twin) for selected setpoints

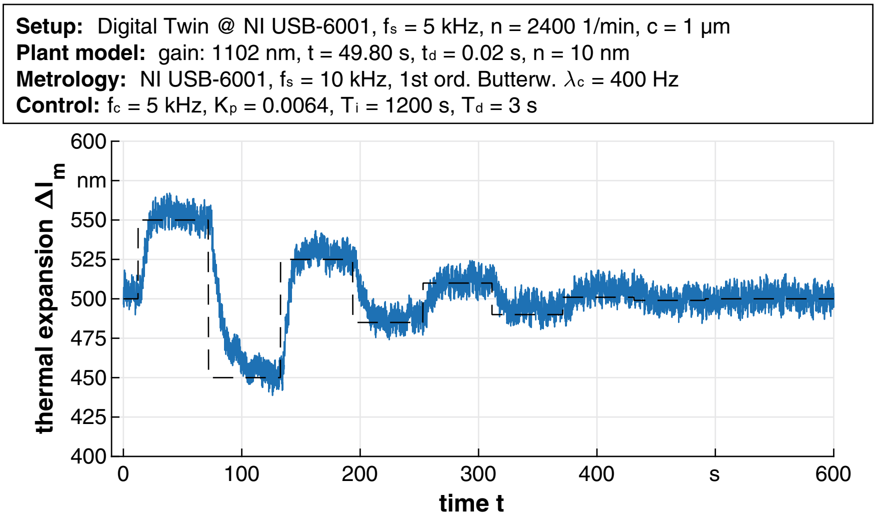

Setup: Digital Twin @ NI USB-6001, f_s = 5 kHz, n = 2400 1/min, c = 1 µm
Plant model: gain: 1102 nm, t = 49.80 s, t_d = 0.02 s, n = 10 nm
Metrology: NI USB-6001, f_s = 10 kHz, 1st ord. Butterw. λ_c = 400 Hz
Control: f_c = 5 kHz, K_p = 0.0064, T_i = 1200 s, T_d = 3 s

Fig. 30 Control response (Digital Twin) for selected small scale setpoints

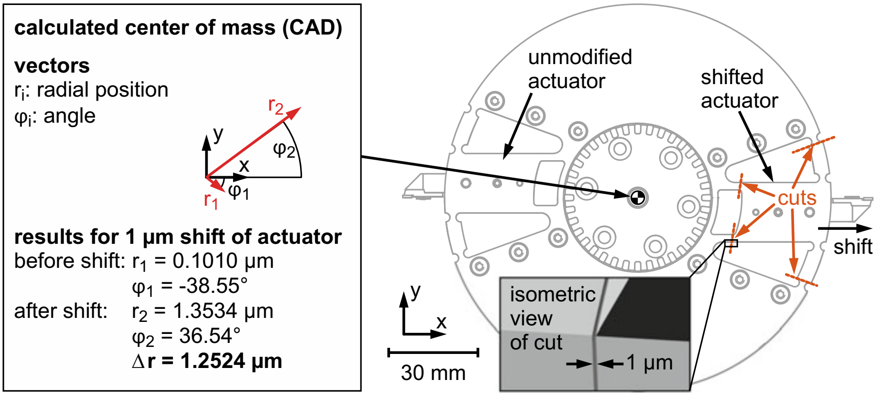

Fig. 31 Calculated unbalances for thermally expanded actuator

8 Influence Multi-tool-holder on General Machining Performance

After the control of the thermal actuator has been successfully demonstrated, this section will focus on potential influences of the tool-holding mechanism on the process itself.

8.1 Impact of Tool-Shift on Unbalances

First, it has been examined whether the tool shift induced by the thermal actuator results in a change of the balancing state of the rotor. Calculations based on the CAD model indicate that shifting one of the actuators by its maximum expansion (1 µm) moves the center of mass of the tool holder by approximately 1.25 µm (see Fig. 31). In theory, this results in a measurable change of the balancing state and could potentially be applied for ultra-fine balancing of the rotor, if a compensation mass is shifted in this way.

In order to verify this, the balancing state was measured experimentally for selected spindle speeds with the actuator at its base length (“cold”) and at its maximum expansion (“heated”). The results are shown in Fig. 32. Generally, the measured unbalance is decreasing with increasing spindle speed. While the mean unbalance is approx. 5 g mm at 900 min^{-1}, it is below 0.31 g mm at 2,500 min^{-1}. Furthermore, no significant change of the unbalance could be detected when the actuator is at its maximum thermal expansion. This also implies that the system cannot be applied for balancing purposes in its current form.

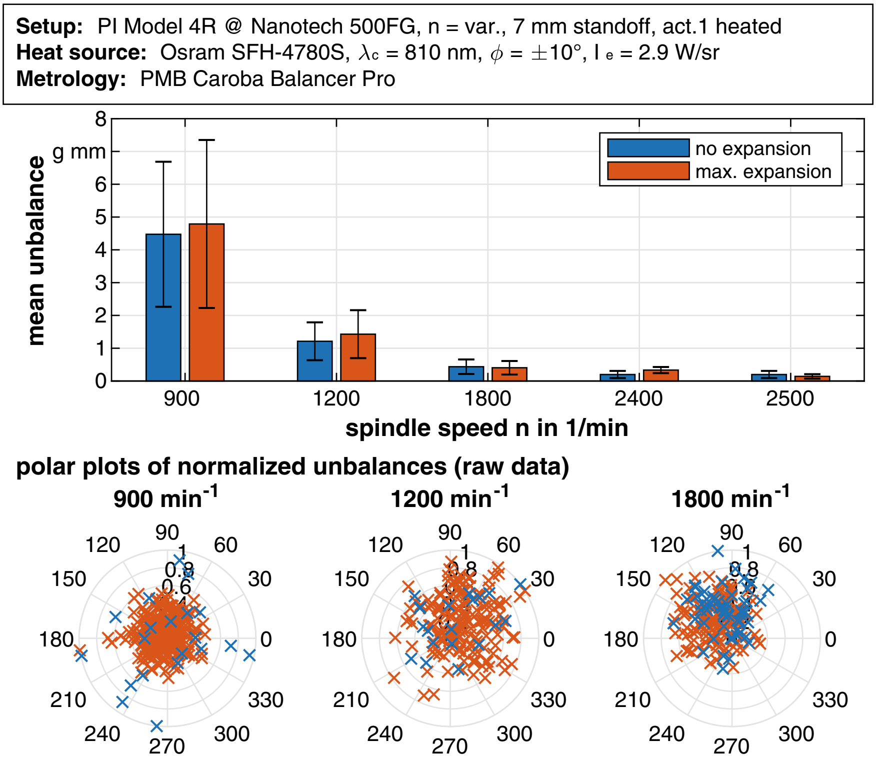

Fig. 32 Effect of tool setting on unbalances: mean unbalance and standard deviation for cold actuator and maximum thermal expansion (top) and normalized unbalances for selected spindle speeds (bottom)

8.2 Influence of Spray Mist Lubricant on Thermal Tool Setting

In the final experiments of this study, the influence of cutting fluid on the performance of the thermal tool setting was analyzed. For this, the cutting experiments described in Sect. 6.2 were repeated with minimum quantity lubrication directed at the cutting zone. The resulting spray mist potentially covers the heated faces of the actuator, thereby cooling the substrate in addition to the forced convection by the spindle rotation. Paraffin oil was selected as cooling fluid for these experiments, because it is electrically non-conductive and thus will not influence the electronics of the ring light system. In addition, it is only applied locally at the tool-workpiece contact point and therefore the influence of capacitive measurement of the reference plane is minimized. An exemplary analysis of both, the expansion measured at the reference plane and the cutting mark depth evaluated from the surface measurements, is shown in Fig. 33.

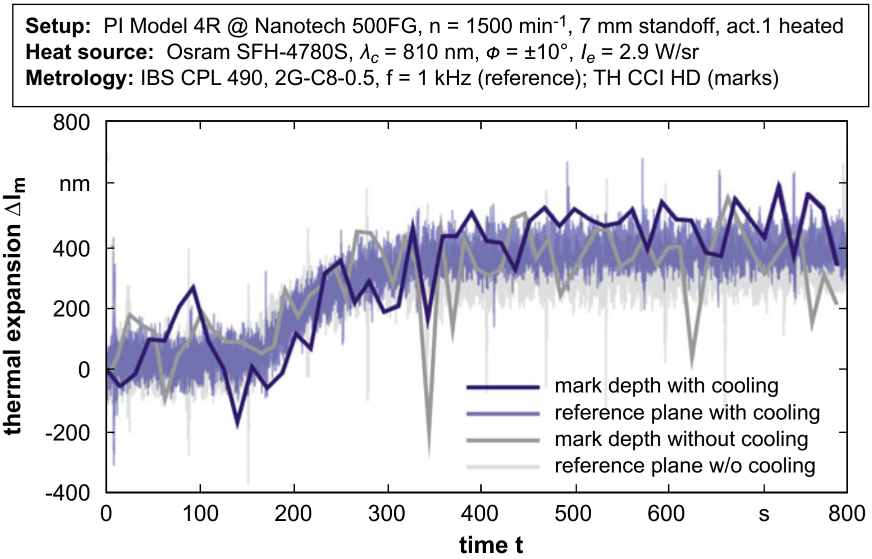

Setup: PI Model 4R @ Nanotech 500FG, n = 1500 min^{-1}, 7 mm standoff, act.1 heated
Heat source: Osram SFH-4780S, λ_c = 810 nm, Φ = ±10°, I_e = 2.9 W/sr
Metrology: IBS CPL 490, 2G-C8-0.5, f = 1 kHz (reference); TH CCI HD (marks)

Fig. 33 Measured expansion of the thermal tool holder (reference plane) and depth change of cutting marks (actual tool shift) for cutting tests with and without cooling fluid

The analysis shows no measurable reduction in actuator expansion and tool shift for machining with cutting fluid. Both parameters indicate an expansion of 400 nm that is achieved after about 400 s.

9 Conclusion and Outlook

Diamond milling using multiple cutting edges offers the potential to significantly increase the productivity of diamond machining. Its broad application is averted by the lack of ultra-precision tool setting mechanisms that can be applied on rotating spindles. Hence, the possibility of a thermally induced tool setting was investigated in this study. By locally heating a specific section of the milling tool, i.e. the tool holder, an actuating mechanism was triggered that causes the attached diamond tool and its cutting edge to shift in radial direction. A closed loop control can then be applied to minimize the deviation between this tool's radius and that of other tools in the setup.

The thermal actuating mechanism was initially analyzed using finite element modeling and later evaluated a static test stand. Based on the findings obtained in these studies, a final design of a milling tool with thermally adjustable holders for two diamond tools was derived. The heat input is generated by a moving ring light with infrared LED which has been specifically designed for this purpose (patent pending).

Additional tests of the novel milling tool on spindle test stands and in machining experiments have confirmed the general applicability of thermal tool setting in diamond milling. It was possible to build a closed loop control of the thermal actuator that evaluates the position of a reference plane during rotation and drives the ring light according to the determined offset. The initial parameterization of the control loop yields acceptable results in terms of setpoint accuracy and speed, but still results in overshoot of the expansion. Thus, an optimized controller using manually tuned parameters has been derived using a Digital Twin of the system. The controller drives the actuator to its maximum expansion in about 200 s and achieved a setpoint accuracy of ±5 nm. Furthermore, it has been demonstrated that the thermal tool setting does not change the balancing state of rotor and even is unaffected by spray mist lubrication of the cutting zone.

In order to mature this concept to an industrially applicable solution, a further analysis of the position stability and repeatability as well as of the impact of the localized heating on the long-term thermal stability of the machine tool is vital. Furthermore, the electronics, software and (setup-)procedures have to be refined in order to be applicable in an industrial environment.

References

1. Bono, M., Hibbard, R.: A flexure-based tool holder for sub-μ positioning of a single point cutting tool on a four-axis lathe. Precis. Eng. **31**(2), 169–176 (2007). https://doi.org/10.1016/j.precisioneng.2006.03.007
2. Brinksmeier, E., Gläbe, R., Autschbach, L.: Novel ultraprecise tool alignment setup for contour boring and ball-end milling. In: 18th ASPE Annual Meeting, Portland/Oregon, USA, October 2013, pp. 271–274. American Society for Precision Engineering (2013)
3. Brinksmeier, E., Preuss, W.: Micro-machining. Philos. Trans. Roy. Soc. A **370**, 3973–3992 (2012). https://doi.org/10.1098/rsta.2011.0056
4. Brinksmeier, E., Riemer, O., Gläbe, R.M. (eds.): Fabrication of Complex Optical Components. Springer, Heidelberg (2013). https://doi.org/10.1007/978-3-642-33001-8
5. Chien, K.L., Hrones, J.A., Reswick, J.B.: On the automatic control of generalized passive systems. Trans. ASME **74**, 175–185 (1952)
6. Dornfeld, D., Min, S., Takeuchi, Y.: Recent advances in mechanical micromachining. CIRP Ann. **55**(2), 745–768 (2006). https://doi.org/10.1016/j.cirp.2006.10.006
7. Fang, F.Z., Zhang, X.D., Weckenmann, A., Zhang, G., Evans, C.J.: Manufacturing and measurement of freeform optics. CIRP Ann. **62**(2), 823–846 (2013). https://doi.org/10.1016/j.cirp.2013.05.003
8. Neugebauer, R., Denkena, B., Wegener, K.: Mechatronic systems for machine tools. CIRP Ann. **56**(2), 657–686 (2007). https://doi.org/10.1016/j.cirp.2007.10.007
9. Schönemann, L., Brinksmeier, E., Osmer, J.: A piezo-driven adaptive tool holder for ultraprecision diamond tool alignment. In: van Brussel, H., Brinksmeier, E., Spaan, H., Burke, T. (eds.) 9th Euspen International Conference, vol. 1, pp. 398–401 (2009)
10. Schönemann, L., Mejia, P., Riemer, O., Brinksmeier, E.: Design and evaluation of a thermal actuator for ultra-precision machining. In: Blunt, L. (ed.) 11th International Conference & Exhibition on Laser Metrology, Machine Tool, CMM & Robotic Performance (Lamdamap 2015), pp. 320–330. Euspen (2015)

11. Schönemann, L., Preuss, W., Riemer, O., Foremny, E., Brinksmeier, E., Kuhfuss, B.: Ultrapräzise Hochgeschwindigkeitsbearbeitung. Teil 1: Steigerung der Flächenleistung durch den Einsatz von Mehrfach- Werkzeugen und HSC-Spindeln. wt Werkstattstechnik **105**(6), pp. 366–370 (2015)
12. Schönemann, L., Riemer, O., Brinksmeier, E.: Control of a thermal actuator for UP-milling with multiple cutting edges. Procedia CIRP **46**, 424–427 (2016). https://doi.org/10.1016/j.procir.2016.03.194. Ed. by Wertheim, R., Ihlefeldt, S., Hochmuth, C., Putz, M
13. Schönemann, L., Riemer, O., Brinksmeier, E.: Arbeitsmaschine mit einem rotierenden Maschinenteilhalter, insbesondere Werkzeugmaschine mit rotierendem Werkzeughalter, Verfahren zum Justieren eines Maschinenteils, insbesondere Werkzeugs, sowie Ringlicht für eine derartige Arbeitsmaschine. German pat. req. 10 2017 119 828 A1. Leibniz-Institut fürWerkstofforientierte Technologien IWT, Universität Bremen, 29 August 2017
14. Schönemann, L., Riemer, O., Brinksmeier, E.: Recent advances in ultra-precision milling with multiple-cutting edges. In: 32nd ASPE Annual Meeting, Charlotte/NC, USA, 29 October–3 November 2017, pp. 175–179. American Society for Precision Engineering (2017)
15. Schönemann, L., Riemer, O.: Thermo-mechanical tool setting mechanism for ultra-precision milling with multiple cutting edges. Precis. Eng. (2018). https://doi.org/10.1016/j.precisioneng.2018.09.003
16. Schönemann, L.: Surface simulation for ultra-precision milling with multiple cutting edges. In: 69th CIRP General Assembly - Part 2, Birmingham, 22 August 2019
17. Schönemann, L., Berger, D., Dörgeloh, T., Riemer, O., Brinksmeier, E., Krüger, R., Schreiber, P., Denkena, B., Hochbein, J., Parsa, N., Schenck, C., Kuhfuss, B.: Synergistic approaches to ultra-precision high performance cutting. CIRP J. Manuf. Sci. Technol. **28**, 38–51 (2020). https://doi.org/10.1016/j.cirpj.2019.12.001
18. Sortino, M., Totis, G., Kuljanic, E.: Comparison of injection molding technologies for the production of micro-optical devices. Procedia Eng. **69**, 1296–1305 (2014). https://doi.org/10.1016/j.proeng.2014.03
19. Sze-Wei, G., Han-Seok, L., Rahman, M., Watt, F.: A fine tool servo system for global position error compensation for a miniature ultra-precision lathe. Int. J. Mach. Tools Manuf. **47**(7–8), 1302–1310 (2007). https://doi.org/10.1016/j.ijmachtools.2006.08.023
20. Transregionaler Sonderforschungsbereich TR4, ed. Prozessketten zur Replikation komplexer Optikkomponenten. Abschlussbericht. Berichtszeitraum 7/2008–8/2012 (2012)
21. Zhang, S.J., To, S., Zhu, Z.W., Zhang, G.Q.: A review of fly cutting applied to surface generation in ultra-precision machining. Int. J. Mach. Tools Manuf. **103**, 13–27 (2016). https://doi.org/10.1016/j.ijmachtools.2016.01.001

Ultra-Precision High Speed Cutting

Daniel Berger, Lars Schönemann, Oltmann Riemer, and Ekkard Brinksmeier

Abstract Today, the technology of high speed machining (HSM) is well understood and established for conventional turning and milling at high material removal rates. However, this is not the case for ultra-precision processes. Consequently, in this project the mechanisms of high-speed machining in the ultra-precision range were investigated for both, non-ferrous metals as well as brittle-hard semiconductor materials, by diamond turning and milling (i.e. fly-cutting). For both material classes, reduced tool wear, lower cutting forces and most important, superior surface quality were achieved. The reason for the advantageous material removal behavior when applying high cutting speeds is the transition to adiabatic shearing, occurring at high temperatures and beneficial pressure in the contact zone.

1 Diamond Milling and Fly-Cutting

Ultra-precision machining is well-known for achieving superior quality in surface and figure, but also for its time-consuming nature. This is particularly true for fly-cutting, as only one diamond tool is conventionally applied for milling [25]. So what is the advantage of fly-cutting, if optical components might be machined faster by diamond turning? A conceivable application is the machining of large mirrors, for which a fast rotational speed cannot be achieved in diamond turning due to weight of the part and acceleration of the work spindle. As a result, the process remains very slow. In fly-cutting, cutting speed only depends on spindle speed and diameter of the tool. Thus, a fast rotating tool spindle is beneficial in this case, making fly-cutting the preferable choice for the machining of large parts.

Also, the spiral tool path in turning operations leads to constantly changing crystal orientations when cutting monocrystalline semiconductors and other anisotropic materials. In turn, fly-cutting is cutting a straight line by definition so that a certain cutting direction on the material can only be guaranteed in milling.

D. Berger (✉) · L. Schönemann (✉) · O. Riemer · E. Brinksmeier
MAPEX Center for Materials and Processes, University of Bremen, Bremen, Germany
e-mail: schoenemann@iwt.uni-bremen.de

D. Berger
e-mail: berger@iwt.uni-bremen.de

Leibniz Institute for Materials Engineering IWT, Bremen, Germany

E. Brinksmeier and L. Schönemann (eds.), *Ultra-precision High Performance Cutting*,
Lecture Notes in Production Engineering, https://doi.org/10.1007/978-3-030-83765-5_3

As fly-cutting is the "simplest" of all diamond milling operations, the basic calculations of cutting speed and feed speed are straightforward. At first, the value for kinematic roughness R_{kin} is defined. In most cases, diamond machined surfaces should have optical features, i.e. values of $R_{kin} < 10$ nm need to be generated. Taking this value, a maximal feed f of 7.8 µm is allowed for achieving this surface figure when using a typical diamond tool with a corner radius of $r_\varepsilon = 0.78$ mm, according to Eq. 1.

$$R_{kin} \approx \frac{f^2}{8r_\varepsilon} \leq 10\,\text{nm} \rightarrow \; f \; \leq \sqrt{8r_\varepsilon \cdot R_{kin}} \tag{1}$$

The feed speed v_f directly correlates with the cutting speed v_c in milling operations, according to Eqs. 2–4.

$$v_f = n \cdot f \tag{2}$$

$$v_c = \pi \cdot d \cdot n \tag{3}$$

$$v_f = \frac{v_c \cdot f}{\pi \cdot d} \tag{4}$$

where n is the rotational speed of the tool spindle and d is the diameter of the fly-cutter.

In order to enhance ultra-precision fly-cutting operations, the most obvious approach to decrease main process times is the increase of feed speed. As feed f is already maximized by Eq. 1, the only way to increase feed speed is the increase of spindle speed. This approach is well-known for conventional, but not for ultra-precision machining. Thus, in this research the mechanisms of material removal of HSM on ductile and brittle materials were analyzed.

2 High Speed Machining

High speed machining (HSM) has its origins as early as the 1930s in a patent granted to Salomon [26]. However, due to a lack of suitable HSM machines and cutting materials, it was not possible to make use of this patent initially. However, from the 1960s onward, HSM was increasingly used in machining [33]. First in Japan, but also in Germany, the potentials were recognized and, above all, decisively influenced by the work of several researchers [24, 28, 29]. Today, particularly heat-distortion-sensitive and thin-walled components, such as those for the aerospace industry, are produced by high-speed machining. Compared to conventional machining, HSM is characterized by a higher material removal rate, lower cutting forces and better surface quality. A disadvantage is the decreasing tool life, which is due to the increasing thermal load on the cutting edge.

High-speed machining is currently not defined based on physical principles, although scientists have already provided several suggestions. For example, Schneider proposed a fixed allocation of cutting speed ranges for conventional machining (0 to 500 m/min), for high-speed machining (500 to 10,000 m/min) and for ultra-fast machining (<10,000 m/min) [31]. Schulz mentioned the allocation of separate speed limits for individual materials [30]. Ben Amor succeeded for the first time in developing an analytically based definition for HSM based on experimental force and power measurements [3].

It was observed that for almost all metallic materials a typical force curve as a function of cutting speed is obvious. Interestingly, the cutting and feed forces run asymptotically against a constant value, which is designated Fc_∞ in the case of cutting force. Ben Amor was able to show that the variable cutting force component can be well described by an exponential decay function (Eq. 5).

$$F_c\left(v_c\right) = F_{c,\infty} + F_{c,var} \cdot e^{\frac{-2v_C}{v_{HG}}} \tag{5}$$

For this purpose, a speed limit v_{HG} was introduced. v_{HG} is apparently the speed at which the variable part of the cutting force has decreased by 86.5% (exponent -2) according to Eq. 5.

During high-speed cutting of metallic (ductile) materials, a significant decrease in cutting force and other cutting force components can be observed for all materials investigated. Bäeker explains this decrease with a reduction of the flow stress, which is caused by an adiabatic chip formation [2]. During a cutting process, material compression and chip shearing occur alternately as a cycle. Initially, compression occurs along the contact zone, while shearing occurs near the surface. Furthermore, the material-specific strength values are exceeded with the following onset of shear localization and shearing of a segment. Shear localization occurs when thermal softening exceeds mechanical hardening so that softening leads to centralization of plastic deformation. As a result, the process itself accelerates as a further temperature increase with further deformation centralization sets in [1].

Even if for some materials the material separation mechanisms remain the same compared to conventional machining, the advantage of the increased material removal rate still exists, which is accompanied by superior economic efficiency.

The research unit Ultra-Precision High Performance Cutting (UP-HPC) aims at reducing primary and secondary process times while diamond machining, inter alia by high speed cutting (HSC).

Especially for the generation of complex freeforms, as needed for e.g. (IR) applications, diamond milling (“fly-cutting”) and off-axis turning are frequently applied. In most cases, moderate cutting speeds (200 to 600 m/min) are set to avoid high thermal loads or high frequency excitation of structural loops [24]. As the final product is high-end equipment, long primary and secondary process times are acceptable, because the added value still exceeds the production costs by far. However, the reduction of primary and secondary process times is naturally desirable when manufacturing higher batch numbers [31]. Consequently, the influence of high (i.e. v_c = 4,000 m/min in this study) and conventional cutting speeds (i.e. $v_c = 4.00$ m/min) on the material removal mechanism of non-ferrous metals (ductile materials, Sect. 3) and semicon-

Table 1 Ductile materials processed by High Speed Machining

Metallic materials
OFHC copper
Brass CuZn30
Brass CuZn39Pb3
Aluminum AlMg3
Aluminum AlMg5
NiP (electroless nickel)

ductors (brittle materials, Sect. 4) were investigated in this study by off-axis diamond turning and fly-cutting.

3 Ultra-Precision High-Speed Cutting of Metallic Materials

In this section, the analysis of the material removal mechanisms while machining non-ferrous metals, listed in Table 1, at high cutting speeds is presented.

The impact of HSC on the transition to adiabatic shearing was examined by analyzing the cutting forces in on-axis turning and is presented in Sect. 3.1. The influence of HSC on mechanical abrasive and thermo-chemical tool wear in fly-cutting is discussed in Sects. 3.2 and 3.3, respectively. Eventually, the effects of high cutting speeds on surface topography are presented in Sect. 3.4.

3.1 Cutting Forces and the Transition to Adiabatic Shearing

In order to record the cutting forces with a continuous increase in cutting speed between 150 m/min and 4,500 m/min, a facing test was designed (Fig. 1).

Two tool types (carbide indexable insert and diamond radius tool) and three different infeeds ($a_p = 30$, 40 and 50 µm) were selected for machining. The tool holder was mounted to a Kistler force dynamometer MiniDyn 9256C1, which was fixed to the C-axis of the machine tool. The workpiece was mounted on a Professional Instruments spindle model 4R and rotated with 9,600 min^{-1}.

The feed speed was reduced inversely proportional to the distance from the turning center so that the material removal rate remains constant ($Q = 200\,\text{mm}^3/\text{min}$) in all tests. Feed direction was varied from the inside to outside and vice versa to exclude systematic influences. In the middle of the workpiece a hole was made to record the zero-force level before and after cutting, allowing for drift compensation.

The recorded cutting force curves show excellent reproducibility, regardless of whether it is turned from the inside out or from the outside in (Fig. 2).

Further typical cutting forces for the three selected infeeds, when cutting brass CuZn39Pb3 with monocrystalline diamond, are shown in Fig. 3. A drop in the cutting

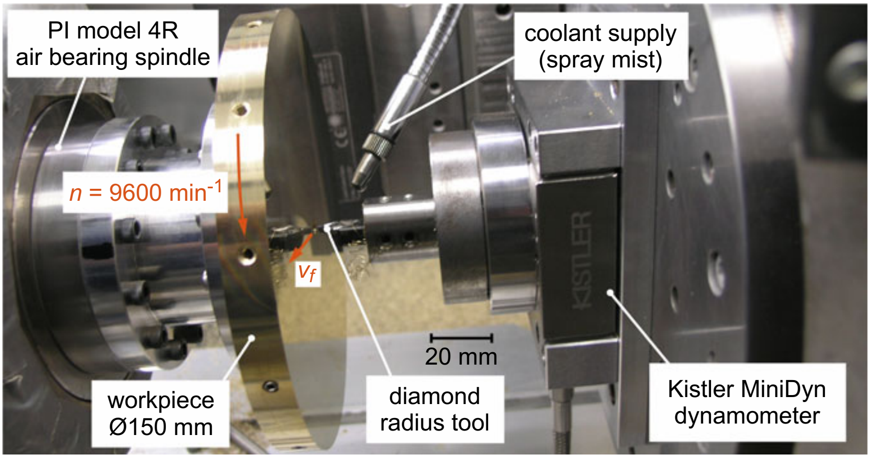

Fig. 1 Facing test with constant material removal volume for recording cutting forces as a function of cutting speed

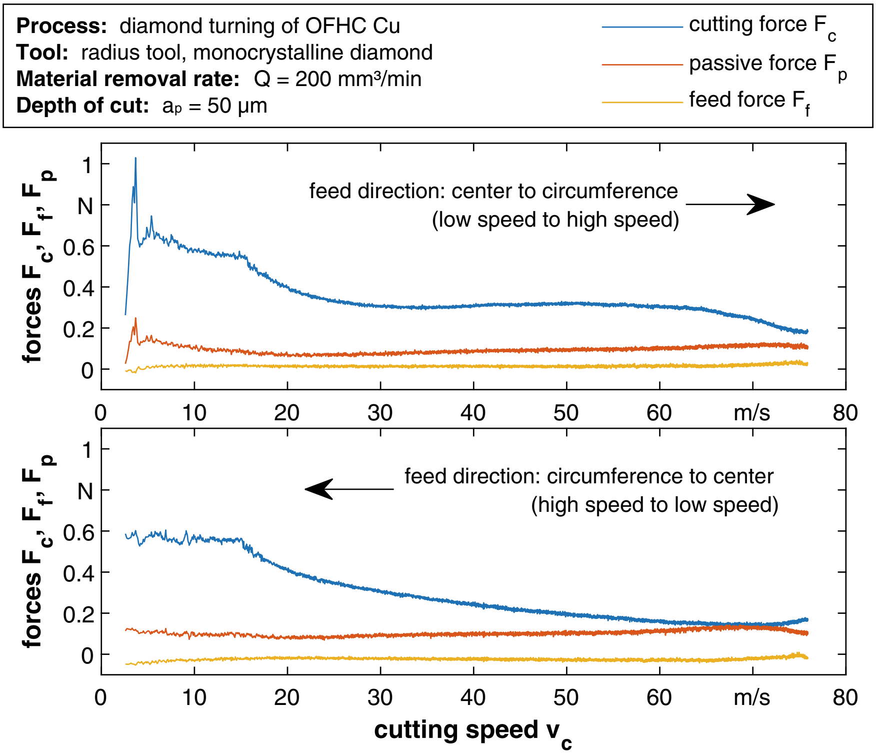

Fig. 2 Reproducibility of process force curves at inverse feed directions

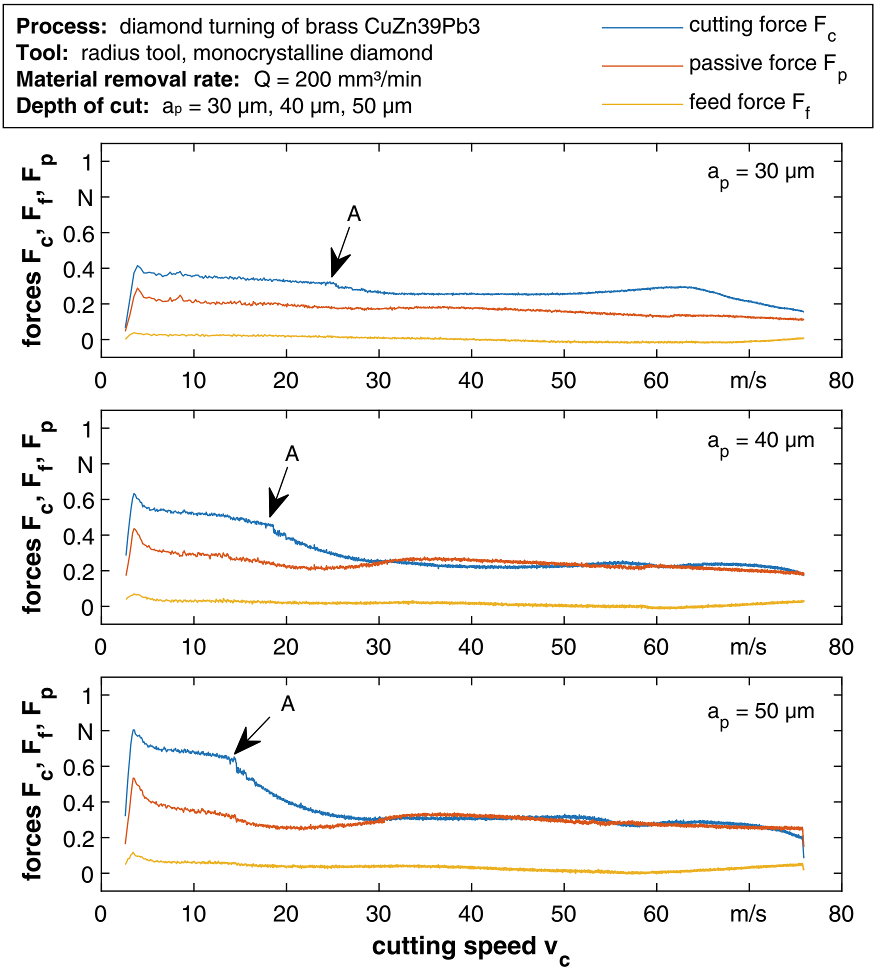

Fig. 3 Cutting forces as a function of the cutting speed at constant material removal rate. *A* denotes the transition to adiabatic shearing

force to a new, approximately constant level can be observed from a relatively clearly defined point (marked with “A” in Fig. 3). This starting point, which indicates the beginning of the transition to adiabatic shearing, has not been elaborated in literature before this investigation, as no continuous cutting force curves have been recorded up to this level of cutting speed.

With increasing cutting depth and decreasing hardness of the material, the starting point shifts to lower cutting speeds (critical cutting speed v_c^*, Table 2). More detailed results are shown in [5, 8, 27].

Exemplarily, a 3D simulation of the cutting force curve while diamond turning of OFHC copper with a radius tool was carried out. As can be seen in

Table 2 Ductile materials and the critical cutting speeds causing a transition to adiabatic shearing

Material	**Critical cutting speed v_c^*@$a_p = 50\,\mu m$** [m/min]
Brass CuZn39Pb3	1,300
OFHC copper	950
Aluminum AlMg5	900
Electroless nickel	1,250

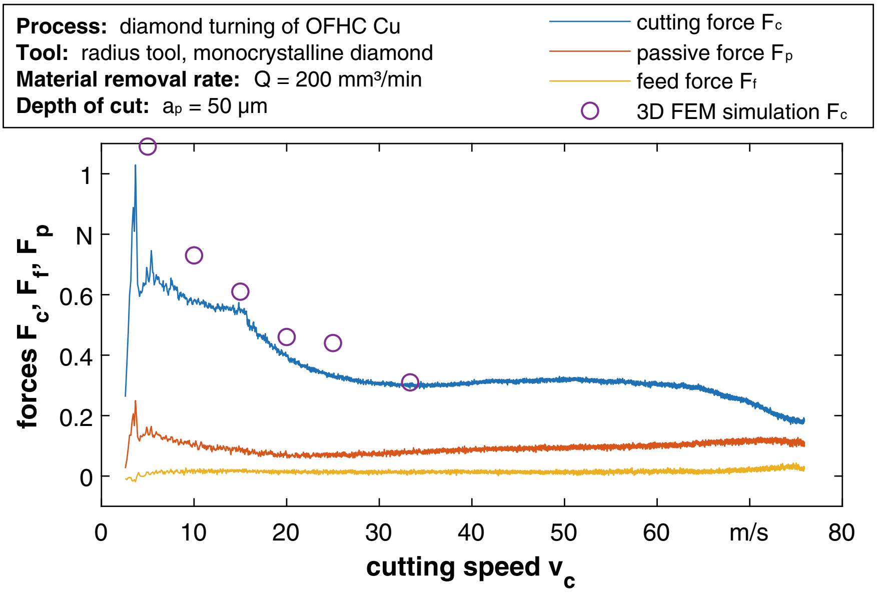

Fig. 4 3D simulation of the cutting force curve during diamond turning of OFHC copper and comparison with the forces measured in the experiment

Fig. 4, the simulation reproduces the measured cutting force in the range between $v_c = 600$ m/min and 2,000 m/min quite well. The starting point of the cutting force drop at $v_c = 800$ m/min can not be confirmed, however, probably due to the wide intervals of the cutting speed.

3.2 *Investigation of the Dependence of Tool Wear on Cutting Speed*

A quantitative investigation of the cutting speed's influence on diamond tool wear during the cutting of "diamond machinable" materials is very time-consuming, as very low wear occurs. Thus, a limitation to the two materials brass CuZn39Pb3

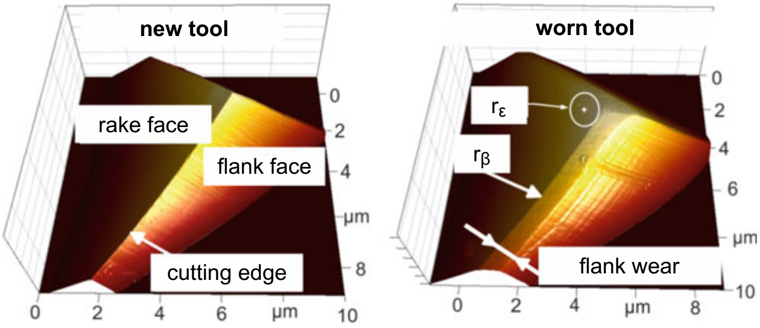

Fig. 5 AFM image of a V-shaped diamond blade before (left) and after (right) a wear test

with the Vickers hardness $HV130$ and electroless nickel with the Vickers hardness $HV530$ was made and wear experiments were only carried out with one low ($v_c \approx$ 380 m/min) and one high ($v_c \approx$ 3,800 m/min) cutting speed. In addition, relatively fragile V-shaped diamond blades with an included angle of 90° were used, as even minimal tool wear can be easily detected on this geometry.

A tool was slowly worn out by milling V-shaped grooves in alternating up- and down-milling mode into a 150 × 75 mm rectangular disc. The effective contact length L_c, defined as the distance accumulated up to a certain point in time at which the cutting edge was in contact with the workpiece, was chosen as the criterion for the load duration for the cutting edge. The width of flank wear land was selected as the criterion for wear evaluation.

After equal effective contact lengths, the tools were removed to measure the cutting edge geometry with an atomic force microscope and to determine the width of flank wear land (Fig. 5).

Plotting the wear land widths measured in the four tests against the effective contact length in Fig. 6 shows clearly that tool wear is reduced at high cutting speeds in comparison to lower speeds, possibly due to the shorter contact time at high cutting speeds. The diamond tool life is therefore longer in the HSC range when applying processes with interrupted cuts [5].

3.3 Investigation of Thermo-Chemically Induced Wear During HSC Diamond Milling of Steel

Steel is one the most important mold materials, but it is well-known that it is not capable for diamond machining according to catastrophic tool wear. The underlying mechanisms of the thermo-chemically induced wear of diamond tools during the processing of steel have not yet been conclusively clarified. In the recent past, ultrasonic machining was proven to be suitable for diamond machining of steel due to short contact times during tool engagement. Therefore, it seemed worthwhile to

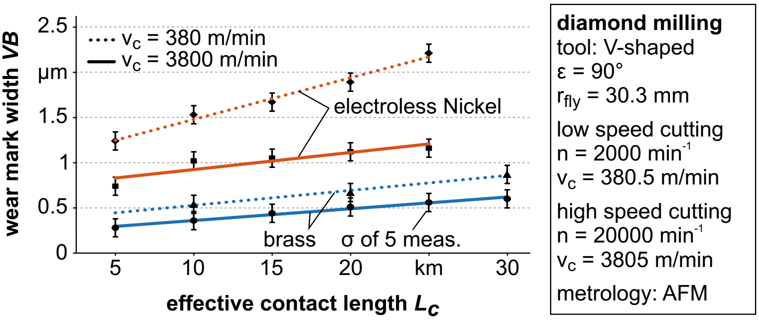

Fig. 6 Flank wear when milling electroless nickel and brass CuZn39Pb3 at low and high cutting speeds

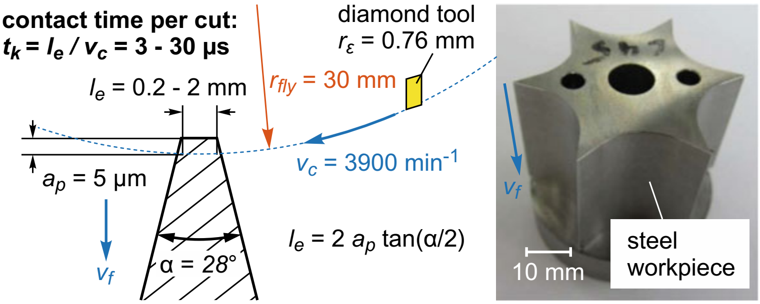

Fig. 7 Variation of the contact time t_k per intervention by varying the infeed a_p on a wedge-shaped steel substrate

investigate edge wear as a function of contact time during HSC milling. For this purpose, an experiment was designed in which the contact time could be varied by varying the infeed a_p on a wedge-shaped steel substrate (Fig. 7).

The flank wear land and cutting edge radius r_β as a function of the effective contact length L_c for different contact times are shown in Fig. 8.

With decreasing contact time, the wear of diamond tools is reduced considerably. This argues against a formation of an iron oxide layer on the cut surface of the steel substrate as assumed by Zhang et al. as an explanation for the reduction of tool wear observed in ultra-sonic diamond machining of steel [36]. Rather, the wear rate seems to depend only on the contact time. Figure 9 shows the flank wear land measured at the shortest contact time that could be realized in the experiment (3 µs) as a function of the effective contact length [7]. Although the rate of thermo-chemically induced wear could be reduced by a factor of 30 compared to the so-called "catastrophic" wear at permanent contact, this reduction is not sufficient to establish HSC diamond milling of steel as a practical method.

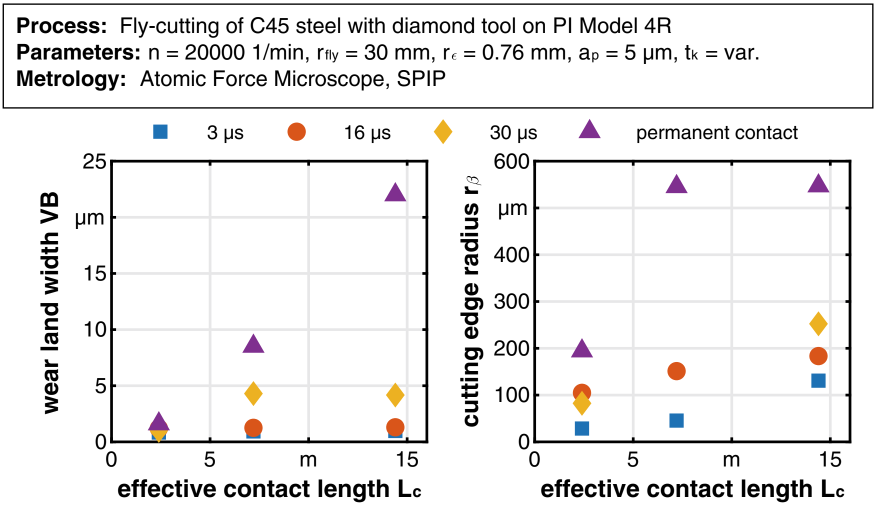

Process: Fly-cutting of C45 steel with diamond tool on PI Model 4R
Parameters: n = 20000 1/min, r_{fly} = 30 mm, r_ϵ = 0.76 mm, a_p = 5 µm, t_k = var.
Metrology: Atomic Force Microscope, SPIP

Fig. 8 Measured wear land width (left) and cutting edge radii r_β (right) as a function of the effective contact length L_c at different contact times t_k

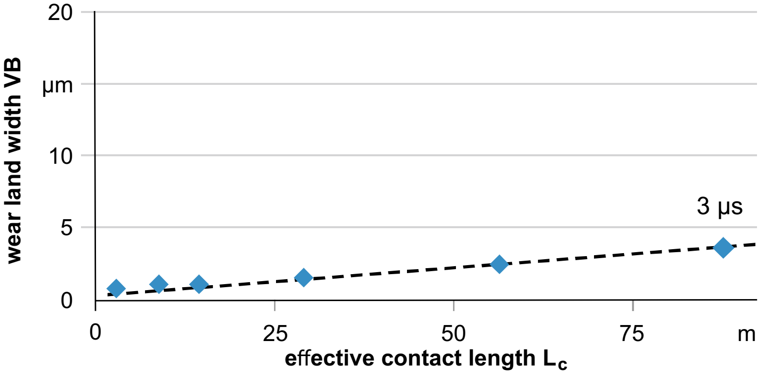

Fig. 9 Increase in wear mark width against effective contact length L_c for thermo-chemically induced wear at a contact time per intervention of 3 µs

3.4 Investigation of the Surface Topography of HSC Diamond Milled Surfaces

Almost all metal substrates suitable for diamond machining have a grain structure which, due to the differential elastic springback of the grain Δh_{el}, leads to a material-dependent surface roughness during machining. As the cutting forces are reduced during HSC diamond machining (see Sect. 3.1), it is to be expected that the differential

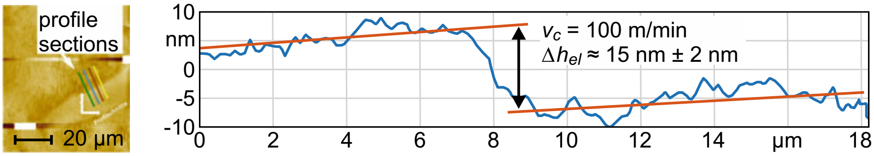

Fig. 10 AFM image and profile section of a cut grain boundary in OFHC copper

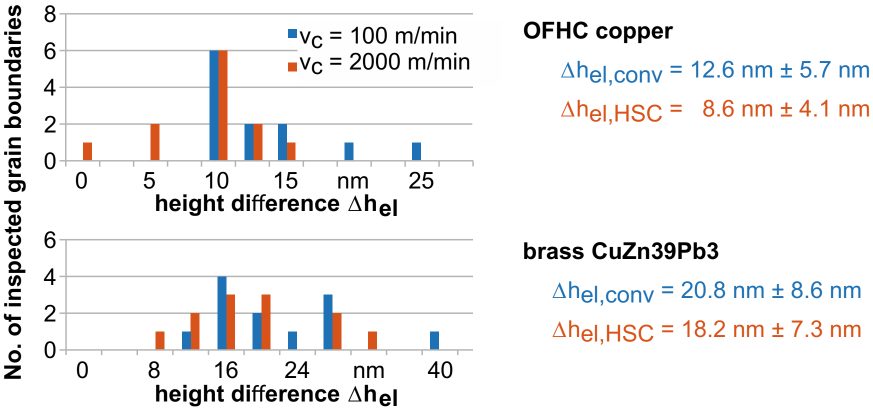

Fig. 11 Distribution of the measured grain height differences

elastic springback of the grains will also decrease so that an even better surface roughness may be expected.

In the experiments designed for this purpose, 12 grain boundaries were selected from approx. 120 grain boundaries identified on OFHC copper and brass CuZn39Pb3, which were then cut at a low cutting speed ($v_c = 100$ m/min). Subsequently, a very small shift by an infeed of 5 μs was applied before a second cut was made at high cutting speed (v_c = 2,000 m/min). The step heights of the cut grain boundaries were documented by an atomic force microscope (Fig. 10).

As the histograms in Fig. 11 show, it can be statistically proven that grain boundaries remaining after the application of high cutting speed have a slightly smaller height difference than those cut at low cutting speed. A more detailed presentation of the results is given in [7].

3.5 Conclusion on UP-HSC of Ductile Materials

In Sects. 3.1 to 3.4, the effects of high speed cutting were examined and have revealed the following essential results:

1. With increasing cutting speed, a transition to adiabatic shearing occurs in the chip forming zone, associated with an exponential decrease of the cutting force.
2. At high cutting speeds, abrasive tool wear is reduced due to low contact times during tool engagement. It could also be shown that thermo-chemically induced tool wear decreases too when cutting steel substrates. But despite this favorable effect in high speed cutting, the tool wear remains still too high for machining large sized optics.
3. The achievable surface roughness slightly improves with increasing cutting speed due to the reduced springback of the grains.

Accordingly, ultra-precise high-speed diamond machining offers considerable advantages in terms of process technology as well as significantly shorter machining times.

4 High-Speed Machining of Brittle-Hard Materials

Ductile regime machining of brittle-hard materials has received a great deal of attention from scientific studies around the world. It is well known that a prerequisite for plastic deformation is the presence of a hydrostatic pressure state in the contact zone, which was already stated by King and Tabor in 1954 [17]. The first researcher, however, to demonstrate the positive influence of the hydrostatic stress state on the deformability of brittle-hard materials, as predicted by Mohr's theory, was Theodore von Kármán in 1911 [16]. A review on the status of ductile regime machining was compiled by Neo et al. in 2012 [23]. Most importantly this review revealed that critical machining parameters to handle are feed, depth of cut and the tool geometry to maintain a process constantly with a chip thickness below a critical value. Concerning the tool, especially the negative rake angle and a large tool edge radius support ductile regime machining by inducing a hydrostatic pressure [23].

Diamond machining of semiconductor materials, like silicon or germanium, is well researched, but in most cases conventional cutting speeds are applied. High speed cutting (HSC) of semiconductor materials has not gained much attention in research. Liu et al. have investigated the characteristics of high speed micro-cutting of tungsten carbide and found that HSC could also be applied on brittle materials, when depth of cut and feed rate are low. They have applied a cutting speed of 741.4 m/min [20].

In this section, the application of high cutting speeds up to 4,000 m/min was investigated on elemental (Si, Ge) and compound semiconductors (ZnS, ZnSe). All experiments for investigations on high-speed machining of those materials were carried out on a Moore Nanotech 350FG ultra-precision machine tool. For the determination of critical chip thickness and surface integrity while high speed cutting, both off-axis turning and fly-cutting were investigated. In order to be able to reach high cutting speeds while turning, the radius of the workpiece mounting fixture on the work spindle was maximized (i.e. the radius of the workpiece's center was set

Table 3 Tool and workpiece specifications

	Specification	**Value**
Radius tool	Cutting material	Single-crystal diamond
	Corner radius	$r_\varepsilon = 0.76\,\mathrm{mm}$
	Cutting edge radius	$r_\beta = 50$ to $150\,\mathrm{nm}$
Workpiece	Materials	Monocrystalline silicon (Si), germanium (Ge), zinc sulfide (ZnS), zinc selenide (ZnSe)
	Orientation	(100) / (110) / (111)
	Geometry	$10 \times 10 \times 0.5\ \mathrm{mm}^3$
	Cutting direction	<110> for all crystallographic orientations

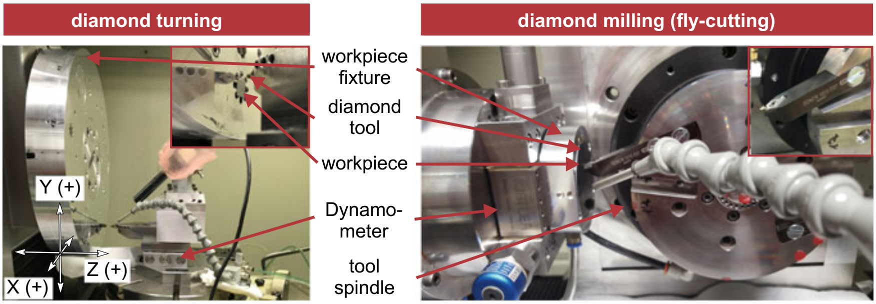

Fig. 12 Experimental setup for off-axis turning and fly-cutting

at 110 mm) and designed to adapt three square workpieces ($10 \times 10\ \mathrm{mm}^2$ each), see Fig. 12. The resulting work spindle speed was 531 min^{-1} for low cutting speed (400 m/min) and 5,310 min^{-1} for high cutting speed (4,000 m/min). Plunging into the material (a_p) was enabled by moving the Z-axis, while the Y-axis generated the v_c-dependent feed speed (v_f).

The turning experiments were conducted using the main spindle of the 350FG while for milling (fly-cutting), a Professional Instruments ISO 3.375B air bearing spindle was mounted on the Z-axis of the machine tool and used as tool spindle.

Turning and milling experiments were performed with a single-crystal diamond radius tool. To exclude wear effects, a tool in fresh condition was applied for each set of cutting speeds. Process forces were measured on the tool side when turning, and on the workpiece side for milling. The specifications for tool and workpiece are shown in Table 3 and the experimental setups for both processes are illustrated in Fig. 12. Cutting direction was <110>, as this is the only direction existent on all crystallographic orientations. Additionally, this direction shows a beneficial behavior for ductile machining according to literature [9, 32, 37].

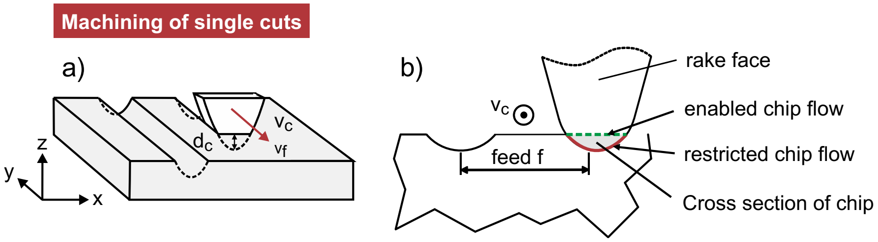

Fig. 13 Process strategy for high speed off-axis diamond turning and milling of single cuts for determination of critical depth of cut d_c

Table 4 Parameters for turning and milling of single cuts

Parameter	Values
Cutting speed v_c	400/4,000 m/min
Feed speed v_f	160/1,600 mm/min
Rake angle γ	0°/−20°/−30°
Depth of cut a_p	var. (0 to >500 nm)

4.1 Dependence of the Cutting Speed on Critical Chip Thickness and Surface Integrity

Maintaining the critical chip thickness is essential for the ductile machining of brittle-hard materials. The application of high speed machining is expected to increase critical chip thickness by amplifying the prevailing pressure in the contact zone. To test this hypothesis, the machining of single cuts by turning and milling aimed at investigating the dependence of the critical depth of cut (d_c) on process parameters. The process strategy is displayed in Fig. 13.

The feed rate was set to $v_f = 160$ mm/min when machining with a cutting speed of $v_c = 400$ m/min, while it was v_f =1,600 mm/min for v_c = 4,000 m/min, resulting in equidistant cuts on each of the specimens. All relevant machining parameters are listed in Table 4.

The determination of the critical depth of cut d_c, which is the value where a transition from ductile to brittle machining takes place, was performed by analyzing the maximum height Sz in the center of the machined single cuts. Sz describes the difference between the highest peak and the deepest valley of the surface topography and is therefore a suitable parameter for describing the nature of the material removal mechanism (ductile/brittle). With increasing depth of cut, Sz also increases and the single cuts can be separated in ductile (a), ductile-brittle (b) and brittle (c) workpiece regions, as defined in Fig. 14. These regions can be separated by means of the Sz distribution. In ductile mode, Sz linearly increases. This trend continues in ductile-brittle mode, but scatter is present. Brittle mode starts when Sz varies widely and no linear trend is apparent anymore. The analysis has been performed by a MATLAB

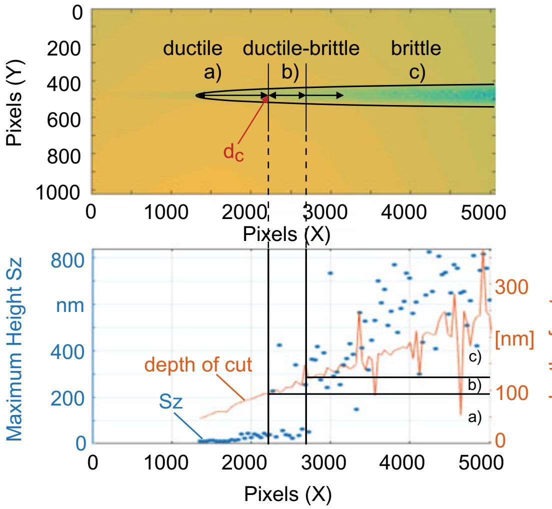

Fig. 14 Automated analysis of depth of cut a_p and maximum height Sz in single cuts to define ductile-brittle transition

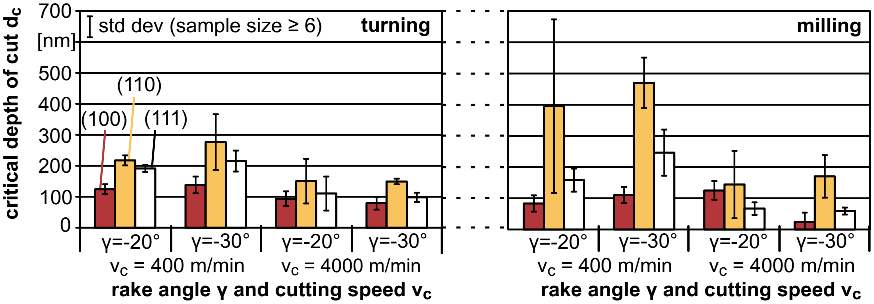

Fig. 15 Critical d_c for silicon, machined with low and high cutting speed

script, which runs through the single cuts and determines Sz on a 40 × 30 pixel area in intervals of 40 pixels. Pixel area and intervals have been chosen to maximize the covered area and minimize the offset of linearized area of curvature. 100 μm in X- and Y-direction corresponds to 306 pixels. The strong variation of a_p in the brittle region results from chipping.

Figure 15 shows the results for the critical depths of cut d_c, where the transition from ductile to ductile-brittle mode takes place, for both turning and milling. For low as well as high cutting speed, d_c increased with rising negative rake angles, especially for crystal orientation (110). However, the usual rake angles for the machining of brittle-hard materials (−20° and −30°) lead to minor values of the d_c when high cutting speeds are applied.

Fly-cutting was performed on the elemental semiconductors monocrystalline silicon (Si) and germanium (Ge) and additionally on the compound semiconductor materials zinc sulfide (ZnS) and zinc selenide (ZnSe). The latter materials are applied

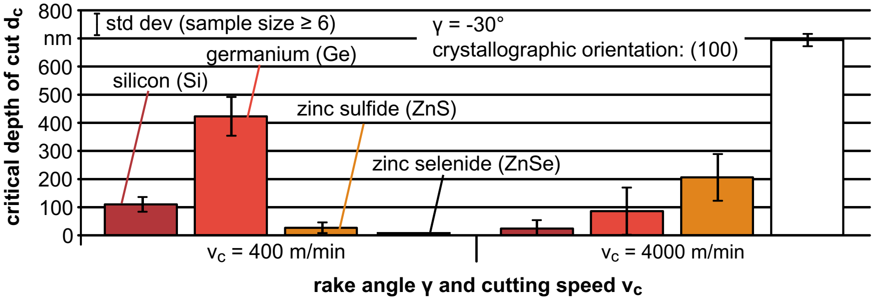

Fig. 16 Critical depth of cut d_c for silicon, germanium, zinc selenide and zinc sulfide, machined by fly-cutting with low and high cutting speed

Table 5 Detected specific cutting forces while machining of single cuts

v_c = 400 m/min	F_n [N]	F_c [N]	A_{max} [μm^2]	k_c [GPa]	d_c [nm]
Si 100	0.22	0.21	14.9	14.1	110
Ge 100	0.15	0.12	8.1		423
ZnS 100	0.44	0.27	18.1		27
ZnSe 100	0.86	0.83	56.0		1
v_c = 4,000 m/min	F_n [N]	F_c [N]	A_{max} [μm^2]	k_c [GPa]	d_c [nm]
Si 100	0.40	0.21	14.9	14.1	24
Ge 100	0.40	0.20	13.4		86
ZnS 100	0.45	0.18	12.1		206
ZnSe 100	0.42	0.22	14.8		694

for infrared optics and are experiencing a growing demand [14, 15, 19, 22]. Critical depths of cut are examined by the same procedure as for silicon and are displayed in Fig. 16.

While germanium shows the same behavior as silicon regarding the influence of the increased cutting speed, that is a reduction of d_c, the values of the two compound semiconductors zinc selenide and zinc sulfide behave in exactly the opposite way. At a cutting speed of $v_c = 400$ m/min, only a comparatively small critical chip thickness can be determined. Zinc selenide shows almost no signs of ductile cutting at conventional cutting speed. However, this changes when the cutting speed is increased to $v_c = 4,000$ m/min. Since this behavior occurs in both compound semiconductors investigated, it can be assumed that the ductile cutting ability is related to the bonding of the ions within the zinc blende structure.

To support this hypothesis, the measured normal and cutting forces (Z- and Y-direction, respectively) during machining are displayed in Table 5. Combined with the (constant) cross-section of the tool plunging into the material while cutting (A_{max}),

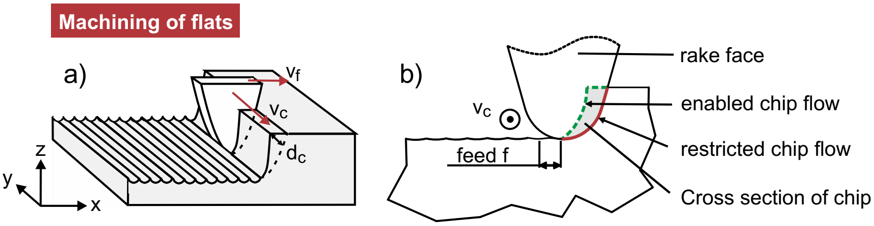

Fig. 17 Process strategy for high speed off-axis diamond turning and milling of optical flats

Table 6 Parameters for milling of flats

Parameter	Value
Cutting speed v_c	400/4,000 m/min
Feed speed v_f	5/7.5/10 μm/rev
Depth of cut a_p	3 μm
Rake angle γ	−30°

the specific cutting force k_c was calculated, giving an information on the prevailing pressure in the contact zone.

It is known from literature that the ductile machining of semiconductor materials required machining pressures of 8.8 to 16 GPa in the shear zone [12, 18]. The specific cutting forces for the machining of zinc selenide and sulfide with low cutting speed are beyond this range. Simultaneously, these are the only materials where no or only partly ductile material removal was present ($d_c < 27$ nm). For high cutting speed, all materials could be machined in ductile mode as the specific cutting forces remain in a range of 12 to 15 GPa. Obviously, the cutting of compound semiconductors requires a higher pressure in the contact zone for ductile machining.

4.2 *Process Window for HSC Machining of Optical Surfaces*

To analyze the capabilities of HSC milling optical surfaces, flats were produced by adding a feed movement in X-direction (Fig. 17). The machining of single cuts revealed that a rake angle of $-30°$ is to be preferred for machining due to higher mean values for d_c at low cutting speed and lower standard deviations at high cutting speeds. Consequently, this angle was chosen for the machining of optical surfaces.

The parameters applied in experiments for machining of optical flats are shown in Table 6.

Subsequent to the experiments, surface roughness and subsurface damage were determined in order to evaluate the influence of cutting speed on the machined surface layer. Roughness was measured by a Taylor Hobson CCI HD white light interferometer. The arithmetic mean height Sa was chosen for analysis of the machined

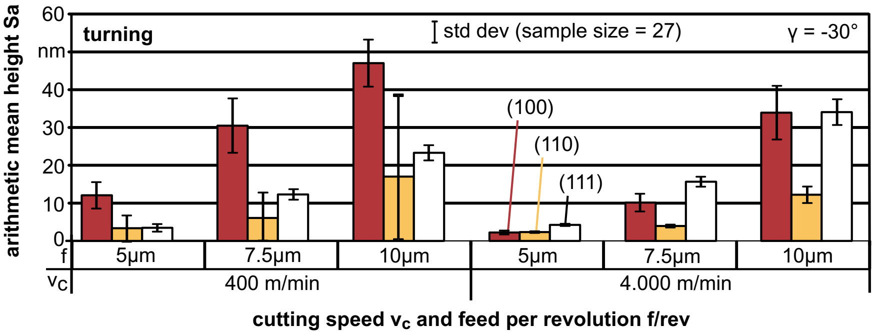

Fig. 18 Arithmetic mean height Sa for turned flats on silicon with different crystallographic orientations over cutting speed v_c and feed f for γ of $-30°$

flats in contrast to the single cuts (Sz), as this is a common parameter for areal characterization of optical surfaces.

Subsurface damage was investigated by polishing a wedge with a defined slope into the workpiece. Polishing was followed by an etching process with diluted hydrofluoric acid (0.1% HF) for exposing cracks.

Turning Experiments

Figure 18 reveals that only for workpieces with a crystal orientation of (111), a cutting speed of 400 m/min leads to superior surface quality compared to a cutting speed of 4,000 m/min, although the differences between roughness values are marginal, at least for feeds of 5 and 7.5 µm. When (100)-workpieces were machined, the arithmetic mean height for 7.5 µm feed per revolution differed between 10 nm ($v_c = 4,000$ m/min) and 30 nm ($v_c = 400$ m/min). By implication, ductile machining of this material is not possible when applying the selected parameters (Table 6) at low cutting speeds, while the high cutting speed at feeds per revolution of 5 and 7.5 µm leads to a surface roughness below 10 nm.

The reason for the superior surface quality when applying high cutting speeds in diamond turning is the evolution of high temperatures in the cutting zone. These could be observed by spark formation, as seen in Fig. 19.

Temperature measurements by infrared failed due to low resolution of the camera and a tool-sided temperature measurement could not be set up due to the tools' rotation. This is why the estimation was only made by comparing the sparking with a table for the emission of electromagnetic radiation (incandescence), as shown in Fig. 19. According to this, a temperature of 950 to 1,000 °C is present. These temperatures lead to a hardness decrease of silicon in the shear zone by a magnitude of 10 [34]. The decrease of hardness is accompanied by an indirect increase of the critical chip thickness d_c, which is a material based parameter and can be calculated by the following Eq. 6, which considers the Young's modulus E, the fracture toughness K_c and the Vickers hardness HV of the material [4]:

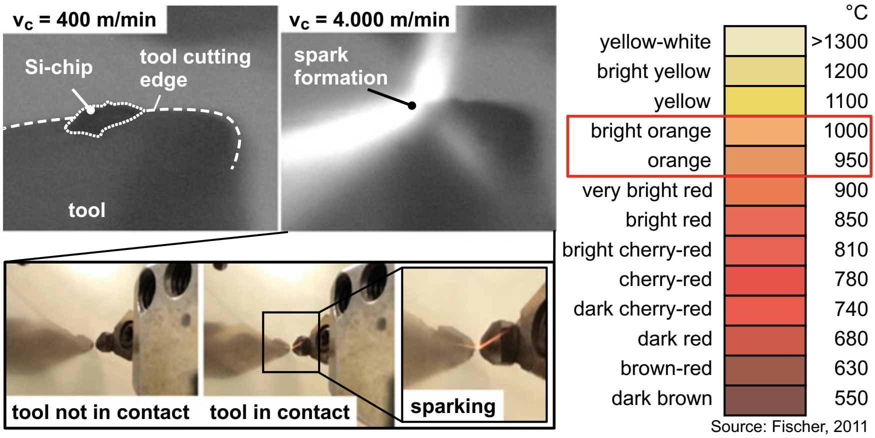

Fig. 19 Comparison between conventional cutting speed (400 m/min, top left) and high cutting speed (4,000 m/min, top middle), where sparking is present, estimated with temperatures up to 1,000 °C by annealing colors (right)

$$d_c \propto \frac{E}{HV} \cdot \left(\frac{K_c}{HV}\right)^2 \qquad (6)$$

The decrease of hardness in high speed machining is relatable to the decrease of cutting forces, as shown in Fig. 20. Process forces were measured by a force dynamometer (Kistler Type 9119AA2) with a sampling rate of 20 kHz for the slower cutting speed and 50 kHz for v_c= 4,000 m/min. Because the natural frequency of the setup and the applied filtering have to be taken into account when determining force values, the natural frequency was experimentally determined by using an impulse hammer (Kistler Type 9722A) and a triaxial acceleration sensor (Kistler Type 8764B). Resulting natural frequencies were 2.8 kHz for the X- and Y-axis and 3.8 kHz for the Z-axis. It is recommended by Kistler to use only one third of these frequencies for filtering the force signals. Consequently, a 1st order Butterworth filter was applied with cutoff frequencies of 0.93 kHz for the X- and Y-axis (F_p and F_c) and 1.3 kHz for the Z-axis (F_f). The results in Fig. 20 show both the filtered and the unfiltered forces.

Although a reduction in cutting forces is discernible after filtering, this has to be attributed to the filter characteristics and the lack of datapoints for the higher cutting speed. The unfiltered values show similar peak heights for the cutting force. An on-axis turning operation was not performed due to the crystallographic orientation of semiconductor materials. The rotating workpiece would lead to varying cutting directions which result in a change of cutting force due to the occurring hardness variation.

Finally, sub surface damage (SSD) was detected for silicon on all machined crystallographic orientations by determination of the deepest crack which could be detected in the subsurface. Therefore, a wedge was polished into the machined

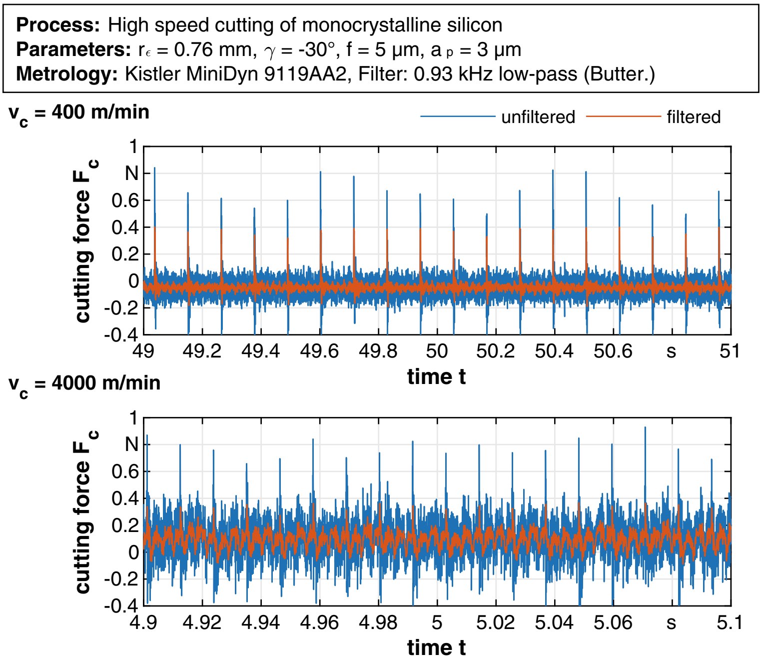

Process: High speed cutting of monocrystalline silicon
Parameters: r_ϵ = 0.76 mm, γ = -30°, f = 5 µm, a_p = 3 µm
Metrology: Kistler MiniDyn 9119AA2, Filter: 0.93 kHz low-pass (Butter.)

Fig. 20 Cutting Force F_c for off-axis turning of silicon with low and high cutting speed [27]

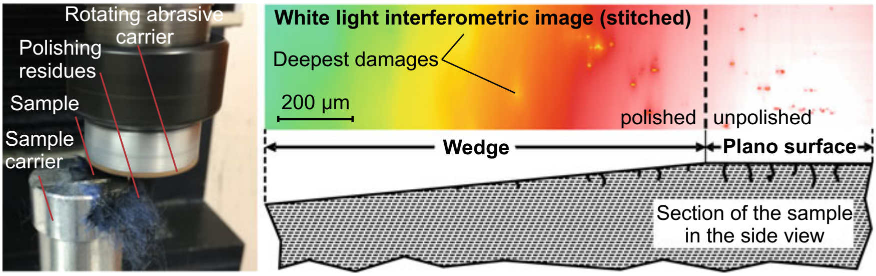

Fig. 21 Polishing procedure (left) and etching (not displayed) and subsequently performed subsurface damage detection (right)

surface with an angle of 0.08°, which results in a linearly increasing depth up to 6 µm over a length of 4.5 mm. After etching with hydrofluoric acid, the damages were detected by white light interferometry, as illustrated in Fig. 21.

A correlation between the crack depth, shown in Fig. 22, and surface roughness (Fig. 18) can be drawn. This relationship has also been reported earlier in several investigations [11, 13]. For crystal orientations (110) and (111), the influence of cutting speed on crack depth was low, while it is pronounced for (100) specimens. In general, deeper cracks occur for this crystal orientation. For lower feed rates

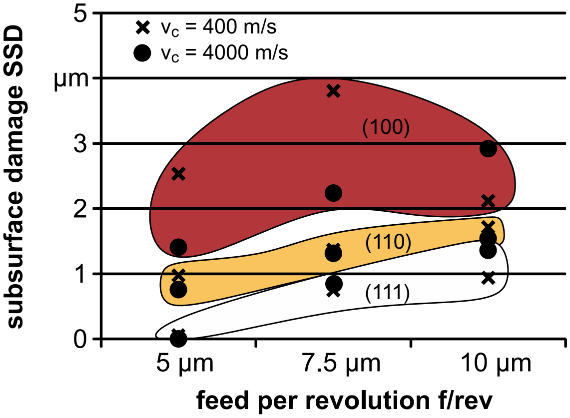

Fig. 22 Subsurface damage for turned and milled flats

(5 and 7.5 µm), higher cutting speeds are advantageous regarding crack depth, while this changes to the opposite for the high feed rate (10 µm). The crack depth varies strongly and does not follow the trend of the lower feed rates anymore. This could be explained by the brittle material removal, which occurred at such high feed rates when machining (100) specimens.

Milling (Fly-Cutting) Experiments

The milling experiments were again, like for the machining of single cuts, conducted on elemental and also on compound semiconductors.

In Fig. 23, the measurement results for surface roughness are shown by surface topographies from all machined materials in (100)-orientation. Cutting direction was <110>, respectively. In all cases, a high cutting speed leads to similar or even lower values for arithmetic mean height Sa. Additionally, Sq and Sz were measured (not displayed here), showing the same behavior.

The evaluation of the influence of different parameters on the critical chip thickness of germanium shows that it behaves similar to silicon with the same variations, though the order of magnitude of the respective critical chip thickness is higher. One hypothesis to explain this behavior is the heat capacity C and thermal conductivity k of both materials. Comparing the thermal conductivities of silicon (150 W/(m k)) and germanium (60 W/(m k)) yields a ratio of 2.5:1. The ratio for the heat capacities (silicon at 0.75 kJ/(kg K) and germanium at 0.31 kJ/(kg K)) is practically identical (2.4:1). This means that germanium reaches a higher temperature near the contact zone than silicon in a comparable process. A higher temperature can also be inferred from sparking that occurs at high cutting speeds. In the milling process used here, however, no spark formation could be observed, which is attributed to the short contact time between tool and workpiece.

While turning, the tool cuts through the whole width of the workpiece (10 mm), while the contact length l_k for milling is calculated using Eq. 7.

$$l_k = \sqrt{2 \cdot r_{fly} \cdot a_p} \tag{7}$$

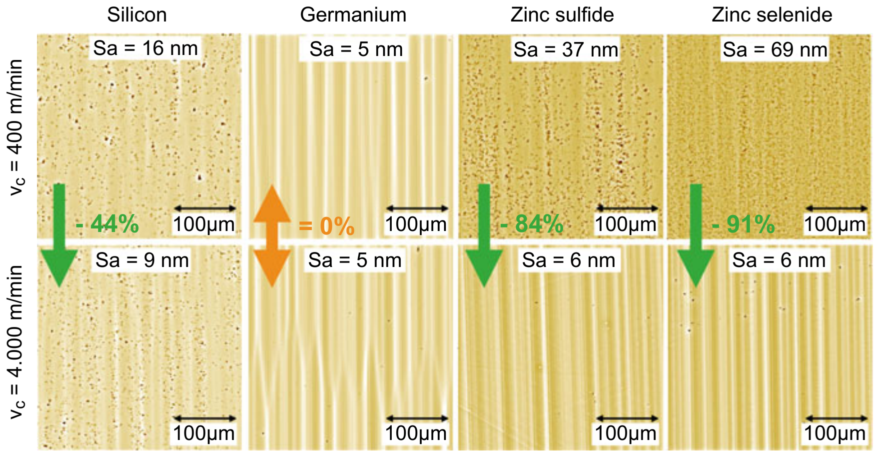

Fig. 23 Topographies of milled flat surfaces with low (top) and high (bottom) cutting speed

Table 7 Depths of last SSD occurrence for different semiconductor materials in (100)-orientation, machined by fly-cutting

Cutting speed [m/min]	**Silicon** [nm]	**Germanium** [nm]	**Zinc sulfide** [nm]	**Zinc selenide** [nm]
$v_c = 400$	500	60	730	930
$v_c = 4{,}000$	400	330	470	260

With the fly-cut-radius of $r_{fly} = 94.5$ mm and the depth of cut of $a_p = 3$ µm this calculates to $l_k = 0.75$ mm. Nevertheless, such thermal effects are also conceivable when milling germanium and would explain the observations here, because a decrease in hardness promotes ductile material behavior with increasing critical chip thickness.

The high amounts for critical cutting depths at high cutting speed for compound semiconductors zinc sulfide and zinc selenide are striking here in comparison to the elemental semiconductors. At a conventional cutting speed, hardly any ductile material behavior occurs due to the level of surface roughness, while high cutting speeds lead to an optical surface. An improvement by one order of magnitude of the roughness values between low and high cutting speed is promising, as this has never been revealed before and offers a chance to simplify the ductile machining of compound semiconductors only by increasing the cutting speed.

Subsurface damage was also analyzed after milling experiments with the same procedure as for the turning experiments (Fig. 21). However, only one specimen of each material could be examined due to the effortful procedure of polishing and etching. Results are shown in Table 7 for (100)-orientation for all materials.

Similar to the turning tests, the variation of the cutting speed had an inferior effect on the subsurface damage introduced in silicon. On germanium, the other hand, at a cutting speed of $v_c = 400$ m/min, no major subsurface damage could be detected.

Table 8 Parameters for rough and fine cuts for examination of tool wear

Parameter	**Values**	
	Rough cuts	Fine cuts
Cutting speed v_c	400/4,000 m/min	400/4,000 m/min
Feed rate f	24.5 µm	7.5 µm
Depth of cut a_p	10 µm	3 µm
Rake angle γ	−30°	−30°

At the specified depth of 54 nm, there was only one final small noticeable feature within the surface without any major damage being detected. Other results could be observed regarding the influence of the cutting speed on the subsurface damage when machining zinc sulfide and zinc selenide. Here, an increase of cutting speed causes a reduction in the depth of damage introduced. Again, it is noticeable that the two materials with the ionic bond in the crystal lattice behave similarly to each other and in the opposite direction to the elemental semiconductors.

4.3 Tool Wear as a Function of Cutting Speed

The experimental setup for detecting wear as a function of cutting speed was similar to the setup shown in Fig. 12. The aim of the experimental investigations was the identification of a tool condition as a limit for ductile machining. The abort criterion was determined by the arithmetic mean height Sa, measured by white light interferometry after equidistant cutting lengths. Experiments were carried out on monocrystalline silicon with orientation (110) due to low acquisition costs for wafers and market availability. In diamond milling, with its short contact times between tool and workpiece and low chip thicknesses, tool wear is slowly progressing. In order to keep the experimental investigations in a reasonable time frame, cutting was classified into rough cuts and fine cuts, see Table 8.

Rough cuts were performed in order to generate material removal volume and provoke wear, while fine cuts were carried out to evaluate the tool's ability to cut in ductile-regime. Rough cuts were performed by raster milling on 2″ wafers with high width of cut a_e (Fig. 24, left). For the abort criterion, a finish cut was made on a 10×10 mm^2 workpiece, like on the milling experiments in Sect. 4.2 (Fig. 24, middle). This criterion was set by measuring arithmetical mean height Sa after every 0.8 km of effective cutting length L_c by white light interferometry. The arithmetic mean height Sa was detected after fine cuts. The evolution of surface texture with rising contact length and accompanying tool wear is shown in Fig. 24, right.

Tool wear was determined by three wear parameters, e.g. flank wear land, dislocation of the cutting edge and cutting edge radius r_β. Those parameters were detected at the tool's cutting edge, as schematically shown in Fig. 25 (left), by atomic force

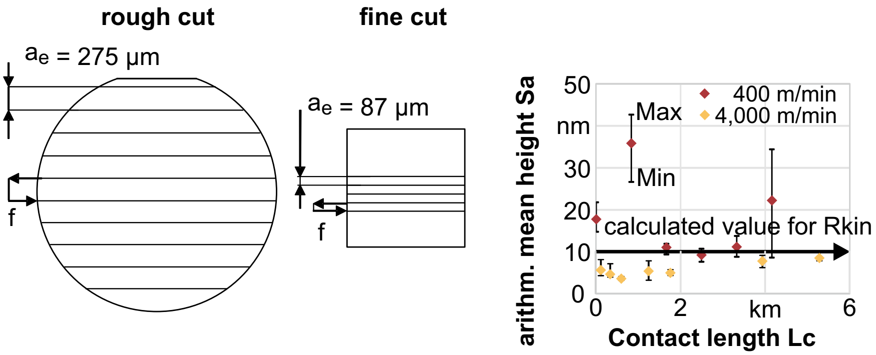

Fig. 24 Process strategies for rough and fine cuts and evolution of surface texture with rising contact length

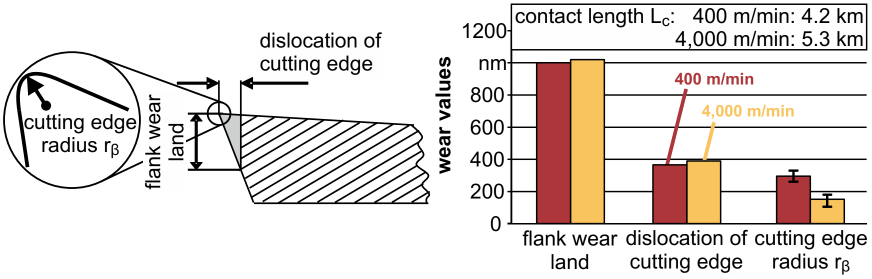

Fig. 25 Detected tool wear parameters (left) and measured values (right)

microscopy. Wear was determined after an effective contact length L_c of 4.2 km for low cutting speed and 5.3 km for high cutting speed, respectively. The different values represent the distance as long as ductile machining could be maintained. Once the values exceeded 10 nm, experiments were terminated and the final wear values were determined, as displayed in Fig. 25 (right).

Most importantly, high cutting speed does not decrease tool life. Moreover, the values for flank wear land and dislocation of cutting edge were almost the same for both applied cutting speeds, although the cutting length was 25% higher for high cutting speed. At the same time, certain values for flank wear land and dislocation of the cutting edge should not be exceeded for maintaining ductile-regime machining, which are 1,000 nm and 400 nm, respectively.

According to a schematic model of the contact geometry between diamond tool and workpiece (Fig. 26), proposed by Yan et al. [35], the cutting edge radius has an effect on the surface in contact with the workpiece material due to a change in the resultant force F. The resultant force F and its effective angle ϕ provide information on the extent to which the cutting edge radius causes a change in the machining pressure. Contact areas S_1, S_2 and finally S_{eq} are directly influenced by

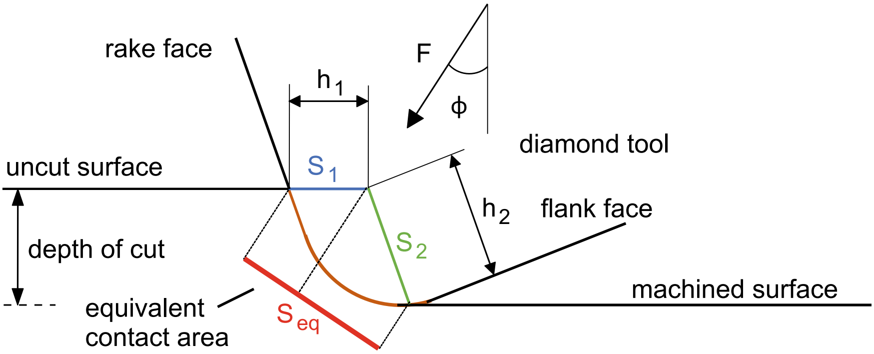

Fig. 26 Schematic model of the contact geometry between diamond tool and workpiece according to [35]

Table 9 Dependence of shear zone pressure on cutting edge radius and speed

Cutting speed v_c [m/min]	**Cutting edge radius r_β** [nm]	**Shear zone pressure k_c** [GPa]
400	28 (fresh)	1.9
	294 (worn)	3.2
4,000	64 (fresh)	13.8
	151 (worn)	8.3

this. A detailed description how the geometrical contact conditions are calculated can be found in [35].

By measuring the tangential and normal forces, the resultant force and its effective angle were calculated and set in relation to the equivalent contact area S_{eq}. The results for prevailing machining pressure, depending on the tool wear (fresh condition and abort criterion) for low and high cutting speed are shown in Table 9.

For the high cutting speed the stress decreased with increasing cutting edge radius, which is reflected in the higher roughness values with increasing machined volume, visible in Fig. 24. As only one measurement for the Sa-value exceeded 10 nm, it is assumed that the stress has not fallen below the limit value for maintaining a hydrostatic pressure and thus, no real transition to brittle machining has occurred. As already stated in Sect. 4.1, at least 8.8 GPa of pressure must be present in the shear zone to reach a ductile material removal [12, 18]. Here, the prevailing pressure while milling with conventional cutting speed remained below 8.8 GPa, which correlates with the higher Sa-values. In almost every condition the material removal was at least partly brittle, so that pressure could unload by crack propagation.

The dominant material removal mechanism was additionally analyzed by highfrequency- impulse-measurement (HFIM) with a QASS Optimizer 4D, utilizing a piezoelectric effect. The analysis is performed on structure-borne sound amplitudes, also known as acoustic emission (AE), which are plotted over time and frequency in

Table 10 Origins of emitted frequencies when cutting materials after [21]

Frequency [kHz]	Origin
0 to 32.3	Noise, elastic and plastic deformation
32.3 to 62.5	Microcavities
62.5 to 125	Shearing
125 to 250	Cleavage and microfractures
250 to 500	Inclusions
500 to 1,000	Intercrystalline microfractures

three-dimensional diagrams. Based on solid state vibrations, which cause frequencies in the audible sound range, acoustic emission is furthermore evoked by plastic deformation of the machined material. With its high sampling rates of up to 50 MHz, the origin of the emitted frequencies can be determined. According to Dhulubulu [10], the maximum values of structure-borne sound signals should depend on the strength properties of the materials and brittle failure as well as the rate of deformation, whereas the predominant frequency range can be traced back to the separation process caused in the workpiece material (see Table 10). Thus, low frequency ranges show a ductile cutting process, while the high frequency ranges are responsible for the initiation of fractures [21].

Exemplary sound amplitudes AE_{max} of the performed cutting experiments with high and low cutting speeds are shown in Fig. 27 and compared to the idle speed of the tool spindle.

Depending on the frequency range under consideration, the signal shows the interaction between tool and workpiece, as well as the background noise generated by the machine. During high speed cutting, amplitudes appear exclusively at frequency bands <125 kHz. According to Table 10, this indicates material removal in ductile mode. In contrast, the high frequency ranges, representative for brittle machining, do not show any significant signals. This is consistent with the surface characteristics and machining pressures from Fig. 24 and Table 9. Although it is not possible to distinguish between background noise and tool interaction, it can be assumed that no damage, such as microfracturing, was present.

In Fig. 28, the sums of the frequency ranges from Table 10 were calculated and the percentage of the total sum is displayed. The fine cuts in the performed sequence are shown for low and high cutting speed, respectively. The first four frequency ranges show a tendency to decrease their percentage share. In comparison, the remaining two frequency ranges tend to increase with increasing tool contact length and number of fine cuts.

Brittle material removal is characterized through the initiation and propagation of cracks into the machined material. The high amount of energy, released in very short time when cracks occur, leads to high propagation speed of the AE wave within the material. The immediate energy rise lets the atoms vibrate at high frequencies, while ductile machining generates a smoother distribution at different frequency

Process: fly-cutting of monocrystalline silicon (110)
Tool: radius tool, monocrystalline diamond, $r_\beta < 65$ nm, $r_\epsilon = 760$ µm
Parameters: $a_p = 10$ µm, $f = 24.8$ µm, v_c = var.
Metrology: QASS Optimizer 4D, FFT of acoustic emission, shaded = min/max

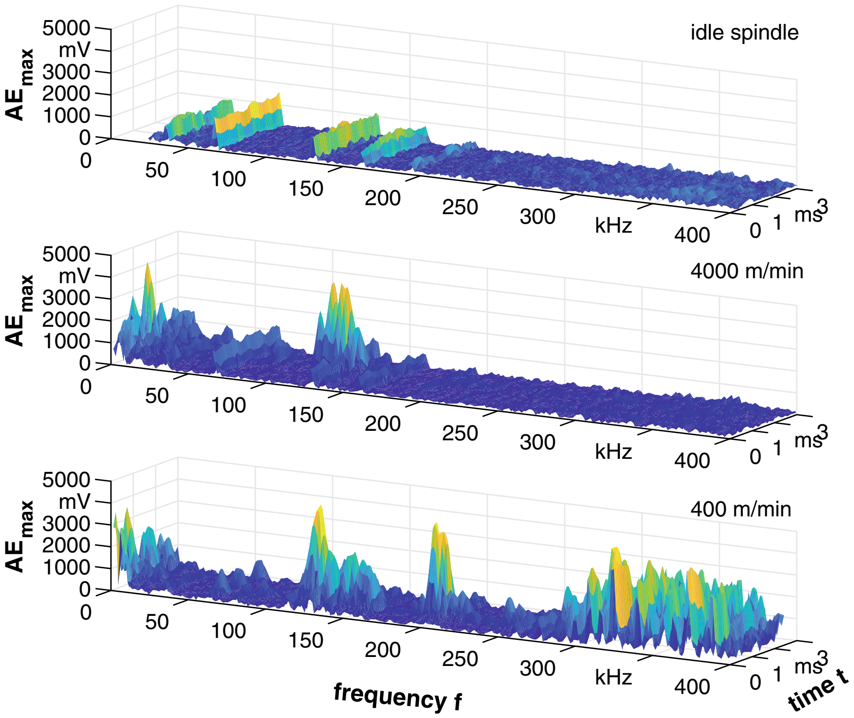

Fig. 27 Sound amplitudes of experiments with low and high cutting speed, compared to idle speed

ranges. These mechanisms are visible in Fig. 28, as the experiments with low cutting speed lead to a higher amount of brittle damage than high cutting speed and at the same time leads to a higher amount of AE signals in a high frequency range (250 to 500 kHz). Eventually, AE could not enable the in-process monitoring of tool wear, but it was capable for the characterization of the material removal mechanism.

4.4 Conclusion on UP-HSC of Brittle Materials

The aim of the study within this section was the fundamental investigation of the material behavior at high speed cutting of brittle materials, e.g. elemental semiconductors (Si, Ge) and compound semiconductors (ZnS, ZnSe). Off-axis diamond turning and fly-cutting were performed for the determination of critical depth of cut,

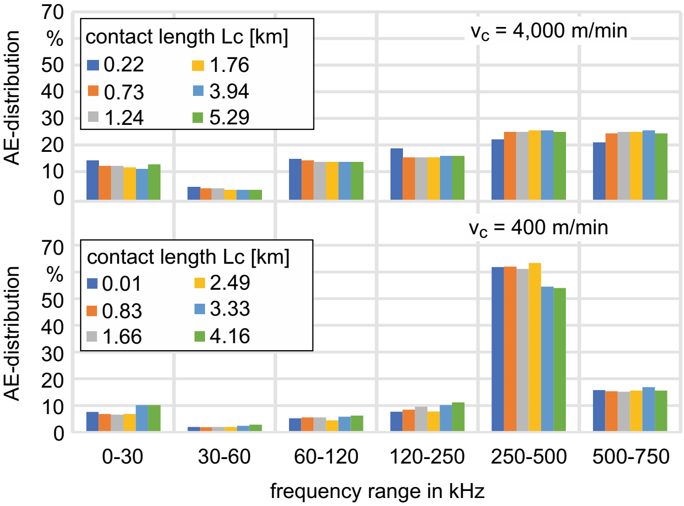

Fig. 28 Topographies of milled flat surfaces with low (top) and high (bottom) cutting speed

surface roughness and subsurface damage. Additionally, the progression of the tool wear was analyzed.

The main results are highlighted again below and prove for the first time that ductile machining of brittle materials can be significantly improved by just increasing the cutting speed.

The critical depth of cut for machining of single grooves is not increased by high speed cutting for elemental semiconductors, while it is for compound semiconductors. This circumstance is related to the ion bonding within the zinc blende structure of the compound semiconductors, which makes these IR materials brittle (lower hardness and similar fracture toughness compared to elemental semiconductors). While machining with conventional cutting speed, the machining pressure in the contact zone is not sufficient for ductile material removal (hydrostatic pressure) and results in brittle material removal. This changes with the application of HSC, where the machining pressure is in a range between 9 and 15 GPa, considered in literature as the suitable range for ductile machining [12, 18].

The achievable surface roughness when flat turning or milling improves with increasing cutting speed, which is related to the elevated machining pressure in the contact zone. In off-axis turning at high contact lengths per cut, temperature development plays a major role for the plasticization of the material, which promotes ductile chip formation instead of brittle material removal. The temperatures in the contact zone were estimated to 950 to 1,000 °C. These high temperatures were not detected while fly-cutting due to short contact lengths per cut, and consequently the reduction of surface roughness while the machining of elemental semiconductors was not as distinct as for off-axis turning. Still, all machined surface textures did not deteriorate in comparison to conventional cutting speeds so that the advantage of reduced machining times is valid without restrictions. For compound semiconductors, the reduction of surface roughness when HSC was 84% and 91% for ZnS and ZnSe, respectively.

Subsurface damage was detected by polishing and etching all machined materials and correlates to the surface roughness, particularly demonstrated in fly-cutting experiments.

For turning operations, tool wear increases with elevated cutting speed due to high temperatures in the contact zone, which lies above the thermal stability of the diamond tool. For milling operations, tool wear decreases by 25% when high cutting speeds are applied, which is related to the shorter contact times, as it has already been stated in Sect. 3.2 for ductile materials.

The process analysis by acoustic emission was not suitable for tool wear detection, but a procedure for the analysis of material removal mechanism (ductile/brittle) was proposed. When the signals are located in high frequency ranges, a brittle material removal occurs, while ductile machining is connected with an even distribution of frequencies over the whole analyzed range.

5 Conclusion and Outlook

It was shown in this research work that high cutting speeds are beneficial for ultra-precision machining, not only for reducing the required machining time, but also for improving the material removal behavior, by reducing the process forces and wear in metal cutting and facilitating a ductile-mode cutting of brittle materials.

Overall, this offers a great potential for improving the economic viability of industrially applied diamond milling, as long as the feed rates are increased as well (see Chap. 3) and the auxiliary processes for balancing are automated (see Chap. 4).

References

1. Abouridouane, M.: Bruchverhalten von Leichtmetallen unter Impact- Beanspruchung. Ph.D. thesis. RWTH Aachen (2005)
2. Bäker, M.: An investigation of the chip segmentation process using finite elements. Tech. Mech. **23**(1), 1–9 (2003)
3. Ben Amor, R.: Thermomechanische Wirkmechanismen und Spanbildung bei der Hochgeschwindigkeitszerspanung. Berichte aus dem IFW 03/2003 (2003)
4. Bifano, T.G., Dow, T.A., Scattergood, R.O.: Ductile-regime grinding: a new technology for machining brittle materials. J. Eng. Ind. **113**(2), 184 (1991). https://doi.org/10.1115/1.2899676
5. Brinksmeier, E., Ohlsen, I., Preuss, W.: Dependence of the cutting forces on cutting speed in high speed diamond turning. In: 29th ASPE Annual Meeting, Boston, USA, 9–14 November 2014, vol. 29, pp. 492–493 (2014)
6. Brinksmeier, E., Menten, A., Preuss, W.: Tool wear in high speed diamond milling. In: 29th ASPE Annual Meeting, Boston, USA, 9–14 November 2014, vol. 29, pp. 494–495 (2014)
7. Brinksmeier, E., Preuss, W., Riemer, O., Rentsch, R.: Ultraprecision high speed cutting. In: 30th ASPE Annual Meeting, pp. 58–63 (2015)

8. Brinksmeier, E., Preuss, W., Riemer, O., Rentsch, R.: Cutting forces, tool wear and surface finish in high speed diamond machining. Precis. Eng. (2017). https://doi.org/10.1016/j.precisioneng.2017.02.018
9. Chao, C.L., Ma, K.J., Liu, D.S., Bai, C.Y., Shy, T.L.: Ductile behaviour in single-point diamond-turning of single-crystal silicon. J. Mater. Process. Technol. **127**(2), 187–190 (2002). https://doi.org/10.1016/s0924-0136(02)00124-3
10. Dhulubulu, A.: Acoustic Emission (AE) monitoring of the milling process with coated metal carbide inserts using TRIM C270 cutting fluid. MA thesis. University of Toledo (2015)
11. Esmaeilzare, A., Rahimi, A., Rezaei, S.M.: Investigation of subsurface damages and surface roughness in grinding process of Zerodur® glass-ceramic. Appl. Surf. Sci. **313**, 67–75 (2014). https://doi.org/10.1016/j.apsusc.2014.05.137
12. Goel, S., Luo, X., Agrawal, A., Reuben, R.L.: Diamond machining of silicon: a review of advances in molecular dynamics simulation. Int. J. Mach. Tools Manuf **88**, 131–164 (2015). https://doi.org/10.1016/j.ijmachtools.2014.09.013
13. Hed, P.P., Edwards, D.F.: Relationship between subsurface damage depth and surface roughness during grinding of optical glass with diamond tools. Appl. Opt. **26**(13), 2491 (1987). https://doi.org/10.1364/ao.26.002491
14. Hodgson, B., Lettington, A.H., Stillwell, P.F.T.C., Baker, L.R., Masson, A.: Diamond turning of infra-red components. In: Infrared Technology and Applications. SPIE, May 1986. https://doi.org/10.1117/12.951967
15. Jasinevicius, R.G.: Influence of cutting conditions scaling in the machining of semiconductors crystals with single point diamond tool. J. Mater. Process. Technol. **179**(1–3), 111–116 (2006). https://doi.org/10.1016/j.jmatprotec.2006.03.106
16. Kármán, T.V.: Festigkeitsversuche unter allseitigem Druck (Strength tests under pressure from all sides). In: Zeitschrift des Vereines Deutscher Ingenieure 55 (1911). (in German)
17. King, R.F., Tabor, D.: The strength properties and frictional behaviour of brittle solids. Proc. Royal Soc. Lond. Ser. A. Math. Phys. Sci. **223**(1153), 225–238 (1954). https://doi.org/10.1098/rspa.1954.0111
18. Kovalchenko, A.M., Milman, Y.V.: On the cracks self-healing mechanism at ductile mode cutting of silicon. Tribol. Int. **80**, 166–171 (2014). https://doi.org/10.1016/j.triboint.2014.07.003
19. Li, S., Zhang, Y.: Application of single point diamond turning in infrared optics. In: 2016 International Symposium on Advances in Electrical, Electronics and Computer Engineering. Atlantis Press (2016). https://doi.org/10.2991/isaeece-16.2016
20. Liu, K., Li, X.P., Rahman, M.: Characteristics of high speed micro-cutting of tungsten carbide. J. Mater. Process. Technol. **140**(1–3), 352–357 (2003). https://doi.org/10.1016/s0924-0136(03)00758-1
21. Mian, A.J., Driver, N., Mativenga, P.T.: Chip formation in microscale milling and correlation with acoustic emission signal. Int. J. Adv. Manuf. Technol. **56**(1–4), 63–78 (2011). https://doi.org/10.1007/s00170-011-3185-x
22. Navare, J., Kang, D., Zaytsev, D., Bodlapati, C., Ravindra, D., Shahinian, H.: Experimental investigation on the effect of crystal orientation of diamond tooling on micro laser assisted diamond turning of zinc sulfide. Proc. Manuf. **48**, 606–610 (2020). https://doi.org/10.1016/j.promfg.2020.05.088
23. Neo, W.K., Kumar, A.S., Rahman, M.: A review on the current research trends in ductile regime machining. Int. J. Adv. Manuf. Technol. **63**(5–8), 465–480 (2012). https://doi.org/10.1007/s00170-012-3949-y
24. Nieminen, I., Paro, J., Kauppinen, V.: High-speed milling of advanced materials. J. Mater. Process. Technol. **56**(1–4), 24–36 (1996). https://doi.org/10.1016/0924-0136(95)01817-4
25. Preuss, W.: A Guide to Diamond Machining. Shaker-Verlag (2019)
26. Salomon, C.: Verfahren zur Bearbeitung von Metallen oder bei einer Bearbeitung durch schneidende Werkzeuge sich aehnlich verhaltenden Werkstoffen. DE523594C. Krupp AG, 27 April 1931

27. Schönemann, L., Berger, D., Dörgeloh, T., Riemer, O., Brinksmeier, E., Krüger, R., Schreiber, P., Denkena, B., Hochbein, J., Parsa, N., Schenck, C., Kuhfuss, B.: Synergistic approaches to ultra-precision high performance cutting. CIRP J. Manuf. Sci. Technol. **28**, 38–51 (2020). https://doi.org/10.1016/j.cirpj.2019.12.001
28. Schulz, H., Spur, G.: High speed turn-milling - a new precision manufacturing technology for the machining of rotationally symmetrical workpieces. CIRP Ann. **39**(1), 107–109 (1990). https://doi.org/10.1016/s0007-8506(07)61013-0
29. Schulz, H., Moriwaki, T.: High-speed machining. CIRP Ann. **41**(2), 637–643 (1992). https://doi.org/10.1016/S0007-8506(07)63250-8
30. Schulz, H.: Hochgeschwindigkeits-Bearbeitung - Technologie mit Zukunft. Werkstatt und Betrieb **127**(7/8), 539–541 (1994)
31. Schneider, T.: Aufwand, Nutzen und Grenzen des Hochgeschwindigkeitsdrehens. German. Darmstädter Forschungsberichte für Konstruktion und Fertigung. Shaker Verlag, Aachen, 25 July 1996
32. Shibata, T., Fujii, S., Makino, E., Ikeda, M.: Ductile-regime turning mechanism of single-crystal silicon. Precis. Eng. **18**(2–3), 129–137 (1996). https://doi.org/10.1016/0141-6359(95)00054-2
33. Tönshoff, H.K., Karpuschewski, B., Blawit, C.: Hochgeschwindigkeitszerspanung - Stand der Technik und Entwicklungstendenzen. VDI-Z **139**(9), 26–33 (1997)
34. Vandeperre, L.J., Giuliani, F., Lloyd, S.J., Clegg, W.J.: The hardness of silicon and germanium. Acta Mater. **55**(18), 6307–6315 (2007). https://doi.org/10.1016/j.actamat.2007.07.036
35. Yan, J., Asami, T., Harada, H., Kuriyagawa, T.: Fundamental investigation of subsurface damage in single crystalline silicon caused by diamond machining. Precis. Eng. **33**(4), 378–386 (2009). https://doi.org/10.1016/j.precisioneng.2008.10.008
36. Zhang, X., Liu, K., Kumar, A.S., Rahman, M.: A study of the diamond tool wear suppression mechanism in vibration-assisted machining of steel. J. Mater. Process. Technol. **214**(2), 496–506 (2014). https://doi.org/10.1016/j.jmatprotec.2013.10.002
37. Zhong, Z.W., Tok, W.H.: Grinding of single-crystal silicon along crystallographic directions. Mater. Manuf. Processes **18**(5), 811–824 (2003). https://doi.org/10.1081/amp-120024977

Electromagnetic Ultra-Precision Linear Guide

Rudolf Krüger, Benjamin Bergmann, and Berend Denkena

Abstract While electromagnetic levitation systems are already available for ultra-precision applications, they are limited to inspection or measurement tasks and non-mechanical processing due to their severely limited stiffness. This contribution introduces a novel electromagnetic linear guide, which was specifically developed for use in ultra-precision high performance machining. The active guide system features a position noise and a mean positioning error in the low nanometer range. At the same time, it provides sufficient dynamic stiffness for diamond machining. Furthermore, the actuator and sensor capabilities of the electromagnetic linear guide are applied to increase motion dynamics while reducing dynamic disturbances in motion phases by up to 75%. The capability of the new electromagnetic linear guide is finally shown for a reference diamond machining process.

1 Electromagnetic Bearings in Production Engineering

The performance of ultra-precision machine tools is largely influenced by the configuration of the feed and rotary axes. In particular, the implemented bearing solutions (including rotational bearings and linear guides) represent a limiting factor with regard to applicable motion dynamics and productivity. Conventional bearing technologies, such as roller bearings, typically rely on mechanical connections. Due to their high mechanical tolerances and considerable friction during operation, they are rarely used for the main axes of ultra-precision machine tools. Hydrostatic and aerostatic bearings, on the other hand, utilize fluid media for force transmission and

---

R. Krüger (✉) · B. Bergmann (✉) · B. Denkena
Institute of Production Engineering and Machine Tools IFW, Leibniz University Hannover, Garbsen, Germany
e-mail: bergmann@ifw.uni-hannover.de

R. Krüger
e-mail: Krueger_r@ifw.uni-hannover.de

E. Brinksmeier and L. Schönemann (eds.), *Ultra-precision High Performance Cutting*,
Lecture Notes in Production Engineering, https://doi.org/10.1007/978-3-030-83765-5_4

allow for almost frictionless operation. Hydrostatic bearings in particular exhibit exceptional stiffness and damping due to the use of viscous fluids. However, with increasing motion dynamics, they become more susceptible to fluidic friction and thermal issues, which may ultimately affect accuracy or even dynamic transmission behavior (i.e. stiffness and damping). As a consequence, there is usually a trade-off between permissible motion dynamics and positioning accuracy.

In this context, electromagnetic levitation represents a promising technology for rotational bearings and linear guides in ultra-precision machine tools. Electromagnetic bearings provide contactless force transmission and truly friction-free operation, which, in turn, allows for extremely fast motion without sacrificing positioning accuracy or stiffness. Moreover, active control of the electromagnetic bearings provides additional functions that can be beneficial for the setup and operation of ultra-precision machine tools. The integrated air gap sensors enable continuous position monitoring of the levitating component in up to five degrees of freedom. At the same time, the integrated actuators can be used to manipulate the position (perpendicular to the feed direction) and orientation of the levitating component. Practical applications of these functions include the compensation of geometric errors, feed forward control of dynamic disturbance forces and active damping of structural vibrations, which may be introduced through the machining process or the feed drives [2–4].

Electromagnetic levitation systems for ultra-precision applications are already available, however, they are limited to inspection or measurement tasks and non-mechanical processing because of their severely limited stiffness [12, 13]. On the other hand, known electromagnetic bearings and linear guides for machining applications do not provide the required accuracy for ultra-precision machining processes [1, 4, 15, 16]. Hence, the first objective of the presented research project is the design of an electromagnetic linear guide that combines sufficient accuracy and stiffness for ultra-precision diamond machining. In this context, general requirements for ultra-precision machining include a form accuracy of 100 nm and a kinematic surface roughness of less than 10 nm. The second objective is to investigate the potential of electromagnetic linear guides for increased productivity in ultra-precision machining by applying the active guide system's actuator and sensor functions.

First, this chapter begins with design considerations for the new electromagnetic linear guide and its integration in a three-axis milling machine prototype (Sect. 2). Then, modeling and model-based control design are presented (Sects. 3 and 4). Following an initial proof of concept (Sect. 5), the distinct properties and functionalities of the electromagnetic linear guide are examined in more detail to obtain key performance figures (Sect. 6). In particular, the position noise (Sect. 6.1), the micro-positioning capability (Sect. 6.2) and the dynamic stiffness (Sect. 6.4) of the active guide system are determined. Next, advanced functions of the electromagnetic linear guide with regard to compensation of systematic errors and feed-forward control of dynamic disturbance forces are investigated (Sect. 7). Afterwards, the capability of the new linear guide is evaluated for the use in ultra-precision diamond machining (Sect. 8). The chapter closes with a conclusion, discussing the presented findings and research questions for future work (Sect. 9).

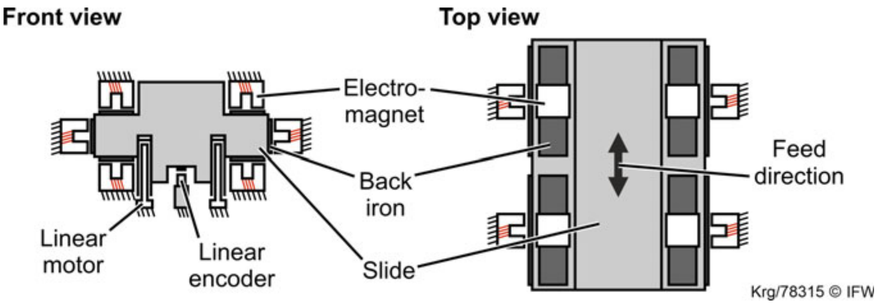

Fig. 1 Conceptual design for the electromagnetically guided feed axis [10]

2 Design and Assembly of the Electromagnetic Linear Guide

The following section introduces the fundamental design considerations for the new electromagnetic linear guide. Here, functional requirements of electromagnetic levitation systems as well as design principles for ultra-precision machines are considered. Furthermore, the implementation of the new guide system into a 3-axis milling machine tool as well as the layout of power, measurement and control electronics are considered.

2.1 Mechanical Setup

The design of electromagnetic levitation systems usually involves an iterative approach as the arrangement and specification of the electromagnets have a significant impact on the overall mechanical structure of the machine, which, in turn, may affect the requirements for the electromagnetic actuators. For this reason, a systematic approach is proposed in [5], which breaks down the complex design procedure into several work steps, including requirements definition, electromagnet arrangement and design, integration of feed drive and sensor systems, as well as material selection. With the proposed procedure, a set of twelve electromagnets in differential arrangement, with each two opposing magnets forming a bidirectional actuator, was selected for the functional basis of the new linear guide system, see Fig. 1. In comparison to a purely symmetrical arrangement with angled electromagnets, a differential arrangement requires more individual electromagnets. However, at the same time, the differential arrangement enables a more compact electromagnet design. Furthermore, it allows for a higher level of functional independence when controlling the levitating slide's five degrees of freedom.

In feed direction, the slide is actuated by two ironless linear motors with an optical scale for position feedback. Here, the use of two smaller motors instead of a single large one supports a compact, rigid and symmetrical design of the slide body. The linear motors are mounted recessed in the slide. Together with the magnet arrangement, this measure aims at a force application close to the slide's center of gravity to minimize unwanted tilting moments when actuating the levitating slide. In the same way, the linear encoder is recessed in the slide to minimize the impact of Abbe errors on the measured feed position.

Further, all active components are mounted to the guide frame to allow for a completely passive slide design, which avoids supply lines as potential sources of friction effects. The structural components of the linear guide are made from natural granite for improved material damping and thermal stability.

2.2 Electromagnet Design

The specific design of an electromagnet presents a challenging task due to highly non-linear properties and multiple parameter interdependencies. For the application at hand, a multi-stage design and optimization procedure utilizing a finite element simulation (FEM) and a multi-objective genetic algorithm was applied [7]. First, the electromagnet dimensions were estimated using an analytical force model with the specified force requirements. Then, a parametric finite element simulation was set up to validate the analytical model and to investigate the effect of electrical and geometrical parameters. Finally, the finite element simulation was coupled to a multi-objective genetic algorithm to identify a parameter set which satisfies the force requirements with minimum electrical losses.

The final design is based on a compact E-shaped magnet core made from laminated electrical steel (M250-35A) with a copper coil around the center pole (see Fig. 2 on the left). The design further incorporates aluminum fixtures and an integrated safety bearing made from brass. Moreover, a capacitive probe is mounted to the electromagnet in order to measure the air gap directly at the core. The spatial proximity of sensor and actuator aims to reduce the uncertainty for the identification of the control variable (i.e. the air gap). However, it also leads to considerable signal noise levels of the capacitive measurement system. In particular, the use of pulse width modulation (PWM) to adjust the referenced coil current can result in severe interference between the electromagnets and the capacitive probes [9]. Hence, the introduction of electrical isolation between electromagnet and probe, but also between back iron and measurement target, presents an imperative measure to reduce the signal noise levels. Accordingly, sensor holders made from a machinable glass ceramic (Macor) were used to attach the capacitive probes to the electromagnets. In combination with resolute grounding measures, the signal noise was reduced by more than 44% in average compared to aluminum sensor holders. Further, the use of the glass ceramic material reduced the thermal deflection of the sensor surface to less than 1 μm in the thermal steady state [9].

The electromagnet is complemented by a magnetic back iron made from low alloy steel (S355J2(+N)) to transfer the magnetic pulling force to the granite slide as

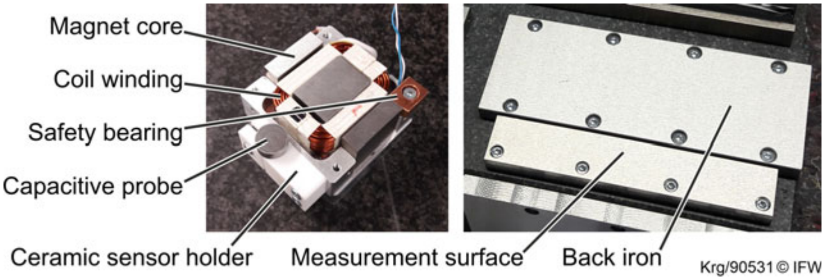

Fig. 2 Electromagnet and back iron design for the new guide system [9]

Table 1 Technical specification of the final electromagnet design

Specification	Value
Pole surface	$8.25\,\mathrm{cm}^2$
Air gap	0.2 mm
Number of turns	50
Coil inductivity (@ 1 T)	3.95 mH
Coil resistance	0.084 Ω
Coil current (nominal/maximum)	6.2 A/12 A
Flux density (nominal/maximum)	1 T/1.6 T
Magnet force (nominal/maximum)	300 N/700 N

well as a separate measurement surface made from high-strength steel (X5CrNi18-10, see Fig. 2 on the right). The measurement targets are electrically separated from the magnetic back iron and wired to a central grounding point, which connects to the reference ground input of the capacitive measurement amplifiers. The technical specifications of the final electromagnet design are summarized in Table 1.

2.3 Specification and Assembly

With the specification of the electromagnets, the initial concept was transferred into a detailed design which also considered additional components, such as linear motors and feedback systems, with their technical specifications. Figure 3 shows the components of the electromagnetic linear guide in an exploded view without the guide frame.

The final design includes capacitive probes with a dynamic resolution of 2.5 nm at 10 kHz (PISeca D-510.051 with E-852.10 signal amplifier). The ironless linear motors (Tecnotion UM9) provide a total maximum force of 600 N, which allows for an acceleration of up to $14\,\mathrm{m\,s}^{-2}$ for the slide with a mass of 42 kg. Additional motor filters (Copley Controls XTL-FA-01) are used to reduce current noise and

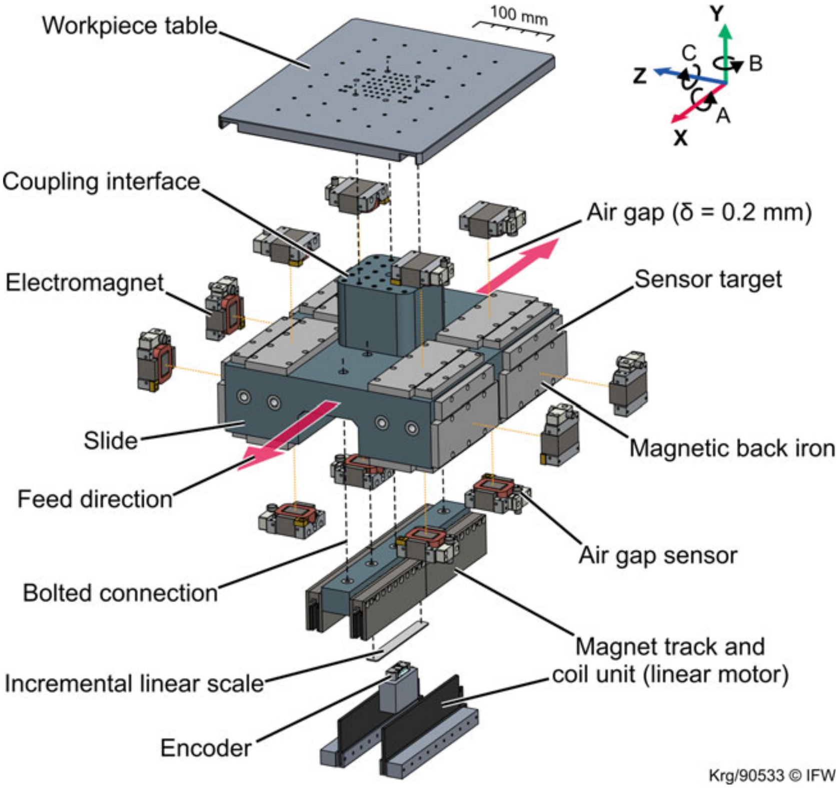

Fig. 3 Setup of the electromagnetically guided feed axis (exploded view without frame)

standstill jitter. Position feedback in feed direction is provided by an incremental linear scale (Renishaw RELM with TONiC T1011 encoder) with a resolution of up to 1 nm. Figures 4 and 5 provide further impressions of the actual design for the electromagnetic linear guide.

2.4 Integration in a 3-Axis Milling Machine

The desired fly-cutting reference process requires at least three controlled degrees of freedom in linear directions for feed, infeed and crossfeed [14]. Thus, the electromagnetically guided feed axis was combined with a secondary axis (Z-direction) guided by porous media aerostatic bearings for a 2-axis positioning stage. The stage features a box-in-a-box design for a minimum error budget and structural components made from natural granite. The 2-axis stage is complemented by a portal construction with a vertical axis (Y-direction) and a high-speed air bearing spindle (Professional

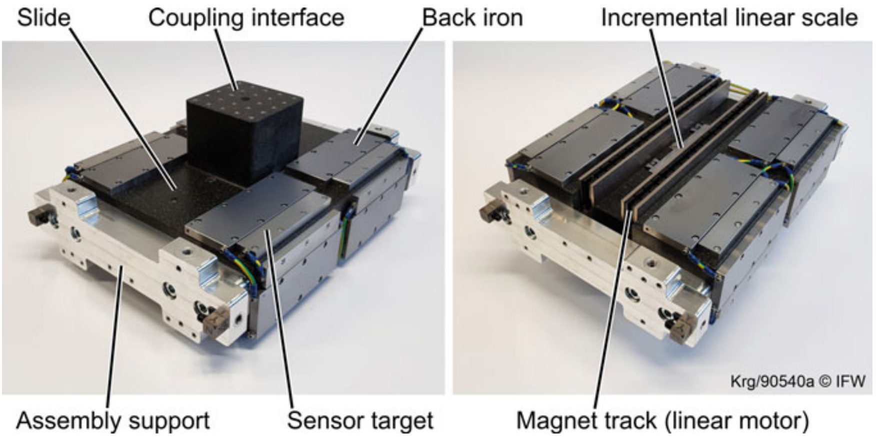

Fig. 4 Granite slide of the constructed test bench (top and bottom view) [14]

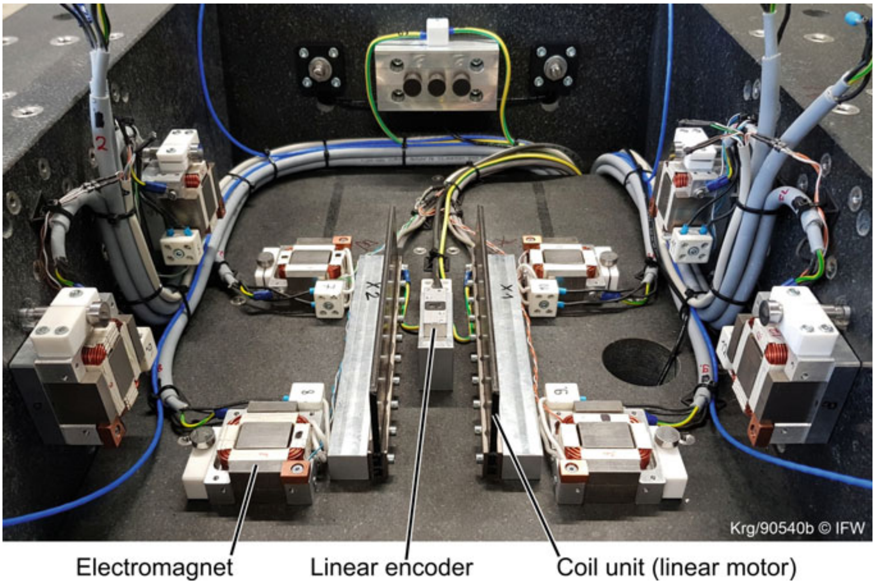

Fig. 5 Open guide frame (without top plate) of the constructed test bench [14]

Instruments Block-Head 4R). The vertical Y-axis features a servo motor, a reduction gearbox, roller bearings as well as two encoders for motor commutation and position feedback. The vertical Y-axis is primarily used for the infeed, which is static for the intended machining processes. Hence, motion accuracy of the Y-axis is of secondary importance and roller bearings are applicable in this case. The complete 3-axis milling machine tool prototype is shown in Fig. 6. Moreover, the machine tool design provides the flexibility for different configurations, e.g. to enable micro

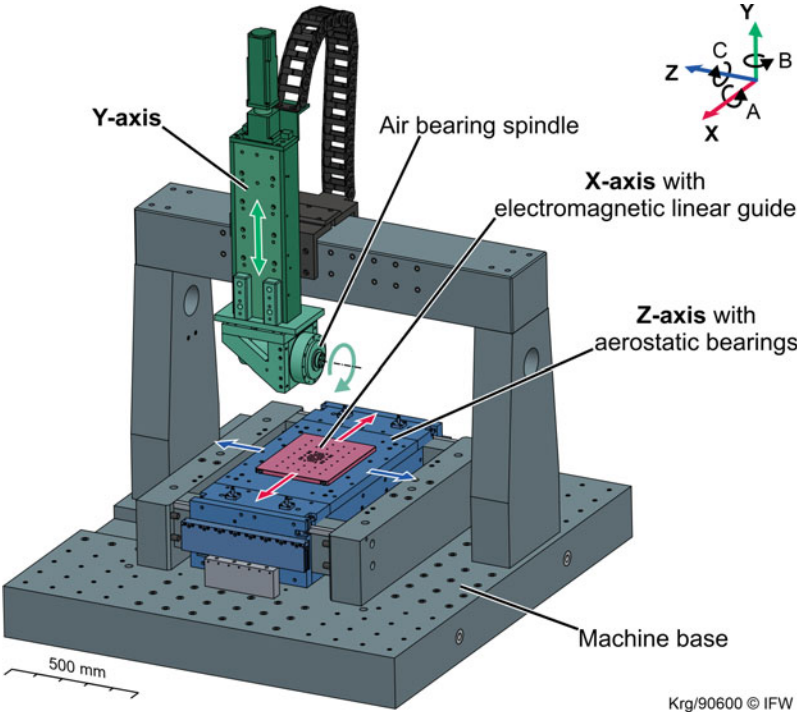

Fig. 6 3-axis milling machine prototype

milling with a vertically mounted spindle or high-precision planing with stationary diamond tools.

2.5 Power, Measurement and Control Electronics

In addition to structural components, actuators and sensors, the electromagnetic linear guide requires further hardware components, e.g. to evaluate sensor signals, calculate control variables and supply current to the electromagnets and linear motors. The complete hardware structure of the electromagnetically guided feed axis is illustrated in Fig. 7.

An industrial computer (Beckhoff C6930) is used as a central control system for the entire test bench. It provides a real-time control environment (TwinCAT) and an Ethernet-based real-time communication protocol (EtherCAT). Due to the large amount of data and the real-time requirements of the control application, an EtherCAT port multiplier is used for parallel data handling. Communication with the servo controller for the linear motors (Copley Controls XE2-230-20) is directly established via EtherCAT connection with a sample rate of 16 kHz (according to

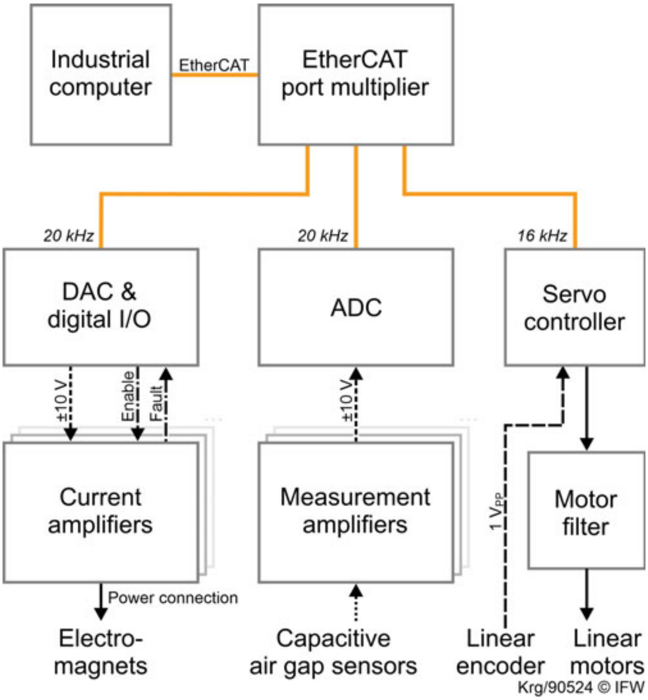

Fig. 7 Functional components as well as power and data connections of the magnetically levitated feed axis

the servo controllers PWM frequency). The servo controllers run in current control mode, the position and velocity control loops are implemented in the TwinCAT control environment. The signals of the capacitive measurement system are transferred to the control environment via analog-to-digital converters. Similarly, digital-to-analog converters provide reference values for the current amplifiers of the electromagnetic levitation system (Copley Controls JSP-180-020). Additional digital terminals control the current amplifiers' switch-on command, synchronization and fault detection. Communication between the industrial computer and the various terminals is established via EtherCAT with a maximum sample rate of 20 kHz, which corresponds to the current PWM switching frequency of the current amplifiers. The base time of the overall control system is set to 12.5 μs to cope with the different sample rates of the electromagnetic levitation system and the feed drives.

3 Modeling of the Mechatronic System

Electromagnetic bearings utilizing magnetic reluctance forces are inherently unstable systems. Accordingly, stable levitation requires a control system which continuously monitors the magnetic air gaps and adjusts the magnetic forces by calculating the appropriate coil currents for the electromagnets. However, due to the unstable and highly non-linear characteristics of electromagnets, commonly used heuristic control design methods cannot be applied for electromagnetic bearings and linear guides. Therefore, model-based control design methods present a purposeful way to determine stable control parameters without the risk of damaging or destroying the magnetic levitation system. For this, a simulation model is required that reproduces the fundamental properties and relationships of the real system [6]. The following section considers a mechanical model of the magnetic levitation system, coordinate transformation and force allocation mechanisms, as well as a model of the non-linear force characteristics of electromagnets.

3.1 Mechanical System

The mechanical system model of an electromagnetic linear guide usually consists of a single levitating object. The levitating component can be described by its equation of motion (1) with the matrices $\boldsymbol{M}$, $\boldsymbol{D}$ and $\boldsymbol{K}$, characterizing mass, damping and stiffness, as well as the generalized coordinates $\boldsymbol{q}$ and the generalized forces $\boldsymbol{Q}$, see Eqs. (2) and (3) The levitating slide's center of gravity is used as reference for the presented modeling approach.

$$\boldsymbol{M}\ddot{\boldsymbol{q}} + \boldsymbol{D}\dot{\boldsymbol{q}} + \boldsymbol{K}\boldsymbol{q} = \boldsymbol{q} \tag{1}$$

$$\boldsymbol{q} = \begin{bmatrix} x & y & z & a & b & c \end{bmatrix}^T \tag{2}$$

$$\boldsymbol{Q} = \begin{bmatrix} F_x & F_y & F_z & M_x & M_y & M_z \end{bmatrix}^T \tag{3}$$

Typically, a levitating component exhibits no significant friction or damping. In case of an electromagnetic levitation system, these properties are imposed by controlling the magnetic forces. Hence, the kinematic and dynamic properties of the magnetically suspended component can be described with the inverse mass matrix $\boldsymbol{M}^{-1}$ and a double integrator according to Eq. (4).

$$\ddot{\boldsymbol{q}} = \mathbf{M}^{-1}\boldsymbol{Q} \tag{4}$$

Using experimental modal analysis, the first natural frequency (i.e. the first eigenmode) of the slide was identified at approximately 1,600 Hz. This frequency value greatly exceeds the expected actuator dynamics. In this case, assuming a rigid slide body presents a valid approach and the structural dynamics can be neglected in the simulation model.

3.2 Coordinate Transformation

Using generalized coordinates, i.e. the translational and rotational degrees of freedom according to (2), presents an intuitive approach to describe the motion state of the electromagnetically levitated component. The generalized coordinates $\boldsymbol{q}$ can be obtained from the sensor values of the capacitive probes $\boldsymbol{d_S}$ using the Moore-Penrose inverse of the Jacobian matrix $\boldsymbol{J_S}$ according to Eqs. (5) and (6), where n is the number of electromagnets and sensors and m the number of generalized coordinates. The configuration of the Jacobian matrix only depends on geometrical considerations, hence, a reasonable estimation for the matrix entries can be obtained from available CAD models. Note that the entries of the Jacobian matrix (6) contain variable values that change with the feed position of the levitating slide as its center of gravity shifts in the fixed actuator coordinate system.

$$\boldsymbol{q} = \boldsymbol{J_S}^{+}\boldsymbol{d_S} = (\boldsymbol{J_S}^T\boldsymbol{J_S})^{-1}\boldsymbol{J_S}^T\boldsymbol{d_S} \tag{5}$$

$$\boldsymbol{J_S} = \left(\frac{\partial d_{S,i}}{\partial q_j^T}\right)_{i=1\ldots n;\, j=1\ldots m} \tag{6}$$

3.3 Force Allocation

Similar to the coordinate transformation of the sensor values, the actuator forces $\boldsymbol{F_A}$ can be calculated from the generalized forces and moments $\boldsymbol{Q}$ using the Jacobian matrix $\boldsymbol{J_A}$, see Eqs. (7) and (8). This approach also allows for a consistent force allocation for the overdetermined system. Note that for differential magnet arrangements, the actuator forces $\boldsymbol{F_A}$ have to be converted to individual pulling forces $\boldsymbol{F_M}$ of the involved electromagnets. Here, this is achieved by allocating positive actuator forces $\boldsymbol{F_A} > 0\,\mathrm{N}$ to the electromagnets pulling in positive coordinate direction, and negative actuator forces $\boldsymbol{F_A} < 0\,\mathrm{N}$ to the electromagnets pulling in negative coordinate direction.

$$\boldsymbol{F_A} = (\boldsymbol{J_A}^{+})^T\boldsymbol{Q} = \mathbf{J}(\boldsymbol{J_A}^T\boldsymbol{J_A})^{-1}\boldsymbol{Q} \tag{7}$$

$$\boldsymbol{J_A} = \left(\frac{\partial F_{A,i}}{\partial Q_j}\right)_{i=1\ldots n;\, j=1\ldots m} \tag{8}$$

The entries of the Jacobian matrices $\boldsymbol{J_A}$ and $\boldsymbol{J_S}$ depend on geometrical parameters of the magnetic levitation system, namely the distance of the sensors and actuators from the reference point, i.e. the levitating slide's center of gravity. Since a feed motion in X-direction results in a relative displacement of the center of gravity in the stationary sensor and actuator coordinate systems, individual entries of the Jacobian matrices will vary with the feed position. To ensure accurate coordinate transformation and force allocation, the pseudo-inverse of the Jacobian matrices must be updated according to the momentary feed position of the slide. For this, the Jacobian matrices as well as their pseudo-inverses include a symbolic variable for the feed position (i.e. the x-coordinate). The coordinate transformation and force allocation matrices are recalculated in consideration of the momentary feed position with each call of the control algorithm. Equation (9) exemplarily shows the force allocation matrix with the symbolic coordinate x and the geometrical parameters $l_X = 85\,\text{mm}$, $l_Y = 19.2\,\text{mm}$ and $l_Z = 86.5\,\text{mm}$, which represent the distance between the actuators and the slide's center of gravity in X-, Y- and Z-direction (see Fig. 3).

$$(\boldsymbol{J_A}^{+})^T = \begin{pmatrix} \frac{l_X + x}{4l_X} & \frac{l_Y}{4l_Z} & \frac{1}{4l_Z} & 0 & \frac{1}{4l_X} \\ \frac{l_X - x}{4l_X} & \frac{l_Y}{4l_Z} & \frac{1}{4l_Z} & 0 & \frac{1}{4l_X} \\ \frac{l_X - x}{4l_X} & -\frac{l_Y}{4l_Z} & -\frac{1}{4l_Z} & 0 & -\frac{1}{4l_X} \\ \frac{l_X + x}{4l_X} & -\frac{l_Y}{4l_Z} & -\frac{1}{4l_Z} & 0 & -\frac{1}{4l_X} \\ 0 & -\frac{l_X + x}{2l_X} & 0 & \frac{1}{2l_X} & 0 \\ 0 & -\frac{l_X - x}{2l_X} & 0 & -\frac{1}{2l_X} & 0 \end{pmatrix} \tag{9}$$

3.4 Inverse Model of Non-linear Magnetic Force Characteristics

The reluctance force (i.e. magnetic pulling force) of an electromagnet depends on the magnetic air gap and the flux inducing coil current. Variations of these values change the resulting pulling force in a non-linear fashion. A simple linearization for a working point of an electromagnet would severely limit its operating range. For the application at hand, a rather large operating range is required to account for varying loads (e.g. due to position-dependent bearing forces and dynamic feed forces) and air gap deviations (e.g. due to micro-positioning of the slide). Thus, it is not possible to define a single working point for all the electromagnets of the linear guide. Consequently, the application of linear control techniques requires the use of a model representation of the non-linear relationship $\boldsymbol{i} = f(\boldsymbol{\delta}, \boldsymbol{F_M})$ between the magnetic air gap $\boldsymbol{\delta}$, the required pulling force $\boldsymbol{F_M}$ and the respective coil current $\boldsymbol{i}$.

Fig. 8 Inverse function $i = f(\boldsymbol{\delta}, \boldsymbol{F_M})$ for the electromagnets of the experimental setup

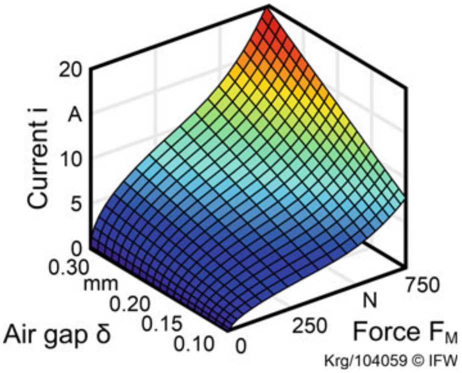

The pulling force characteristics of the electromagnets $\boldsymbol{F_M} = f(\boldsymbol{\delta}, i)$ was initially obtained using numerical simulations (i.e. finite element methods) in the design phase. This approach produces reliable results if the magnetization curves of the involved magnetic materials are known with sufficient accuracy. While this information is available for a selection of common engineering materials, it may be necessary to identify the magnetization curves of specific metal alloys since changes of composition or thermal treatment can significantly alter the magnetic properties. For this reason, the pulling force characteristics of the electromagnets were directly measured using an experimental setup. Then, the characteristic diagram was mathematically inverted to obtain the inverse function for the calculation of the coil current reference (see Fig. 8). The inverse functional relationship was implemented as a 2D look-up table within the control environment.

4 Control Design for the Electromagnetic Linear Guide

This section proposes a systematic model-based control design approach for electromagnetic levitation systems using reluctance force actuators. In the following, a lean simulation model based on the model components from Sect. 3 is introduced. It allows for the identification of robust control parameters without the risk of unstable operation and damage to the actual electromagnetic levitation system. Furthermore, the final controller layout for the implementation in the industrial control environment is presented at the end of the section.

The mechanical model of the levitating component from Sect. 3.1 provides the basis for the simulation. Accordingly, the simulation is based on generalized coordinates and generalized forces. Assuming that the geometrical parameters for the Jacobian matrices and the characteristic diagram of the electromagnets are known with sufficient accuracy, it is feasible to neglect the coordinate transformation, the force allocation and the non-linear force characteristics in the simplified simulation model. This implies that the calculated reference force values are reliably transferred

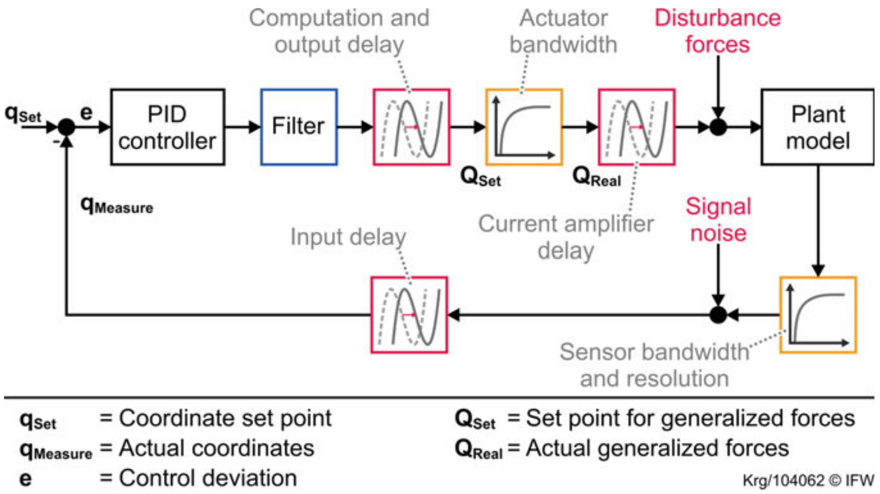

Fig. 9 Simplified simulation model for control parameter identification

into actuating forces with the correct amplitude and direction. Model deviations in this respect lead to minor amplitude errors of the regulated variables (i.e. the magnetic pulling forces), although no relevant impact in the control performance is expected. However, model components such as filters, signal delays and bandwidth restriction of actuators and sensors significantly affect the phase margin of the closed loop system and with this the control performance and stability. Thus, they are considered in the simplified model for a reliable real-world representation, see Fig. 9. The input delay of the control system corresponds to the cycle time of 50 μs. The computation of the control variables and the data output operation require another control cycle, which results in a further delay of 50 μs. The delay of the current amplifier amounts to 150 μs from the time a target current is set until the commanded current is reached.

For the application at hand, a set of five discrete proportional-integral-differential (PID) controllers is used to individually control the slide's five degrees of freedom. Each degree of freedom can be represented by a linear transfer function including the control parameters K_P, K_I and K_D (i.e. the proportional, integrative and derivative constants) for each PID controller. The simple simulation model allows for very fast computation, so that common optimization algorithms can be applied to efficiently identify control parameters for a desired performance objective (e.g. control bandwidth, reference tracking or disturbance rejection). Moreover, the simulation model allows for further testing of the identified control parameters in consideration of varying set point values or disturbance forces. For the implementation into the industrial control environment, the controller is extended by the coordinate transformation and force allocation mechanisms as well as the inverse model of the non-linear force characteristics from the previous section. The actual controller layout is depicted in Fig. 10.

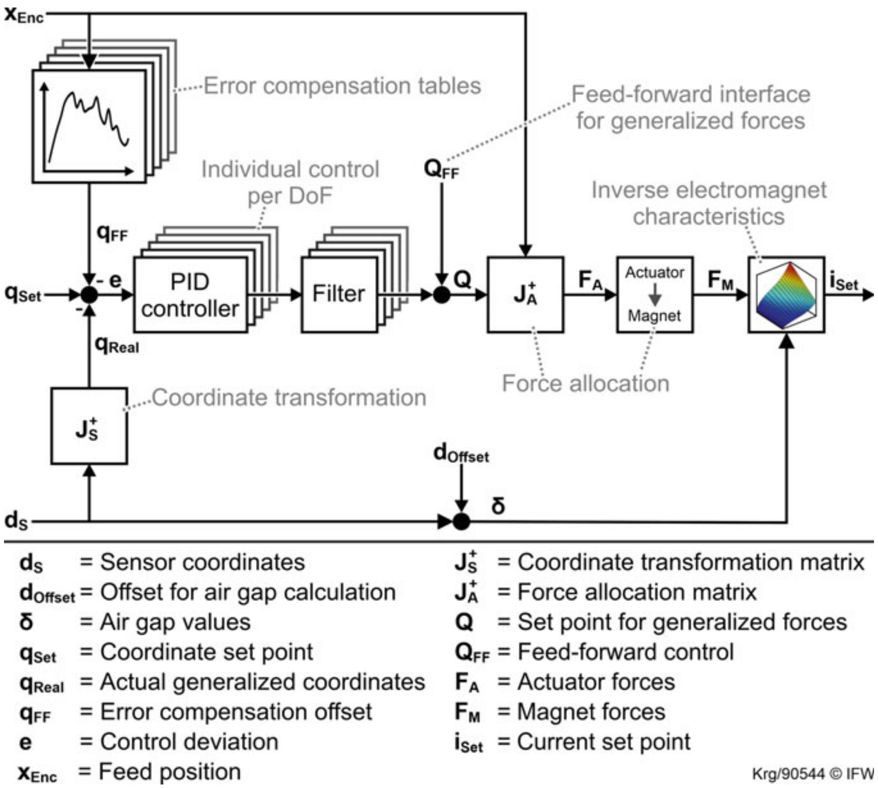

Fig. 10 Controller layout for implementation in the industrial control environment

5 Commissioning of the Electromagnetic Linear Guide

This section covers the procedure for the commissioning of the electromagnetic linear guide. First, a set of control parameters was identified using the approach from Sect. 4 for the initial start-up and operation of the electromagnetic levitation system. In operation, the system was subjected to a specified control deviation via a position reference step to evaluate robustness, reference tracking and decoupling of the generalized coordinates. The micro-positioning capability was explored in more detail to obtain preliminary results on the positioning accuracy of the electromagnetic levitation system.

The initial control parameters were set for a positioning bandwidth of 100 Hz in all five degrees of freedom according to the control design approach from Sect. 4. While the initial parameter set allowed for stable levitation, oscillations around 2,300 Hz occurred in the *b*-coordinate under external load—without causing instability though. Hence, a notch filter with a central rejected frequency of 2,300 Hz was implemented as a set point filter for the torque M_y. Consequently, the control parameters were then

Table 2 Control parameters for the electromagnetic linear guide

q	y	z	a	b	c
K_P	3,891,742	3,288,660	58,836	96,015	73,715
K_I	112,188,962	82,149,795	2,210,569	3,446,513	2,604,057
K_D	33,750	32,913	391	668	522

recalculated for the PID controller of the b-coordinate. The full control parameter set for the electromagnetic linear guide is summarized in Table 2. Further details on the commissioning strategy can be found in [8].

Note that the control system of the electromagnetic levitation system is initialized with non-variable matrices for coordinate transformation and force allocation. This is due to the fact that the incremental linear scale requires a homing procedure to provide absolute position information for the x-coordinate. For the initial launch of the electromagnetic linear guide, the feed position is assumed to be $x = 0$ mm, which does result in tracking errors in the rotational degrees of freedom but still allows for stable levitation (see Sect. 7.2). After the homing procedure, the coordinate transformation and force allocation matrices switch to position-dependent operation.

In order to evaluate the control performance of the electromagnetic linear guide, the control system was subjected to a reference step of 1 µm for the y-coordinate. The response was monitored with the integrated capacitive measurement system, see Fig. 11. Note that the control system was tuned for a practical compromise between reference tracking and disturbance rejection, thus, enabling high repeatability and accuracy when micro-positioning, as well as high stiffness and damping for the machining process. Since the control system is designed to react to small position deviations in the nanometer range, a reference step of 1 µm represents a rather excessive error for the position algorithm and results in a significant overshoot for the considered coordinate. Despite the extremely high excitation, the measurement data in Fig. 11 still shows a reliable decoupling of the five controlled coordinates.

The minimum step size for the micro-positioning motion is determined by the signal noise in the respective generalized coordinates. In the y-coordinate, for instance, the signal noise level allows for a reliable separation of 100 nm steps as demonstrated in Fig. 12. Note that the overshoot observed in Fig. 11 completely disappears for small reference steps in the submicron range.

6 Characterization of the Electromagnetic Levitation System

Following the commissioning process, the electromagnetic linear guide was investigated in more detail using additional measurement hardware to obtain reliable performance figures. First, position noise and positioning accuracy of the electro-

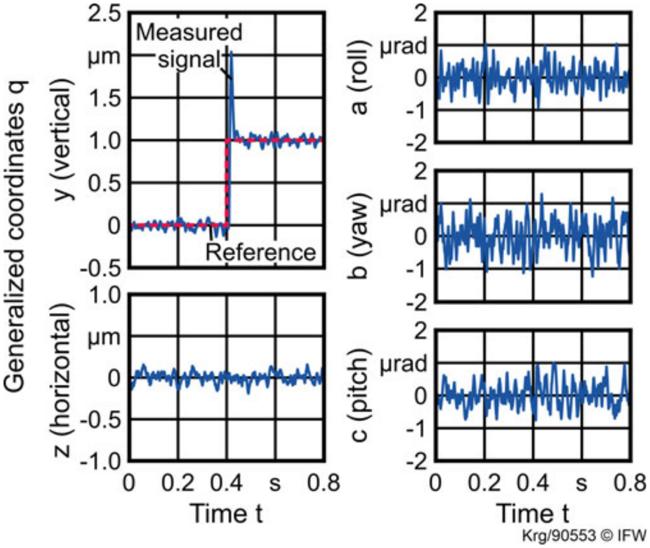

Fig. 11 Generalized coordinates for set point step in y-coordinate

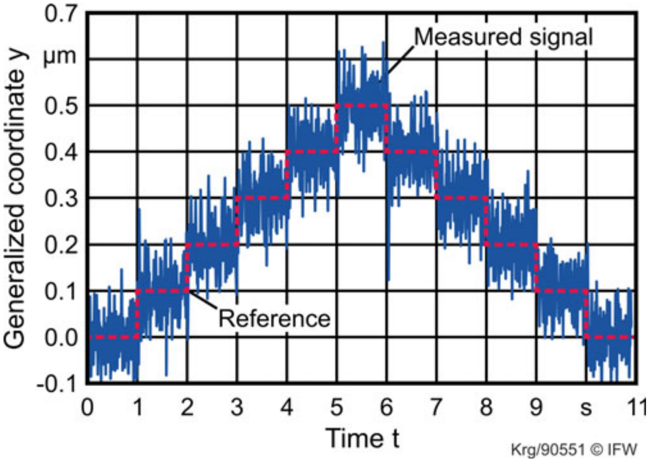

Fig. 12 Fine positioning in y-coordinate with 100 nm steps (measured with internal sensors)

magnetic linear guide were considered as they directly translate to surface and form deviations of the machined workpiece. In addition to the static positioning accuracy, the bandwidth of the micro-positioning motion was determined to assess up to which frequency position errors can still be compensated. Finally, the dynamic stiffness of the active guide system was investigated via an experimental modal analysis to evaluate its capability to reject dynamic disturbance forces. Other performance figures, for example those concerning the feed motion, are discussed in Sect. 7.

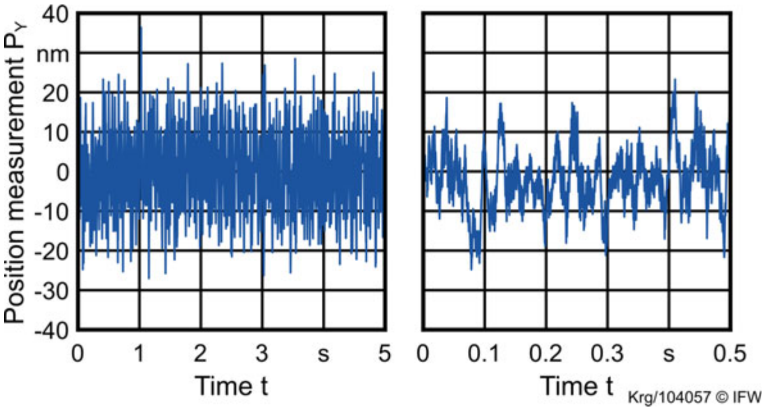

Fig. 13 Position noise of the levitating slide in the y-coordinate

6.1 Position Noise

Being a controlled system, the levitating slide of the electromagnetic linear guide exhibits a position noise at standstill. In a machining process, the position noise directly affects the generated workpiece surface and can ultimately compromise the surface quality. While the integrated capacitive measurement system provides information on the slides position and orientation, it cannot be used to reliably determine the actual position noise. The signals of the capacitive probes are susceptible to interference from the adjacent electromagnets and show increased noise levels as soon as the guide system is active. Hence, an external capacitive probe (Lion Precision 2G-C8-0.5 with CPL490 measurement amplifier) with a dynamic resolution of 0.33 nm at 15 kHz was used to measure position noise of the y-coordinate against the workpiece table of the levitating side. Figure 13 shows the measured position signal. The position signal has a standard deviation of 7.6 nm. According to the 3-sigma rule, 99.7 % of all measurements can be allocated to an interval of 22.8 nm.

The observed position noise occurs due to various disturbances within the closed loop system. For example, the sensor noise of the capacitive air gap measurement system propagates through the control loop and leads to noisy control variables (i.e. current set points). Moreover, time-discrete control algorithms and data processing delays introduce additional noise to the closed loop system. The measurement shown in Fig. 13 also includes the sensor noise of the external capacitive probe as well as possible vibrations of the additional sensor holder. Accordingly, the real position noise is probably even smaller than estimated with the measurement.

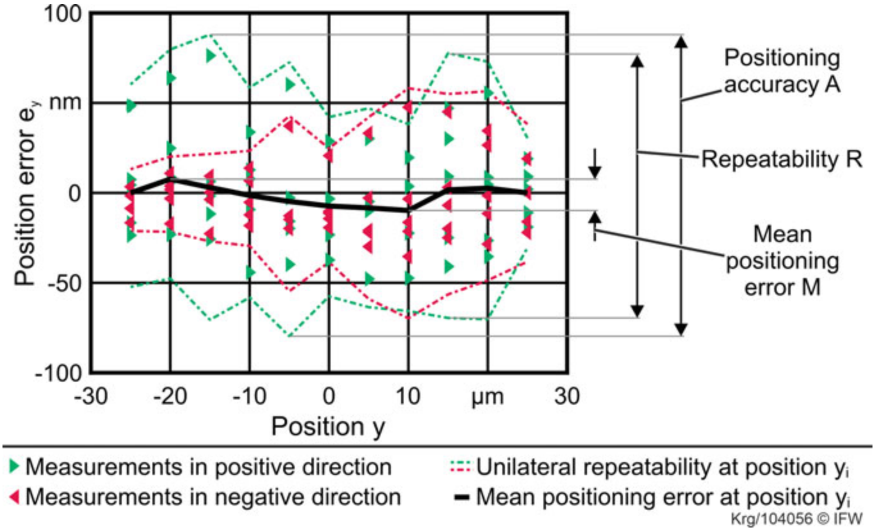

Fig. 14 Position error of the electromagnetic linear guide in y-direction according to ISO 230-2 (with the mean positioning error M, the repeatability R, and the position accuracy A)

6.2 Positioning Accuracy

Since the motion constrains of an electromagnetic linear guide are imposed by the control systems, it is feasible to specifically position the levitating slide within the air gap, i.e. in two degrees of freedom perpendicular to the feed direction, and in all three rotational degrees of freedom. In order to determine the static positioning accuracy of the electromagnetic linear guide, the micro-positioning motion was measured with a laser interferometer (Renishaw ML-10) according to ISO 230-2. Figure 14 shows the exemplary position error measurement for y-coordinate motion, which includes repeated position measurement for eleven positions over 50 µm (back and forth).

Compared to the initial results presented in [11], the overall positioning accuracy was further improved through an optimized sensor integration (i.e. improved electrical isolation of the capacitive probes and grounding of the measurement targets, compare Sect. 2.2) which reduced the signal noise significantly. Thus, the electromagnetic linear guide exhibits mean positioning errors below 50 nm for the linear and less than 0.3 µrad for the rotational degrees of freedom. Further, the repeatability mainly determines the absolute positioning accuracy due to the lack of friction and high linearity of the capacitive measurement system. The repeatability, in turn, is affected by the noise levels of the measurement system and the resulting position uncertainty.

Table 3 shows the accuracy parameters for all five controlled degrees of freedom (compare Fig. 14 for the statistical accuracy parameters). Different accuracy parameters for the individual degrees of freedom results from a different number of sensors

Table 3 Position accuracy of the electromagnetic linear guide according to ISO 230-2 over 50 µm for the y- and z-coordinates, and over 300 µrad for the a-, b- and c-coordinates (with the mean positioning error M, the repeatability R, and the position accuracy A)

$\boldsymbol{q}$	y	z	a	b	c
M	0.017 µm	0.040 µm	0.30 µrad	0.25 µrad	0.23 µrad
R	0.134 µm	0.291 µm	1.85 µrad	1.14 µrad	1.56 µrad
A	0.168 µm	0.303 µm	1.87 µrad	1.31 µrad	1.78 µrad

for the respective coordinates. Notably, accuracy deviations in the rotational degrees of freedom can be attributed to the measurement accuracy of the interferometer, which is specified with ±0.5 µrad. The positioning accuracy in the submicron range indicates a general suitability of the new electromagnetic linear guide for precision application. In particular, the positioning accuracy of 0.168 µm for the y-coordinate is very close to the required form accuracy of ultra-precision workpieces which is generally specified with 0.100 µm. However, the positioning accuracy alone does not allow for a definitive statement regarding the final quality of the workpiece. The surface formation depends on further effects during the machining process, such as the interaction between cutting forces and the finite dynamic stiffness of the machine structure. Hence, a final evaluation of the electromagnetic linear guide's capability requires machining experiments (compare Sect. 8).

6.3 Positioning Bandwidth

In addition to the positioning accuracy, the positioning bandwidth of the electromagnetic linear guide was investigated. The positioning bandwidth indicates up to which frequency a specified displacement can be reliable set and determines the motion dynamics in the electromagnetic linear guide's controlled degrees of freedom. For the investigation of the positioning bandwidth, a stepped sine signal was used for the position reference and the system response was measured with the integrated capacitive probes. A set-point amplitude of 1 µm was used for the linear coordinates (y and z) and an amplitude of 10 µrad for the rotational coordinates (a, b and c). The frequency of the sine function was incrementally increased from 1 to 500 Hz. Figure 15 exemplarily shows the frequency response for the y-coordinate, while Table 4 summarizes the overall results of the experimental investigation. The identified bandwidths match the design specification from Sect. 5 of 100 Hz, except for the bandwidth of the b-coordinate. Here, the control parameters were increased with the implementation of the notch filter (see Table 2). While the filter effectively suppressed the oscillations around 2,300 Hz, the corresponding bandwidth limitation for the b-coordinate from the simulation was not observed for the real system. This indicates further potential to increase the positioning bandwidth of the other coordinates of the electromagnetic linear guide by further control parameter opti-

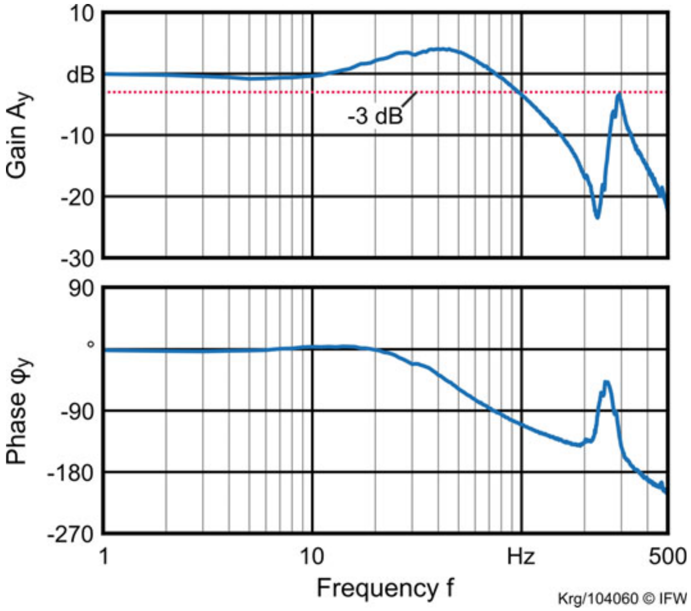

Fig. 15 Frequency response for reference excitation in the y-coordinate (for an amplitude of 1 µm with a frequency of 1 to 500 Hz)

Table 4 Positioning bandwidth of the electromagnetic linear guide in five degrees of freedom (for an amplitude of 1 µm in y and z, and 10 µrad in a, b and c)

q	y	z	a	b	c
f_{-3dB}	96 Hz	97 Hz	113 Hz	239 Hz	136 Hz

mization. However, increasing the feedback gain of the control system inevitably leads to a trade-off between positioning accuracy and bandwidth as the signal noise of the capacitive measurement system is also amplified by the control loop. While the use of digital filters allows for reduced signal noise levels, it also affects the phase margin and the electromagnetic linear guide's dynamic disturbance rejection.

6.4 Dynamic Stiffness

The dynamic stiffness represents a directional and frequency-dependent performance figure, which indicates the external force required to deflect the levitating slide by a certain distance. The dynamic stiffness of the functional prototype was determined through experimental modal analysis. For this, the levitating slide was excited with an impulse hammer (PCB-086C03) at the tool center point (TCP). The frequency-

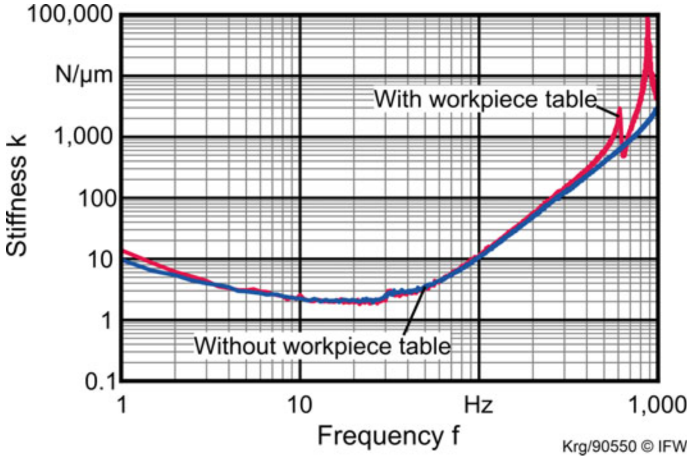

Fig. 16 Dynamic stiffness of the electromagnetic guide at the TCP in Y-direction (with and without workpiece table)

dependent response was measured in close proximity to the excitation point using a laser vibrometer (Polytec OFV-303 with OFV-3001 controller) and a three-axis accelerometer (PCB-356A16), both coupled to a modal analysis system of the type LMS Instruments SCADAS III. For the evaluation of the measurements, the signals of the vibrometer and the accelerometer were combined using sensor data fusion to obtain a broadband and low-noise signal. The frequency response function was measured for an excitation at the workpiece table and directly at the coupling interface of the slide. The measurement results are shown in Fig. 16. While the low frequency range is dominated by the control algorithm, the mass and structural dynamics of the electromagnetic linear guide become increasingly important for higher frequencies. As a result, the static stiffness is basically infinite, if the external load is smaller than 2,800 N (which is the load capacity of the electromagnetic levitation system). As expected, the lowest stiffness occurs near the control bandwidth limit, which is around 25 Hz for the experimental setup. Beyond that, the electromagnetic levitation guide does not show any critical natural frequencies up to 2,300 Hz. Adding the aluminum workpiece table (compare Fig. 3) introduces a natural frequency at 644 Hz, which is, however, very well damped, see Fig. 16.

The minimum stiffness of the electromagnetic linear guide is $1.9\,\mathrm{N}\,\mu\mathrm{m}^{-1}$ at 25 Hz. Other relevant frequency and stiffness values result from the specified reference processes of the research unit. Conventional fly-cutting with a single diamond tool and a spindle speed of $2{,}000\,\mathrm{min}^{-1}$ results in an excitation frequency of 33 Hz ($2.6\,\mathrm{N}\,\mu\mathrm{m}^{-1}$). Using the dual tool holder described in Chap. 2 for fly-cutting with $2{,}000\,\mathrm{min}^{-1}$ leads to a tool engagement frequency of 66 Hz ($5.0\,\mathrm{N}\,\mu\mathrm{m}^{-1}$). Finally, the desired high-performance fly-cutting process with a single tool and $20{,}000\,\mathrm{min}^{-1}$ produces an excitation frequency of 333 Hz ($166.7\,\mathrm{N}\,\mu\mathrm{m}^{-1}$). In consideration of the expected cutting forces of less than 1 N, the resulting deflection of the electromagnetic linear guide is estimated to be in the single digit nanometer range for the high-performance cutting process.

7 Advanced Functions of Active Magnetic Bearings

After the identification of the fundamental performance figures (see Sect. 6), advanced functions specific to the electromagnetic levitation system are considered. In order to minimize straightness and inclination errors for improved overall accuracy over the travel range, the capability of the electromagnetic linear guide system to compensate quasi-static errors was investigated. Afterwards, a feed-forward control mechanism was considered to reduce the levitating slides tilting motion in acceleration and deceleration phases, aiming at increased motion performance in combination with reduced tilting errors.

7.1 Compensation of Straightness and Inclination Errors

In case of the electromagnetic linear guide, the straightness and tilting errors over the travel path primarily result from shape deviations of the sensor targets for the capacitive air gap measurement system. Since the sensor targets were produced using conventional machining (i.e. milling and grinding), they show shape deviations in the single-digit micrometer range. These shape deviations translate to deviations from the ideal zero position and orientation of the levitating slide, which results in straightness and inclination errors over the travel path. However, since those errors occur systematically, the micro-positioning capability can be used to compensate the shape deviation of the sensor targets and effectively improve straightness and inclination errors of the feed axis.

A multi-axis calibrator (Renishaw XM-60) was used to obtain initial measurements for the error motion in all six degrees of freedom of the machine axis along the travel path (see Fig. 17). Again, ISO 230-2 was applied, using 19 measurement positions over a travel range of 90 mm. Naturally, inclination errors around the slide's main axes of inertia result in translational errors at the tool center point. Hence, a multi-stage approach was chosen for the systematic error compensation.

First, the position-dependent inclination errors from the initial measurement were used to calculate correction values for the a-, b- and c-coordinates. The correction values were stored in individual look-up tables, which provide corrective offsets depending on the momentary slide position in feed direction. With the first stage of the compensation activated, the measurement was repeated to identify remaining feed position and straightness errors. This measurement confirmed a significant correlation between the pitch angle error (c-coordinate or rotation around z) and the feed position (x-coordinate) due to the position of the electromagnetic linear guide's the linear encoder (compare Sect. 3.2) and the placement of the multi-axis calibrator's launch unit on the workpiece table. In fact, after the compensation of the inclination errors, the remaining position error in feed direction was in the range of the position uncertainty, hence, further compensation for the x-coordinate was not considered. The impact of the inclination errors on the straightness, on the other hand, is less pronounced. Since relevant straightness errors still occurred with the first compensation stage, look-up tables with corrective offsets for the y- and z-coordinate were derived from the measurement and implemented in the control environment. Finally, the measurement was repeated once again to evaluate the effectiveness of the compensation approach.

Figure 17 shows the measurement results of the fully compensated system in comparison to the initial measurement. The measurements indicate a mean straightness error of less than 1 μm and mean inclination errors smaller than 2 μrad (less than $0.4''$) with systematic error compensation. These figures imply a general suitability of the electromagnetic linear guide for use in ultra-precision machine tools. While these errors were identified for a travel range of 90 mm, it is feasible to achieve the same straightness and inclination over larger travel paths if systematic error compensation is applied. For long travel paths, electromagnetic bearings offer the potential to exceed conventional bearings in ultra-precision feed axes with regard to the remaining straightness and inclination errors as well as the setup effort.

7.2 Feed Forward Control of Dynamic Disturbance Forces

Applying any kind of external force to the levitating slide results in position deviations due to the finite stiffness of the electromagnetic linear guide. The initial deflection ultimately results from the dead time of the controlled system, i.e. the time it takes to detect a disturbance, calculate appropriate control variables and supply the coil currents to counter the external load. In any case, the overall delay is primarily determined by hardware restriction and dictates the performance limit regarding the dynamic stiffness of the electromagnetic linear guide, which is basically its ability to reject disturbance forces (see Sect. 6.4). In view of the application at hand, i.e. ultra-precision diamond machining, random disturbance forces occur due to the cutting process and are relatively small with typical cutting force values of 1 N and less (especially for increased cutting speed as shown in Chap. 3). However, feed forces accelerating and decelerating movable components lead to considerable disturbances. Since feed forces are rarely applied in the exact center of gravity, they mostly introduce unwanted torque and, thus, unwanted inclination and position errors at the tool center point. Depending on the rotational stiffness of the implemented bearing technology, this effect limits the applicable motion dynamics of ultra-precision machine tools.

While feed forces present dynamic disturbances, they are highly systematic – especially for friction-free motion systems. The actively controlled electromagnetic linear guide provides sensory capabilities to identify and evaluate the error motion in acceleration and deceleration phases. Moreover, its actuator capabilities enable a

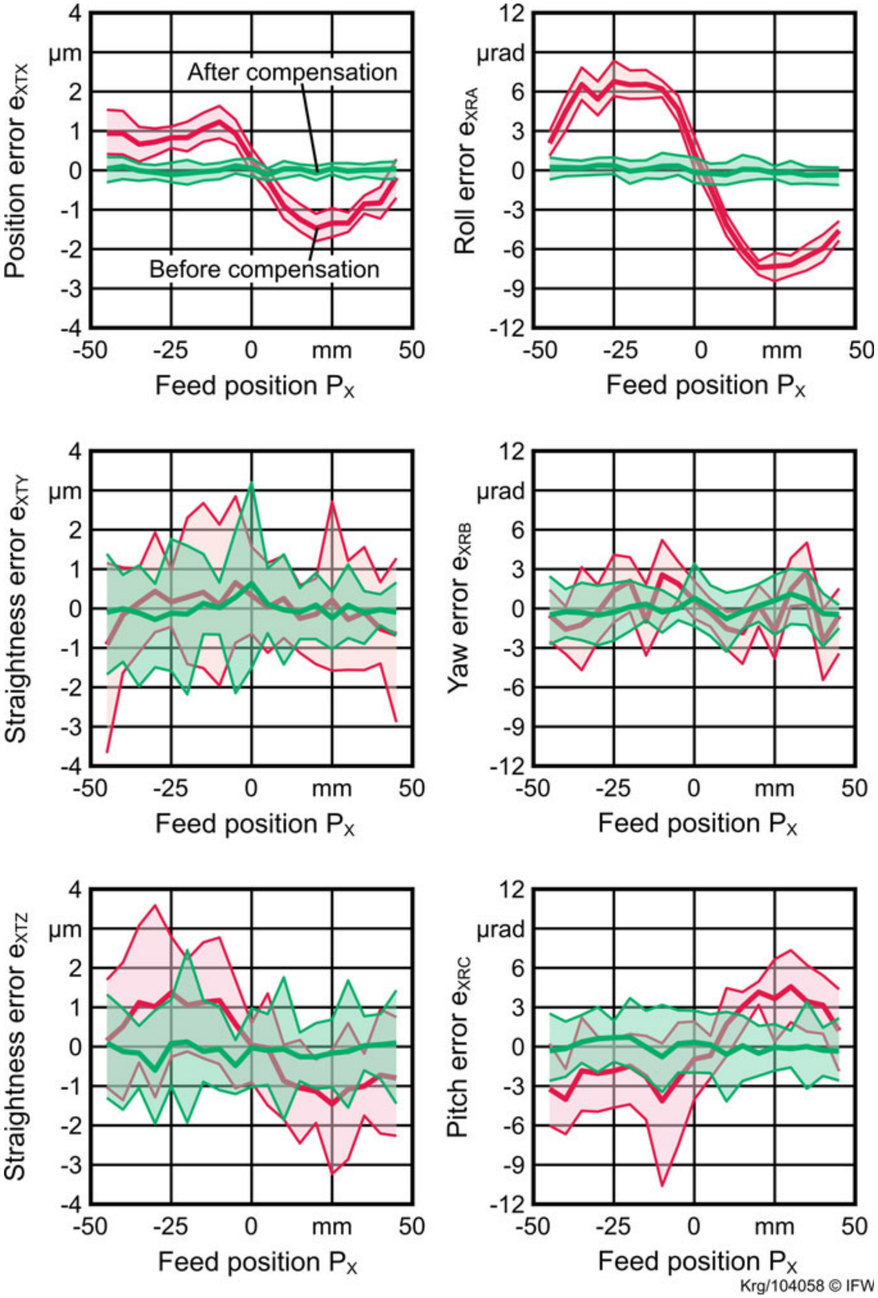

Fig. 17 Compensation of straightness and inclination errors over the travel path

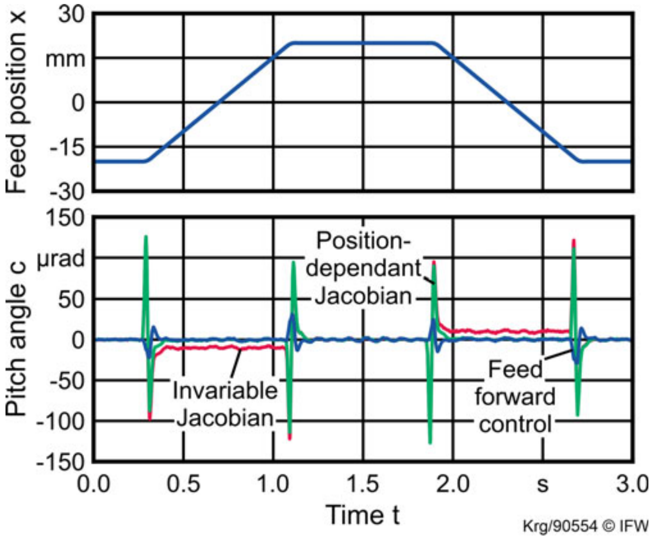

Fig. 18 Inclination errors during feed motion with non-variable and position-dependent inverse Jacobian matrices as well as with feed-forward control of dynamic disturbance forces

feed-forward control of systematically occurring disturbance forces. For a practical implementation of the feed-forward control mechanism, the acceleration set point for the feed drives was considered as a suitable reference.

In order to explore this approach, a reference motion over a stroke of 40 mm with the target velocity of 3,000 mm min^{-1} was considered. The acceleration was limited to 5 ms^{-1} to prevent damage to the test bench. The lateral displacement and inclination of the levitating slide were monitored with the integrated capacitive measurement system. First, the reference motion was carried out with the initial non-variable coordinate transformation and force allocation matrices. While the system remained stable, it showed considerable pitch angle errors (in the c-coordinate) in acceleration and deceleration phases. Furthermore, a constant tracking error in the c-coordinate was observed during the feed motion as the control system is unaware of the shifting center of gravity and adjusts the corrective forces over the fairly slow integrative feedback component. Switching to position-dependent matrices completely eliminates the constant tracking error, however, inclination errors still occur at the beginning and the end of the motion profile with the same magnitude (see Fig. 18).

Using an empirical approach, the acceleration was correlated with the observed disturbance torque M_z for the c-coordinate. Using a feedback gain of −4.455 kg m and a delay of 1.75 ms to calculate the corrective torque from the acceleration set point. The applied feed-forward control mechanism for systematically occurring disturbances has the same effects as an increased torsional stiffness of the electromagnetic bearing. Accordingly, maximum pitch angle errors in acceleration and deceleration phases were reduced by 75% as demonstrated in Fig. 18.

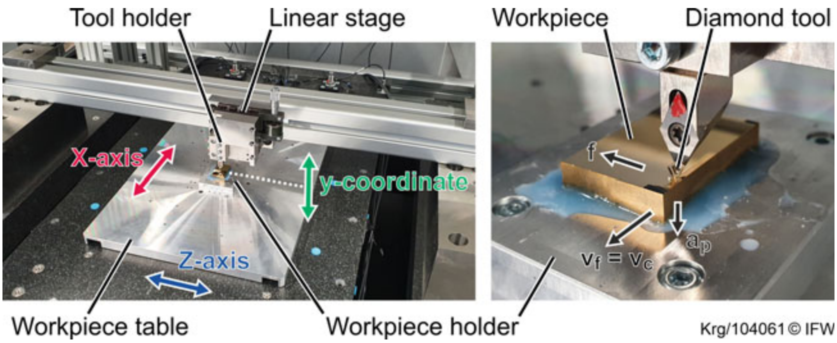

Fig. 19 Experimental setup for diamond machining (planing process with stationary tool)

8 Application in Diamond Machining

For the in-process evaluation of the new electromagnetic linear guide, machining tests were carried out to investigate the impact of the performance figures from Sects. 6 and 7 on the workpiece quality. The purpose of the machining tests was to identify the achievable surface roughness and form deviation at usual and severely increased feed rates. This should clarify whether electromagnetic bearings are basically suitable for ultra-precision machining, and whether they allow for increased productivity of diamond machining processes.

Ultra-precision planing with a stationary diamond tool was specified as the initial cutting process to minimize complexity and interdependencies which would be inevitably introduced with a spindle and a rotating tool. The planing process allows for the machining of single grooves and complete workpiece surfaces as well as individual pockets using the electromagnetic guide's micro-position capability. The experimental setup is shown in Fig. 19 and includes an additional portal with a custom holder for the diamond tool (C0.76mLFCi/0.25 by Contour Fine Tooling, NL) and a manually actuated miniature stage for the coarse adjustment of the depth of cut—fine adjustment of the depth of cut was done with the y-coordinate of the electromagnetic linear guide. The brass workpiece (CuZn40Pb2) was attached to the workpiece fixture with wax.

The cutting parameters for the machining experiments, i.e. line-by-line planing, were varied within the following boundaries:

1. Cutting velocity $v_c = 10 \ldots 6{,}000\,\text{mm}\,\text{min}^{-1}$,
2. depth of cut $a_p = 3 \ldots 15\,\mu\text{m}$,
3. lateral feed $f = 10 \ldots 50\,\mu\text{m}$.

First, machining of single lines with increasing cutting velocity and depth of cut were considered to confirm the stability of the cutting process. Note that the feed rate of the machine axis v_f is equivalent to the cutting velocity v_c for the planing process. Then, single line planing with the above-mentioned parameter range was

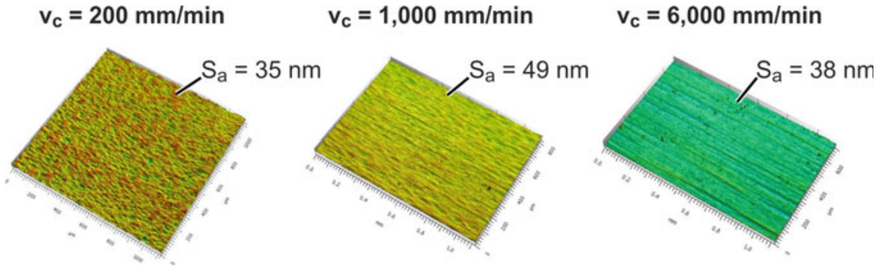

Fig. 20 Surface quality evaluation for workpiece areas machined with different cutting speeds v_c

used to generate individual surfaces on the brass workpiece. Here, the process was designed around the micro-positioning capability of the electromagnetic levitation guide: After the setting process, the levitating slide was raised by a specific amount to create the desired depth of cut a_p; after the cutting motion, the slide was lowered to allow for enough clearance to reposition the workpiece for the next cut. For this, the y-coordinate of the electromagnetic linear guide was configured as a NC-axis, which allowed for interpolated motion synchronized with the main feed axis in X- and Z-direction. With this approach, 3-axis machining was feasible, e.g. for the machining of individual pockets as shown in Fig. 21 on the left. The arithmetical mean height Sa was used to evaluate the surface quality. Figure 20 summarizes the results for three surfaces machined with different cutting velocities (for constant tool engagement conditions with $a_p = 2\,\mu\text{m}$ and $f = 10\,\mu\text{m}$). Notably, regenerative chatter was observed at some point for all cutting velocities. During tool engagement the impact of the process forces was visible in the generalized forces $\boldsymbol{Q}$ of the electromagnetic levitation system, however, vibrations of the levitating slide were not detected. Hence, the cause for the chatter effects rather lies in the structure on the cutting tool side. Since the chatter marks predominantly occurred at the boarder of the machined surface, sufficiently large surface patches without chatter were available to evaluate the surface quality using a confocal microscope of the type Confovis TOOLinspect. Here, the increase of the cutting velocity, i.e. faster slide movement, did not affect the surface quality in a negative way, as the measured mean height was in the same range between 35 nm and approximately 50 nm, see Fig. 20.

Finally, a complete workpiece surface of $20 \times 30\,\text{mm}^2$ was machined using rough cutting ($v_c = 3{,}000\,\text{mm min}^{-1}$, $a_p = 5\,\mu\text{m}$, $f = 10\,\mu\text{m}$) and finishing operations ($v_c = 200\,\text{mm min}^{-1}$, $a_p = 2\,\mu\text{m}$, $f = 10\,\mu\text{m}$), see Fig. 21 on the right. Again, the achieved surface roughness was approximately Sa $\approx$ 40 nm, which appears to be the limit for the experimental setup and conducted cutting investigations. However, it is not clear whether this limitation can be attributed to the electromagnetic linear guide or other machine components (such as the aerostatic bearings or the tool sided machine structure). This issue will be addressed in future machining experiments. Here, different processes (e.g. planing in Z-direction or fly-cutting) can be used to isolate the effects of individual components. Moreover, a reduced lateral feed f in

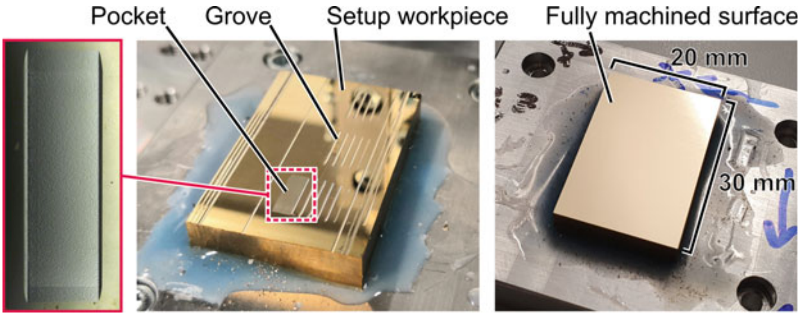

Fig. 21 Individual pocket (left) and fully machined surface (right) using high-precision planing (i.e. single line cutting)

combination with an even further increased cutting velocity v_c presents a promising approach to increase productivity without sacrificing surface quality.

9 Conclusion and Outlook

In the following, the presented content and main findings of this contribution are summarized. Also, the main results are discussed to derive further research question for future research activities.

9.1 Project Summary

This contribution introduced a novel electromagnetic linear guide, which satisfies both precision and stiffness requirements for high-precision diamond machining. First, design considerations were presented to combine functional requirements of electromagnetic bearings and fundamental design principles of precision machine tools. Then, a practical modeling and control design was proposed. After a basic proof of functionality, the new electromagnetic linear guide was extensively tested to obtain key performance figures. Moreover, the actuator and sensor properties of the electromagnetic linear guide were exploited to reduce straightness and inclination errors over the travel path as well as dynamic disturbances in acceleration and deceleration phases. Finally, the electromagnetic linear guide's capability in diamond machining was investigated.

The new electromagnetic linear guide displayed a position noise <23 nm and a positioning accuracy ≤ 300 nm or <1.9 µrad. Using a multi-stage compensation approach, mean straightness errors were reduced to less than 1 µm and inclination errors to less than 2 µrad over a considered travel range of 90 mm. The minimum dynamic stiffness is 1.9 N μm^{-1} at 25 Hz, however, it increases for the desired reference processes up to 166.7 N μm^{-1} at 333 Hz for the high-performance fly-cutting process. The frequency response function of the electromagnetic linear guide exhibits no critical natural frequencies up to 2,300 Hz. Despite the finite stiffness, the maximum inclination errors due to feed forces were effectively reduced by 75 % (to 31 μrad) with a feed-forward control algorithm. To conclude the experimental investigation, the new electromagnetic linear guide was used in diamond machining, achieving a surface quality of Sa $\approx$ 40 nm.

9.2 Discussion and Outlook

While the presented performance figures do not fully satisfy ultra-precision specifications, they are very close to the respective accuracy requirements for ultra-precision components (i.e. form deviations $\leq$100 nm and surface roughness $\leq$10 nm). Apart from the positioning accuracy in the sub-micron range, the new electromagnetic linear guide provides a sufficient dynamic stiffness for diamond machining. Hence, it represents the first electromagnetic levitation system for use in high-precision machining applications. In addition, the presented results demonstrate the capability of electromagnetic linear guides to reduce positioning errors which result from manufacturing or mounting tolerances or other deviations of the underlying machine structure. Also, a feed-forward control was applied to reduce the impact of dynamic disturbance forces while accelerating or decelerating the levitating component. Hence, it is feasible to improve the overall accuracy of the machine axes, e.g. with regard to straightness or inclination errors. In the present case, the travel range was limited to 100 mm. However, the presented compensation approach can be applied to any travel range and can also consider errors from subordinate machine structures, which helps to reduce the required manufacturing and setup effort, especially for long-travel motion systems.

The performance of the electromagnetic linear guide is mainly determined by the resolution and robustness of the integrated sensor system and the delays within the data processing system. Improving the signal-to-noise ratio of the position signal translates to increased position accuracy and reduced noise of the magnetic levitation system. Here, a decoupling of the air gap measurement (which is required to calculate the appropriate coil current based on the force reference) and the coordinate measurement of the levitating slide, e.g. by implementing an additional coordinate frame close to the tool center point) may proof beneficial. Reducing the delay of the data processing system results in faster reaction and increased dynamic stiffness.

Further measures include software-based optimization, e.g. the use of observer-based state space control to reduce the system-inherent signal noise and position uncertainty. The substitution of the PID controller's derivative component with an observer for velocity estimation allows for increased feedback gain, which, in turn, may further improve the dynamic stiffness within the control bandwidth. Note that above the control bandwidth, the frequency response function is mainly determined by the slide's mechanical properties, i.e. mass and structural dynamics. Here, a higher slide mass provides increased stiffness above the control bandwidth limit, but reduces the positioning bandwidth at the same time. Finally, the use of more elaborate models for the feed-forward control mechanism holds significant potential to further reduce systematic disturbances in acceleration and deceleration phases. This, in turn, allows to significantly increase motion dynamics while maintaining accuracy requirements for diamond machining.

References

1. Denkena, B., Kallage, F., Ruskowski, M., Popp, K., Tönshoff, H.K.: Machine tool with active magnetic guides. CIRP Ann. **53**(1), 333–336 (2004). https://doi.org/10.1016/s0007-8506(07)60710-0
2. Denkena, B., Hackeloeer, F., Neuber, C.-C.: 5-DOF harmonic frequency control using contactless magnetic guides. CIRP J. Manuf. Sci. Technol. **2**(1), 21–28 (2009). https://doi.org/10.1016/j.cirpj.2009.07.002
3. Denkena, B., Hackelo, F.L.: Multi-sensor disturbance force measurement for compliant mechanical structures. In:IEEE SENSORS. IEEE (2010). https://doi.org/10.1109/icsens.2010.5690446
4. Denkena, B., Guemmer, O., Floeter, F.: Evaluation of electromagnetic guides in machine tools. CIRP Ann. **63**(1), 357–360 (2014). https://doi.org/10.1016/j.cirp.2014.03.130
5. Denkena, B., Dahlmann, D., Krueger, R.: Electromagnetic levitation guide for use in ultra-precision milling centres. Procedia CIRP **37**, 199–204 (2015). https://doi.org/10.1016/j.procir.2015.08.008
6. Denkena, B., Dahlmann, D., and Krüger, R.: Control system for an ultraprecision electromagnetic linear guide. In: 16th Euspen International Conference & Exhibition. P. 2.16. May 30-June 3, Nottingham (2016)
7. Denkena, B., Dahlmann, D., Krüger, R. : Design and optimisation of an electromagnetic linear guide for ultra-precision high performance cutting. In: byWertheim, R., Ihlefeldt, S., Hochmuth, C., Putz, M. (eds.) Procedia CIRP, vol. 46. pp. 147–150 (2016). https://doi.org/10.1016/j.procir.2016.02.056
8. Denkena, B., Dahlmann, D., Krüger, R. : Experimental investigation of an electromagnetic linear guide for ultra-precision high performance machining. In: 17th Euspen International Conference & Exhibition. Hannover, GER, May 30–June 2, pp. 447–448 (2017)
9. Denkena, B., Bergmann, B., and Krüger, R.: LevitationHigh-performance machining. design & realisation – electromagnetic ultra–precision linear guide. In: Mikroniek, vol. 1, pp. 29–33 (2018)
10. Denkena, B., Bergmann, B., Krüger, R.: Enabling electromagnetic levitation technology for ultra-precision high performance machining'. In: 18th Euspen International Conference & Exhibition. P.2.15. Venice, IT, June 4-8, pp. 161–162 (2018)
11. Denkena, B., Bergmann, B., Krüger, R.: Elektromagnetische Linearführung für die hochpräzise Zerspanung. ZWF Zeitschrift für wirtschaftlichen Fabrikbetrieb **113**(7–8), 443–447 (2018). https://doi.org/10.3139/104.111938
12. Kim, W.-J., Trumper, D.L.: High-precision magnetic levitation stage for photolithography. Precis. Eng. **22**(2), 66–77 (1998). https://doi.org/10.1016/s0141-6359(98)00009-9
13. Lu, X., Dyck, M., Altintas, Y.: Magnetically levitated six degree of freedom rotary table. CIRP Ann. **64**(1), 353–356 (2015). https://doi.org/10.1016/j.cirp.2015.04.107
14. Schönemann, L., et al..: Synergistic approaches to ultra-precision high performance cutting. CIRP J. Manuf. Sci. Technol. **28**, 38–51 (2020). https://doi.org/10.1016/j.cirpj.2019.12.001

15. Stamann, M., Schallschmidt, T., Leidhold, R.: Electromagnetic rotary tables for mill and drill machining. WSEAS Trans. Syst. Control **9**, 199–207 (2014)
16. Weck, M., Wahner, U.: Linear magnetic bearing and levitation system for machine tools. CIRP Ann. **47**(1), 311–314 (1998). https://doi.org/10.1016/s0007-8506(07)62840-6

Spindle Balancing for Ultra-Precision High Speed Cutting

Timo Dörgeloh, Nasrin Parsa, Christian Schenck, Oltmann Riemer, Ekkard Brinksmeier, and Bernd Kuhfuss

Abstract Due to the high resulting centrifugal forces, high speed spindles require an extremely well balanced setup. Within this project, an automatic system for precision balancing of air bearing spindles was developed, which has the potential to supersede manual balancing completely and thus reduce setup times considerably. The scientific challenges of this approach are the measurement and compensation of extremely small residual unbalances, which lie below the detection threshold of conventional sensor systems.

1 Introduction to UP-Balancing and Motivation of the Research

Over the past decades, balancing has played a minor role in ultra-precision machining. The long non-productive times as well as the resulting high costs were accepted by industry, as there was no alternative for this process. However, due to the latest developments of high-frequency spindles, this topic gained new relevance for the performance and robustness of the production process in ultra-precision high-performance machining. The economic efficiency of ultra-precision (UP) processes is also becoming increasingly important due to the growing spread of UP machining in industry. Due to their physical principle, air-bearing spindles have a lower stiffness and load capacity compared to spindles with other bearing technologies. Therefore, air-bearing spindles have to be balanced exceptionally precise in order to prevent

---

T. Dörgeloh · O. Riemer (✉) · E. Brinksmeier
Leibniz Institute for Materials Engineering IWT, Bremen, Germany
e-mail: oriemer@iwt.uni-bremen.de

T. Dörgeloh
e-mail: doergeloh@iwt.uni-bremen.de

N. Parsa · C. Schenck · B. Kuhfuss
Bremen Institute for Mechanical Engineering bime and MAPEX Center for Materials and Processes, University of Bremen, Bremen, Germany
e-mail: parsa@bime.de

C. Schenck
e-mail: schenck@bime.de

E. Brinksmeier and L. Schönemann (eds.), *Ultra-precision High Performance Cutting*,
Lecture Notes in Production Engineering, https://doi.org/10.1007/978-3-030-83765-5_5

damage to the air bearings due to unbalanced rotor displacement on the one hand and to avoid a negative impact on the production result due to vibration excitation of the machine structure on the other [25].

A rotor unbalance generally exists if the axis of mass inertia does not coincide with the geometric axis of rotation. This shift of the mass inertia axis is caused, for example, by imprecise assembly or manufacturing of the rotor. Tool wear also leads to a certain change in the mass inertia axis. An unbalance can be detected by different sensors based on the resulting vibrations. The most common sensors for measuring the vibration amplitude are displacement, velocity or acceleration sensors. The latter have become established in the field of unbalance detection and can detect even the smallest unbalance-induced vibrations of the rotor due to their high sensitivities. However, this sensitivity is not always sufficient. For example, relatively small unbalances at low speeds cannot be measured with sufficient precision. This is due to the low amplitude of the resulting vibration in this range, which is below the detection threshold of the sensors. A correct calculation of the amplitude and phase of the unbalance is therefore not possible.

Balancing of air-bearing spindles in industry is still done manually and requires several iterations, which is uneconomical and should be avoided [15]. Due to the high demands on the balancing quality for protection of the air-bearing, balancing masses in the range of a few µg have to be used. The conventional approach in ultra-precision machining—to use set screws as counterweights—is therefore limiting the achievable balance quality. This applies in particular to the fly-cutting process, in which the rotating tool has a much larger oscillation radius than in ball head milling, in which the same set screw has a much smaller influence on the balancing quality. The high spindle speeds required to achieve higher material removal rates and a reduction in production time in ultra-precision high-performance cutting therefore impose new challenges on the balancing process. Since the centrifugal force has a quadratic growth with increasing angular velocity and the balancing must be performed at operating speed, manual balancing is not suitable for high performance cutting applications in ultra-precision machining. An automatic balancing system with the ability to generate small counterbalances at operating speed is therefore desirable for achieving an optimal surface finish.

However, the common surface roughness parameters are not suitable to describe the finish of optical surfaces adequately and, moreover, do not allow any statement to be made about the influence of certain process variables and parameters on the balancing state [12]. The standard DIN EN ISO 25178 defines further parameters for surface characterization in addition to the classical roughness parameters [10]. Methods such as "Wolf pruning" were successfully used for an alternative description of surface quality. "Wolf pruning" segments a surface into individual regions on the basis of previously defined threshold values of height differences. The number and size of these regions allows the characterization of the investigated surface section. However, even with these additional values for characterization it is not possible to draw detailed conclusions on the influence of individual process parameters such as rotor unbalance [16]. As a result, there is a great need for research on the influences of rotor imbalance, structural and drive dynamics on the generated surface structures and finish in the area of ultra-precision machining [26].

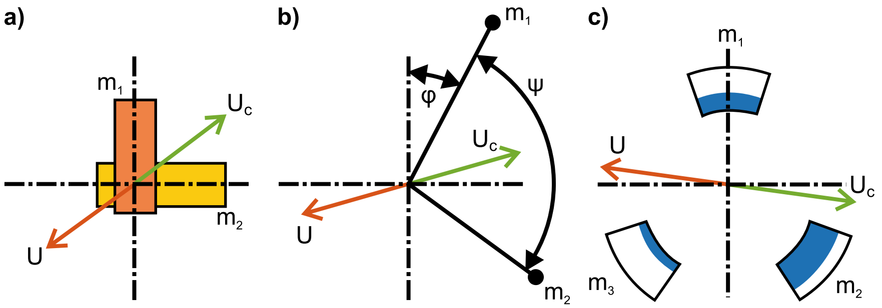

Fig. 1 Balancing an unbalance (U) by generating a counterbalance U_c with multiple masses (m_1, m_2, m_3) **a** by orthogonal mass redistribution (m_1, m_2) **b** by rotary redistribution (ψ, ϕ) of masses (m_1, m_2) **c** by addition or removal of mass (m_1, m_2, m_3) on defined circumferential positions

1.1 Balancing of Ultra-Precision Air-Bearing Spindles

Centrifugal forces and moments in a freely rotating system potentially lead to vibrations with transmission to the bearing. If this is the case, an unbalance is present. Unbalances can be represented graphically as eccentric masses in relation to the rotor axis. A distinction can be made between two types of unbalance, static and dynamic unbalance, whereby these two types usually occur in combination. A static unbalance is present if either the center of mass and the center of rotation or the center of mass and the unbalance of the rotor are in one plane. If center of mass and unbalance are out of plane, this is called a dynamic unbalance. While the static unbalance can be detected and compensated without operating speed of the rotor, the dynamic unbalance requires the rotor to be brought up to operating speed in order to be measured. In contrast, the compensation of the unbalance by adding a counterbalance usually requires the rotor to be stopped to zero speed.

The detection of unbalances of rotating spindles is usually achieved by measuring the resulting vibrations in amplitude and phase. Acceleration sensors are often used as a measuring instrument for this purpose, as they have a very high sensitivity and a high bandwidth. However, force or displacement sensors can also be used, depending on the requirements. If the unbalance in the individual measuring and compensation planes is known, a counterbalance can be realized by adding, removing or redistributing masses m_i on diverse radii r_i using various principles, as shown in Fig. 1.

The resulting vector of the counterbalance $\mathbf{U_c}$ should be as close as possible to the inverse of the measured unbalance $\boldsymbol{U}$ in order to balance the rotor (see Eq. 1).

$$\mathbf{U_c} = \sum m_i \cdot \mathbf{r_i} = -\boldsymbol{U} \tag{1}$$

Depending on the unbalance, the resulting centrifugal forces have a corresponding influence on the radial and axial rotor displacements of air bearing spindles [13].

In various manufacturing processes, these displacements can have a negative effect on the form accuracy and surface quality to a not negligible extent [21]. If the residual unbalance is excessively large, the air bearing of the spindle can be damaged. In order to minimize these negative influences, it is recommended to look into the standard DIN ISO 21940, in which the permissible unbalances for various applications are defined as balance quality grades (cf. Fig. 2).

The balance quality grade represents the maximum permissible angular velocity of the rotor center of mass over the entire speed range. For example, the balance quality grade $G0.16$ represents an angular velocity of $v_{rot} = 0.16\,\mathrm{mm\,s^{-1}}$. According to Eq. 2, the permissible specific unbalance e_p depends on the rotational frequency ω [11] and therefore decreases with increasing rotational frequency:

$$G = v_{rot} = e_p \cdot \omega = \text{const.} \tag{2}$$

whereas in conventional ultra-precision machining, the rotational speeds are in the range of $n = 100\,\mathrm{min^{-1}}$ to $2{,}000\,\mathrm{min^{-1}}$, Ultra-Precision High Performance Cutting (UP-HPC) is aimed at rotational speeds greater than $n = 10{,}000\,\mathrm{min^{-1}}$ in order to achieve increased productivity. If we assume a rotational speed of $n = 20{,}000\,\mathrm{min^{-1}}$, the permissible specific unbalance is $e_p = 0.076\,\mathrm{g\,mm\,kg^{-1}}$ at the balance quality grade $G0.16$ defined in the ISO standard. For the UP-HPC application, it was agreed that a balance quality grade of $G0.064$ should be achieved, which is close to the factory balancing quality of air-bearing spindles [14]. This is the next balancing quality grade after $G0.16$ according to the ISO standard and can be seen in Fig. 2.

At the reference speed $n = 20{,}000\,\mathrm{min^{-1}}$ the permissible specific unbalance for the balance quality grade $G0.064$ is $e_p = 0.03\,\mathrm{g\,mm\,kg^{-1}}$ and can be seen in Fig. 2. The permissible residual unbalance mass m_p according to Eq. 3 with a rotor weight of $m_r = 4.5\,\mathrm{kg}$ and a correction radius $r_c = 60\,\mathrm{mm}$ is therefore 2.25 mg.

$$m_p = \frac{e_p \cdot m_r}{r_c} \tag{3}$$

The most common method for balancing air-bearing spindles in ultra-precision machining is the manual adding or removing of set screws of known weight on the circumference of the rotor (see Fig. 1c). The fact that set screws, even in a size of M3 × 3, still have a weight of approx. 80 mg clearly shows that achieving a residual unbalance mass of 2.25 mg in the manual process is very challenging. Another method which is used is the relocation of two masses on a circular path and is based on the spread angle method shown in Fig. 1b). Since this method requires the use of larger dimensions in order to balance a wide range of residual unbalances, it requires very precise manual adjustment by a few angular minutes or seconds to achieve balancing quality level $G0.064$.

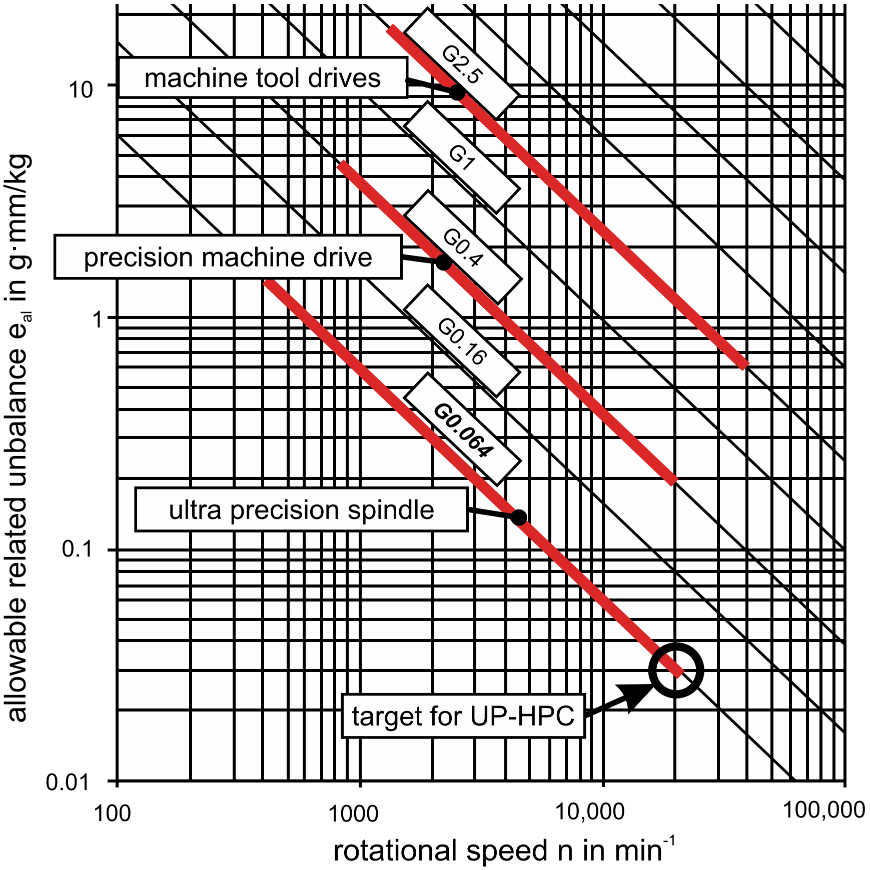

Fig. 2 Balancing grades following DIN ISO 21940 with an extended balancing grade of *G*0.064, in accordance to [11]

1.2 Shock Response of Spindle Rotor and Spindle Housing

Commonly, the unbalances are detected by measuring the vibrations that occur in the housing of the spindle. Due to the air bearing between the spindle housing and the rotor, the impact of unbalances on the rotor and the transfer of this effect to the spindle housing was investigated to verify the capability of unbalance detection by this method. Therefore, the transfer function of the rotating system was identified beforehand.

To remove the effect of feed axis on the vibrations, the spindle was mounted on a granite clamping table. The spindle was tested at different spindle speeds between 0 to 9,600 min^{-1} with 960 min^{-1} increments. To find out the transfer function of the system, the tool holder mounted on the rotor was excited with an impact hammer

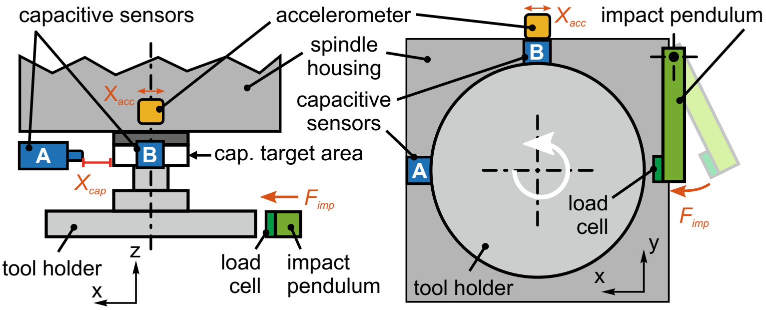

Fig. 3 Experimental setup for shock response measurements [7]

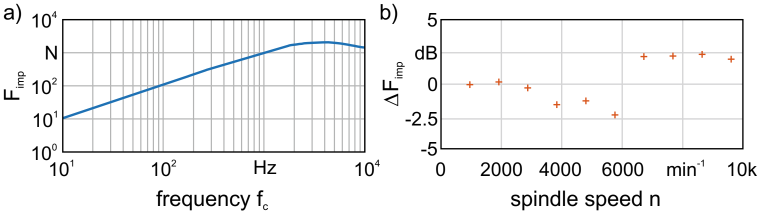

Fig. 4 Impulse signal response and variation of the peak impact force at different spindle speeds [7]

which was mounted on a pendulum. After exciting the spindle by the pendulum, the displacement of the spindle and also the vibrations of the spindle housing were measured.

Figure 3 illustrates the schematic procedure used for the excitation of the spindle. A load cell was used to measure the amount and duration of the impulse signal. To regenerate predefined impulse signals, the displacement of the pendulum was controlled by a mechanical stop. Thus, the resulting impulse duration was about 0.3 ± 0.01 ms and the impact force was approximately 1,200 N. To analyze the impulse signal, the frequency response of the signal was measured at 10 kHz sampling frequency for selected spindle speeds. Figure 4 shows the average impulse signal spectrum and the peak impact force at different spindle speeds.

The displacement of the rotor was measured by two capacitive sensors (see Fig. 3). The sensors which were used in the experimental setup were CPL490 probes from IBS Precision Engineering (Eindhoven, NL). The transfer function was calculated from the impulse signal and resulting vibrations of the spindle. In the next step, the transfer function between the impulse signal and the vibrations on the spindle housing was calculated. To measure the vibrations, two triaxial piezoelectric CCLD acceleration sensors type 4506 manufactured by Hottinger Brüel & Kjær GmbH (Darmstadt, Germany) were applied. They offer a sensitivity of $100\,\mathrm{mV\,g^{-1}}$ and were connected to a charge amplifier type 2692 by the same manufacturer. Sensor A, located in the opposite side of the impact direction, was used for measuring the actual

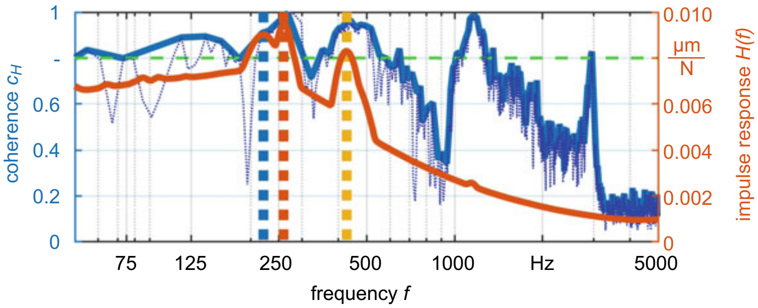

Fig. 5 Average normalized shock response spectrum $H(f)$ and the coherence c_H of sensor A with eigenfrequencies at 250 Hz, 260 Hz and 425 Hz. A minimum value of 0.8 (green dashed line) is accepted for the coherence function [7]

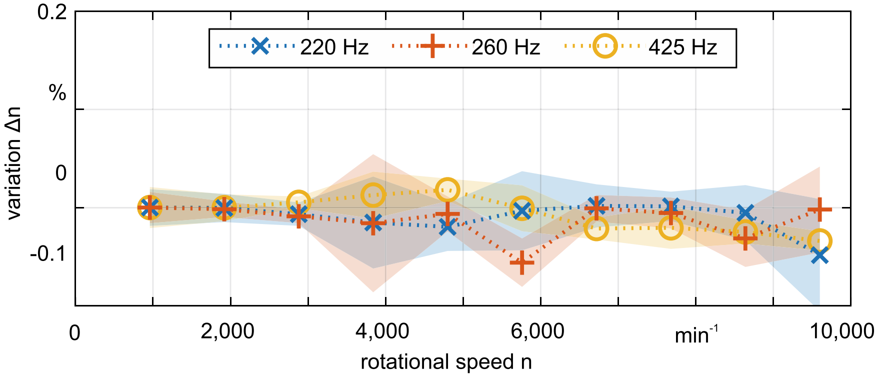

Fig. 6 Effect of spindle speed on impulse response. The spindle speed did not influence the dynamic behavior of the rotor [7]

impulse response, whereas sensor B, positioned perpendicular to the impact signal, was applied for identifying the direction of the vibration. The average shock response spectrum $H(f)$ of sensor A is shown in Fig. 5 together with the corresponding coherence function c_H and the identified eigenfrequencies.

A good coherence ($c_H \geq 0.8$) for the impulse response of sensor A was detected up to 600 Hz. In addition, three eigenfrequencies at 250 Hz, 260 Hz and 425 Hz, could be identified in the impulse response signal. In order to assess the effect of different spindle speeds on the impulse response the measurement was repeated for different spindle speeds while monitoring the amplitudes of the eigenfrequencies (see Fig. 6). As no significant dependency was found, this result suggests that the spindle speed did not influence the dynamic behavior of the rotor.

Furthermore, the impulse response of the acceleration sensor on the spindle housing was evaluated. The first analysis showed that the X-axis of the acceleration sensor was affected by the impulse signal due to the alignment of the sensor. The average impulse response and the coherence function of the X-axis is shown in Fig. 7.

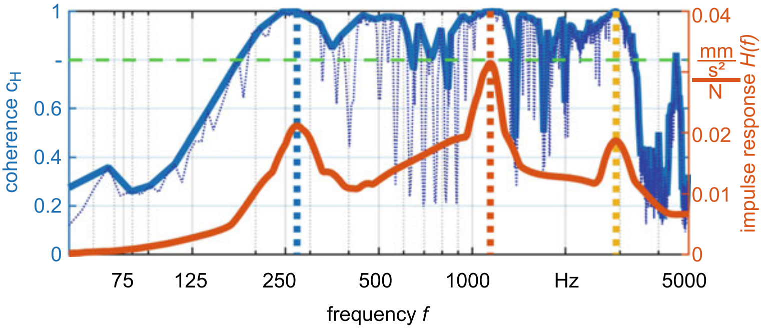

Fig. 7 Average normalized shock response spectrum $H(f)$ with eigenfrequencies at 274 Hz, 1,150 Hz and 2,900 Hz and coherence c_H of the accelerometer (minimum value of 0.8 is accepted for the coherence function) [7]

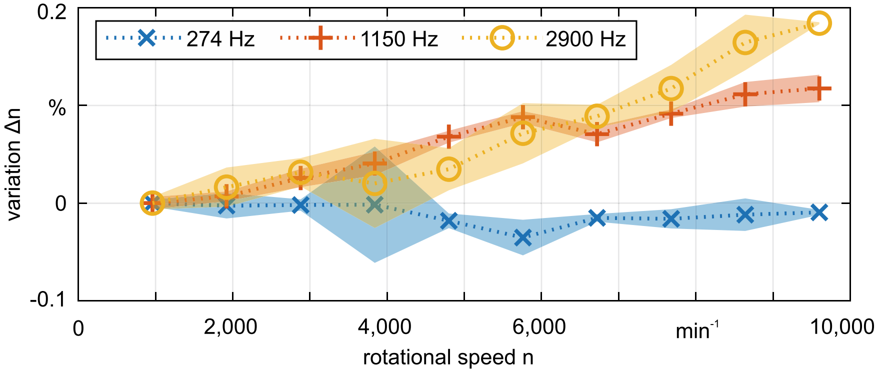

Fig. 8 Effect of spindle speed on the amplitude of three significant eigenfrequencies identified in impulse response measurements [7]

The coherence function exceeds 0.8 only at frequencies higher than 200 Hz indicating that the vibration of spindle housing in this range was caused by the excitation of the rotor.

The impulse signal shows three eigenfrequencies at 274 Hz, 1,150 Hz and 2,900 Hz. To check the effect of the spindle speed n on the impulse signal, the amplitudes of the eigenfrequencies were monitored after changing the spindle speed (see Fig. 8). It can be seen that the amplitude of the lower eigenfrequency (274 Hz) is nearly leveled off and remains unaffected by the spindle speed. However, the variation at higher frequencies increased and consequently the transfer function must be regarded as a function of the spindle speed n.

In conclusion, it can be stated from these experiments that the displacement measurement by capacitive sensors is suitable for frequencies lower than 425 Hz, while the typical setup of an accelerometer on the spindle housing is a better solution for the identification of unbalances at higher frequencies. Because measurement of the

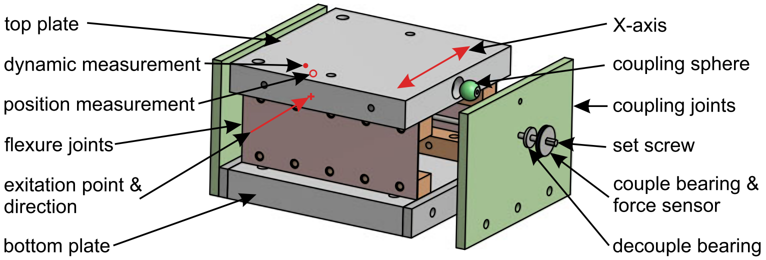

Fig. 9 Structure of the coupling system [6]

low frequencies is essential for balancing the spindle at typical operation speeds, the capacitive measurements would be the preferable choice. However, these measurements are significantly more expensive (in terms of equipment) and delicate in handling. Therefore, they are not generally suitable for industrial application [7].

2 Amplification of Vibrations for Measuring Tasks by Using Flexible Couplings

One possibility to improve the unbalance detection by using acceleration sensors is a temporary mechanical amplification of the unbalance excited vibrations at the spindle housing by changing the dynamic stiffness between spindle housing and machine frame. This approach was realized by a coupling system with tunable stiffness, based on a flexure joint concept (Fig. 9).

2.1 Experimental Setup

The coupling system basically consists of a top and a bottom plate connected via flexure and coupling joints (Fig. 10). The coupling joints are attached to the bottom plate and adjusted by set screws to switch between an operational state (coupled) and a setup state (decoupled).

In the operational state, the top plate is connected to the bottom plate by the flexure joints and clamped in place it via the coupling joints, effectively restricting a lateral motion along the X-axis. This connection resulted in a high stiffness state between spindle and the base. The dynamic behavior of the system changed in the setup state by disconnecting the coupling joints from the top plate. In this state, the bottom and top layer are only connected via the flexure joints allowing limited motion along the X-axis.

To ensure a repositioning with high precision, the coupling spheres are fixed to the coupling joints with individually shaped joint sockets using a polymer/metal

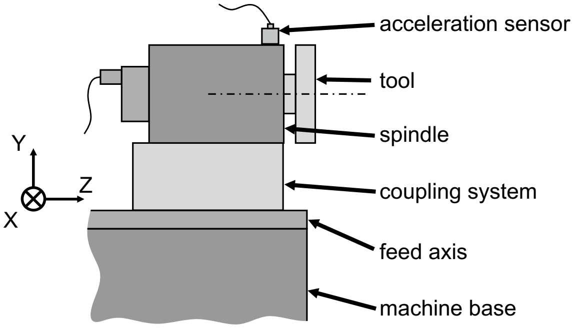

Fig. 10 Implementation of the coupling system [6]

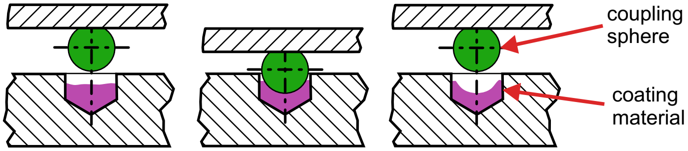

Fig. 11 Adjusting joint sockets to coupling spheres at the top plate by coating material (Moglice) [8]

compound (Moglice), see Fig. 11. For changing the coupling state, the coupling spheres are pressed into the joint sockets with a setscrew. The setscrew is additionally equipped with a force sensor to measure the applied clamping force.

The clamping force was measured by a piezoelectric sensor 1-CLP/62kN (Hottinger Brüel & Kjær GmbH, Darmstadt, Germany) with a sensitivity of $-4.3\,\text{pC}\,\text{N}^{-1}$ and a maximal load of 62kN using a Kistler 5007 amplifier (Kistler Instrumente GmbH, Sindelfingen, Germany) with an uncertainty of about ±50 N. Dynamic properties of these two states were examined as well as the repositioning of the plates after each experiment. The displacement of the top plate along the X-axis was measured using a ML10 laser interferometer (Renishaw plc, Wotton-under-Edge, UK) with a resolution of 1 nm. An accelerometer sensor (Hottinger Brüel & Kjaer with sensitivity of $1\,\text{mV}\,\text{ms}^{-2}$ and 2 to 7,000 Hz working frequency) was used to measure the vibration. The experiments were carried out in two phases. At first, the dynamic properties and feasibility of the designed structure was tested. Subsequently, the positioning accuracy during re-coupling was determined.

2.2 *Measurement of Dynamic Properties*

In both states, operational and decoupled, the system was excited by an impulse hammer at the same position. For analysis, the normalized frequency response was calculated. Figure 12 shows the final impulse response of the system in two different stiffness states.

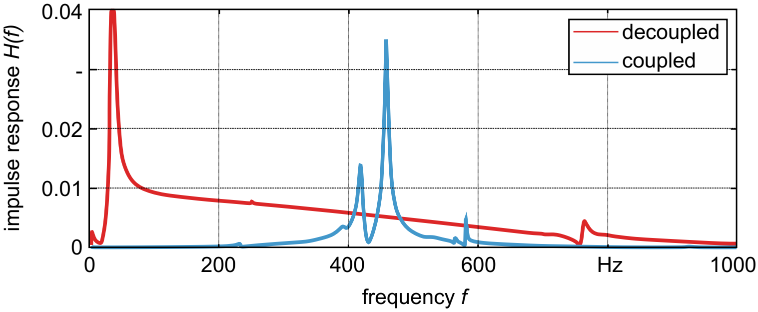

Fig. 12 Impulse response of two states of the system [6]

Three major characteristics were detected from the impulse response. First, the peak amplitude in the setup state is higher than the operational state by a factor of 28.3. Second, the frequency with the highest value in the operational state is about 485 Hz, however, in the setup state the frequency is shifted down to 35 Hz. And finally, in the setup state there are only two eigenfrequencies, whereas in the operational state three eigenfrequencies can be detected.

2.3 Repeatability of the Coupling

Two tests were carried out to analyze the state and dynamic performance of the system after each change of state. At first, different amounts of coupling forces were applied to detect their effect on the dynamic behavior and repositioning of the system (cf. Fig. 13a). It was found that the first and second eigenfrequencies remained relatively constant (cf. Fig. 13b); however, there is a considerable change in the third eigenfrequency at about 500 Hz, which is linearly dependent on the applied coupling force. In other words, instead of measuring the coupling force directly, it may be

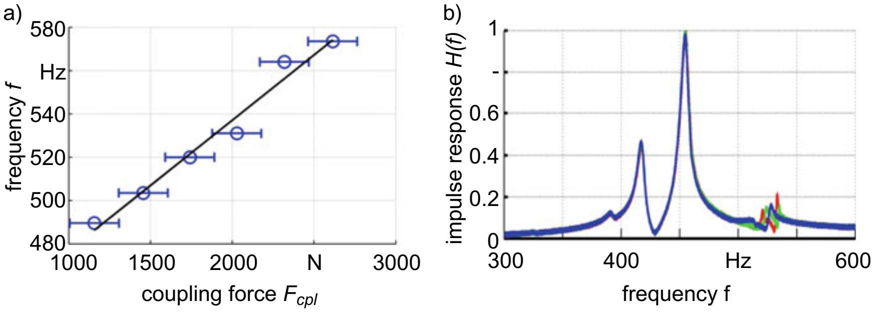

Fig. 13 Shift of the third eigenfrequency by changing the coupling force [8]

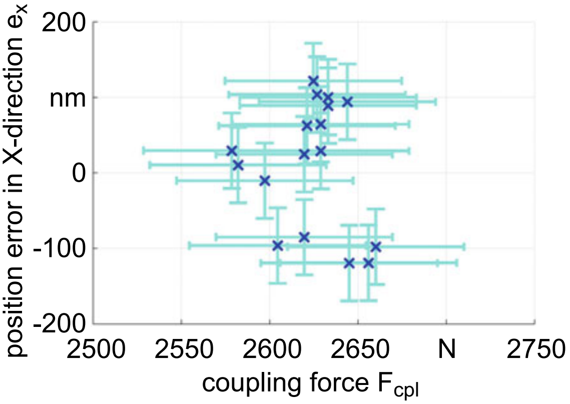

Fig. 14 Repositioning uncertainties of the plates with applying same amount of force [8]

controlled by tuning the third eigenfrequency to achieve more precise and more repeatable results (Fig. 13).

In order to test the repositioning to the operational state, the coupling force was kept constant within the uncertainty of the force sensor (2,600 N ± 50 N). The accuracy of the repositioning was determined by measuring the displacement between two coupled states to -12 ± 84 nm (Fig. 14). This precision should hold for many applications. Otherwise, the more sophisticated method by eigenfrequency controlled clamping is applicable.

2.4 Applicability of Coupling System for Spindle Balancing

In order to test the suitability of the coupling system for the balancing process, tests were carried out in the two operational states of the system. For this purpose, a spindle was mounted on the coupling system and regular balancing was carried out up to a point where the residual vibrations remained below the detection threshold of the sensors. The system was then changed to the setup state, which amplified the residual unbalance-excited vibrations. By further balancing in this state, the residual unbalance could be reduced even further, see Fig. 15. The results clearly demonstrate the suitability of the newly developed method for use in ultra-precision machining.

3 Balancing Concepts for UP-HPC

Automatic balancing systems are widely used in conventional milling or grinding operations. The conventional systems can balance the rotor within a few milliseconds sufficiently to achieve the required unbalance tolerances. However, these systems are unsuitable for ultra-precision machining, because they do not achieve the required

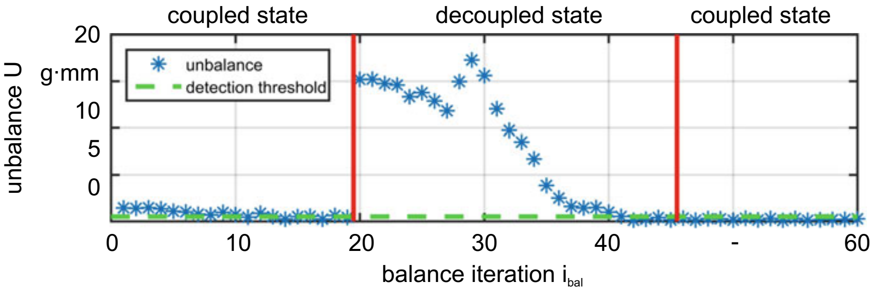

Fig. 15 Balancing process with application of the developed coupling system [6]

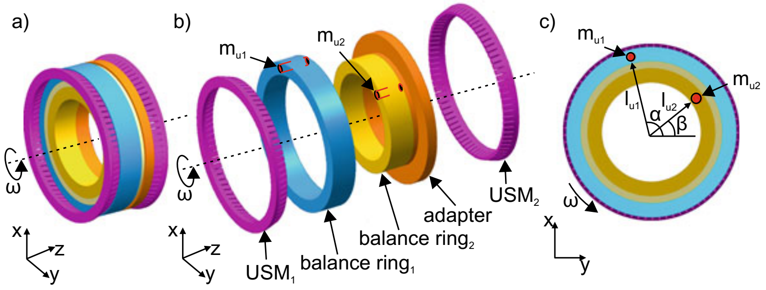

Fig. 16 Rotatory redistribution concept by two ultrasonic motors on the rotor of the working spindle; **a** exploded view, **b** assembly drawing, **c** angular positions of masses [9]

balancing precision or cannot be adapted without affecting the process. Since the most common systems in conventional machining are based either on the spread angle method or fixed-position correction via liquid media, these two methods were investigated with respect to their performance and balancing precision in two prototypes of a balancing system.

3.1 Rotary Mass Distribution via Ultrasonic Motors

The first concept of an automatic balancing system enables to balance the spindle with the use of a rotatory redistribution concept. In the designed setup, the position of the two masses m_{u1} and m_{u2} can be changed while the spindle is running without changing their distance from the center of the rotor. Therefore, a ring-shaped ultrasonic traveling wave motor was applied (Fig. 16).

The masses and their distance from the center were designed so that the following formula is satisfied:

$$|\mathbf{l}_1| \cdot m_{u1} = |\mathbf{l}_2| \cdot m_{u2} \tag{4}$$

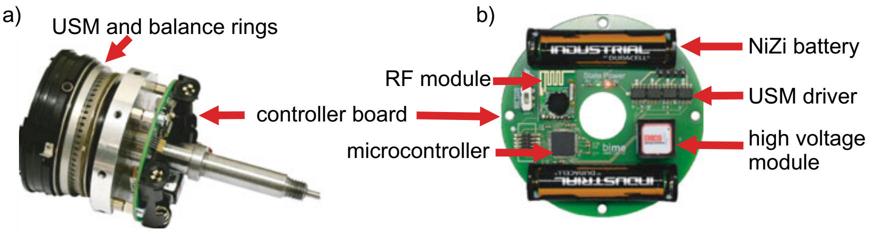

Fig. 17 Experimental setup with one ultrasonic motor: **a** assembled system **b** controller board [9]

where the specific masses m_{u1} and m_{u2} are connected to the respective balance rings at the specific vectors ($\mathbf{l_1}$ and $\mathbf{l_2}$) [17].

Each balance mass produces its specific centrifugal force. By changing the positions of the masses, the total centrifugal force can be varied. The balance force is calculated by the sum of the vectors:

$$F_u = \omega \sum_{n=1}^{2} \boldsymbol{l_n} \cdot m_u \tag{5}$$

where ω is the angular velocity of the spindle.

The balance masses can be shifted independently and by changing the position, the direction and amount of the resultant force vector can be adjusted for compensating the unbalances on the spindle. With an angular offset of $|\alpha - \beta| = 180°$ the centrifugal forces compensate each other, resulting in no effective unbalance. If both balancing masses are located in the same direction ($\alpha = \beta$), the maximum balancing force is generated [9, 23].

Setup and Operation Principle

The control board on the rotor consists of a microcontroller, a frequency module (RFM) for receiving signals from the operator, a driver responsible for controlling the ultrasonic motor rotation and a power supply (Fig. 17). In the following, a brief explanation about the major components which were used in the control board is presented.

The precision of the balancing system is determined by the smallest angular increment. Therefore, an ultrasonic motor from an autofocus camera lens was chosen for rotary distribution of the masses, i.e. to drive balance rings. This type of actuator already features a ring-shaped geometry with multiple piezoelectric elements working in two interleaved groups and allows for tiny rotational movements. By applying an electric voltage, the piezo elements are mechanically strained against the balance ring. Using two traveling wave signals provided by a microcontroller to drive the two groups of actuators, this strain is converted to a rotary motion. While the motor is powered off, the balance ring is self-locked by the preload force (see Fig. 18) [9, 22]. The amplitude and phase of the applied signals from the microcontroller regulate the

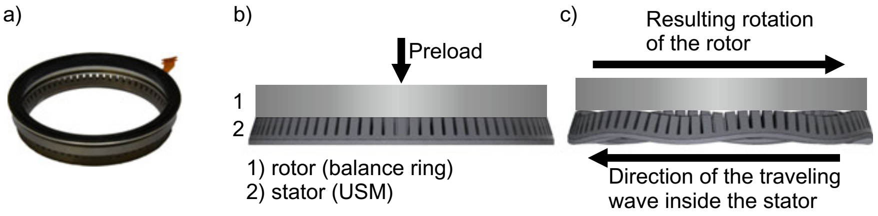

Fig. 18 Ultrasonic motor: **a** overview, **b** idle state, **c** in motion [9]

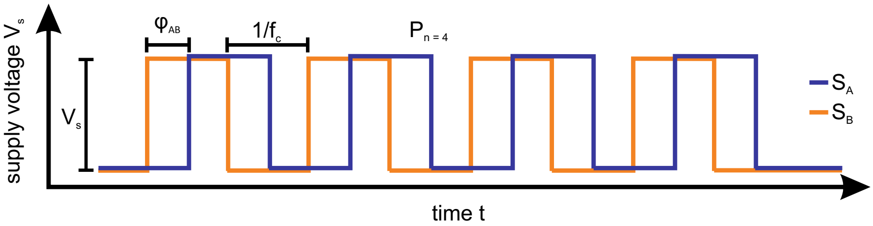

Fig. 19 The controlling signals from the microcontroller for motor driver [9]

mechanical strain of the piezoelectric elements on the stator and hence the rotational speed and direction of the rotor.

Two different signals are applied to the rotor to produce the traveling wave motion, SA and SB (Fig. 19). The traveling wave is generated in the piezoelectric elements due to the phase shift between these signals. This results in a rotational motion due to the frictional force, which pushes the rotor (balance ring) in opposite direction of the traveling wave propagation [20]. The phase shift ϕ_{AB} between the signals can be adjusted between 90° and −90° to change the direction of the rotation. Furthermore, some additional factors affect the operation of the motor such as the frequency of the signals f_c and the number of commutation pulses that are sent to the ultrasonic motor P_n [9].

The required supply voltage for the ultrasonic motor should be higher than 40 V. In the experiments, the generated signal from the microcontroller was adjusted by four operational amplifiers (LTC6090 by Linear Technology, Milpitas/CA, USA). These amplifiers were applied as motor drivers to transform the low current outputs of the microcontroller to the required supply voltage for the ultrasonic motor. Two NiZi-batteries were applied as basic energy supply. The required voltage was produced by a boost converter up to 100 V. Finally, the output of the boost converter was regulated and stabilized by eight 22 μF ceramic capacitors.

For sending and receiving signals from the operator to the motor, two RFM73 transceiver modules from HopeRF (HOPE Microelectronics CO., Ltd., Shenzen, China) were used for the experimental setup. This module works in the 2,400–2483.5 MHz frequency band. One RFM module was installed on the spindle. Due to the rotatory motion of the spindle, the Doppler effect to the sending and receiving signals should be taken into account. In general, the Doppler effect constraints the selection of the component to design the system and is defined as:

$$f_0 = \frac{v}{c} f_0 = r \cdot \frac{\omega}{c} f_0 \tag{6}$$

where v is the circumferential speed of the spindle, $c \approx 3 \times 10^8\,\mathrm{ms^{-1}}$ is the propagation velocity of radio frequency signals, $f_0 = 2.4\,\mathrm{GHz}$ is the carrier frequency, $r = 20\,\mathrm{mm}$ is the distance from the center of the rotor and $\omega = 470\,\mathrm{rad\,s^{-1}}$ is the angular velocity of the rotor. The maximum amount of calculated frequency shift which is produced by Doppler effect is equal to $f_{0_{\max}} = 11.3\,\mathrm{Hz}$. This value is small compared to the operational frequency and therefore, the Doppler effect can be neglected.

The applied microcontroller was an ARM PSoC5 from Cypress Semiconductor. It controlled the ultrasonic motor by sending signals to the driver of the ultrasonic motor (USM) as well as controlling the communication between the operator and the USM motor. Producing of a pulse signal is time-consuming when the (CPU) of the microcontroller is engaged in the signal generation. Hence, it can affect the speed and the quality of the system operation. To avoid this problem, universal digital blocks (UDBs) of the PSoC5 were utilized which allowed for executing small operations and commands without using the CPU. Therefore, the pulse signals could be produced in UDB while CPU was busy with communication [9].

Experimental Validation of Balancing System
In order to verify the feasibility of ultrasonic motor for balancing the spindle, the generated torque by the USM (M_u) and its ability for shifting the balancing mass and the accuracy of the step size for the balancing system were analyzed. In addition, the ability of the ultrasonic motor to keep the balancing mass in the desired location during rotation of the spindle as well as capability of the USM to shift the balancing mass based on the defined step sizes were examined. The behavior of the ultrasonic motor was analyzed while changing different parameter values when the spindle was stationary. Figure 20 and Fig. 21 show the torque (M_u) and rotation angle (γ) for changing supply voltage (V_s), commutation pulse numbers (P_n) and commutation frequency (f_c). The rotation angle was measured with a laser triangulation sensor (optoNCDT 2300 by Micro-Epsilon Messtechnik GmbH & Co. KG, Ortenburg, Germany). During the measurements, one of the three parameters was varied while the others were kept constant. The standard parameters values were:

$V_s = 80\,\mathrm{V}$,
$P_n = 35$ and
$f_c = 31.5\,\mathrm{kHz}$.

The phase difference (ϕ_{AB}) remained constant at 90° during the measurements [9].

The effect of the supply voltage on the measured torque of the ultrasonic motor is illustrated in Fig. 20a. When the voltage falls below 40 V, the motor is not able to rotate and the resulting torque is 0. From 40 to 60 V, the torque increases considerably

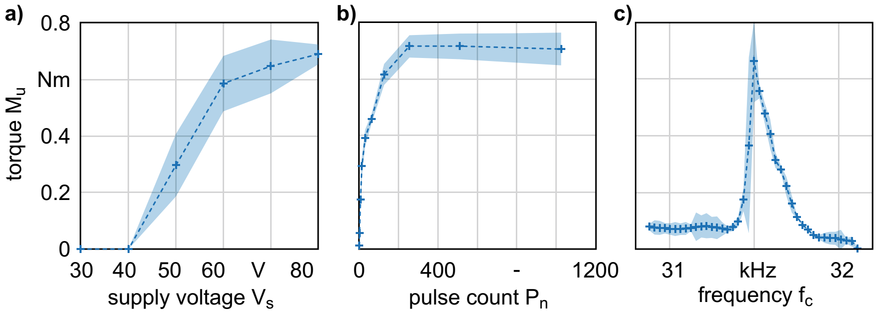

Fig. 20 Measurement of torque by changing the parameters with indication of threefold standard deviation: **a** supply voltage, **b** pulse number, **c** frequency [9]

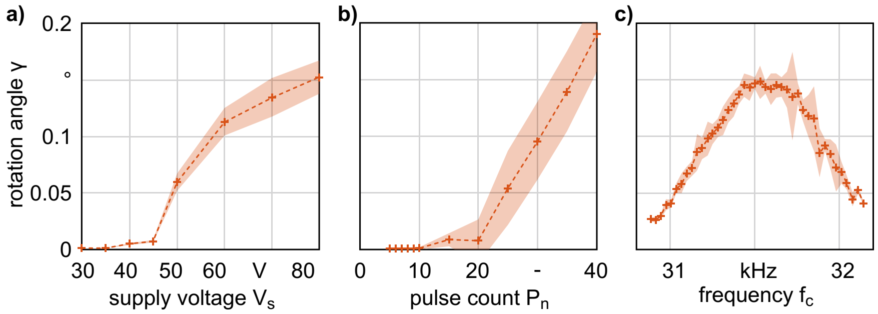

Fig. 21 Measurement of rotational angle by changing the parameters with indication of threefold standard deviation: **a** supply voltage, **b** pulse number, **c** commutation frequency [9]

from 0 to about 0.6 Nm. By increasing the supply voltage from 60 to 80 V, the curve eases off towards about 0.7 Nm torque.

The effect of commutation pulse number on the torque of the motor is shown in Fig. 20b. The commutation pulse number was varied from 2 to 1,024 pulses. At first, there is a sharp increase in torque when the commutation pulse number is increasing from 2 to 256. By further increasing the pulse number, the torque was stabilized to a constant value.

Finally, the effect of the commutation frequency can be seen from Fig. 20c. The frequency was varied from 29.8 to 31.4 kHz. The torque raises suddenly at 31.4 kHz, afterwards, it drops slightly to less than 0.1 Nm at about 31.8 kHz. The effect of parameters (V_s, P_n and f_c) on the step size is shown in Fig. 21.

When the supply voltage was lower than 40 V, there was no rotation of the motor. Increasing the voltage supply increased the rotation angle up to about 0.15° at 80 V. Investigating the commutation pulse number showed that very small step sizes (about 0.01°) could be achieved with $P_n \approx 15$. The curve shows a steep rise from $P_n = 20$ to $P_n = 40$ as it is illustrated in Fig. 21b.

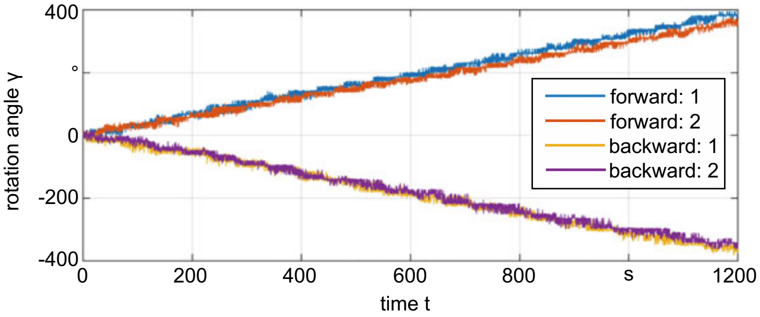

Fig. 22 Changing of angular position of the balancing mass during the rotation of the spindle [9]

To observe the effect of commutation frequency on the rotation angle, the frequency was varied from 29.8 to 32.2 kHz. By increasing the frequency to 31.5 kHz, the rotation angle was increased gently and reached its maximum value at about 0.17°. With higher values, the curve is decreasing again.

To analyze the capability of the ultrasonic motor for changing the balance state of the spindle and its accuracy, the operation of the ultrasonic motor was observed during the rotation of the spindle. The experiments were performed at $\omega = 150\,\mathrm{rad\,s^{-1}}$ ($1{,}432\,\mathrm{min^{-1}}$). The balancing state was changed with a balance mass $m_u = 2.1$ g at a radius of 30 mm which provided a balancing capacity of 63 g mm. The position of the balance mass was detected by two external photoelectric sensors with one of the sensors detecting the angle of the balance mass (ϕ_b) and the other detecting the angle of the experimental setup (ϕ_e). As a result, at constant rotational speed, the angle of the balance mass could be measured ($\alpha = \phi_e - \phi_b$).

Furthermore, the supply voltage was set to $V_s = 64$ V, the commutation frequency to $f_c = 31.5$ kHz, the commutation pulse number to $P_n = 100$ and the phase of controlling signals was kept constant at −90°. The experiment was repeated four times and each time with 600 commutation pulse packages (each with $P_n = 100$). After every 30 packages, the motor was stopped for 10 s to test the ability of the motor for holding the balance mass in the desired position. In parallel, the balance state of the spindle was measured with a “Vibrobalancer 41” by SCHENCK RoTec GmbH.

Experimental Results

Figure 22 shows the rotational shift of the counter mass and the resulting balance state during rotation of the spindle. It can be seen that the ultrasonic motor is able to rotate the balance mass in both direction and hold it in its position during the rotation of the spindle.

Initially, the balancing process was performed with one USM to change the balance state by shifting one balance mass to change the direction of the unbalance force. Hence, the initial unbalance of the system could not be fully compensated. The measured vibration of the spindle relative to the rotor position is shown in Fig. 23.

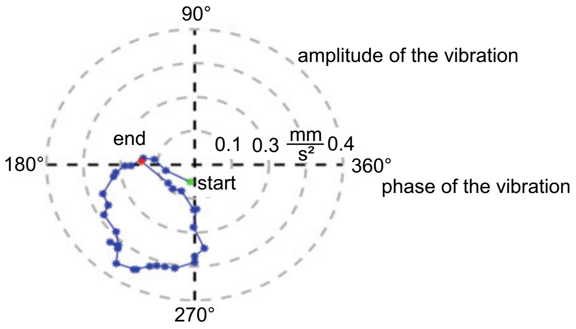

Fig. 23 Measurement of changing balancing state in terms of amplitude and phase of the vibrations of the spindle during the rotational shift with one USM [9]

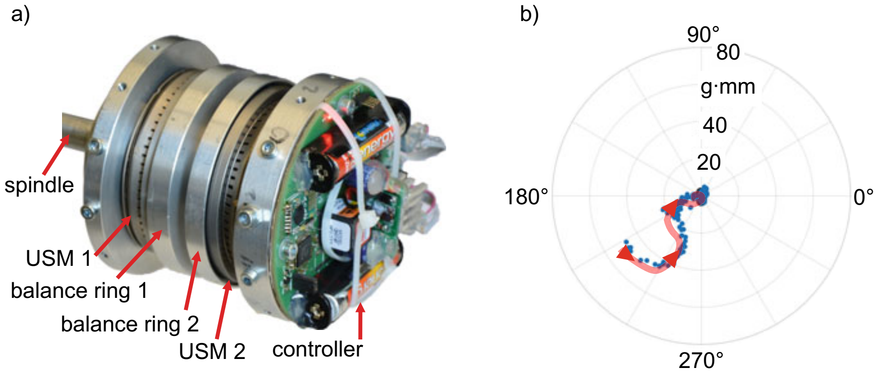

Fig. 24 Balancing with two ultrasonic motors: **a** setup, **b** measured balancing state

The experimental setup was able to change the balance state of the spindle by changing the position of the balance mass. In addition, the system was able to balance the spindle to 0.055 g mm by adjusting the balance mass with the amount of 2.1 g, which is better than ISO grade (0.064 g mm) [9].

In the next step, the experiment was applied with two USM to demonstrate the full balancing capability. In this setup, the balancing force could be adjusted more precisely due to the second balance mass (see Fig. 24a). The experimental results showed that the system was able to reach the balance state of less than 0.04 g mm.

3.2 *Mass Removal via Microfluidic Actuator*

A balancing concept used in industry for many years is based on adding fluidic masses to predefined tanks. This concept is realized, for example, in conventional grinding applications by patented fluidic balancing systems [1]. For this purpose, the cooling lubricant required in the grinding process is injected into the balancing system in a controlled amount via nozzles during rotor rotation. As soon as the spindle stops, the

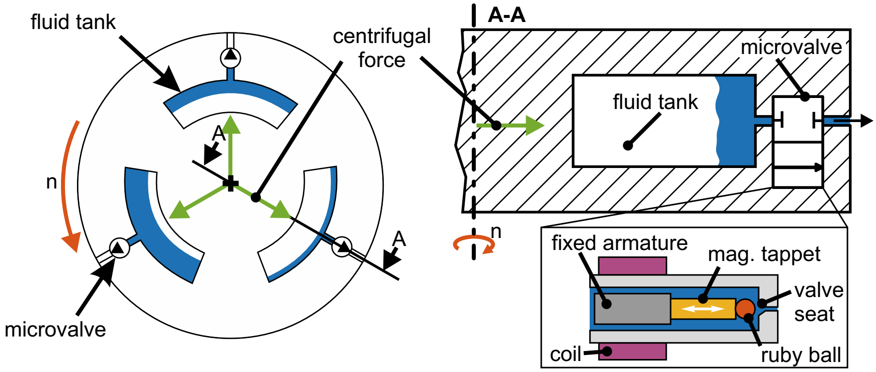

Fig. 25 **a** Scheme of a face-mounted microfluidic balancing disk, **b** working principles for the microvalve during spindle rotation

fluid is released via the open design of the system and must be re-injected during a re-balancing process.

Concept and Preliminary Analyses

In general, such balancing systems are primarily designed for use on hydrostatic or roller bearing spindles in order to compensate large unbalances as quickly as possible. Due to the large installation space of the systems, the low balancing precision and the inability to keep the balancing state, however, they are unsuitable for use on air-bearing high-frequency spindles in ultra-precision machining. In contrast, a spindle-mounted subtractive balancing system, in which a fluid is evacuated from pre-filled chambers, has not been utilized or considered in both conventional and ultra-precision machining. In addition, by using sealed tanks, the balancing condition could be kept for future use, eliminating the need for re-balancing after spindle restart.

For the above-mentioned designated balancing grade of $G0.064$ for UP-HPC machining, a subtractive balancing system has to be able to extract masses in the order of approx. 1 mg. Therefore, the concept of a microfluidic balancing system is presented below, which achieves this balancing precision by means of microvalves [3]. In order to open the selected microvalve, which is based on the principle of electromagnetism, a magnetic tappet inside the valve has to be pulled against a fixed armature, thus retracting a ruby ball positioned in a sapphire glass insert (valve seat). As soon as the electromagnetic field can no longer hold back the tappet, the valve closes as an integrated spring pushes the ruby ball back into its seat. This mode of operation has the advantage that the valve is additionally pressed into the seat by the fluid and centrifugal force acting during rotation. Therefore, an increased leak resistance is expected. The schematic design of the microfluidic balancing system with three evenly distributed microvalves on the circumference is shown in Fig. 25. In the three fluid tanks located behind the valves, the fluid forced outwards by centrifugal force is shown schematically.

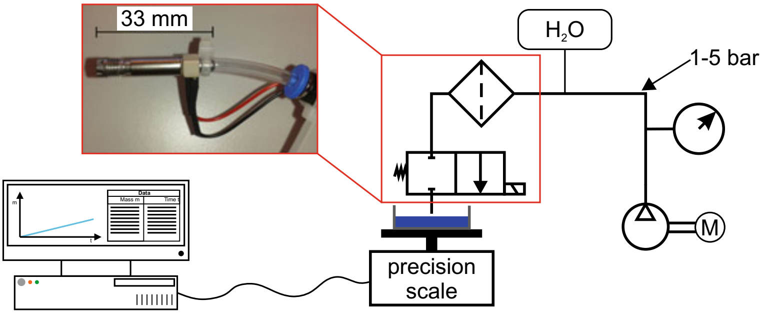

Fig. 26 Schematic drawing of the experimental setup and devices applied for the microvalve

To determine the achievable balancing precision of the microfluidic balancing system, the minimum amount of transported fluid was measured under different experimental conditions in a static test setup. Distilled water was used as fluid to be transported in the experiments, as this should have a negligible effect on process safety. The microvalve was connected to a tube filled with distilled water and supplied with compressed air (see Fig. 26). By varying the pressure of the compressed air from 1 to 5 bar in the experiments, centrifugal force conditions at different rotation speeds which act on the fluid are simulated. The opening times of the microvalve were varied from 0.1 to 50 ms in the experiments and the transported fluid mass was detected by a digitally readable precision scale (see Fig. 26).

Figure 27 shows the average values of the transported masses of 1,000 valve openings over the varying opening times. The results show that a precise dispensing of <1 mg can be achieved with the valve under all test conditions. With an opening time of 0.1 ms to 0.5 ms and a supplied air pressure of 1 to 5 bar, a mass of minimum 0.065 mg to maximum 0.21 mg per valve opening was transported. Starting with a valve opening time of 1 ms, a linear behavior with a proportional increase of the opening time can be recognized at all air pressures. It can also be seen that a proportional increase in air pressure is not accompanied by a proportional increase in the transported mass. This suggests that a saturated state would result if the air pressure continues to increase. These properties simplify the creation of a characteristic curve in the control concept. The results in Fig. 27 imply that an automatic balancing system with the tested microvalves has the potential to achieve a balancing quality of at least $G0.064$ for air-bearing spindles.

Prototype Design for an Automated Precision Hydrobalancer

Based on the previous findings, a prototype of an automatic balancing system was designed [4]. Various boundary conditions were defined for the suitability of the balancing system for use in ultra-precise high-speed cutting. Three main conditions should be fulfilled:

1. Wireless communication with a master computer, which sends the commands to open the individual valves to create a defined counterbalance in amplitude and phase.

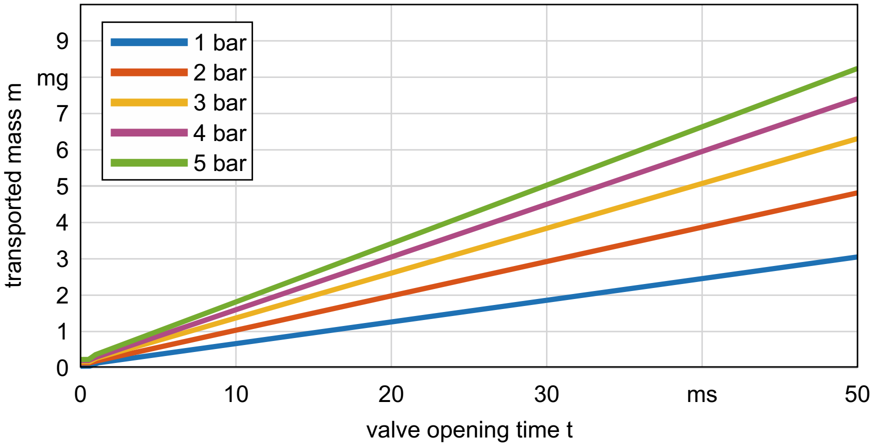

Fig. 27 Measurement of the transported fluid by varying the applied pressure and the release time of the electromagnetic valve

2. Integrated power supply, e.g. in order to avoid sliding contacts or mercury baths for the power supply. These systems would not have a tolerable influence on the rotor behavior and would also mean increased installation costs.
3. Achieving a balance grade of $G0.064$ at a cutting speed of $v_c > 2{,}000\,\mathrm{m\,min}^{-1}$ to enable in-process balancing in ultra-precise high-speed cutting.

In Fig. 28 the prototype of the automatic balancing system is shown. The balancing system uses three microvalves, which are evenly distributed at 120° intervals on the circumference of the outer surface. This minimum number of valves is sufficient for balancing due to the dosing precision shown in Fig. 27 and saves both weight and installation space. Nickel-zinc accumulators are placed on the circuit board, which supply the valves and the microcontroller with defined voltage and current via voltage converters. The microcontroller based on an ATMEL ATmega328 chip receives the opening commands of the valves from the master computer via a wireless 2.4 GHz radio interface. In addition, three tool holders were mounted on the base plate, one of which can be used in the machining process while the other two are implemented to maintain symmetry and will not contain a cutting edge. In comparison to the USM system, low voltages are sufficient to control the valves, which leads to a longer operating time due to the lower power consumption.

Experimental Validation

The performance of the balancing system was investigated by semi-automatic balancing experiments. Based on the calculated amplitude and phase, the corresponding valve was opened to discharge a certain amount of fluid from the tanks. The execution of the tests is based on the manual balancing process, i.e. the spindle speed was gradually increased in order to protect the air bearing from damage due to large unbalance-induced centrifugal forces. However, in contrast to the manual

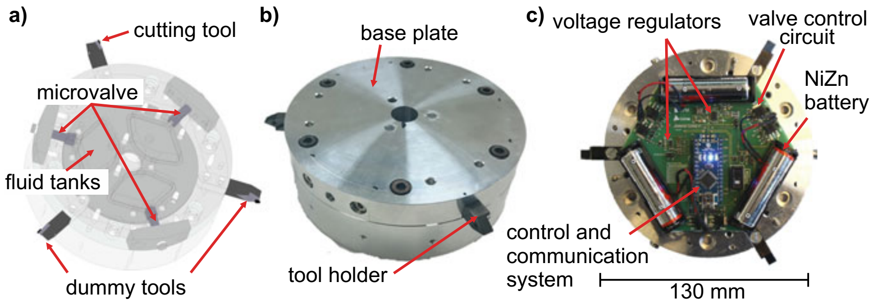

Fig. 28 Prototype of the automatic balancing system based on electromagnetic microvalves: **a** CAD design, **b** fully assembled system, **c** PCB inside the balancing system with mounted components

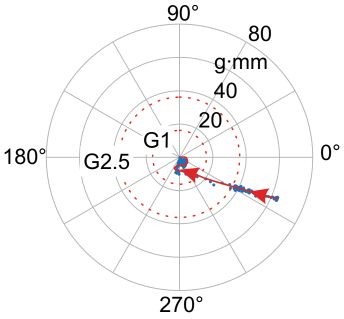

Rotational speed	3,000 min^{-1}
Rotor weight	4.5 kg
Balancing concept	fixed position
Initial balance state	G4.4
Final balance state	G0.02
Initial unbalance	63.22 g·mm @ 337.14°
Final unbalance	0.29 g·mm @ 325.44°

Fig. 29 Balancing protocol of a semi-automatic balancing procedure, achieving a balance state of $< G0.064$ at $n = 3{,}000\,\text{min}^{-1}$

balancing process, it is no longer necessary to stop the spindle in between balancing steps. This semi-automatic procedure already allows time savings of up to 75% compared to manual balancing (manual: 60 min; semi-automatic: 15 min). At $n = 3{,}000\,\text{min}^{-1}$, the defined balancing quality level of $G0.064$ is already over-achieved with the present prototype balancing system, which can be seen in Fig. 29.

Both of the investigated balancing concepts proof to be sufficiently suitable for the automatic balancing of air-bearing spindles. The balancing concept with the ultrasonic motors convinces by its speed and the elimination of the application of any additional masses. However, the high voltage power supply for the ultrasonic motors is not yet sufficient to guarantee their use in a fully functional system.

The microfluidic balancing system convinces by its superior balancing precision and the easier control by low voltage. It is on the other hand limited in its total balancing capacity as the pre-filled tanks ultimately will be depleted after a certain number of procedures. Nevertheless, due to its precision and practicability, the concept of the microfluidic balancing system will be further investigated in the following chapter and transferred to a fully automatic balancing system.

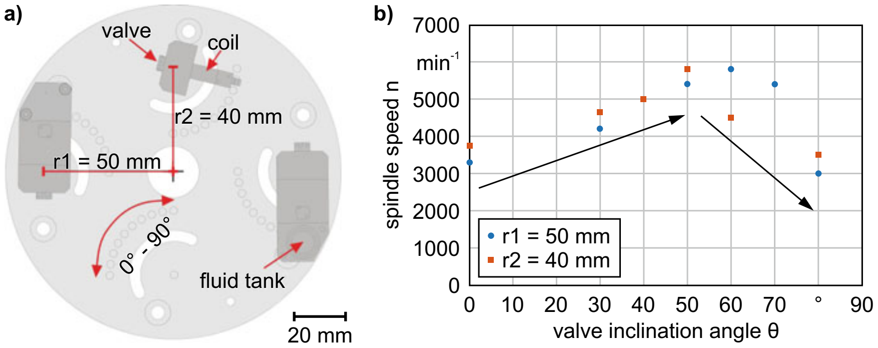

Fig. 30 **a** Concept drawing of the test tool with multiple possible valve inclination angles and two radii, **b** Maximal achievable rotational speed *n* at specific valve inclination angle θ

Fully Automatic Balancing with Microfluidic Actuators

Preliminary tests have shown that the valves of the microfluidic balancing system can only be opened up to a spindle speed of 3,000 min^{-1}. At higher speeds, the centrifugal force acts against the force provided by the electromagnetic field of the coils and thus the mobile armature for opening the valves can no longer be pulled back, leaving the valves closed. Possible solutions are either to increase the magnetic field, to reduce the balancing speed or to reduce the centrifugal force acting on the opening behavior of the valves. Since an increase of the magnetic field would not be possible without a development of new coils and a reduced balancing speed is not appropriate, the best approach was seen in the reduction of the centrifugal force acting on the mobile armature.

Therefore, it was investigated at which angle of inclination, relative to the lateral surface, the valve still opens and closes reliably. For this purpose, a test base plate was used in which the angle of inclination of the valves can be varied from 0–90° on two different radii (see Fig. 30a). The results of the test displayed in Fig. 30b show the maximum achievable speed at which the valve at a given inclination angle reliably opens and closes. It can be seen that the maximum speed of $n = 5{,}800\ \text{min}^{-1}$ is achieved at an angle of inclination of 50° for $r_2 = 40$ mm and at 60° for $r_1 = 50$ mm. At an angle of inclination $\geq 60°$ the valve could be opened, but it did not close after the voltage was removed. Presumably, the centrifugal force caused the mobile armature to lock up so that it could no longer bounce back.

Revised Hydrofluidic Balancing System

For a revised version of the balancing system a radius of 40 mm and an angle of inclination of 50° was therefore specified for the placement of the valves in order to maximize the achievable speed. Furthermore, additional requirements were defined for the second version of an automatic balancing system with the aim of easier handling and an increased performance.

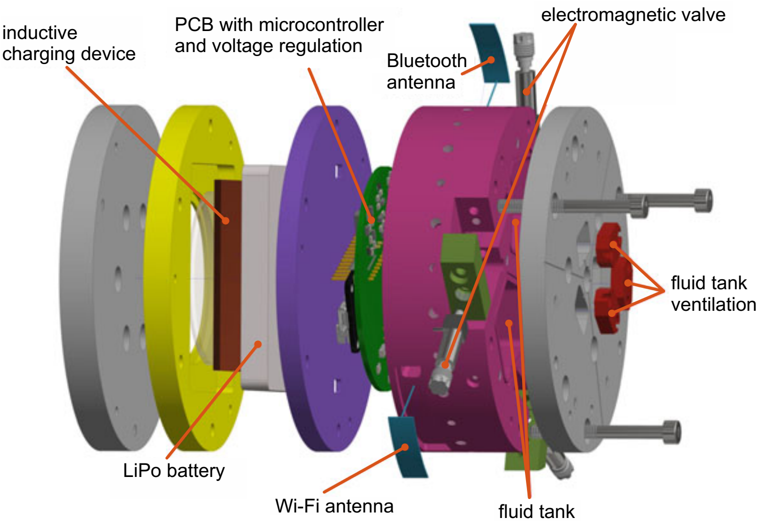

Fig. 31 Explosion drawing of the automatic balancing system for air-bearing spindles

1. Replacement of the nickel-zinc accumulators with a lithium-ion polymer (LiPo) battery, which requires less installation space.
2. Integration of a charge controller and wireless charging station so that the system does not need to be opened to change or charge the battery.
3. Connection of the balancing system to a cloud-based service in order to facilitate the exchange of measurement data.
4. Control and monitoring of the balancing system via an application for mobile devices to improve usability in a shop floor environment.

The implementation of the requirements in the hardware can be seen in Fig. 31. The explosion drawing shows the valves positioned in 50° angle, the new LiPo battery, the contactless charging interface, as well as the Bluetooth and Wi-Fi antenna for communication with the cloud based service.

By connecting the balancing system to the Internet, data can be exchanged between several systems. Figure 32 shows the schematic structure of the interface control. After the user has started the balancing process, the unbalance is measured, evaluated and the corresponding control commands are sent to the cloud. Here the microcontroller, which is mounted on the spindle, picks up the data and opens the corresponding valves. While the valves are open, the unbalance is continuously monitored and the measured data is graphically displayed to the user in the computer application and his mobile device. If the balancing process fails, the user can stop the balancing process and stop the spindle.

To ensure a smooth data transfer between both microcontrollers, a data structure based on semaphores is used. Data is only transmitted or retrieved if a corresponding signal is transmitted. As long as, for example, the valves in the automatic balancing

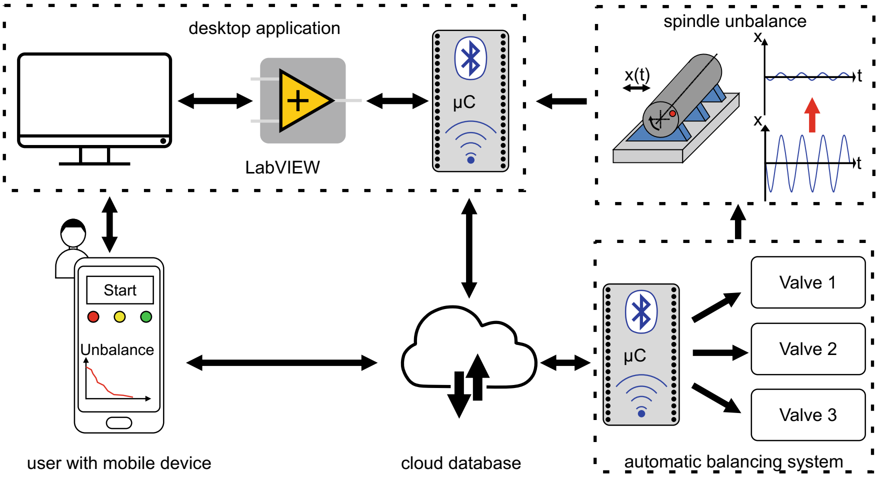

Fig. 32 Schematic structure of the interface control between balancing device and operator

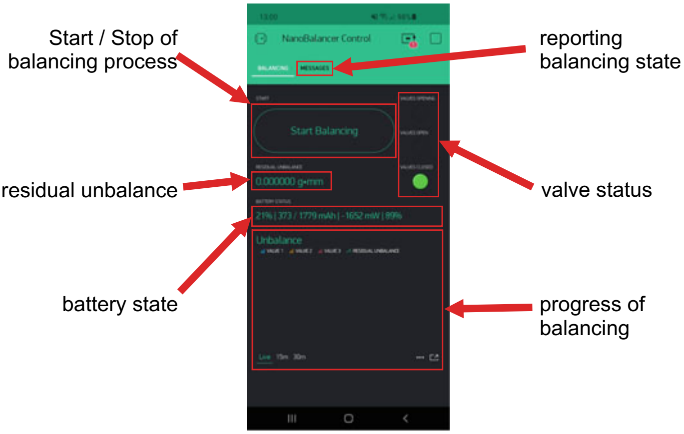

RESIDUAL UNBALANCE
0.000000 g·mm

BATTERY STATUS
21% | 373 / 1779 mAh | -1652 mW | 89%

Fig. 33 Application interface displaying the operator the balancing state and further information e.g. the battery status

system are open, no new opening commands are requested, as the microcontroller of the balancing system does not issue a permission. These states are signaled to the user via a traffic light display in the application as seen in Fig. 33. The user can also monitor the state of charge, discharge rate and battery health in the application.

The complete balancing process will be started by the operator by pressing the "Start Balancing" button and can be stopped by pressing the same button with the switched caption "Stop Balancing". When the balancing process is finished, a report function can be used to send the balancing result and history to the operator by mail.

4 Control System for Automatic Balancing Systems

The control system is a decisive component in the automatic balancing process. The goal is that the balancing process takes place with as little user intervention as possible that and the risk of bearing damage is avoided. For these reasons, a control system based on the graphical programming system LabVIEW from National Instruments was developed, which also offers the possibility to communicate with the systems of the other developments within the FOR1845 and thus provides an easy integration into the overall system. Due to the design principle of air-bearing spindles and the assumption of a rigid rotor behavior in the intended speed range as presented from Cao et al. [2], the influence coefficient method can be used to determine the unbalance. Furthermore, due to the design of the existing spindles, it is only possible to balance in one plane, as no access to the rear part of the rotor is provided.

To determine the influence coefficients for conventional balancing in one plane, two test runs must be carried out, between which the spindle must be stopped and accelerated again. During the first test run, the spindle is accelerated to operating speed and a measurement of the vibrations generated is carried out by the balancing measuring system. Then the spindle is stopped and a test mass is applied at a defined location. The amount and the position of the attached test mass is then transferred to the measuring system and a measurement is done at operating speed again. The influence coefficients can then be calculated from these two measurements. Using these coefficients, it is known how much mass must be attached or removed at which position on the rotor to compensate the unbalance.

In addition to this method, the control system enables a determination of the influence coefficients at runtime without stopping the spindle to be used with the automatic balancing system (see Fig. 34). This method uses the defined release of fluid to generate the required trial mass. The time advantage of this method is obvious, since the spindle does not have to be stopped to generate the test mass and calculate the coefficients. Once the coefficients have been calculated, they are stored in a file and loaded into the control system when required. Since the influence coefficients only include the system state at a certain speed, a new influence coefficient matrix must be calculated for a changed speed. In conventional balancing, this would imply multiple manual starts and stops of the spindle and the application of test masses. With the control system in automatic balancing, the rotational speed can easily be adjusted and the generation of the influence coefficients can be carried out automatically if no influence coefficient matrix has been previously generated.

A special feature of the control system is that it enables a fully automatic balancing process up to the desired operating speed. In Fig. 35 the flowchart of an automatic balancing process is displayed. If it is possible to control the rotational speed of the air-bearing spindle via an interface, the target operational speed for the machining process can be directly entered. The automatic balancing process then starts at a low speed for pre-balancing and the speed is incrementally increased until the operational speed is reached, while the unbalance is monitored in the individual intermediate steps and any required adjustments are automatically carried out.

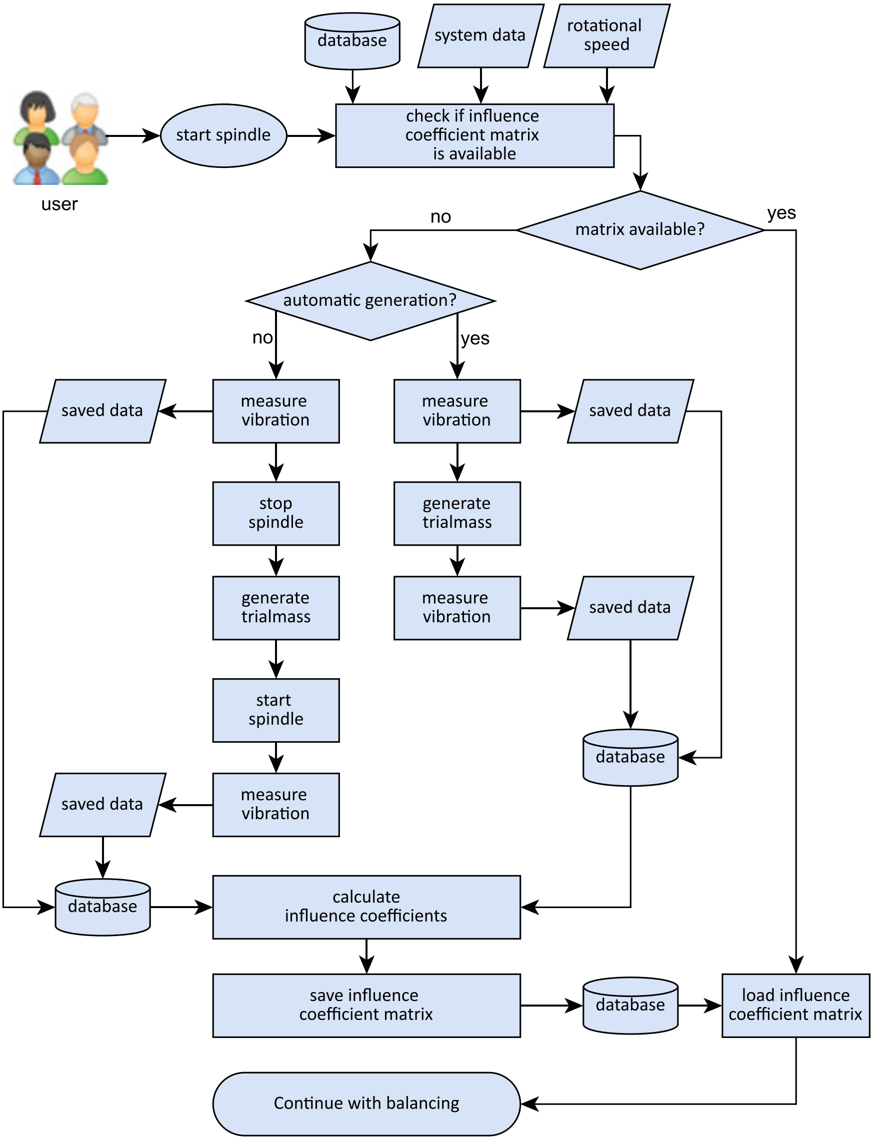

Fig. 34 Flowchart of an automatic generation of influence coefficients

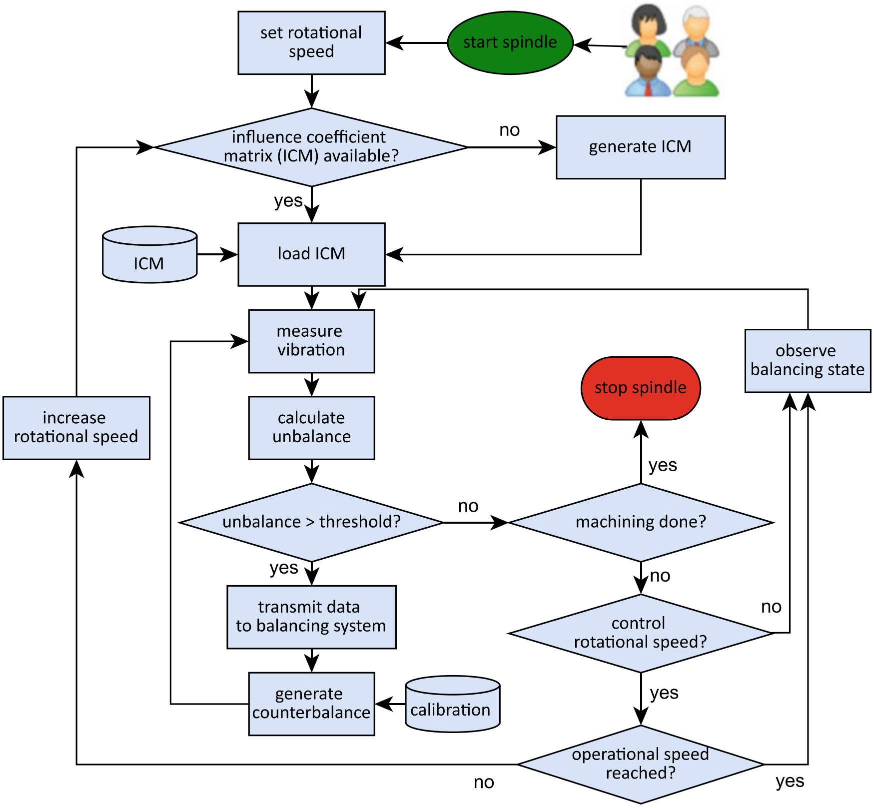

Fig. 35 Flowchart of an automatic balancing process for static or variable rotational speed

4.1 *Validation of the Automatic Balancing Process*

The validation of the system was separated into multiple parts. For testing the functionality and precision of the microvalves at different speeds, the automatic balancing system was mounted on a 4R air-bearing spindle by Professional Instruments Company (Hopkins/MN, USA). This spindle is able to provide a maximum rotational speed of 7,500 min^{-1} at a radial and axial bearing stiffness of approx. 80 $\mathrm{N\,\mu m}^{-1}$ and 230 $\mathrm{N\,\mu m}^{-1}$, respectively. The experimental setup is displayed in Fig. 36. As in previous investigations, the unbalance-induced vibrations are detected by acceleration sensors with a sensitivity of 1,000 $\mathrm{mV\ g}^{-1}$ and forwarded to the measurement system. The assignment of the measurement data to each revolution is enabled via a trigger sensor. A high system stiffness is achieved by mounting the air-bearing spindle to a granite measuring table via fixtures.

In Fig. 37 the resulting unbalance changes ΔU for varying rotational speeds are displayed for each electromagnetic valve. These data were used to calculate a regres-

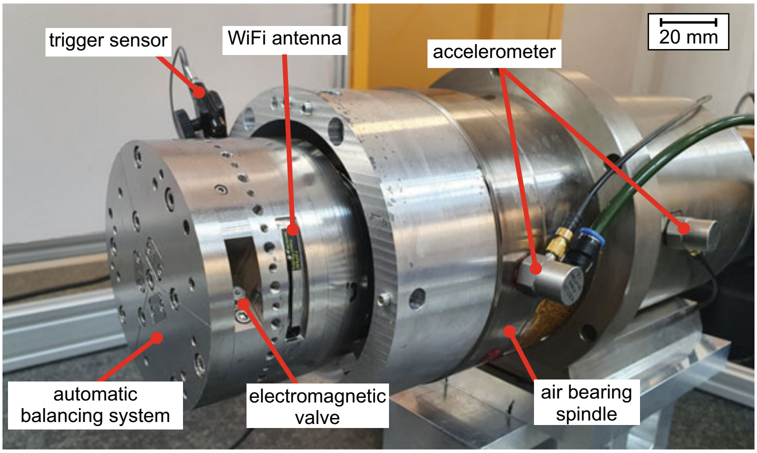

Fig. 36 Experimental setup for testing the automatic balancing system on an air bearing spindle

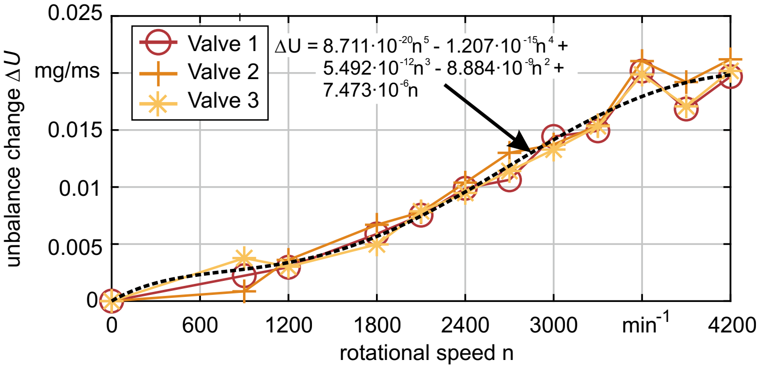

Fig. 37 Resulting unbalance change at varying rotational speeds for each electromagnetic valve and the calculated regression function

sion function for the valves to be saved in the control system. Due to the proximity of all results, a single regression function is sufficient and can be used for all valves in the automatic balancing procedure. This function enables an assignment of the mass to be removed with respect to a rotational speed and is taken as the reference for calculating the valve opening time.

4.2 Results

The results of the balancing tests of the new control system with the new automatic balancing system are shown in Figs. 38, 39 and 40 as residual unbalance U versus the

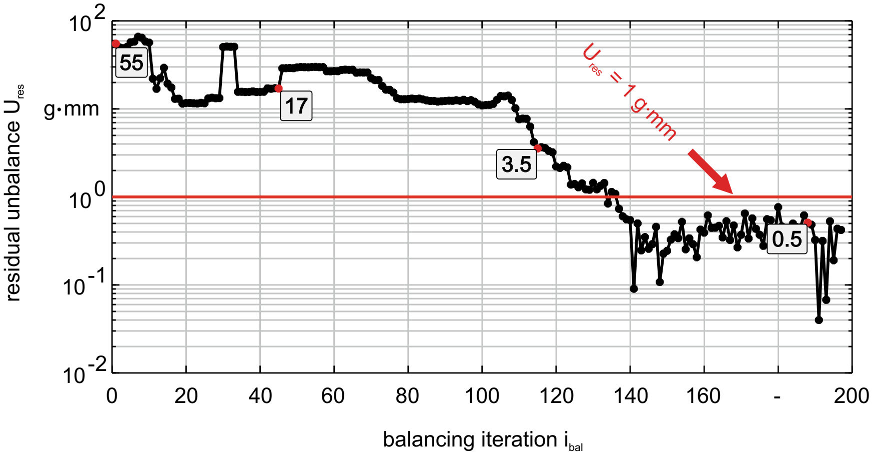

Fig. 38 Automatic balancing of a Professional Instruments 4R air-bearing spindle at 1,800 min^{-1}

balancing iteration i_{bal}. The first test was a pre-balancing at low speed. At this point, it is essential that large unbalances are reliably reduced to an acceptable value. The limits of the rotational speed and the unbalance to be achieved depend on the spindle used, since the bearing stiffness is the decisive factor here. For the spindle used in the experimental setup, a rotational speed of n = 1,800 min^{-1} and a permissible residual unbalance of $U \leq 1$ g mm were defined. With this residual unbalance, it is possible to safely accelerate to higher rotational speeds and perform precision balancing. The results of the first test are shown in Fig. 38.

As the results in Fig. 38 illustrate, pre-balancing is possible in a process-safe manner. Even if an incorrect measurement leads to an overcompensation of the unbalance, this is eliminated in the subsequent balancing iterations. After the pre-balancing was carried out at n = 1,800 min^{-1}, the next step was to select a speed that was significantly higher than that of the pre-balancing. Therefore, the next test was an automatic balancing at a rotational speed of n = 4,200 min^{-1}. The target for the residual unbalance to be achieved was chosen to be $U < 0.065$ g mm. The results of this test are shown in Fig. 39.

After a residual unbalance of $U = 0.88$ g mm was detected, the residual unbalance was successively reduced to $U \approx 0.046$ g mm. When this value of the residual unbalance is reached, it is possible to accelerate the spindle up to the operating speed without any risk of damage to the air bearing.

The next test is to investigate up to which maximum rotational speed the automatic balancing system can reliably operate. In the preliminary tests in paragraph 3.2, it has been shown that the microvalves can operate at 50° up to a rotational speed of n = 5,800 min^{-1}. However, in Fig. 40 it can be seen that at a rotational speed of n = 4,500 min^{-1} the functionality is no longer given.

The results show the measured residual unbalance while a valve opening between the seventh and eleventh measurement iteration at which the valve was unable to

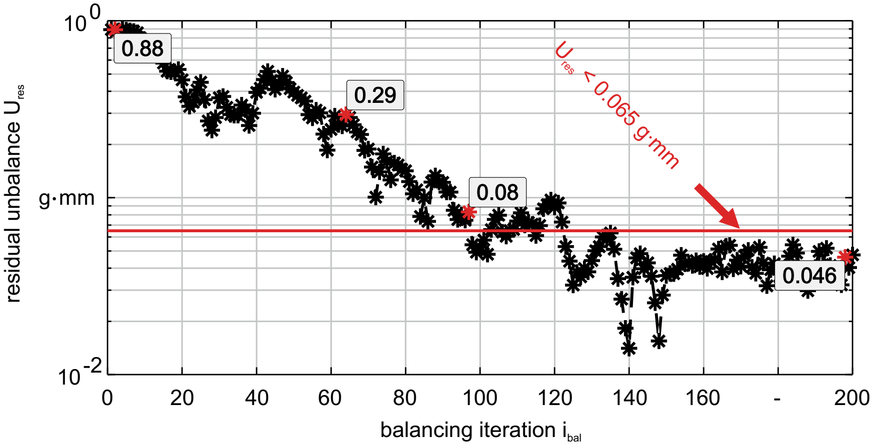

Fig. 39 Automatic balancing of a Professional Instruments 4R air-bearing spindle at 4,200 min^{-1}

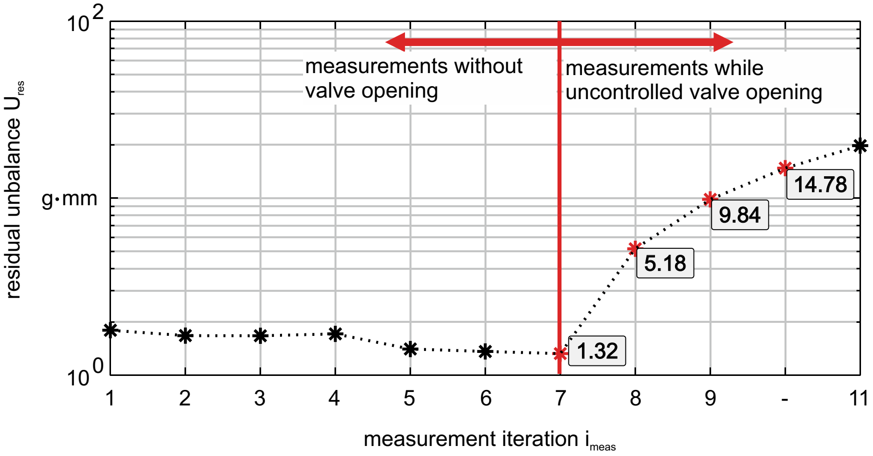

Fig. 40 Valve opening with the automatic balancing system at 4,500 min^{-1} on a Professional Instruments 4R air-bearing spindle

close. This result is surprising since the angle and radius of the preliminary tests were adopted in the final system. However, this is not a problem for reliable balancing the air-bearing spindle, since the unbalance-induced vibrations can already be detected safely and reliably with the acceleration sensors at 3,000 min^{-1} $< n <$ 4,500 min^{-1}.

The results of the balancing experiments show that a safe balancing is possible with the automatic balancing system in combination with the control system.

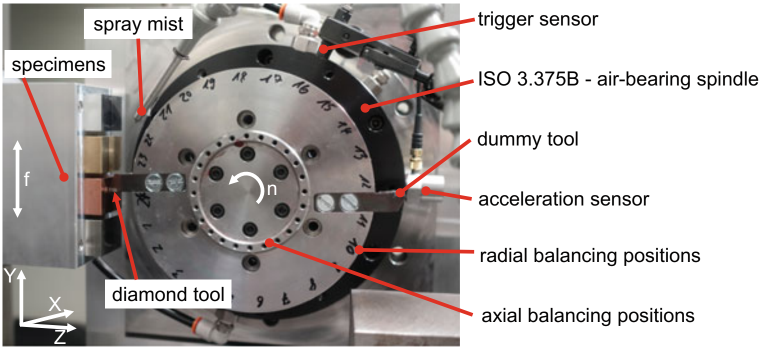

Fig. 41 Experimental setup for fly-cutting experiments with ISO 3.375B spindle on Moore Nanotechnology 350 Freeform Generator

5 Influence of Unbalance on Surface Generation

In order to be able to evaluate which balance grade is sufficient for ultra-precise high-speed machining with multiple tools, the rotor behavior of an air-bearing spindle was analyzed more closely. Of particular interest here is how the rotor behaves with varying rotor unbalance ($U = 0.1$, 1 and 10 g mm) and cutting velocity ($v_c = 1,000$ and $4,000\,\text{m min}^{-1}$). A proven method is to measure the displacement of a measurement artifact with several sensors in order to extract the rotor behavior from these measured data. In these investigations, however, only the measurement artifact was mounted on the spindle and set in rotation. Since the dynamic behavior is of particular interest for the process, a tool was mounted in addition to the measurement artifact to analyze the rotor behavior not only in the static case (without machining) but also in the dynamic case (during machining). The dynamic case can also be used to investigate how the rotor behavior is reflected in the workpiece surface. Therefore, investigations were carried out on a Moore Nanotech 350FG ultra-precision milling and turning machine (Moore Nanotechnology Systems, LLC, Swanzey/NH, USA) with a mounted ISO 3.375B air-bearing spindle from Professional Instruments Company (Hopkins/MN, USA) on the Z-axis.

Four non-ferrous metals were selected as workpiece materials for the machining experiments (aluminum AlMg3, OFHC copper, brass CuZn39Pb3 and nickel silver CuNi18Zn19Pb1). All specimens were simultaneously mounted in a clamping device on the main spindle of the machine (see Fig. 41, left) and face-turned ultra-precisely to ensure a uniform surface plane and thus a constant cutting depth of $a_p = 20\,\mu\text{m}$ for the subsequent cutting tests. The fly-cutter (swing radius $r_{fly} = 82$ mm), which was mounted on the ISO 3.375B spindle for machining the plane surfaces, was equipped with a monocrystalline diamond tool with a cutting edge radius $r_\varepsilon = 0.797$ mm. For precise balancing, the fly-cutter offers 24 evenly distributed axial M3 and radial M4 screw threads in the front or lateral surface respectively.

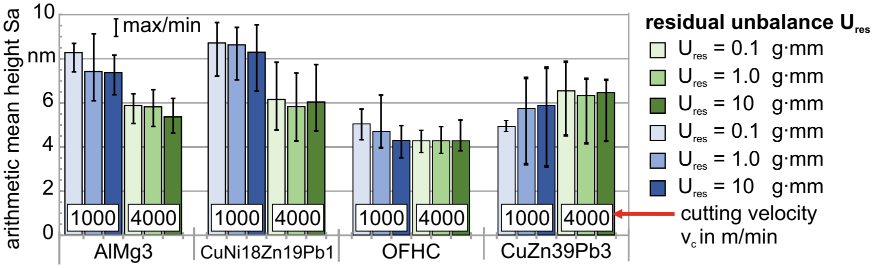

Fig. 42 Arithmetic mean height Sa resulting from cutting experiments with various cutting velocities and unbalance states

A balancing measurement system based on the influence coefficient method in combination with highly sensitive accelerometers with a sensitivity of 1,000 mV $g^{-1} \pm 10\%$ enabled a precise measurement of the balancing condition. Due to is inherent independence from the spindle specifications, the residual unbalance U was used as a parameter for setting the unbalance states instead of the balance quality grade from the DIN ISO 21940-11:2017 standard [11]. For the machining tests, the residual unbalance U was intentionally set to 0.1, 1 and 10 g mm for the cutting speeds $v_c = 1{,}000\,\mathrm{m\,min}^{-1}$ and $4{,}000\,\mathrm{m\,min}^{-1}$.

5.1 Cutting Experiments

The machined surfaces were measured with a white-light interferometer and afterwards analyzed using the image processing software “SPIP”. Figure 42 shows the arithmetic mean height Sa (applied L-filter of 80 μm) for all materials over the residual unbalance and the cutting speed. Each column represents the mean value of four measurements along the machined surface. The error bars represent the maximum and minimum of the respective measurement series.

The results from high speed milling (cf. chapter 3) suggested that the values of the arithmetic mean height Sa in Fig. 42 decrease with increasing cutting speed. However, a negative influence of the residual unbalance on the Sa value cannot be determined in the results. At the same cutting speed the Sa values can be considered constant if the error bar is taken into account. The reduction of the Sa values with increasing unbalance, which can be seen in the results for AlMg3, CuZn39Pb3 and OFHC Cu, can be considered negligible, as the change of the values is much smaller than the error bar. The same applies to the increasing Sa values for CuZn39Pb3.

These results are surprising at first sight because usually vibrations in the machine system, caused by the rotor unbalance, have an influence on the surface topography. On closer inspection, however, the fly-cutting process presented here involves the surface being machined with only one cutting edge and this cutting edge periodically oscillates at almost the same circumferential position to cut the workpiece. Neverthe-

Fig. 43 Experimental setup for measuring the rotor displacement in X- and Y-direction by two capacitive sensors

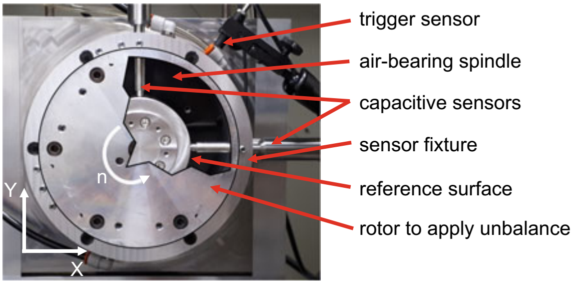

less, it could be interesting to consider the situation when several tools are used, as the tools cut the workpiece at different phase positions. For an improved evaluation of the achieved results it is essential to know the rotor behavior during cutting.

5.2 *Rotor Behavior Analysis*

The rotor behavior under varying unbalance and rotational speed was analyzed by measuring the rotor displacement without a machining process. To measure the rotor displacement in the X- and Y-axis, two highly sensitive capacitive displacement sensors of the type CPL490 from IBS Precision Engineering (Eindhoven, NL) were positioned against a measurement artifact, as shown in Fig. 43.

The measuring artifact was manufactured on an ultra-precise machine tool and mounted between the spindle and an additional element, which was used to adjust the defined residual unbalance. The adjusted residual unbalance and rotational speeds are identical to those of the milling experiments to ensure comparability.

The recorded measurement data of the rotor displacement display a superimposed noise and were therefore filtered by the complementary ensemble empirical mode decomposition (CEEMD) method [24] as described in [5]. Through this method, it is possible to extract the frequency components from the measurement signal for evaluation, which have a significant influence on the signal amplitude and are related to the rotational frequency of the rotor. The data processed by this method were used to determine the position deviation of the contact point between a hypothetical tool cutting edge and the workpiece surface. For this purpose, the position data were read out at the point where the signal of the trigger sensor switches to high. In this way, the rotor position deviation can be reliably read out at identical angular positions for each revolution of the rotor. The detected position deviation in X-direction are displayed in Fig. 44 at the same residual unbalance but for a varying cutting velocity.

The acquired measurement data support the findings of the surface measurement data. At a lower cutting velocity, higher position deviations are evident at the contact point between the cutting edge of the tool and the surface of the workpiece. For example, the average position deviation in the measured X-direction decreases from

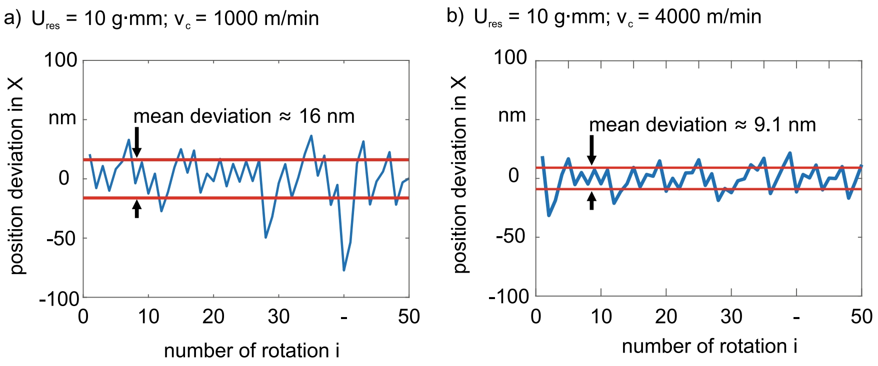

Fig. 44 Measured deviation of the tool contact point in x direction for **a** $U = 10\,\text{g}\,\text{mm}$; $v_c = 1{,}000\,\text{m}\,\text{min}^{-1}$ and **b** $U = 10\,\text{g}\,\text{mm}$; $v_c = 4{,}000\,\text{m}\,\text{min}^{-1}$

16 to 9.1 nm at a residual imbalance of $U = 10\,\text{g}\,\text{mm}$ and $v_c = 1{,}000\,\text{m}\,\text{min}^{-1}$ as well as $v_c = 4{,}000\,\text{m}\,\text{min}^{-1}$, respectively. A varying residual imbalance of the rotor has no significant influence in this context (cf. [5]).

The results of the rotor displacement study show that the positive effect of an increased spindle speed on the surface topography during the machining tests also has a positive effect on the rotor behavior.

5.3 Surface Characterization

In order to verify the impact of the unbalance induced rotor displacement on the machining process, the resulting surface was calculated numerically using a geometric model of a milling process (the 3D-analysis of the generated surface is presented in [18] and [19]). For this, the milling tool was modeled as a torus, featuring the swing radius of the milling tool ($r_{fly} = 82\,\text{mm}$) as its primary and the nose radius of the tool ($r_\varepsilon = 0.792\,\text{mm}$) as its secondary radius. This torus was positioned to intersect with a planar surface at equidistant intervals defined by the feed and the raster spacing ($f = 80\,\text{m}$ and $s = 8\,\text{m}$, respectively) while the difference to the previous result was kept for the subsequent iteration.

To analyze the optical surfaces, the arithmetic mean height value Sa was used. To get a deeper insight, some signal analysis based on two-dimensional Fourier transform/spatial frequency analysis was performed. In order to apply the spatial frequency analysis to the surfaces quality examinations, a two-dimensional fast fourier transformation (FFT2) was applied to the simulated surface and the magnitude of the result was analyzed in lower and higher frequency domains by the characteristic values P_1 and P_2. To separate the lower and higher frequency effects on the quality of the surface, the FFT2 results around $0\,\mu\text{m}^{-1}$ with $\pm 5\,\mu\text{m}^{-1}$ deviation were

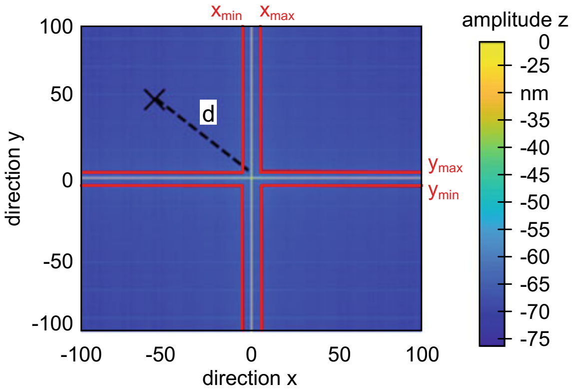

Fig. 45 Basic definitions of parameters in the FFT2 coefficient domain for calculation of the characteristic values P_1 and P_2

considered as low frequency result (see Fig. 45). For an improved evaluation of the FFT2 results, the logarithmic function was applied to the FFT2 values.

The parameter P_1 is defined by summing up the low frequency content of the FFT2 results of the optical surface (see Eq. 7). For the higher frequencies, based on the distance from the center, the value of each point is weighted and all the values of all calculated FFT2 coefficients are summed up to build the P_2 parameter (see Eq. 8).

$$P_1 = \sum_{x=x_{\min}}^{x_{\max}} \sum_{y=L}^{R} \text{fft2}(S) + \sum_{y=y_{\min}}^{y_{\max}} \sum_{x=L}^{R} \text{fft2}(S) - \sum_{x=x_{\min}}^{x_{\max}} \sum_{y=y_{\min}}^{y_{\max}} \text{fft2}(S) \tag{7}$$

$$\begin{aligned} P_2 = &\sum_{x=L}^{x_{\min}} \sum_{y=L}^{y_{\min}} \text{fft2}(S) \times d + \sum_{y=L}^{x_{\min}} \sum_{y=y_{\max}}^{R} \text{fft2}(S) \times d + \\ &\sum_{x=x_{\max}}^{R} \sum_{y=L}^{y_{\min}} \text{fft2}(S) \times d + \sum_{x=x_{\max}}^{R} \sum_{y=y_{\max}}^{R} \text{fft2}(S) \times d \end{aligned} \tag{8}$$

Within the formulas, S is a matrix that represents the height values in Z-direction of the optical surface. The limits of the integration area to calculate P_1 are defined by $(x, y)_{\min}$ and $(x, y)_{\max}$ respectively (see Fig. 45). In addition, L ($-100\,\mu\text{m}$) and R ($100\,\mu\text{m}$) define the left and right margin of the square surface in X- and Y-direction and d is the distance of each surface point to the center.

For the surface simulation generation, the following parameters were set: feed $f = 7\,\mu\text{m}$ in cutting direction, fly-cut radius $r_{fly} = 60 \times 10^3\,\mu\text{m}$, raster spacing $s = 60 \times 10^3\,\mu\text{m}$ and size of the simulated surface $A = 210 \times 210\,\mu\text{m}^2$.

The characteristic values for the first simulated surface (surface 1) were calculated to Sa = 2.7 nm, $P_1 = 1.9 \times 10^8$ nm and $P_2 = 4.8 \times 10^{-3}\,\text{nm}\,\mu\text{m}^{-1}$.

For the next step (surface 2), the deviation of the eccentricity is applied to the simulation with 40 dB signal-to-noise ratio. This deviation leads to the fol-

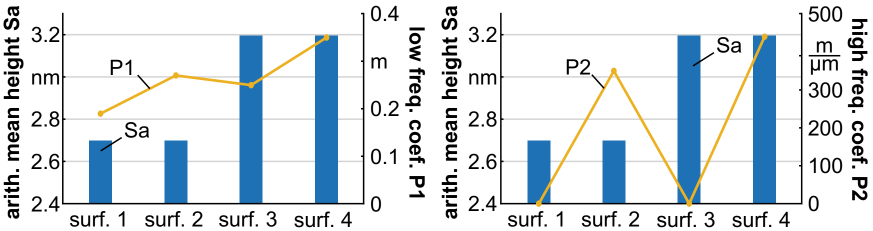

Fig. 46 Calculated Sa, P_1 and P_2 values for simulated surfaces

lowing surface roughness parameters: Sa = 2.7 nm, $P_1 = 2.7 \times 10^8$ nm and $P_2 = 3.5 \times 10^{11}$ nm mm^{-1}. Although the Sa value revealed to be not sensitive to this change of the surface, the characteristic value P_2 , which is related to the effect of higher frequencies, increases significantly.

By adding 0.1 nm deviation in fly-cut radius in the surface simulation (surface 3), the values change to Sa = 2.7 nm, $P_1 = 1.9 \times 10^8$ nm and $P_2 = 4.9 \times 10^{-3}$ nm µm^{-1}. The effect of this deviation is identifiable by the P_1 and P_2 parameters.

A change in feed rate in cutting direction from 70 to 100 µm and an additional noise level of 40 dB in the simulation (surface 4) led to the following surface roughness parameters: Sa = 3.2 nm, $P_1 = 3.5 \times 10^8$ nm and $P_2 = 4.4 \times 10^{11}$ nm µm^{-1}.

This indicates the efficiency of using spatial frequency analysis in surface quality measurements, including additional information about the morphology of the optical surfaces (Fig. 46).

6 Conclusion

The precise balancing of high-speed air-bearing spindles is a challenging but necessary task in ultra-precision machining to avoid vibrations and damage to the bearing. While many processes in production technology are already automated, it was not yet possible to automatically and precisely balance an ultra-precision air-bearing spindle. Therefore, the possibility of automatic balancing of air-bearing spindles was investigated in this study. Two balancing systems in combination with a system for more precise measurement of unbalance-induced vibrations at low speeds enabled highly accurate balancing down to a balancing grade of $G0.064$. In addition, a monitoring and control system could significantly increase system safety. Two prototypes based on the spread angle principle and on the fixed position method have been developed, which use ultrasonic ring motors and microfluidic actuators for balancing, respectively. Both systems proved the ability to perform the required balancing grade of $G0.064$. Furthermore, the system for increasing the measurable unbalance-induced vibrations significantly improved unbalance detection. As a result, it was possible to measure unbalances below the detection threshold of conventional accelerometers. It was also shown that an unbalance measurement on the rotor, and not as usual on the stator, enables a measurement up to a spindle speed of $n \leq 1{,}800\,\text{min}^{-1}$. In combination with the implemented control system, the final automatic balancing system is capable of balancing an air-bearing spindle up to a rotational speed of $n \leq 4{,}200\,\text{min}^{-1}$ to a desired unbalance in magnitude and phase. Additionally, two characteristic values were introduced that could enhance the analysis of optical surfaces with relation to unbalances in machining.

References

1. Birkenstack, D., Jager, O.: Multi-chambered fluid balancing apparatus. U.S. Patent 3 950 897. Gebr. Hofmann KG, 20 April 1976
2. Cao, H., Dörgeloh, T., Riemer, O., Brinksmeier, E.: Adaptive separation of unbalance vibration in air bearing spindles. Procedia CIRP **62**, 357–362 (2017). https://doi.org/10.1016/j.procir.2016.06.069
3. Dörgeloh, T., Beinhauer, A., Riemer, O., Brinksmeier, E.: Microfluidic balancing concepts for ultraprecision high speed applications. Procedia CIRP **46**, 185–188 (2016). https://doi.org/10.1016/j.procir.2016.03.174. Wertheim, R., Ihlefeldt, S., Hochmuth, C., Putz, M. (eds.) 7th CIRP Conference on High Performance Cutting (HPC 2016)
4. Dörgeloh, T., Riemer, O., Brinksmeier, E.: Automated microfluidic balancing system for high speed air-bearing spindles. Procedia CIRP **77**, 263–266 (2018). https://doi.org/10.1016/j.procir.2018.09.011. 8th CIRP Conference on High Performance Cutting (HPC 2018)
5. Dörgeloh, T., Schönemann, L., Riemer, O., Brinksmeier, E.: Analysis of rotor behavior in ultraprecision high speed cutting. In: 34th ASPE Annual Meeting, pp. 69–74. American Society for Precision Engineering (2019)
6. Foremny, E., Schenck, C., Kuhfuss, B.: High precision coupling system. In: Annoni, M., Fassi, I., Wiens, G.J., Dimov, S. (eds.) 10th International Conference on Micromanufacturing (4M/ICOMM 2015), Milan, Italy, pp. 205–208 (2015)
7. Foremny, E., Schenck, C., Kuhfuß, B.: Dynamic behavior of an ultra precision spindle used in machining of optical components. Procedia CIRP **46**, 452–455 (2016). https://doi.org/10.1016/j.procir.2016.04
8. Foremny, E., Schenck, C., Kuhfuss, B.: Coupling system for ultra precision machining. J. Mech. Eng. Autom. **6**(6), 301–306 (2016)
9. Foremny, E., Schenck, C., Kuhfuss, B.I.: Integrated ultrasonic driven balancer for ultra precision high speed machine tools. Procedia Technol. **26**, 316–323 (2016). https://doi.org/10.1016/j.protcy.2016.08.041. 3rd International Conference on System-Integrated Intelligence: New Challenges for Product and Production Engineering
10. ISO: Geometrical product specifications (GPS)—surface texture: areal—part 2: terms, definitions and surface texture parameters. Standard ISO 25178-2 (2012)
11. ISO: Mechanical vibration—rotor balancing—part 11: procedures and tolerances for rotors with rigid behaviour. Standard ISO 21940-11 (2017)
12. Jiang, X.J., Whitehouse, D.J.: Technological shifts in surface metrology. CIRP Ann. **61**(2), 815–836 (2012). https://doi.org/10.1016/j.cirp.2012.05.009
13. Knapp, B., Arneson, D., Oss, D., Liebers, M., Vallance, R., Marsh, E.: The importance of spindle balancing for the machining of freeform optics. In: ASPE Spring Topical Meeting, vol. 51, pp. 74–78. ASPE, Raleigh (2011)
14. Levicron GmbH. Coorporate Website (2017)
15. Moon, J.-D., Kim, B.-S., Lee, S.-H.: Development of the active balancing device for high-speed spindle system using influence coefficients. Int. J. Mach. Tools Manuf **46**(9), 978–987 (2006). https://doi.org/10.1016/j.ijmachtools.2005.07.048

16. Rebeggiani, S., Rosén, B.G., Sandberg, A.: A quantitative method to estimate high gloss polished tool steel surfaces. J. Phys: Conf. Ser. **311**, 012004 (2011). https://doi.org/10.1088/1742-6596/311/1/012004
17. Riemer, O., Schönemann, L., Dörgeloh, T., Beinhauer, A., Foremny, E., Brinksmeier, E., Kuhfuss, B.: Balancing concepts for high speed aerostatic spindles. In: 30th ASPE Annual Meeting, pp. 273–274 (2015)
18. Schönemann, L.: Surface simulation for ultra-precision milling with multiple cutting edges. In: 69th CIRP General Assembly - Part 2, Birmingham, 22 August 2019
19. Schönemann, L., Berger, D., Dörgeloh, T., Riemer, O., Brinksmeier, E., Krüger, R., Schreiber, P., Denkena, B., Hochbein, J., Parsa, N., Schenck, C., Kuhfuss, B.: Synergistic approaches to ultra-precision high performance cutting. CIRP J. Manuf. Sci. Technol. **28**, 38–51 (2020). https://doi.org/10.1016/j.cirpj.2019.12.001
20. Smith, G.L., Rudy, R.Q., Polcawich, R.G., DeVoe, D.L.: Integrated thin-film piezoelectric traveling wave ultrasonic motors. Sens. Actuators A Phys. **188**, 305–311 (2012). https://doi.org/10.1016/j.sna.2011.12.029. Selected papers from The 16th International Conference on Solid-State Sensors, Actuators and Microsystems
21. Tauhiduzzaman, M., Yip, A., Veldhuis, S.C.: Form error in diamond turning. Precis. Eng. **42**, 22–36 (2015). https://doi.org/10.1016/j.precisioneng.2015.03.006
22. Uchino, K.: Piezoelectric ultrasonic motors: overview. Smart Mater. Struct. **7**(3), 273–285 (1998). https://doi.org/10.1088/0964-1726/7/3/002
23. Wallaschek, J.: Piezoelectric ultrasonic motors. J. Intell. Mater. Syst. Struct. **6**(1), 71–83 (1995). https://doi.org/10.1177/1045389X9500600110
24. Yeh, J.-R., Shieh, J.-S., Huang, N.E.: Complementary ensemble empirical mode decomposition: a novel noise enhanced data analysis method. Adv. Adapt. Data Anal. **02**(02), 135–156 (2010). https://doi.org/10.1142/S1793536910000422
25. Zhang, S.J., To, S.: A theoretical and experimental study of surface generation under spindle vibration in ultra-precision raster milling. Int. J. Mach. Tools Manuf. **75**, 36–45 (2013). https://doi.org/10.1016/j.ijmachtools.2013.08.003
26. Zhang, S.J., To, S., Zhu, Z.W., Zhang, G.Q.: A review of fly cutting applied to surface generation in ultra-precision machining. Int. J. Mach. Tools Manuf. **103**, 13–27 (2016). https://doi.org/10.1016/j.ijmachtools.2016.01.001

Ultra Precision High Performance Axis Control

Per Schreiber, Johannes Hochbein, Benjamin Bergmann, Christian Schenck, Bernd Kuhfuss, and Berend Denkena

Abstract Axis controls of ultra-precision machine tools have to fulfill demanding requirements regarding position and velocity tracking accuracy, disturbance rejection, and avoidance of vibration. Within this project, an axis concept for ultra-precision machining utilizing an electromagnetic linear guide is investigated. The axis concept offers additional, redundant degrees of freedom for error compensation and sensory information for monitoring tasks. It is shown that input shaping and feed forward control of disturbance forces allow for significant improvement in machining performance. To investigate the axis behavior of the multi-axis motion, an external measurement device with sufficient travel range and sub-micron resolution is needed. This task is solved with a novel speckle position sensor that is described in this chapter as well.

1 Introduction

Ultra-precision (UP) machining requires guiding the workpiece and tool with sufficiently high accuracy and low vibration such that high form accuracy and low surface roughness can be achieved. Often axis dynamics are limited deliberately in order to reduce the excitation of vibration and dynamic path errors from tilting slides or lacking trajectory tracking performance. Hence, a new motion system is required to allow for UP-machining at significantly increased axis dynamics. Characteristics of

---

P. Schreiber (✉) · B. Bergmann · B. Denkena
Institute of Production Engineering and Machine Tools IFW, Leibniz University Hannover, Garbsen, Germany
e-mail: Schreiber@ifw.uni-hannover.de

J. Hochbein · C. Schenck · B. Kuhfuss
Bremen Institute for Mechanical Engineering bime and MAPEX Center for Materials and Processes, University of Bremen, Bremen, Germany
e-mail: hochbein@bime.de

E. Brinksmeier and L. Schönemann (eds.), *Ultra-precision High Performance Cutting*,
Lecture Notes in Production Engineering, https://doi.org/10.1007/978-3-030-83765-5_6

the feed motion are largely determined by trajectory planning, axis controls, and the applied bearing and drive technology and its transmission characteristics. The Ultra-Precision High Performance Cutting (UP-HPC) machine concept, which is described in Sect. 2 and shown in Fig. 1 is a three-axis machining concept. It incorporates an electromagnetic guide which adds five additional degrees of freedom (DoF). They are partly redundant and can be utilized as additional fine positioning axes. The dynamic properties of those redundant axes differ significantly from the other machine axes. Also, axis dynamics are subjected to variations of the system setup such as changing mass from the workpiece or the workpiece fixture. Thus, system models used for instance for model based control or controller tuning not only need to be accurate but also adaptable. Therefore, in order to obtain a model that fulfills the requirements of UP-machining, Sect. 3 of this work presents an approach to estimate actual parameters of a state-space model during runtime. The proposed approach is able to learn and adapt to varying conditions even if these conditions are not implemented in the initial model. Moreover, the section addresses how substantial differences of sub-system dynamics can be handled by the use of residual sub-band models.

Besides online parameter adaptation, another prerequisite for designing and optimizing a complex axis control system is a feasible, external system to gain comparable data on multi-axis positioning behavior [6]. Available systems such as laser tracker and grid encoders lack either resolution or range. Therefore, in Sect. 4 a new approach is introduced which combines the precision of laser speckle measurements with a suitable measurement range. This contactless system operates without a corporal solid measure and can easily be adapted to different kinematic set-ups and machine tools.

Dynamic errors that are induced by the acceleration and jerk of axis feed motion can affect machining quality. Thus, in UP-machining feed velocity, acceleration, and jerk values are commonly limited to a large extent. However, in order to achieve the targeted performance within the UP-HPC approach other measures to mitigate dynamic errors are required. In Sect. 5, the capabilities of an active guide in combination with vibration avoidance in order to improve process performance and productivity are shown. In order to mitigate the excitement of vibration, input shaping is investigated for the feed axis system. Altintas and Khoshdarregi [1] and Sencer et al. [14] showed that input shaping can effectively suppress vibration in conventional machining. The use of this approach in ultra-precision machining has not been investigated in depth. Secondly, the input shaping is investigated in combination with a force feed forward control of acceleration loads. It is shown that both approaches can improve productivity significantly. Further it is shown that the preferable choice of compensation approaches in order to improve productivity depends on the aimed cutting velocity and form deviation. To further support process and compensation parameterization the capability of internal sensor data in order to predict workpiece form deviations is evaluated. Finally, the results of this chapter are concluded and an outlook on future work is given in Sect. 6.

2 System Description

Central element of the research group is a machine prototype for ultra-precision high performance cutting. The prototype supports fly-cutting as well as planing with stationary tool. This section describes the kinematic axis structure of the prototype, the structure of the control system as well as the experimental setup for initial cutting tests.

2.1 Prototype Axis System Description

This section concerns the axis controls of the machine prototype which was developed and set up in the project. The design of the prototype is shown in Fig. 1. The kinematic design comprises three macro axes X, Y, Z. Another five fine-positioning DoF are contributed by the electromagnetic guide of the X-axis. Those DoF are denoted with their generalized coordinates $\boldsymbol{q}_y$ and $\boldsymbol{q}_z$ for the redundant linear DoF and $\boldsymbol{q}_a$, $\boldsymbol{q}_b$, and $\boldsymbol{q}_c$ for the angular DoF. The X-axis is placed within the slide of the Z-axis as a box-in-a-box design. Details on the design of the electromagnetic guide are given in Chap. 4. The Z-axis is guided by conventional porous media aerostatic bearings. Both, the X- and Z-axis are driven by two iron-less linear drives. The Y-axis utilizes a conventional roller guide, driven by a rotary motor with a mechanical brake. The Z-axis position is acquired by two linear encoders. The X- and Y-axis are equipped with one encoder each.

In a machining process, the macro axes X, Z provide the motion for feed and crossfeed and vice versa. Infeed is provided by the fine-positioning axis $\boldsymbol{q}_y$, while the macro Y-axis is used for pre-adjustment of the spindle and tool position in advance of the machining process. The Y-axis clamped and kept stationary with the brake during the process. The Y-axis can carry a fly-cutting spindle or a stationary tool for planing. Figure 1 shows the setup with the fly-cutting spindle.

2.2 Real-Time Control Architecture

The controllers of all motion axes as well as acquisition and processing of the sensor data are executed on an industrial PC (IPC) system (Beckhoff). To this end, a modular control framework was developed. The basic structure of the framework is shown in Fig. 2. Modularity concerns flexible involvement of the prototypes' nine DoF in motion and machining as well as modularity of each of the axes' controller and compensation modules. Online change of axis configuration as well as change of controller and compensation properties, was a fundamental requirement. This is due to the fact that an offline change and recompilation of modules would require shutting down the levitating axis. Shutting down the levitating axis however can

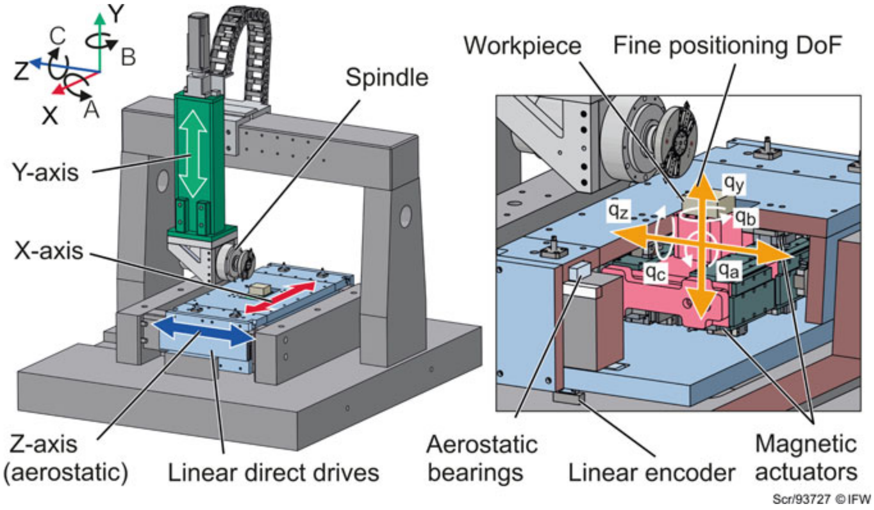

Fig. 1 Machine prototype for UP-HPC-cutting

lead to diverging from a thermostatic state and is thus not feasible for conducting repeatable experiments. A state machine module handles system and module states such as macro axis clearance depending on the levitation axis state or activation of compensation parameters depending on axis states. Also base functionalities such as homing are coordinated by the state machine. Set-point values for the axes are generated by a G-code interpreter which also handles interpolation for up to three linear axes. The modular system allows for flexible multi-axis interpolation with the fine-positioning DoFs of the magnetic levitation guide in any combination with the macro axes. Additional signals can be linked onto the output of the interpolation system for compensation applications. The individual axis controller modules are developed in Simulink and exported as IEC-61131 structured text using the Matlab PLC-Coder extension. The controller modules, which control position and velocity, are executed at 16 kHz on the IPC. The controller output, the drive current set-point value is transferred to the servo drive controllers via an ethernet for control and automation technology (EtherCAT) bus system. The current control is executed by the servo drive controllers. They also connect the position encoders to the system and transfer actual position and velocity to the IPC. For details regarding the control structure of the magnetic guide system please consider Chap. 4, Sect. 4.4.

2.3 *Setup for Cutting Experiments*

Cutting experiments were conducted, in order to evaluate the behavior of the axis and control system and compensation approaches in terms of their impact on the

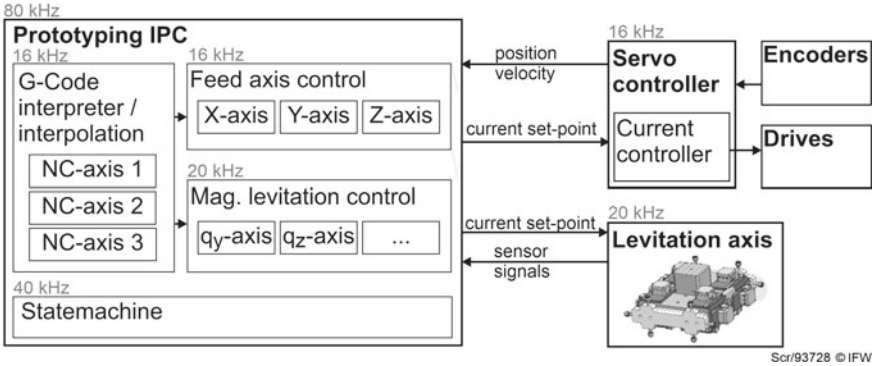

Fig. 2 Structure of the realtime control system

machining quality. For the experiments a planing process with stationary tool attached to the Y-axis was implemented. A planing process was chosen in order to evaluate the axis control system. In contrast to a fly-cutting process planing allows to exclude certain effects from the machining result. Those effects are for instance vibrations from spindle imbalances. Another disadvantage of fly-cutting in terms of investigating axis controls is that it leads to a form of "undersampling". For a typical fly-cutting spindle speed of 1,500 min^{-1} and a single cutting edge there is a short tool-workpiece contact at a frequency 25 Hz. Hence, axis and prototype behavior above 12.5 Hz would already be distorted by aliasing effects in the machining result. The setup for planing experiments is shown in Fig. 3. The stationary tool, is attached to the Y-axis such that the tool center point (TCP) is close to the TCP for the fly-cutting set-up. Thus, a part of the effects from structural dynamics of the Y-axis can be expected to be apparent in both, the fly-cutting and planing set-up. A manual linear stage was used for presetting the tool position while the depth of cut (a_p) is set by the fine positioning DoF q_y of the electromagnetic axis. The direction of cut corresponds to the Z-axis. For avoiding tool-workpiece contact during the retracting movement of the Z-axis, the q_y-axis was lowered to maximum extent while resetting the workpiece. In advance of the actual cutting experiments workpieces were planed entirely in this setup without re-clamping in order to achieve the best possible parallelism of the workpiece surface to the machine axes.

2.4 Process and System Capability

This section gives an overview over the system capability of the described axis and control system as a reference for further experiments. Figure 4 shows an exemplary machining result of a planing process with the above described setup. The workpiece (aluminum EN AW 5754) was machined in multi-axis interpolation with at a cutting speed $v_c = 500\,\text{mm min}^{-1}$ in Z-direction. Regarding axis control settings, the static

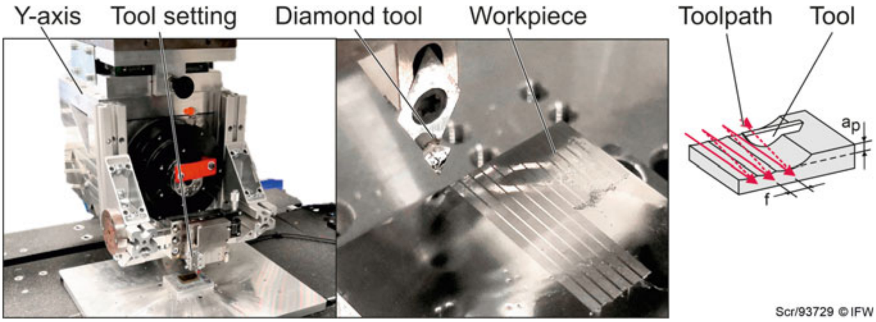

Fig. 3 Setup for cutting experiments (left and center) with the shaping process (right)

compensations and position-depended Jacobians from Chap. 4 were activated. An overlaying motive pattern was realized by varying the depth of cut between 3 µm and 7 µm in the process. The workpiece was lubricated with paraffin oil. Measurements of the workpiece show that a mean deviation ($\overline{\Delta_y}$) from the set point height difference of the pattern (4 µm) amounts to 54 nm. The surface roughness, determined as the arithmetic mean height Sa amounts to 42.8 nm. The theoretical limit of achievable surface roughness for the given tool nose radius r_ε and lateral feed f under otherwise ideal conditions $Sa_{lim} \approx 3f^2/64r_\varepsilon$) amounts to 6.1 nm in comparison. Thus, the residual surface roughness of the aluminum workpiece can be assumed to be the current limit of the experimental setup. This is supported by the finding that it reflects the values that were archived in Sect. 4.8 with a brass workpiece and cutting in X-direction instead of Z-direction. Limiting factors and influences are, among others, tool-sided compliances, effects from chip formation, introduction of external vibration from the non-decoupled foundation, and remaining control deviations of the axis and guiding system.

3 Adaptive Parameter Estimation

Model based axes control for high speed UP-operations demands for high complexity and associated computational costs to represent the machine behavior within the required resolution and accuracy. To reduce the computational costs for realizing real time application, the complexity can be reduced by in-process parameter estimation and adaption that ensures the required precision [5].

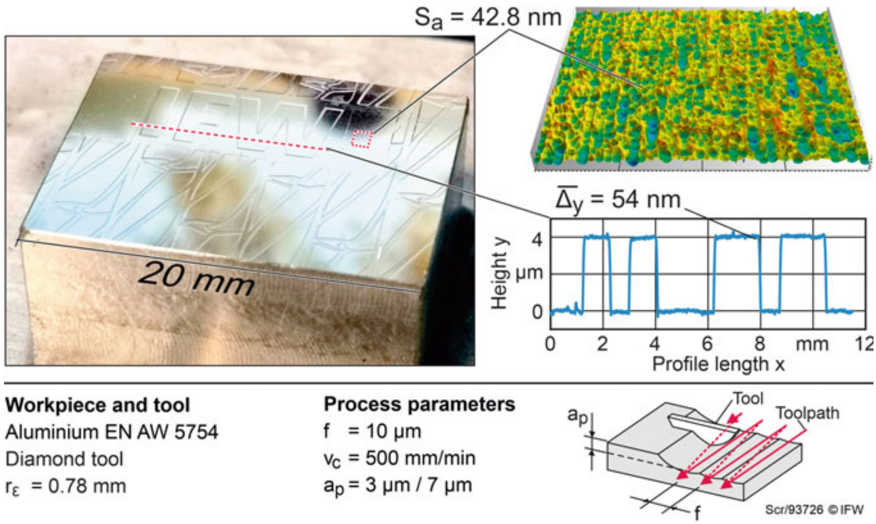

Fig. 4 Overview over system capability with exemplary surface and profile measurement

3.1 Model Structure

The model consists of two sub-models, the motion band sub-model (MBSM) and the residual band sub-model (RBSM). While the MBSM calculates the larger scale motion of the feed axes, vibrations and discrepancies are represented by RBSM. Due to this reduction, the parameters of both sub-models can be estimated separately and in individually suitable cycle times.

Each sub-model is represented as state-space model. In such models, the system is expressed by the state vector $\boldsymbol{x}$ with n state-variables. n was chosen to 8 (MBSM) and 6 (RBSM). Each state variable behaves as energy storage and records the influence of past inputs to the actual state. A state vector at a time t for an input vector $\boldsymbol{u}$ can be calculated as

$$\dot{\boldsymbol{x}}(t) = \boldsymbol{A}\boldsymbol{x}(t) + \boldsymbol{B}\boldsymbol{u}(t) \tag{1}$$

Hereby, $\boldsymbol{A}$ is the state matrix which defines the single state variables interaction and $\boldsymbol{B}$ is the input matrix that defines the input influence on the state variables. The output $\boldsymbol{y}$ of the model can be calculated from the state vector with the output matrix $\boldsymbol{C}$.

$$\boldsymbol{y}(t) = \boldsymbol{C}\boldsymbol{x}(t) \tag{2}$$

The output of both sub-models must be phase corrected and added to the final result. The complete process is shown in Fig. 5.

The parameters of the sub-models were separately estimated based on the predictive error method (PEM) [11]. Therefore, the future model output is estimated with

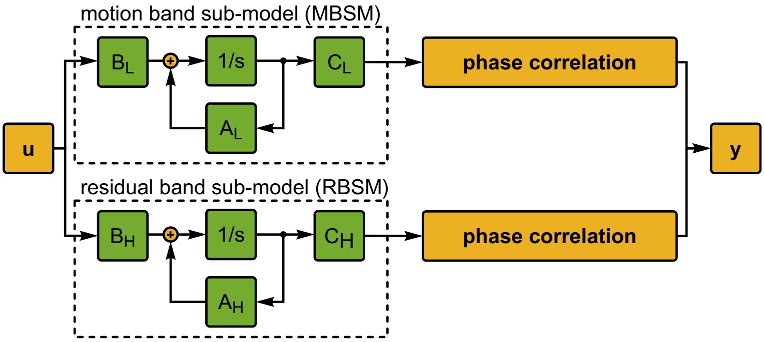

Fig. 5 Model structure with two reduced sub-models; cf. [5]

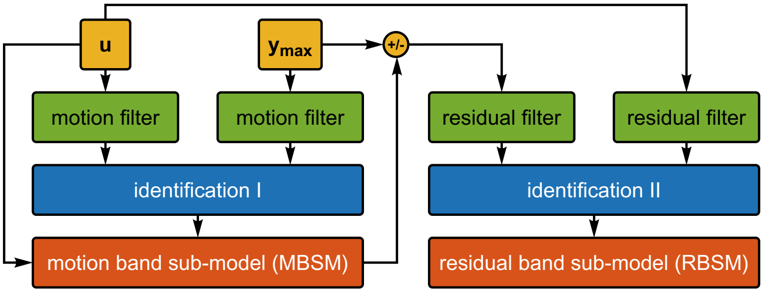

Fig. 6 Parameter identification procedure; cf. [5]

Eq. 2 and compared to the measurement at that time. The lowest deviation was then found with the Levenberg-Marquardt method [10]. The separation of the estimated and the measured data was realized with equiripple low-pass finite impulse response filters due to their constant group delay. This feature ensures that the unavoidable distortion of the motion data in time domain is independent of the velocity. For the MBSM parameter estimation all frequencies 20 Hz while for the RBSM parameter estimation all frequencies 200 Hz were suppressed. The procedure is shown in Fig. 6. A window of the measurements with a fixed size of w_{est} samples and the input $\boldsymbol{u}$ is used as input for the parameter estimation. The window lengths were heuristically chosen as 83.33 ms (MBSM) and 50 ms (RBSM). To react to parameter variation of the system, the parameters are estimated in each window individually. After this estimation and a comparison with the previous parameter, the parameters with the lower deviation are chosen as new model parameters. To get a robust system, the parameter changes were limited to 15% of the actual value.

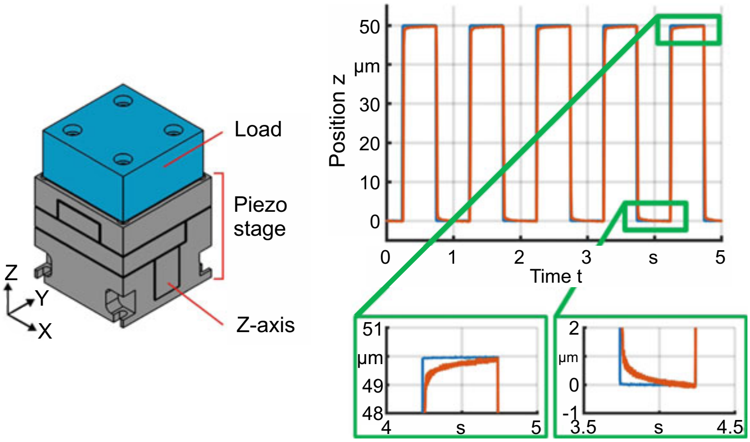

Fig. 7 Model parameter identification **a** Setup **b** Z-position with set-point values (blue) and actual values (red); cf. [5]

3.2 Experimental Setup

The identification algorithm was tested with a piezo stage "NanoCube" (P-611.3, Physik Instumente) in open-loop control mode. After initial identification, an additional load on the NanoCube in z-direction ($0, 22, 31, 52, 77\,\mathrm{g}$) as variable parameter simulated a change in the system and hence its behavior. Both the input to the piezo stage (set-point values) and the internal position sensor of the piezo stage (actual values) were used for the in process parameter estimation. As demanded motion in Z-direction a step function with an amplitude of $50\,\mu\mathrm{m}$ was applied to emulate a positioning task. This demanded trajectory was performed five times in a row with each load. The waiting time between positioning was one second. An example of the set-point trajectory and the corresponding actual trajectory is shown in Fig. 7.

The estimation error as difference between the measured actual position values and the estimated position values calculated by the model is illustrated in Fig. 8. Mean values were calculated during the stand still in the target position. The initial model parameter estimation gains a quite good prediction with an estimation error less than $1\,\mathrm{nm}$. Nevertheless, changing the physical system by additional load increases the estimation error about several nanometers.

4 2D Speckle Position Sensor

To judge the effects of parameter estimation and path control a measuring device based on speckle pattern was developed. This sensor works without a corporal solid

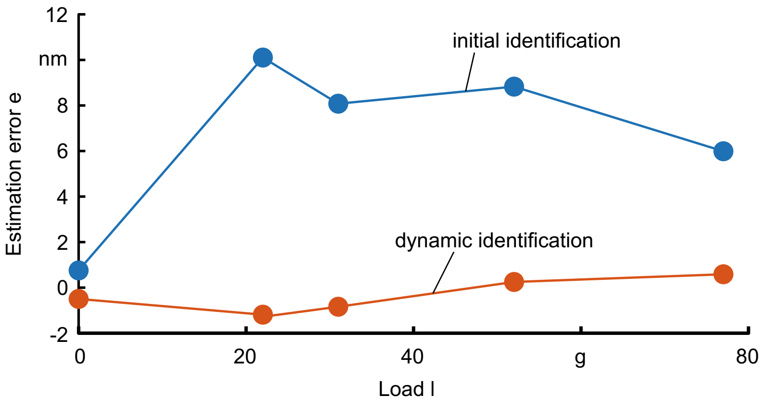

Fig. 8 Mean model estimation error during positioning tests with different loads with static and dynamic parameter estimation

measure and can easily be adapted to different machine tools. The following sections describe the principle of the measurement, the range extension procedure and results.

4.1 Laser Speckle

Laser speckle occur when a surface is illuminated by a laser. Imperfections in the surface cause interference effects that can be monitored by a digital camera as a pattern of light intensity. The distribution of these imperfections is of stochastic nature and unique to the respective surface. Common fields of application are robotics, consumer electronics, deformation analysis and machine tools [7, 12, 16]. A basic sensor setup to track the positions of ultra-precision machine tools was introduced in [3]. The principle of this sensor is shown in Fig. 9.

Due to the uniqueness of the pattern, a displacement of the test surface can be traced by tracing the displacement of the speckle pattern. As long as the displacement is short enough to ensure an overlap of two consecutive images, this shift can be calculated by means of image correlation (see Fig. 10).

4.2 Algorithm for Displacement Calculation

As general procedure, the first image is assumed to be the reference that is placed in a known reference position. All displacements are calculated in respect to this reference. The method to calculate the displacement consists of two steps. In the first step, the position is roughly estimated by two-dimensional cross correlation of the

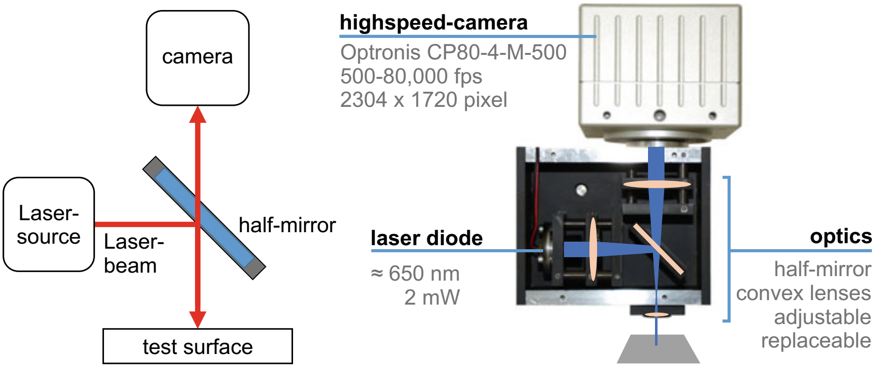

Fig. 9 2D Speckle Sensor; principle (left), experimental setup (right)

Fig. 10 Displacement between images

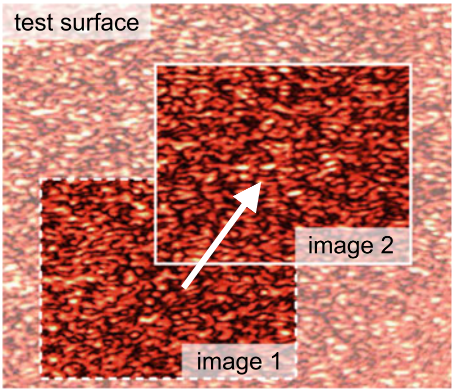

actual image (test pattern) with the reference. These results are highly affected by the boundary values. Therefore, a rectangular window function was applied to set the values at the window margins to zero. These margins were fit to be larger than the maximum expected displacement between two consecutive captures to guarantee an equal amount of summands in the cross correlation calculations. As a result, the displacement is presented as a two-dimensional vector of integer values that represent the number of acquired digital pixels. To enhance this limited resolution a sub-pixel interpolation was applied in a second step. Therefore, a Gaussian function is fitted onto the position of the maximum value of the correlation function and its neighboring pixels. The maximum of the fitted curve represents a better estimation of the displacement. This method of sub-pixel interpolation is performed for both dimensions independently.

For higher displacements, the overlap of the images becomes too small for a precise calculation. To handle this issue, the algorithm was extended with a function for reference pattern changing. Therefore, a threshold value was introduced. In case the displacement exceeds this value, the reference pattern is exchanged with the

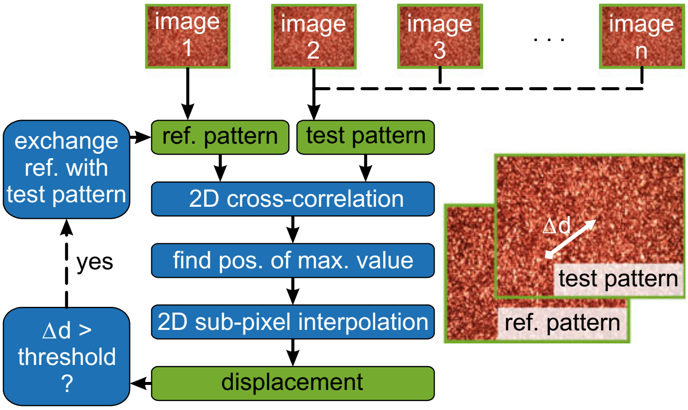

Fig. 11 Algorithm with reference pattern change, picture credit: [13], CC BY 4.0

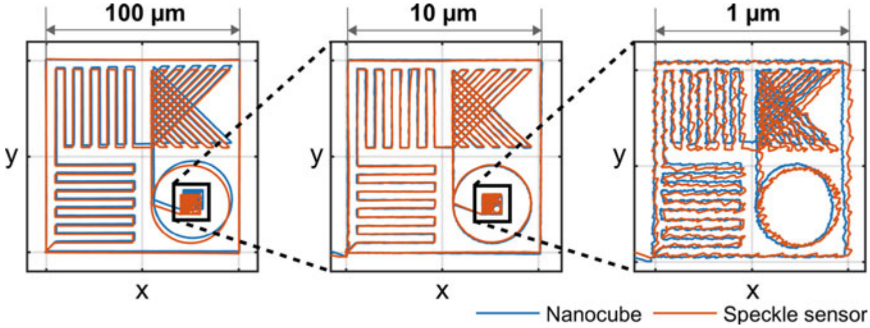

Fig. 12 Test pattern (blue) traced with speckle sensor (orange) in 100 µm, 10 µm and 1 µm scale (cf. [4]), picture credit: [13], License: CC BY 4.0

actual test pattern. For defining an adequate threshold value, divergent effects must be considered. These are basically the effective pixel size that defines the ratio of acquired pixel size and its real dimension [2] and the size of the images [3]. The complete algorithm is shown in Fig. 11.

A test pattern was traced with a piezo stage “NanoCube” (P-611.3, Physik Instrumente) and measured with the speckle sensor in different scales see Fig. 12. Sufficient path accuracy was verified by the internal measuring system. The speckle sensor performed best in the middle scale with a moderate number of pattern changes. In the large scale, the high number of pattern changes reduced the accuracy whereas in the small sub-µm scale the whole system is limited by noise.

A significant reduction of the number of pattern changes could be achieved by a cross-referencing algorithm. For that purpose, mapping of all images that were used as reference patterns allowed for defining the shortest connection between each actual pattern and the initial reference by Dijkstra algorithm for recalculation of the measured shift. Especially for long paths in small areas, the tool center point crosses

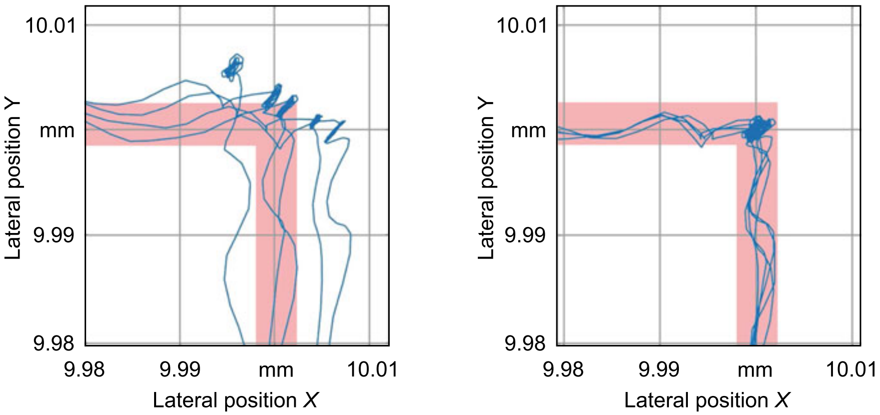

Fig. 13 Deviation of axis movement from test pattern. Left: without cross-referencing; Right: with cross-referencing

its own trajectory several times and the cross-referencing significantly shortens the path that is used in calculations. The effect is illustrated by tracking an edge of a repeatedly covered rectangle, see Fig. 13.

5 Axis Control for Performance Improvement

The following section investigates the application of vibration avoidance and feed forward compensation of dynamic deviations caused by axis motion. Emphasis of the investigation is the impact of the proposed methods on productivity.

5.1 Acceleration Force Feed Forward

Dynamic and static path errors can influence workpiece quality in machining. Due to finite stiffness of components and bearings, the acceleration of machine tool axes lead to displacements and rotations in DoF that are supposed to be locked. In case of the active electromagnetic workpiece slide, such displacements can be measured continuously and actively compensated in order to increase accuracy. Here, position offsets as well as force offsets can be imposed upon the electromagnetic guide set-points. Figure 14 illustrates the basic structure therefore. Position offsets $\boldsymbol{\Delta q}_{pos}$ can be added to the set-point values $\boldsymbol{q}_{\text{set}}$ of the magnetic guide in order to account for static errors such as straightness deviations of the guides. A force feed forward $\boldsymbol{Q}_{ff}$ is added on the output of the electromagnetic guide control adding up to the set-point vector of generalized forces $\boldsymbol{Q}_{set}$. Force feed-forward is utilized to counteract

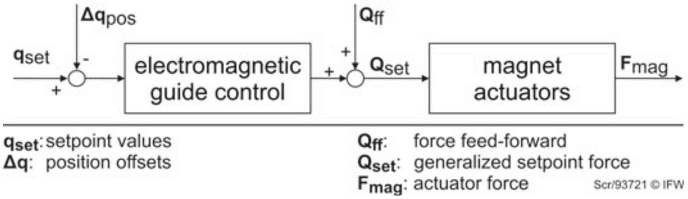

Fig. 14 Block diagram of the dynamic error feed forward, based on [9]

disturbance forces acting on the guide before they can cause a displacement. This requires that these disturbance forces can either be measured with low delay or be predicted. Here, force-feed forward is applied to loads from acceleration of the Z-axis as these are the dominating disturbance forces on the workpiece slide and can be derived from the acceleration set-point.

It was shown in simulation in [9] for the given setup that an acceleration force feed-forward can significantly reduce the tilting error q_a of the magnetic slide's A-axis for accelerated motion of the Z-axis. Empirical analysis showed that significant deviations also appear in q_z. Thus, for feed forward a force vector $\boldsymbol{Q}_{ff}$ is set based on the set-point acceleration $\ddot{z}_{set}$:

$$\boldsymbol{Q}_{ff} = -\ddot{z}_{set}\boldsymbol{P} \tag{3}$$

With the parameter vector $\boldsymbol{P}$:

$$[p_{zx}\ p_{zy}\ p_{zz}\ p_{za}\ p_{zb}\ p_{zc}]^T \tag{4}$$

The elements of $\boldsymbol{P}$ can be interpreted as the masses and inertia respectively. In comparison to [9], an empirically identified $\boldsymbol{P}$ vector was used instead of an analytical vector inferred from the Jacobian and masses. The identified values are $p_{zz} = 46$ to compensate for the deviation q_z in the feed direction and $p_{za} = 1.2$ to reduce a rolling movement of the X-axis. The remaining parameters p_{zx}, p_{zy}, p_{zb}, p_{zc} are set to zero as no significant acceleration response is induced in the corresponding DoF.

As described in Sect. 4.6 it can be necessary to apply a time delay on the $\boldsymbol{Q}_{ff}$ value in order to synchronize the magnetic feed forward force with the axis acceleration. However, this was not required as the Z-axis control loop itself features an acceleration force feed forward. This enables a precise acceleration following behavior of the feed axis. Moreover, since both feed forward values are calculated in the same thread of the control system and are subjected to a similar transport delay from the EtherCAT bus system, force onset of the axis linear drives and the levitation magnets is already sufficiently synchronized without additional delay.

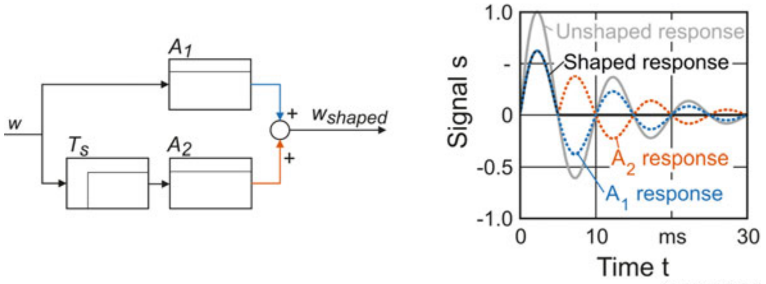

Scr/93730 © IFW

Fig. 15 Block representation of a zero vibration input shaper (left) and impulse response (right) based on [15]

5.2 *Vibration Avoidance with Input Shaping*

Input shaping is an approach to avoid the excitation of certain vibration modes by modification of the set-point trajectory. The concept is described in [15] and shown in Fig. 15. To illustrate the concept of input shaping, a system is assumed which responds as a second order oscillator with an oscillation period T_0 and damping ratio of ζ. To suppress excitation of this vibration, the set-point value w is split into two paths one of which is delayed by $T_s = T_0/2$. This leads to two oscillation responses with a shift of $\pi/2$. If the gains A_1 and A_2 are chosen correctly according to the damping value, those oscillation responses can cancel each other out completely. The gains are chosen as:

$$A_1 = \frac{1}{1+K} \tag{5}$$

and

$$A_2 = \frac{K}{1+K} \tag{6}$$

where,

$$K = e^{\frac{\zeta\pi}{\sqrt{1-\zeta^2}}} \tag{7}$$

This definition of an input shaper is referred to as zero vibration-shaper (ZV-shaper). In academia, various extensions to a ZV-shaper approach are known. In most cases they aim at increasing robustness towards parameter change. Those extensions, such as a zero vibration derivative (ZVD)-shaper suppress vibration in a wider frequency range, result however in an increased delay. Since parameter variations can be handled by the parameter adaptation (3), a ZV-shaper is preferable in this case.

Analysis of the structural behavior of the prototype was conducted using finite element modeling and experimental modal analysis [8]. In the case of Z-axis acceleration, the most prominent oscillation response is seen at 9.2 Hz. This resembles a rigid body motion of the entire machine prototype as identified in experimental

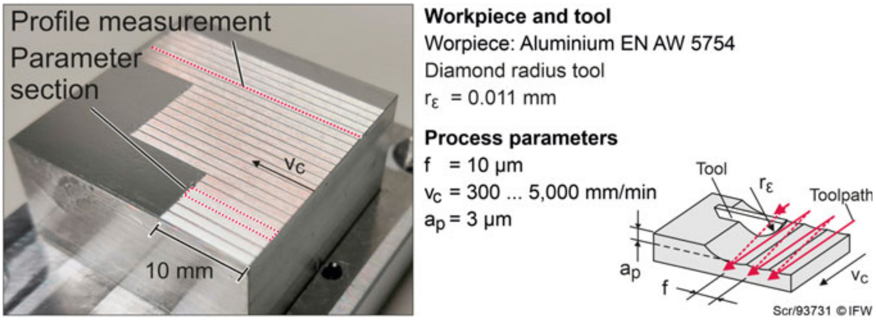

Fig. 16 Workpiece for cutting tests

modal analysis. This oscillation is also present as an oscillation of the electromagnetic X-axis slide relative to the Z-axis slide such that an impact on the workpiece form deviation can be expected and is evaluated in the following.

5.3 Evaluation of Feed-Forward and Input Shaping in Cutting Tests

In order to evaluate the effect of input shaping (IS) and acceleration feed forward (FF), cutting tests with stationary tool according to the setup above were conducted. As shown in Fig. 16 separate sections were planed with three different cutting velocities v_c, two jerk values j and three compensation settings. The acceleration profile of the Z-axis was set as a trapezoidal jerk-limited acceleration profile with an upper acceleration limit of $a_{max} = 5\,\mathrm{m\,s^{-2}}$. This value was however not reached for the jerk and velocity values. As lowest cutting respectively feed velocity, $300\,\mathrm{mm\ min^{-1}}$ was chosen as reference velocity for a typical UP-cutting process. $5,000\,\mathrm{mm\ min^{-1}}$ was chosen as a benchmark velocity for an UP-HPC-cutting process and $2,000\,\mathrm{mm\ min^{-1}}$ as a medium velocity. For each of these velocities, sections were planed with jerk values of $5\,\mathrm{m\ s^{-3}}$, $50\,\mathrm{m\ s^{-3}}$, and additionally $20\,\mathrm{m\ s^{-3}}$ for medium velocity. The lower jerk values serve to benchmark the performance of IS and FF with the conventional approach of limiting axis dynamics. To reduce the effect of cutting forces on the resulting profile, a narrow diamond tool with $r_\varepsilon = 0.011\,\mathrm{mm}$ was applied. For each of the jerk-velocity combinations one section was planed with both, IS and FF activated, both deactivated, and one section with only IS activated. A summary of the process and trajectory parameters can be found in Table 1.

The planed sections were each measured with a tactile profilometer with a spherical probe with $500\,\mu\mathrm{m}$ radius since the focus of this investigation is on the profile deviation rather than roughness. For each section a median profile was calculated from five profile measurements. Figure 17 shows an exemplary median profile for $v_c = 5,000\,\mathrm{mm\,min^{-1}}$. It can be seen that the mentioned rigid vibration mode at

Table 1 Parameter overview for the cutting tests

Section set	Cutting speed v_c mm min^{-1}	Jerk j m s^{-3}	Compensations 1st, 2nd, 3rd section
1	300	5	FF+IS, -, IS
2	300	50	FF+IS, -, IS
3	2,000	5	FF+IS, -, IS
4	2,000	20	FF+IS, -, IS
5	2,000	50	FF+IS, -, IS
6	5,000	5	FF+IS, -, IS
7	5,000	50	FF+IS, -, IS, FF

For all sets: $f = 10\,\mu\text{m}$, $a_p = 3\,\mu\text{m}$, $r_\varepsilon = 0.011\,\text{mm}$, $a_{max} = 5\,\text{m s}^{-2}$

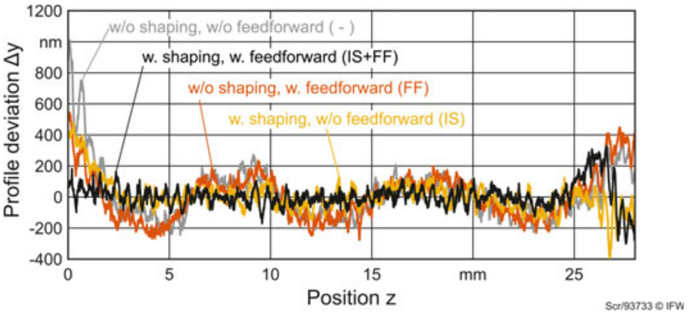

Fig. 17 Exemplary profile measurements of the machined surface for $v_c = 5,000\,\text{mm min}^{-1}$

9.2 Hz results in the dominating waviness in the planed profile with ca. 9 mm wavelength and over 300 nm in amplitude. The waviness is eliminated in the profiles with activated IS, thus showing that the compensation is effective. Regarding FF, it can be seen within the first millimeters of the profile that FF does reduce profile deviation here, since it reduces the tilting of the X-axis. However, quantitative evaluation is not conducted for FF as the spherical probe cannot probe the whole length of the profile and some uncertainty is associated with the alignment of the tactile measurements to each other in Z-direction.

Due to the limitations regarding the quantitative evaluation of FF, only IS is considered below. The analysis focuses on the overall profile deviation. Therefore, the range at the beginning and end of the profile, where the effect from axis acceleration is visible, are cut from the profile measurements for the following analysis. For the remaining part of the profile, the standard deviation S_{std} is calculated as well as the peak-to-peak value S_{p2p} of the profile after filtering with a linear Gaussian profile filter (according to ISO 16610-21) with a cut-off wavelength of 2 mm. S_{std} and S_{p2p} are shown in Fig. 18 for both, profiles with and without IS. It can be seen that for all velocity and jerk combinations, a S_{p2p} value of less than 100 nm is achieved with the use of IS while for deactivated IS S_{p2p} exceeds 100 nm significantly for the higher

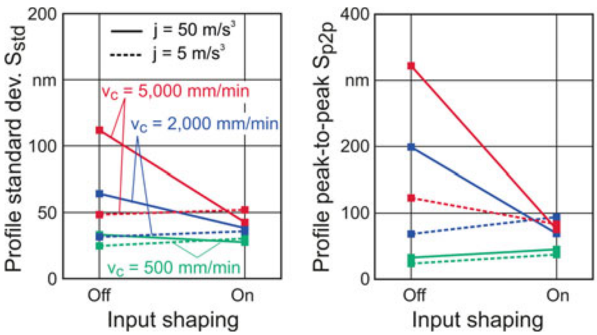

Scr/93737 © IFW

Fig. 18 Profile standard deviation S_{std} (left) and filtered profile peak-to-peak value S_{p2p} (right) for different cutting velocities v_c and jerk values j with and without input shaping

jerk and velocity combinations. This shows that IS can serve to allow for significantly higher feed velocities in UP-cutting applications.

5.4 Internal Sensor Based Prediction of Cutting Quality

A major feature of an active guide is that displacements of the slide position, in this case workpiece-slide position, are available to the control system during the process. Laser Doppler vibrometer measurements at different components of the machine prototype were conducted. They confirmed that the position signal of the levitation guide in Z-direction, which is known from the internal guide displacement sensors, can provide a sufficient estimate for relative tool-workpiece displacements. Therefore, an obvious approach is to predict the resulting form deviation of the workpiece based on the internal sensor signals in order to monitor and predict whether process and controller settings are viable to achieve a specified quality. This can either be done during a cutting process or before the actual process in an air cutting. Given a sufficient reliability of such a prediction, productivity of UP-cutting processes could be improved significantly as scrap parts could be avoided or axis dynamics could be increased with lower safety margins resulting in shorter process times. Furthermore, regarding the assessment of productivity impact, use of internal sensor data allows for analysis over a larger parameter range.

In the following the viability of such an approach is investigated. Figure 19 shows the generalized guide coordinates q_z (feed direction), q_a (roll angle) and x (crossfeed direction) for a feed velocity of $3.000\,\mathrm{mm\,min}^{-1}$ and all combinations with and without FF and IS. It can be seen that the relative effect of IS ad FF can be evaluated more comprehensively by the sensor data than by profile measurements. This is due to higher signal-to-noise ratio as the amplitude is more pronounced in the slide deviation than in the workpiece surface profile. Moreover, disturbances associated with profile measurement are not present. Also, alignment of the profiles is included

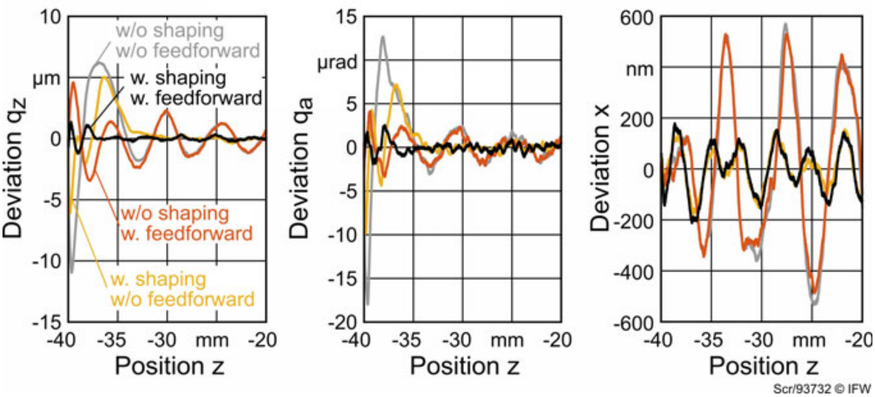

Fig. 19 Internal sensor values for deviation in q_z (left) and roll angle q_a (right) for with and without input shaping and feed forward acceleration compensation for $v_c = 3,000\,\text{mm min}^{-1}$

per se as the Z-position is captured in the same measurement. The discussed effect at 9.2 Hz is also strongly present in all three coordinates and reduced by the use of IS to a large extent.

To the end of evaluating the feasibility of predicting profile deviation based on internal sensor data, the standard deviation S_{std} of the planed sections profiles Sect. 5.3 is compared to the standard deviation values of internal guide sensor data. Figure 20 shows how the S_{std} values for internal guide coordinates q_z and q_a during an air cut correlate with S_{std} values of the measured profiles. The range in z, which is directly affected from axis acceleration, was excluded from evaluation. It can be seen that both, the standard deviation of the q_z and the q_a coordinate show a correlation to the resulting workpiece profile with R^2 values of 0.86 and 0.89 respectively. As expected, the correlation is clearer for higher deviations since the smaller values are more affected by noise and measurement uncertainties. The result shows, that at least for the given vibration mode, the sensory capability of the guide has the potential to predict critical form deviations in the workpiece. The observation that deviations in the guide coordinates are more than a magnitude higher than deviations in the workpiece also highlights the potential of guide position data in terms of sensitivity. However, additional modeling and a higher number of experiments has to be conducted in order to validate the correlation.

5.5 Analysis of Impact on Productivity by Input Shaping and Feed-Forward

This section focuses on evaluating the effect of IS and FF on productivity. The latter section showed that monitoring deviations of the internal guide coordinate

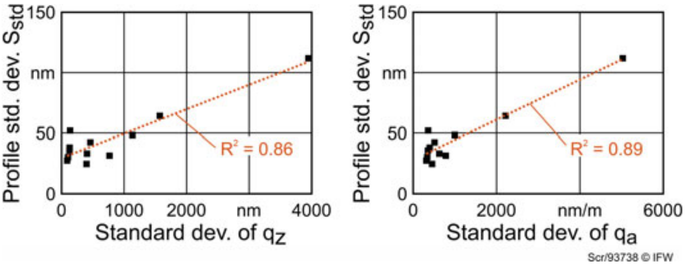

Fig. 20 Comparison of internal signal standard deviation vs profile measurement for q_z (left) and q_a (right)

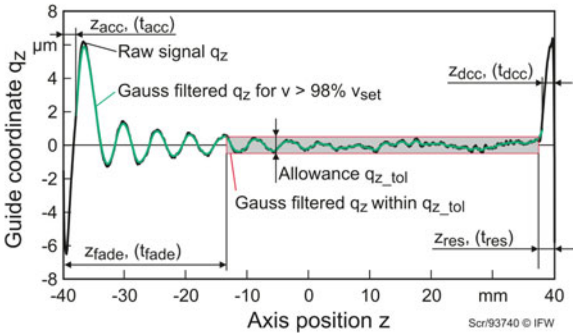

Fig. 21 Definition of the different productivity evaluation times and path lengths

data can be used as a practical tool to predict workpiece form deviations. Thus, the following investigation is based on internal guide coordinate data as they allow for a better sensitivity and more comprehensive parameter combinations. Again, a shaping or line milling process at constant v_c is considered with a jerk limited trapezoidal acceleration profile. Figure 21 shows an exemplary measurement of q_z for a travel range of 80 mm. For further consideration, only the range within which the axis velocity deviates less than 2% from the set-point velocity v_{set} is considered since a constant velocity is assumed to be a process requirement. The path length required to accelerate the slide to 98% v_{set} is referred to as z_{acc} and the corresponding duration as t_{acc}. Analogous, z_{dec} and t_{dec} denote the path length and duration for decelerating the slide from v_{set} to zero. It is assumed that in order to remain below a specified profile deviation, q_z should not exceed an allowance of $\boldsymbol{q_{z\_tol}}$. As the focus is on form deviation, the allowance is applied after low-pass filtering q_z with a linear Gaussian filter at a cut-off wavelength of 2 mm analogously to the profile measurements in the previous section. Based on that, z_{fade} and t_{fade} denote the axis path length and duration required for the dynamic deviations induced by the slide acceleration to decay and to keep within the allowance $\boldsymbol{q_{z\_tol}}$. For deceleration, the residual path length and duration from leaving the allowance $\boldsymbol{q_{z\_tol}}$ to $v = 0$ is denoted with z_{res} and t_{res}.

In order to evaluate the effect of the compensation approaches, the evaluation times and paths z_{fade} and t_{fade} are evaluated depending on different values of $\boldsymbol{q}_{z\_tol}$ for trajectories with different jerk and velocity combinations. The analyzed parameter field includes all combinations of the feed velocities v_{set} of 300, 500, 1000, 2000, 3000, and 5,000 mm min^{-1} and jerk values of 5, 10, 20, and 50 m s^{-3}. An example for how z_{fade} and t_{fade} depend on different values of $\boldsymbol{q}_{z\_tol}$ of up to 2 μm is shown in Fig. 22 for a low velocity of 500 mm min^{-1} and high velocity of 5,000 mm min^{-1}. Due to the high number of parameter combinations, only a selection for reasons of clarity and comprehensibility is shown. The shown characteristics with FF and/or IS as well as without IS and FF are from trajectories with the highest jerk value of 50 m s^{-3}. Additionally, trajectories with a jerk value of 10 m s^{-3} represent the conventional approach of jerk limitation (JL). For both, the figure also shows the values for t_{acc} and z_{acc} as the best possible limit value for each velocity-jerk combination. It can be seen for the lower velocity and high allowances that a high jerk value without any compensations is the best choice of parameters, since higher acceleration time associated with jerk limitation (JL) or the delay from input shaping (IS) are not compensated by reduced fading time. Only below ca. 750 nm allowance, IS gains an advantage as the decay time of the dynamic errors becomes larger than the input shaping delay. For a higher velocity, generally IS is favorable since it effectively reduces the oscillation fading time. Also, it can be seen that FF has higher relative advantage for lower velocities. The reason for this is that FF impacts the slide tilt and displacement mainly during t_{acc}. With t_{acc} becoming shorter in comparison to t_{fade}, the effect of FF also becomes less pronounced.

The chart in Fig. 22 can be used to optimize the process and compensation parameter choice regarding process productivity. However, it also shows that the optimal choice depends largely on the aimed allowances.

In order to discuss the potential to increase productivity by the use of these approaches the solution space for machining an exemplary workpiece is presented. The exemplary workpiece with an extension l_{wp} of 20 mm per line is assumed to be processed in a planing or line milling process. It was shown above that also JL can be beneficial. Thus, all combinations of parameters (jerk, velocity, FF, IS) are included. Further, $\boldsymbol{q}_{z\_tol}$ is set to 1 μm as based on the previous section 1 μm can be assumed to be a reasonable allowance in order to achieve a form deviation of less than 100 nm. Figure 23 shows the time required per line t_{total} and the required axis travel range z_{total}. The time t_{total} is calculated as the sum of t_{fade}, t_{res} and the tool engagement time $t_{\text{cut}} = l_{wp}/v_{set}$. The analog relation applies for z_{total}. The figure depicts resulting values for t_{total} and z_{total} for all feasible parameter combinations. In blue the values for the trajectories with at least one of the presented compensation approaches FF and IS are highlighted. Shown in grey are the resulting values without FF and IS. The most significant improvement in productivity can be seen for higher feed velocities of more than 1,000 mm min^{-1}. This is due to the fact that the tool engagement time for the 20 mm spanning workpiece decreases with increasing feed velocity while the excited vibration amplitude and thus the associated decay time increases. The lowest process time amounts to 0.55 s per line (at $v_c = 5,000$ mm min^{-1}, $j = 10$ m s^{-3}, with IS and FF) with 36.4 mm required axis range. Without IS and FF the lowest process time per

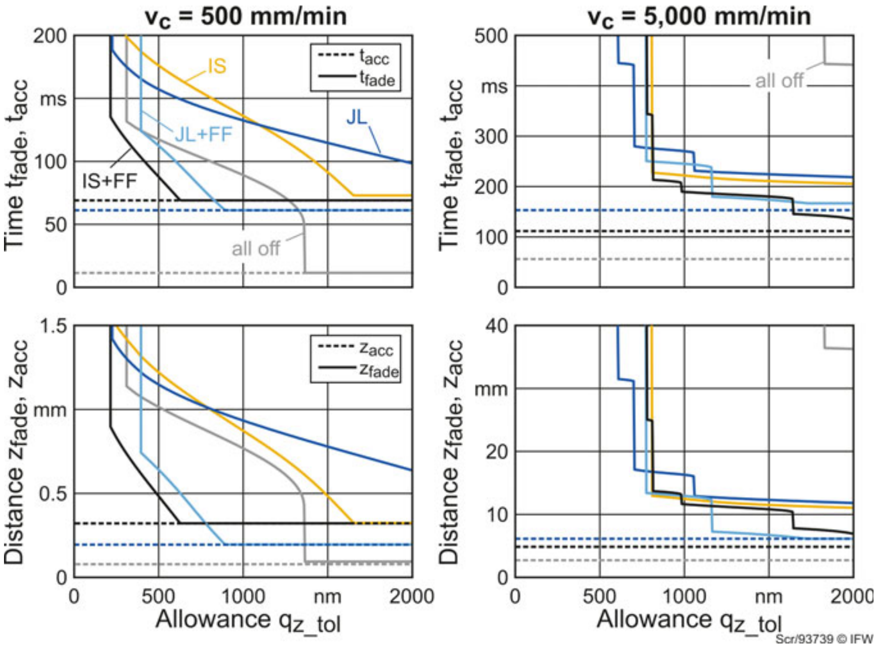

Fig. 22 Times and distances to reach q_{z_tol} for v_c = 500 (left) and 5,000 mm min^{-1} (right). JL = jerk limitation (10 m s^{-3}), IS = input shaping, FF = feed forward

Fig. 23 Solution space for process parameter combinations with and without IS and or FF

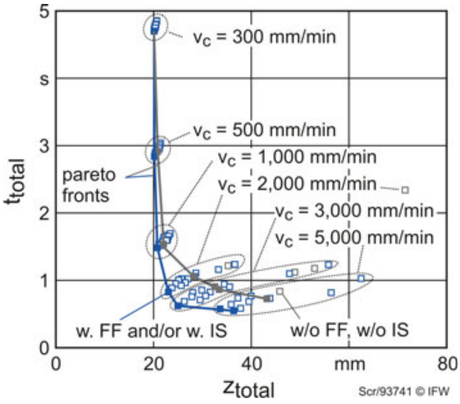

line amounts to 0.73 s at a required axis range of 43.2 mm ($v_c = 5,000\,\text{mm}\,\text{min}^{-1}$, $j = 10\,\text{m}\,\text{s}^{-3}$, without IS and FF). This corresponds to a 24.5% lower process time and 15.7% reduction in required axis range. The results show that IS and FF can allow for significantly increased axis feeds in UP-cutting processes and thus in synergy with the other UP-HPC approaches discussed in the previous chapters increase productivity of UP-cutting processes by large extent.

6 Conclusion and Outlook

The increase in productivity with the UP-HPC approach requires the synergistic interaction of the techniques discussed in the individual chapters. In this chapter, approaches were discussed which allow for increased axis feeds while keeping dynamic workpiece deviations within specified allowances. Firstly, an approach for online parameter estimation of axis models was presented. The methods can be an enabler to increase productivity as it can enable the use for more sophisticated control approaches and reduce the effort to identify system parameters manually. To investigate two-axis motion behavior a laser speckle sensor was introduced that provides a high accuracy and flexibility without the need for a containable grid-plate which often prohibits application during cutting in a machine environment.

With increasing feed velocities, also dynamic errors and excitation of vibration are intensified. Thus, it was investigated how acceleration force feed forward and input shaping can reduce these effects and can thus allow for higher feed velocities and productivity. It was shown that for high velocities above 2,000 mm min^{-1} process times can be reduced by around 24% without increasing feed velocity. Taking into account that such high velocities can only be achieved in combinations with the other approaches developed within the UP-HPC research group, the combined gain in productivity is even higher.

References

1. Altintas, Y., Khoshdarregi, M.R.: Contour error control of CNC machine tools with vibration avoidance. CIRP Ann. **61**(1), 335–338 (2012). https://doi.org/10.1016/j.cirp.2012.03.132
2. Bloem, A., Foremny, E., Schenck, C., Kuhfuss, B.: Using speckle patterns in a direct positioning system. In: 4th International Conference on Nanomanufacturing (nanoMan 2014), Bremen, Germany, 8–10 July 2014 (2014)
3. Bloem, A., Schenck, C., Kuhfuss, B.: 2D position sensor based on speckle correlation. In: Annoni, M., Fassi, I., Wiens, G.J., Dimov, S. (eds.) 10th International Conference on Micromanufacturing (4M/ICOMM 2015), Milan, Italy, pp. 541–544 (2015)
4. Bloem, A., Wilhelmi, P., Schenck, C., Kuhfuss, B.: 2D position sensor based on speckle correlation - experimental setup for high-speed measurements and in field tests. In: 11th International Conference on Micro Manufacturing (ICOMM 2016), Paper No. 17, Irvine/CA, USA (2016)
5. Bloem, A., Schenck, C., Kuhfuss, B.: Adaptive state-space model for ultra-precision feed axis. Procedia Technol. **26**, 20–26 (2016). https://doi.org/10.1016/j.protcy.2016.08.004
6. Bloem, A., Schenck, C., Kuhfuss, B.: Dynamic behavior of ultra precision feed axis at increased velocities. In: Wertheim, R., Ihlefeldt, S., Hochmuth, C., Putz, M. (eds.) Procedia CIRP 46:456-459 (2016). https://doi.org/10.1016/j.procir.2016.04.040.
7. Charrett, T.O.H., Waugh, L., Tatam, R.P.: Speckle velocimetry for high accuracy odometry for a Mars exploration rover. Meas. Sci. Technol. **21**(2), 025301 (2009). https://doi.org/10.1088/0957-0233/21/2/025301
8. Denkena, B., Dahlmann, D., Sassi, N.: Analysis of an ultra-precision positioning system and parametrization of its structural model for error compensation. Procedia CIRP **62**, 335–339 (2017). https://doi.org/10.1016/j.procir.2016.06.054

9. Denkena, B., Bergmann, B., Schreiber, P.: Error compensation strategies for productivity improvement in ultra-precision cutting. In: Euspen's 19th International Conference & Exhibition, Bilbao, ES, June 2019, pp. 562-563 (2019)
10. Gill, P.E., Murray, W., Wright, M.H.: The Levenberg-Marquardt method. In: Practical Optimization, chap. 4.7.3, pp. 136–137. Academic Press, London (1981)
11. Ljung, L.: System Identification: Theory for the User, 2nd edn. Prentice Hall, New Jersey (1987)
12. Peters, W.H., Ranson, W.F.: Digital imaging techniques in experimental stress analysis. Opt. Eng. **21**(3) (1982). https://doi.org/10.1117/12.7972925.
13. Schönemann, L., Berger, D., Dörgeloh, T., Riemer, O., Brinksmeier, E., Krüger, R., Schreiber, P., Denkena, B., Hochbein, J., Parsa, N., Schenck, C., Kuhfuss, B.: Synergistic approaches to ultra-precision high performance cutting. CIRP J. Manuf. Sci. Technol. **28**, 38–51 (2020). https://doi.org/10.1016/j.cirpj.2019.12.001
14. Sencer, B., Dumanli, A., Yamada, Y.: Spline interpolation with optimal frequency spectrum for vibration avoidance. CIRP Ann. (2018). https://doi.org/10.1016/j.cirp.2018.03.002
15. Singhose, W.: Command shaping for flexible systems: a review of the first 50 years. Int. J. Precis. Eng. Manuf. **10**(4), 153–168 (2009). https://doi.org/10.1007/s12541-009-0084-2
16. Tobiason, J.D.: Image correlation displacement sensor. U.S. pat. 8605291. Mitutoyo Corporation (2013)

Achievements and Future Perspectives for Ultra-Precision High Performance Cutting

Lars Schönemann

Abstract This chapter summarizes the final results of the research unit that culminated in a common test stand and gives an outlook on possible future developments.

1 Achievements in Ultra-Precision High Performance Cutting

The capability for ultra-precision (UP) machining at a higher performance has been significantly increased within the scope of the German research unit ("Forschungsgruppe") No. 1845 (FOR1845) funded by the German Research Foundation from 2014 to 2020. The term Ultra-Precision High Performance Cutting (UP-HPC) was coined by the research unit. Generally, the feasibility of the individual approaches has been successfully shown up to prototype level, with many results having the potential to be transferred to industrial applications. In order to show the full synergistic potential of all developments of the FOR1845, a common test stand has been set up (Fig. 1).

With respect to the application of multiple cutting edges in diamond milling (see Chap. 2), it has been shown that a defined and localized thermal expansion of the tool holder substrate is possible. For this purpose, a ring light system was designed that allows for the infrared radiation of the applied light emitting diode (LED) to follow the rotation of the tool spindle up to several thousand revolutions per minute. By continuously measuring the roundness of the tool holder at a reference plane during operation, it was verified that the illuminated thermal actuator expands significantly more than its non-illuminated counterpart at 180° spacing. The expansion may reach up to 1 μm and thus allows for compensating typical mechanical alignment errors of the tools. Furthermore, the expansion is controllable using the capacitive measurement of the reference plane in a feedback loop. This has also been verified in cutting experiments, by comparing the thermal expansion of the reference plane with the actually achieved cutting depth of the diamond tools.

On a fundamental machining level (Chap. 3), it has been demonstrated in an extensive experimental analysis, that for metallic materials the application of high cutting speeds leads to a significant reduction of the resulting cutting forces due

---

L. Schönemann (✉)
Leibniz Institute for Materials Engineering IWT, Bremen, Germany

MAPEX Center for Materials and Processes, University of Bremen, Bremen, Germany
e-mail: schoenemann@iwt.uni-bremen.de

E. Brinksmeier and L. Schönemann (eds.), *Ultra-precision High Performance Cutting*,
Lecture Notes in Production Engineering, https://doi.org/10.1007/978-3-030-83765-5_7

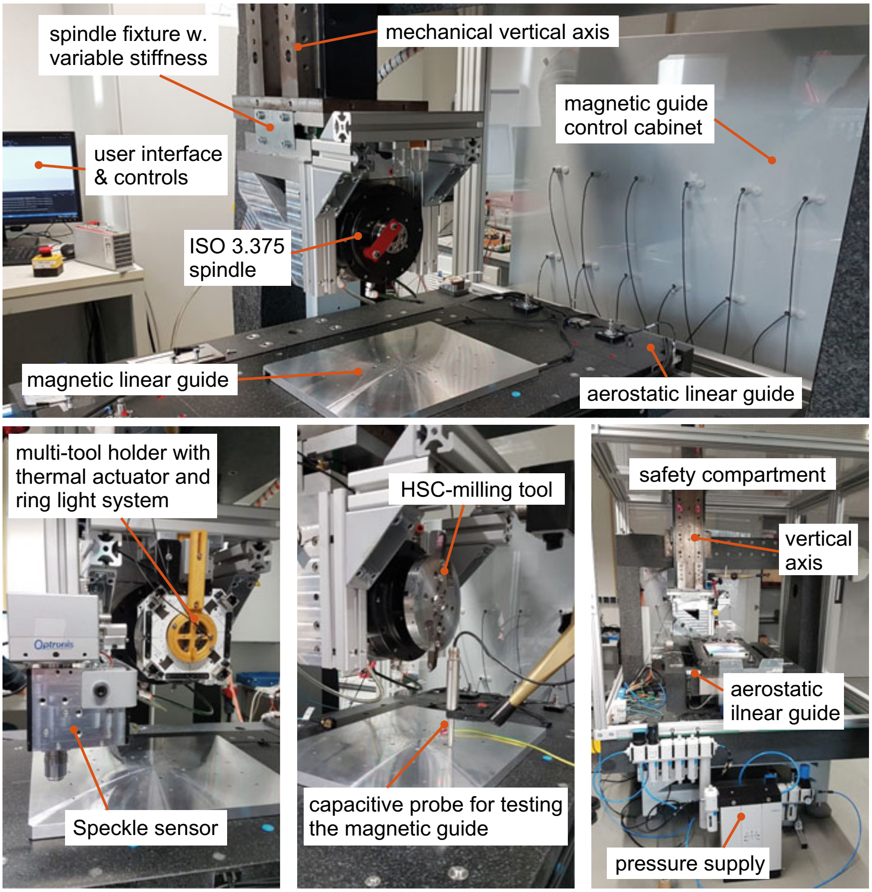

Fig. 1 UP-HPC test stand for evaluating the synergistic performance of all developments

to adiabatic shearing caused in the cutting zone. It is the first time that this effect was demonstrated for ultra-precision machining processes using monocrystalline diamond as a tool material. Along with the reduction of the cutting forces, it was shown that the resulting tool wear is also significantly reduced, extending the tool life in such operations. The short tool-workpiece contact times of UP high speed cutting (HSC) even enable a prolonged machining of steel substrates, although the effect is not as pronounced as e.g. with ultrasonic tool modulation.

For machining brittle materials, a higher critical depth of cut as a result of the increased hydrostatic pressure in the contact zone in HSC could not be generally verified for all materials. Nevertheless, the surface quality after milling was significantly improved for all tested materials when milling at elevated speeds, yielding a reduction of surface roughness up to 91% for selected materials. This may be attributed to an increased ratio of ductile material cutting with this approach, which has been verified offline by an analysis of the subsurface damage as well as during the milling process using acoustic emission (AE) measurements. Overall, UP-HPC has been proven to be beneficial for both metallic and brittle-hard materials.

In order to make full use of the elevated cutting speeds, highly dynamic feed axes are required. For this purpose, an electromagnetic linear guide was designed and built (Chap. 4). This bearing concept not only allows for frictionless movement of the slide at very high accelerations and speeds, but also enables the possibility to compensate movement deviations in six dregrees of freedom (DoF). The realized system offers an acceleration of up to $14\,\mathrm{m\,s^{-2}}$ and a speed of up to $6{,}000\,\mathrm{mm\,min^{-1}}$ with a positioning accuracy of ≤ 300 nm and $<1.9\,\mu\mathrm{rad}$, respectively. By applying a feed-forward control, the impact of dynamic disturbances during acceleration and deceleration of the slide was minimized. Furthermore, the straightness and inclination errors over the complete travel range of 90 mm have been reduced to $<1\,\mu\mathrm{m}$ and $<2\,\mu\mathrm{rad}$, respectively. Moreover, the electromagnetic linear guide exhibits no critical natural frequencies up to 2,300 Hz. Initial tests in a non temperature-controlled environment[1] already showed the capability to machine surfaces with a roughness of less than 40 nm in a planing process using a cutting speed of $6{,}000\,\mathrm{mm\,min^{-1}}$.

Within the FOR1845, significant advances have also been made for the auxiliary processes in diamond machining. It was demonstrated that by using a coupling system with adaptive stiffness, the measurable vibrations of the spindle may be amplified and thereby the sensitivity of unbalance measurements during the setup phase can be improved. In combination with automated balancing systems, a balancing quality grade of $G0.064$ is easily achievable within only a few minutes. For this purpose, two balancing concepts were evaluated for ultra-precision machining applications: a mass-distribution system (spread angle method) based on traveling wave motors and a mass-removing system (fixed position balancing) based on microfluidics. Both systems are capable of reducing the residual unbalance to below the detection threshold of the utilized accelerometers.

On the control side, new approaches for real-time controls with adaptive parameter estimation have been researched. Therefore, the positioning of an exemplary machine axis was modeled and the tracking error between the actual axis movement and the initially identified model parameters was evaluated and compared to a model that could be dynamically parametrized during operation of the axis. It was demonstrated that the latter approach is able to reduce the tracking error from around 10 nm when only using the initial identification to less than 2 nm with the dynamic identification. Furthermore, a speckle-based tracking system was developed that allows for arbitrary machine axes to be tracked in 2D during operation. Moreover, particular attention was given to the control system of the magnetic guide. Here, the influences of dynamic error feed forward (FF) control, jerk limitation (JL) and input shaping (IS) techniques as well as the combination of these approaches were analyzed. It was shown that the settling time of residual vibrations, which are the main source of dynamic errors at high feed velocities, could be successfully reduced by these means. In this way, the

---

[1] As this project was conducted at the Leibniz-University of Hannover, the magnetic axis could not be set up in the temperature and vibration controlled environment of the Laboratory for Precision Machining in Bremen.

machining time is reduced by approx. 25 % without even needing to increase the feed velocity. As this effect is more pronounced at higher speeds, the combined effect of high feed velocities and reduced settling times has the potential to reduce the overall machining times in UP machining even more.

2 Outlook on Possible Future Developments

Over the past few years, the path to achieving high performance in ultra-precision cutting processes has been opened by various developments. Nevertheless, there is still a lot of room for improvements and further developments.

For milling with multiple tools, only the radial offset of the diamond cutting edges has been considered yet to equally engage all applied tools in the cutting operation. In actual machining operations, however, the lateral shift of the tools is just as important for controlling the surface generation of an optical surface, and it has to be evaluated whether the intended localized thermal expansion of the tool holder can be utilized for corrections in this direction as well. Furthermore, a thermal drift of the systems occurs especially at long processing times, which has to be counteracted by improved insulation of the thermal actuator.

In machining, the potential benefit of HSC cutting has been shown for two important material classes—metals and brittle-hard semiconductors—but there are other interesting materials, like glassy carbon for example, for which this benefit still has to be verified.

While the performance of the electromagnetic guide is already excellent under the given circumstances, its performance can be still improved by applying more precise and more robust sensor systems and also by implementing even more sophisticated control techniques. Also, it has to be taken into account that all results so far have been obtained under uncontrolled environmental conditions (temperature, air pressure, humidity, vibration isolation). Thus, it is expected that in a fully controlled environment the performance of the magnetic guide would increase per se.

The automated balancing procedures are already a huge improvement over the typical manual tool and workpiece setting. However, this only automates one part of the time-consuming setup procedure, while other areas, such as part centering or tool alignment, still remain manual work in many cases. Future work should focus on automating those parts as well.

As for the controls, it has been shown once again that achieving a high speed in the machine axes is only one part of the story and that it is just as important to stabilize a machining axis during its acceleration and deceleration phase as well as to identify and compensate dynamic disturbances during operation. Here, machine learning and the use of artificial intelligence are only starting to be researched for their application in error detection and compensation.

Overall, the road towards true ultra-precision high performance cutting and its industrial application is still long, but we have made significant steps to progress towards this goal.